THE UNIVERSITY *of* EDINBURGH

The effect of the *Pdgfb*^{ret} mutation on Cardiovascular Homeostasis

David John Craig

PhD in Cardiovascular Biology

University of Edinburgh

2022

Declaration

I, David John Craig, declare that this dissertation is the result of my own work, except where explicitly indicated in the text.

The data presented in this thesis has not been submitted for any other degree or professional qualification.

Scientific Abstract

Platelet derived growth factor B (PDGFB) / PDGFRβ signalling is a key regulator of the cardiovascular system in development, health, and disease. During angiogenesis PDGFB regulates pericyte migration and proliferation during development and in tissue repair. Pericytes confer vessel stability, maintain vessel integrity, and control vascular tone. In the field of regenerative medicine, pericytes have also risen to prominence as they were discovered to be the *in-situ* counterpart of mesenchymal stem/stromal cells (MSCs). *Pdgfb*$^{ret/ret}$ mutant mice are pericyte-deficient. The PDGFB retention motif is deleted, reducing PDGFB retention in the pericellular space and extracellular matrix and therefore pericyte recruitment during angiogenesis. This reduction in vascular pericyte coverage in *pdgfb*$^{ret/ret}$ mice manifests in phenotypic differences compared with *pdgfb*$^{+/+}$ and *pdgfb*$^{ret/+}$ littermates. Of relevance, is the reported development of vascular associated brain calcification in 4–12-month-old *pdgfb*$^{ret/ret}$ mice and alterations to left ventricular structure from 10 to 20 weeks of age.

In this thesis, I have investigated the hypothesis that calcification develops throughout the vasculature in *pdgfb*$^{ret/ret}$ mice and that alteration of left ventricular structure leads to a progressive decline in heart function. I also hypothesised that disruption to PDGFB/PDGFRβ signalling *in vivo* influences the *in vitro* properties of MSCs. To address my hypotheses, I used a combination of cardiovascular imaging techniques, positron emission tomography/computed tomography (PET/CT) and high-resolution cardiac ultrasound, alongside *in vitro* MSC osteogenic assays.

Contrary to my original hypothesis, results of PET/CT imaging using ^{18}F-NaF, a radioactive tracer with the propensity to bind to hydroxyapatite calcification, did not reveal any areas of ectopic calcification out with the brain in male or female *pdgfb*$^{ret/ret}$ mice. No significant calcification was observed in the aortic arch, the descending thoracic aorta, heart, or kidneys. Indeed, calcification was restricted to the brain at 12 months of age and completely absent from *pdgfb*$^{+/+}$ and *pdgb*$^{ret/+}$ littermates. However, I did observe that the extent and anatomical location of brain calcification was variable in *pdgfb*$^{ret/ret}$ mice. Using high resolution cardiac ultrasound, I next evaluated the cardiac phenotype exhibited in male and female *pdgfb*$^{ret/ret}$ mice over the course of 12 months. The results of this study reveal that both male and female *pdgfb*$^{ret/ret}$ mice

exhibit signs of cardiac dilation with increasing left ventricular end diastolic area at 3 months of age, whereas females exhibit an increase in left ventricular mass that may be the result of hypertrophic remodelling or oedema. However, over the course of 6, 9 and 12 months, this phenotype resolves in both male and female *pdgfb*$^{ret/ret}$ mice and normal contractile function is maintained. Further analysis of cardiac structure and function was performed using speckle tracking echocardiography (STE) in a combined male and female cohort of *pdgfb*$^{+/+}$, *pdgfb*$^{ret/+}$ and *pdgfb*$^{ret/ret}$ mice. Using STE, subtle changes to segmental systolic and diastolic cardiac strain were detected at 9 and 12 months of age in *pdgfb*$^{ret/ret}$ mice. These changes may preclude the onset of deterioration of cardiac function in *pdgfb*$^{ret/ret}$ mice and requires further investigation beyond 12 months of age to conclude. Finally, I examined the effects of the *pdgfb*^{ret} mutation on the osteogenic potential of MSCs derived from large coronary vessels and various vascularised tissues including the kidney, the skeletal muscle, and the heart *in vitro*. Quantification of osteogenic potential saw an increase in calcium deposition in combined *pdgfb*^{ret} MSC tissues. Tissue specific osteogenic potential was highly variable although there was a trend towards an increased osteogenesis in *pdgfb*^{ret} mutant tissues.

Together, data from my studies indicate that *pdgfb*$^{ret/ret}$ mice exhibit a transient cardiac phenotype which is ameliorated and have variable levels of calcification exclusive to the brain at 12 months of age. This data also indicates that MSCs derived from *pdgfb*^{ret} mutants have greater osteogenic potential although the tissue specificity of this potential requires further investigation.

Lay Summary

Communication between the cells of the blood vessel wall is key to maintaining a healthy heart and blood vessels. PDGFB is a messenger molecule sent by endothelial cells that line the blood vessel wall, to attract another type of cell, pericytes, that help stabilise the blood vessel. Using genetically modified mutant mice, with changes to the PDGFB messenger, alongside specialised imaging, and cellular studies, I wished to understand what happens when endothelial cells and pericytes cannot communicate properly. Previous studies have shown that reduced communication between pericytes and endothelial cells in these genetically modified mice results in calcium deposits in the brain and changes to the structure of the heart. Firstly, I wanted to know if there was any calcification elsewhere in these mice. Using specialised imaging of the whole body, I found no evidence of calcium deposits in the heart, kidneys or aorta of mutant mice and that levels of brain calcification were highly variable. Next, I performed ultrasound heart scans on the mutant mice and found that while younger mice showed changes to heart structure these changes largely disappeared as the mice became older. However, subtle changes to heart function persisted which may suggest that further aging could cause in a decrease in heart function. Finally, it is known that stem cells associated with blood vessels generate calcium when cultured in a dish in specialised conditions. Here, I wanted to know whether these cells taken from the heart, kidney, skeletal muscle, and coronary vessels of mutant mice maintain this ability. I observed that these cells did generate calcium, but not more than cells from non-mutant mice. In summary, I characterised the effects of breakdown of PDGFB-mediated communication between pericytes and endothelial cells in various tissues. I found changes to heart structure in young mice that resolve with time and that calcification was confined to the brain in older mutant mice.

Acknowledgements

I would like to thank the British Heart Foundation (BHF) for supporting and funding my doctoral studies.

For her continued guidance and support during my PhD I would like to thank my supervisor Dr Mihaela Crisan. She is an excellent teacher and mentor and embodies what I believe a scientist should be. Her endless enthusiasm and curiosity for science has transferred onto me and kept me motivated even when the times were tough! I would also like to thank my second supervisor Dr Gillian Gray for her time and guidance throughout my PhD especially with reading and reviewing my thesis.

I would like to thank the other members of my thesis committee Professor Leslie Forrester and Dr Adriana Tavares for guidance and help over the course of the PhD and for their feedback in committee meetings. Additionally, I would like to thank Dr Adriana Tavares for all her help in teaching me to analyse my PET/CT and with reviewing that portion of my thesis.

Thank you to the people from the Crisan lab, both past and present; Diana Sa da Bandeira, Zaniah Gonzalez Galofre, Telma Ventura, Jemma Makepeace, Victoria Reid, Ana Barbosa, Madalena Marques, Dorota Stefancova, Kalyani Pandya, Yvan Marc, Heeyoun Hur, Anna Beletski, Tanushree Tripathi, Jenny Shen and Xinyue He. It has been a pleasure and a privilege to work with, learn from and teach such a fantastic group of people. You will all be missed greatly!

I would like to thank Professor Bruno Peault and lab members for their scientific contributions to lab meetings, especially Mario “Big Papi” Gomez and Isaac “Tigre” Shaw, who have helped me with my work and who have been great friends to me over the course of my studies.

I would also like to thank Adrian Thomson and Carlos Alcaide-Corral for performing the ultrasound and PET/CT scans, respectively.

I would like to thank all the facilities and admin staff at CVS and CRM for their help over the years.

I would like to thank the friends I have made over the years during my PhD outside of the lab especially Manolis Solomonidis and Adrian Garcia-Burgos. Hanging out with you guys outside of the lab kept me sane and I wish you both luck on your future ventures and careers! We will have another reunion soon!

For her continued support during my PhD, I want to thank my girlfriend, Eleni Vali. I couldn't have done it without you. The love, care and understanding that you have shown me, even when I was not the easiest person to get along with and through the most challenging times of my life, will never be forgotten. S'agapo poli.

To my mum and my brother John-Anthony, I really don't have the words to express how much your support has meant to me through all my life. John-Anthony, I want you to know all the support you have given me has not gone unnoticed and is greatly appreciated. I hope I make you as proud of me as I am of you and the person you have become. Mum, thank you for the lessons you have taught me and the sacrifices you have made to make me into the person I am. You encouraged me to accomplish all of my goals and dreams, I really can't thank you enough. You are the best mum anyone could wish for. This thesis is as much the product of your hard work as it is mine. Thank you, I love you both.

Finally, I would like to dedicate this thesis to my father John Craig, who we lost last year. If he were here, I would thank him for everything he did for me growing up and in my adult life. I am so lucky to have known him and especially to have had him as my dad. He was my inspiration for continued study of cardiovascular biology. He was also my role model, my friend, and my hero. I miss and think about him every day. This is for you auld yin.

Contributions

I would like to acknowledge the contribution of Diana Sa da Bandeira of the gel image for Figure 2.2 and records of embryonic genotyping data used in Figure 7.1.

I would like to acknowledge the contributions of the following people in performing osteogenic assays, MSC cell culture and MSC osteogenesis images used in Figure 6.2-6.7: Mario Gomez-Salazar, Manon Alexandre, Ana Barbosa and Dorota Stefancova.

Figures; 1.1, 1.3, 3.1, 4.1, 5.1 ,6.1, 6.2 were created with BioRender.com.

Publications, presentations, and awards related to this work:

Oral Presentations

- BHF Student Conference 2022, University of Leeds, UK
- CVS Symposium 2020, Online
- CRM PhD Day 2019, University of Edinburgh, Edinburgh, UK
- CRM Internal Seminar Series 2019, University of Edinburgh, Edinburgh, UK
- CRM Retreat 2019, Peebles, University of Edinburgh, Edinburgh, UK
- Centre for Regenerative Medicine (CRM) PhD Day 2018, University of Edinburgh, UK

Poster Presentations

- CVS Symposium 2022, Edinburgh, University of Edinburgh, Edinburgh, UK
- Scottish Cardiovascular Forum 2022, University of Ulster, Derry/Londonderry, UK
- CRM Poster Day 2019, Edinburgh, University of Edinburgh, Edinburgh, UK
- CVS Symposium 2018, Edinburgh, University of Edinburgh, Edinburgh, UK
- BHF Student Conference 2018, Imperial College London, London, UK

Awards

- 1st Place Poster, Scottish Cardiovascular Forum 2022, University of Ulster
- Best Discussion, Tsukuba Summer Research Program 2019, University of Tsukuba, Tsukuba, Japan
- Best First Year PhD Student Talk, CRM PhD Day 2018
- 2nd Place Poster, CVS Symposium 2018
- 2nd Place Poster, BHF Student Conference 2018, Imperial College London

Publications

- Craig, D. J., James, A. W., Wang, Y., Tavian, M., Crisan, M., & Péault, B. M. (2022). Blood Vessel Resident Human Stem Cells in Health and Disease. *Stem cells translational medicine*, *11*(1), 35–43.
- Craig, D. J., Thomson, A. J., Moran, C. M., Betsholtz, C., Gray, G. A., & Crisan, M., The role of the *pdgfb*^{ret} mutation in cardiac structure and function *in vivo, in preparation*.
- Craig, D. J., Alcaide-Corral, C. Betsholtz, C., Gray GA., Tavares., AAS., & Crisan M., The role of the *pdgfb*^{ret} mutation in vascular calcification *in vivo, in preparation.*
- Craig, D. J., Gomez-Salazar, M., Barbosa, A., Stefancova, D., Alexandre, M., Betsholtz, C., Péault, B., & Crisan, M., The role of the *pdgfb*^{ret} mutation in mesenchymal stem cell osteogenesis *in vitro, in preparation*.

Contents

List of Figures

List of Tables

Chapter 1: General Introduction

The Cardiovascular System

William Harvey, a 15th century physician, devised the modern model of the circulation and the cardiovascular system (Aird, 2011). Harvey discovered that blood circulates not only in the lung but throughout the whole body. This model is the foundation from which our understanding of the cardiovascular system originates. The cardiovascular system consists of two main circulatory systems: the systemic and pulmonary systems.

The function of the systemic circulation is to pump oxygenated blood to the organs and tissues of the body. The heart acts as the pumping mechanism driven by propagation of electrical signals across the myocardial tissue. Blood vessels are an essential part of our circulatory system. There are five major blood vessel types, from largest to smallest, these are arteries, arterioles, veins, venules, and capillaries all with distinct physiological structure. Oxygenated blood is carried in arteries to arterioles then to capillary beds. Here, in organs and tissues, nutrients and oxygens are exchanged. The deoxygenated blood is then sent to venules and veins, back to the heart. Deoxygenated blood is then sent via the pulmonary circulation to the lungs, the major site of oxygen and gas exchange, where it is reoxygenated. Cardiovascular homeostasis is maintained by the balance and interplay between molecules, hormones and the various cell types of the heart and blood vessels.

A thousand years before the model proposed by Harvey, the ancient Greek scholar, Hippocrates believed that an imbalance of the body's intrinsic properties was the major driver of disease pathology. Over two thousand years later, scientists, physicians and the wider medical community are driven to find answers and mechanistic insight into the cause of pathological diseases; including those of the cardiovascular system.

Cardiovascular Disease

Cardiovascular disease (CVD), initially viewed as a disease of modern humans driven by modern diet and contemporary lifestyles, has been present in society from as far back as the ancient Egyptians and in prehistoric societies (Hajar, 2017). Computed

tomography scans of mummified remains from 4 ancient societies from across the world revealed the presence of atherosclerotic lesions in over a third (47/137) of the mummies scanned (Thompson *et al.*, 2013). Today, CVD accounts for over a third of global mortality (Roth *et al.*, 2020).

In the UK, over 168,000 people die each year from heart and circulatory diseases and in 2020 in Scotland, over 17,000 people died due to CVD (Health Intelligence Team, 2022). Although the death rate from CVD disease is in decline, it is still one of the greatest causes of deaths globally (Mensah *et al.*, 2017). CVD is also a major cause of global morbidity and disability, and since 1990 has led to an increase in disability adjusted life years and an increase in years of life lost (Roth *et al.*, 2020). CVD is not a term for a specific disease; in fact, it is an umbrella term that encapsulates many different diseases such as atherosclerosis, stroke, myocardial infarction (MI) and others. Common risk factors for all CVDs include sedentary lifestyle, obesity, smoking, hypertension and hypercholesterolaemia. Aging is also an important risk factor for CVD as it has greater prevalence in the elderly (>75 years of age) but still causes a great number of premature deaths in both males and females under 75 years of age (Rodgers *et al.*, 2019). Aging leads to a number of adverse physiological changes in the heart such as left ventricular hypertrophy, fibrosis, or aortic valve calcification (Merz and Cheng, 2016). These factors combined with an increase in the proportion of the elderly in the population, lead to a substantial CVD-related economic cost to health care providers worldwide.

It is estimated that in 2012/2013, the NHS in England spent approximately £6.8 billion on the treatment of CVD with the highest cost being in emergency care and in prescription of pharmacological treatments (Bhatnagar *et al.*, 2015). This substantial economic burden is not restricted to high-income countries but also affects low- and middle-income countries such as China, Brazil and Mexico. The total economic loss due to CVD to low- and middle-income countries was estimated to $3.7 trillion between 2011-2015 (Gheorghe *et al.*, 2018). In summary, CVD is a global problem affecting the health, welfare, and economics of our society, but what can we do reduce not only the mortality and morbidity of CVD but also its economic burden worldwide?

The answer lies in medical and scientific research performed by scientists and clinicians to investigate CVD in all of its forms. Research is essential in combatting

CVD whether this be through clinical trials of the latest novel anti-hypertensive agents or basic research to understand the fundamentals of molecular and cellular interactions involved in cardiovascular development, health, and disease.

Sex differences in the Cardiovascular System and CVD

Biological sex affects the physiological cardiovascular development and the manifestation of CVD. Differences exist between the healthy hearts of human males and females. In adolescent humans, males have an increased stroke volume and ejection fraction suggesting that sex hormones may play a role in the sexual dimorphisms exhibited in humans in terms of cardiac function (Marcus *et al.*, 1999; Cain *et al.*, 2009). One study reported greater left ventricular volume and mass as measured by magnetic resonance imaging in healthy males than healthy females (Salton *et al.*, 2002). The cardioprotective effect of the female sex hormone, oestrogen, in pre-menopausal females compared with males of the same aged has long been established. However, in certain cardiovascular conditions such as stroke, post-menopausal females have more severe short-term clinical outcomes (Manwani and McCullough, 2012; Rodgers *et al.*, 2019). Females are underrepresented in cardiovascular clinical trials which can lead to the development of treatments that may offer no benefit or is indeed harmful to females (Tobb, Kocher and Bullock-Palmer, 2022). Furthermore, it is estimated that around 80% of rodent studies as of 2009 were conducted in male animals (Zakiniaeiz *et al.*, 2016). As a result of the underrepresentation of females in both clinical and preclinical research, the National Institute of Health in 2015 sent out a “call for action” and asked for the use of male and female animals in preclinical cardiovascular research due to the prominent effects that sex has on cardiovascular function in humans (Arnegard *et al.*, 2020). However, although cardiac development in mouse and humans is similar (Krishnan *et al.*, 2014), direct translation of studies investigating rodent cardiac function and models of CVD is challenging.

In pre-clinical studies, differences in cardiac development and disease between males and females have been shown using transgenic and non-transgenic animal models. Myocardial contraction and relaxation rates differ between male and female mice due to differences in the expression or action of ion channels in cardiomyocytes (Blenck *et*

al., 2016). This is also due to differences in the composition of contractile filaments in male and female rodent hearts (Schaible *et al.*, 1984).

Differences have also been observed in the male and female rodents in numerous CVD models. Aortic banding is a surgical procedure to induce left ventricular hypertrophy and heart failure in rodents. Interestingly, while the use of this technique led to ventricular hypertrophy in both male and female rats, in the long term, only male rats developed heart failure and exhibited chamber dilation (Douglas *et al.*, 1998). Differences between males and females in terms of hypertrophic response have been identified also at the mRNA level in a model of cardiac hypertrophy induced by prolonged angiotensin treatment (Harrington *et al.*, 2017). Sex differences have also been observed in the spontaneously hypertensive rat (SHR), model of hypertension in aging. Both male and female SHR develop progressive hypertension, ventricular hypertrophy, and fibrosis. However, heart failure in male SHRs occurred at 15 months whereas females had a reduced hypertensive response and greater mortality rates until 18 months of age (Chan *et al.*, 2011). Furthermore, several rodent models of MI have exhibited sex differences. For example, MI induced by coronary artery ligation in C57BL/6J mice evoke a similar scar size in male and female mice. However, due to the activation of genes involved in angiogenesis, extracellular matrix deposition and immune response, female mice had a greater survival rate and were less likely to exhibit cardiac dilation (Chen *et al.*, 2010).

The use of both male and females' animals in cardiovascular research to understand both cardiac development and diseases is essential as it will lead to more effective, personalised treatment for a host of CVD in male and female patients.

Vascular Calcification

Vascular calcification is an independent risk factor of cardiovascular events which affects both males and females. It can be broadly based upon the location within the blood vessel as either intimal or medial calcification. Vascular calcification can have significant clinical consequences which can depend greatly upon the severity and location of calcified lesions within the vasculature. Within arteries the formation of calcified lesions may lead to stiffening of the vessel and reduced vessel compliance impairing the ability of the artery to regulate blood pressure which may lead to

hypertension (Zhu *et al.*, 2012). Furthermore, calcification of blood vessels leads to narrowing of the lumen of the vessel adversely affecting blood flow and in severe cases can fully occlude blood flow which may lead to ischaemia and tissue damage (Zhu *et al.*, 2012). Calcification of coronary arteries leads to myocardial infarction and calcification of carotid arteries causes stroke. Additionally calcification of the renal vasculature may also occur impairing kidney function through a reduction of blood flow to the kidneys, subsequently resulting in chronic kidney disease and end stage renal disease (Zhu *et al.*, 2012). Furthermore, in calcification of the medial layer of the aorta is a key feature of aortic aneurysm, a severe disease where the aortic diameter is enlarged to the point of rupture with only a third of patients surviving such an event (Fletcher *et al.*, 2022).. In this disease moderate to high levels of medial microcalcification precedes loss of the elastin leading to lack of vessel compliance, increased diameter and eventual rupture (Fletcher *et al.*, 2022).

Extracellular matrix remodelling, osteo/chondrogenic differentiation and apoptosis of blood vessel cells contribute to vessel calcification (Pescatore, Gamarra and Liberman, 2019). Indeed, all the underlying mechanisms of vascular calcification are not fully understood but a few key processes have been identified. This includes the osteogenic differentiation of vascular smooth muscle cells and other vascular cell types which contribute to the direct formation of calcium crystals in the extracellular matrix. This phenotypic switch includes upregulation of osteochondrogenic markers such as runx2 and osteopontin which are also up regulated in the cells involved in bone formation (Leszczynska *et al.*, 2016). Matrix vesicles released from vascular smooth muscle cells contain enzymes and other factors which promote extracellular matrix mineralization (Pescatore, Gamarra and Liberman, 2019). Inflammation is also a major factor driving calcification of blood vessels as cytokines and proinflammatory molecules interleukin-6 and tumour necrosis factor-α can cause osteogenic differentiation of vascular smooth muscle cells further enhancing calcification (Pescatore, Gamarra and Liberman, 2019). Dysregulation of calcium and phosphate metabolism can also enhance vascular calcification as calcified lesions primarily consist of calcium and phosphate. This has been shown in aging and in individuals with genetic mutations affecting genes involving regulators of calcium and phosphate metabolism. One example being mutations in the Klotho

gene involved in regulation of phosphate metabolism and oxidative stress which leads to vascular calcification (Xu and Sun, 2015)

Computed tomography (CT) scans use x-rays to image calcium deposition in coronary vessels and assign a score between 1-100 to determine cardiovascular risk. Coronary artery calcium scores assessed by CT angiography are greater in males than females and in males their tends be a greater multi vessel involvement (Kim *et al.*, 2021). This suggests that males have a higher risk of adverse cardiac event and multi vessel involvement means that males develop calcification in more than one coronary vessel. Vascular calcification was initially thought to be a passive process occurring because of a high phosphorous and calcium concentration environment; however, as discussed it is a complex active process involving many cell types and occurs in patients with kidney disease, diabetes, hypertension, dislipaemia and atherosclerosis (Singh, Tandon and Tandon, 2021). Differences in vascular calcification in males and females have also been identified. Males develop vascular disease, including atherosclerosis, at an younger age than females, approximately 7 to10 years earlier (Maas and Appelman, 2010). Circulating levels of testosterone are positively associated with vascular calcification (Woodward *et al.*, 2021).In elderly male patients with stable coronary artery disease, serum testosterone levels are inversely associated with vascular calcification (Woodward *et al.*, 2021). Female are protected against cardiovascular disease; until menopause, where changes to a females hormonal profile results in a loss of these protective effects. The decline of oestrogen levels during and post menopause drives the increased incidence of vascular disease. The anatomical location of calcified lesions differs between men and women with men exhibiting a higher level of coronary artery calcification and women having a greater level of calcification in peripheral arteries (Hiramoto *et al.*, 2014; Shaw *et al.*, 2018). Furthermore, in aortic stenosis, the calcification of aortic valve leaflets, men exhibit a greater level of valvular calcification but women present with a greater degree of fibrosis in valve leaflets (Simard *et al.*, 2017). This example further highlights differences in the pathophysiological processes underlying cardiovascular disease in males and females.

Atherosclerosis is a major cause of morbidity and mortality globally (Libby *et al.*, 2019). The atherosclerotic process by which fatty lesions build up in the artery wall and can lead to MI, stroke, and peripheral artery disease (Libby, 2021). Calcification may occur

with atherosclerotic plaques in two phases, with an initial phase of microcalcification and a later phase of macroscopic calcification. In the initial phase, inflammation occurs with macrophages moving into the large lipid core. Micro calcification occurs within the necrotic plaque core as consequence of cell death and apoptosis. From here one of two outcomes can occur; the plaque will sufficiently calcify and become stable through isolation of the inflammatory immune response or the plaque ruptures causing thrombotic occlusion of the vessel (Joshi *et al.*, 2014). The stable plaques are considered the end-stage of the calcifying process leading to macroscopic calcifications whilst plaques liable to rupture are unstable and contain active micro calcification. Vascular calcification is a complex process with many cells resident within the blood vessel walls being implicated in its progression.

Cellular Inhabitants of Blood Vessels in Homeostasis and Disease

The blood vessel wall is comprised of many cell types all of which have unique morphology and functions. Blood vessels range in size in order from the largest being arteries and arterioles, then veins and venules and the smallest being capillaries. Each vessel type shares a common structure but have some changes to their cellular constituents. Arteries and veins have three heterogeneous layers that include the *tunica intima*, *tunica media* and *tunica adventitia* (Figure 1.1A). Capillaries are composed of endothelial cells surrounded by pericytes, that share the basement functions in the maintenance of cardiovascular health or in driving CVD (Figure 1.1B).

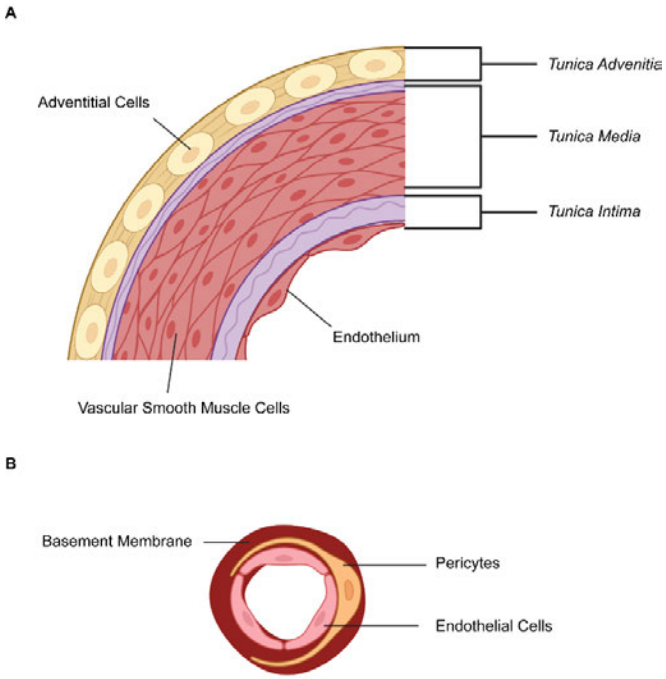

Figure 1.1: Blood Vessel Structure

(A) Larger vessels are comprised of 3 layers. The *tunica adventitia* consisting of connective tissue, nerves, and vasa vasorum and containing resident adventitial cells. *Tunica media,* the middle segment of the vessel containing vascular smooth muscle cells and connective tissue. The *tunica intima*, the innermost layer of arteries and veins consists of a continuous layer of endothelial cells surrounded by subendothelial connective tissue. **(B)** Capillaries lack the adventitial and medial layers and consist of endothelial cells with pericytes wrapped around and both embedded in a shared basement membrane.

Endothelial Cells

Initially, endothelial cells were thought to act as a barrier between the blood and tissue; however, they are active participants in vascular function. The endothelium controls vasoconstriction, vasorelaxation and the transport of macromolecules, hormones, platelets and blood cells between the blood and tissue (Krüger-Genge *et al.*, 2019). However, endothelial cells are heterogenous having different functions depending upon the organs in which they reside and the blood vessel type. Endothelial cells can be characterised and distinguished from neighbouring cells due to their morphology and expression of cellular surface molecules. Common markers include cluster of differentiation 31 (CD31, PECAM-1), CD34, CD144 (VE-cadherin), CD146 (MCAM, S-endo-1) and von-Willebrand factor (vWF) (Craig *et al.*, 2022). Endothelial cells are key in angiogenesis, the growth, and the formation of blood vessels from the existing vasculature. After degradation of the basement membrane and detachment of pericytes, stimulation by angiogenic signals induces functional and morphological changes in endothelial cells called stalk or tip endothelial cells. Stalk cells extend from the surface of the existing vasculature and direct the spout towards angiogenic stimuli (Naito, Iba and Takakura, 2020). The specification into stalk or tip endothelial cells is driven by the notch and vascular endothelial growth factor (VEGF) A signalling (Naito, Iba and Takakura, 2020).

As well as their ability to maintain vessel homeostasis and angiogenesis, endothelial cells have also been shown to play role in CVDs. For example, after MI in mice, endogenous endothelial cells in the heart contribute to neovascularisation through clonal proliferation in the infarct border (Li *et al.*, 2019). In atherosclerosis in mice, transforming growth factor (TGF-β) can cause a phenotypic change in endothelial cells into pro-inflammatory phenotype and inhibition of TGF-β in the endothelium may reverse this process (Howe and Fish, 2019). TGF-β is a known driver of endothelial-to-mesenchymal transition (EndMT). In EndMT, endothelial cells detach, migrate and begin to acquire a mesenchymal cell phenotype while losing their endothelial characteristics (Bischoff, 2019). EndMT is also one mechanism where endothelial cells may contribute to vascular calcification (L. Zhang *et al.*, 2021). In vascular calcification, endothelial cell transition to a mesenchymal osteogenic cell type occurs. Evidence of this comes from the use of the matrix Gla protein null ($MGP^{-/-}$) mouse which develops vascular calcification and endothelial dysfunction (Yao *et al.*, 2015). MGP, a matrix protein, plays a key role in osteogenic process in binding osteogenic molecules, bone morphogenic proteins (BMP) 2,4 and 7 which also promote vascular calcification (Yao, Shahbazian and Boström, 2008). Degradation of the internal elastic lamina in the absence of MGP results in detachment of endothelial cells making them susceptible to undergo EndMT (Yao *et al.*, 2015). This phenotypic switching of blood vessel resident cells is a driving force behind CVDs.

Vascular Smooth Muscle Cells

In CVD, vascular smooth muscle cells (VSMCs) like endothelial cells can change their phenotype as a response to stimuli in the cellular environment in CVD. In healthy vessels, VSMCs play a key role in maintaining vessel structure and regulate intravascular pressure. VSMCs have a long spindle-like morphology, constitute most of the *tunica media* and have a contractile phenotype under homeostatic conditions. This phenotype is characterized by the expression of contractile proteins including α-smooth muscle actin (αSMA) and smooth muscle myosin heavy chain (myosin 11, MYH11). Contractile vSMCs regulate vessel diameter and by extension blood pressure. In healthy vessels, VSMCs also secrete collagen, elastin and other proteoglycans which contribute to the production of extracellular matrix. VSMCs are

not terminally differentiated cells and retain cellular plasticity with the ability to readily change phenotype, changing their morphology and cellular marker expression.

In atherosclerosis, VSMCs acquire a synthetic phenotype and drive plaque formation. This involves migration, proliferation and dedifferentiation of VSMCs which lose normal VSMC marker expression (Bennett, Sinha and Owens, 2016). VSMCs undergoing phenotypic switching may also begin to express macrophage markers and characteristics (Bennett, Sinha and Owens, 2016). However, these macrophage-like smooth muscle cells are distinct in their gene expression from classical monocyte, macrophages and dendritic cells (Vengrenyuk *et al.*, 2015). Lipid accumulation in atherosclerotic plaques may drive the change in VSMCs' phenotype. *In vitro,* cholesterol-exposed VSMCs upregulate inflammatory genes and activate macrophage markers and reduce VSMC markers (Shankman *et al.*, 2015). VSMCs have also been implicated in calcifying mechanisms within atherosclerotic plaques. Hyperphosphatemia, through upregulation of intracellular PIT1 and Runx2, induces an osteochondrogenic phenotype of VSMCs expressing osteopontin, osteocalcin, alkaline phosphatase (ALP) and SOX9 (Leszczynska *et al.*, 2016).

Adventitial Cells

Adventitial cells, reside in the *tunica adventitia,* the outermost layer of the blood vessel wall. The adventitial layer was first believed to solely play a role in maintaining vessel stability due to it containing, fibroblasts, collagens, and nerves. However, the adventitia is also home to immune, blood and lymphatic cells as well as adventitial stem and progenitor cells. The adventitia of arteries also contains vasa vasorum, capillaries which contain endothelial cells and pericytes. Adventitial cells can be identified by the expression of CD34 and lacking the expression of CD31, CD146 and CD45 (Corselli *et al.*, 2012). In response to high vascular pressure the adventitia "stiffness" is the primary factor maintaining vessel integrity (Silver, Horvath and Foran, 2001). The role of the adventitia, however, is complex with resident adventitial cells having important roles in immunomodulation, the inflammatory response and vessel remodelling. Adventitial resident stem cells play a role in tissue turnover and regeneration but also in disease. Adventitial cells have been implicated in the progression of atherosclerosis and vascular calcification. In atherosclerosis, B-cells as

well as other immune cells form tertiary lymphoid organs in the adventitial areas adjacent to atherosclerotic plaques. These lymphoid organs act to enhance the immune response against local stimulating antigens. In advanced atherosclerosis, adventitial B-cells begin to accumulate in atherosclerotic lesions (Kyaw *et al.*, 2011). The adventitial immune response influences plaque stability and the occurrence of thromboembolic events. Sprouting of the vasa vasorum from the adventitial layer to the intimal layer has long been recognised to occur in atherosclerosis and is a mechanism of recruitment of immune cells to atherosclerotic lesions (Kawabe and Hasebe, 2014). The adventitia is home to resident stem/progenitor cells which migrate and contribute to atherosclerosis development by differentiation to VSMCs in mice (Hu *et al.*, 2004). Adventitial cells were also shown to become mesenchymal stem/stromal cells MSCs *in vitro* (Corselli, *et al.*, 2012). In a mouse models of chronic kidney injury, Gli1+ MSCs residing in the adventitial layer were found to migrate into the intima layer in the setting on chronic kidney disease (Kramann *et al.*, 2016). These cells were able to differentiate into VSMCs and then into $Runx2^{+}$ osteoblast-like cells that accumulated in calcified lesions. Adventitial myofibroblasts also contribute to atherosclerosis development and osteogenic processes (Li *et al.*, 2015).

Pericytes

Pericytes, originally called Rouget cells, are almost omnipresent in the microvasculature of organs and tissues throughout the body are also found in the vasa vasorum and sub-endothelial layer of large arteries. They are also known as mural cells and like VSMCs they are found in lining the blood vessel wall. Pericyte are defined in part by their location in the blood vessel found in contact with endothelial cells with long processes embedded within the basement membrane. They are highly heterogenous in terms of their surface marker expression with many different subsets being identified. The expression of certain surface markers is thought to be related to their role in the perivascular niche. Some typical pericyte markers include α-smooth muscle actin (αSMA), neuron-glial antigen 2 (NG2), CD146 and platelet-derived growth factor (PDGF) receptor β (Table 1.1). Pericytes are also further defined by the absence of CD31, and haematopoietic markers CD45 and CD117. It is also important to note that there is no pan pericyte marker which identifies every pericyte population

and extended characterisation using a combination of markers is used to identify different subsets. An extended list of pericyte markers is shown in Table 1.1.

Table 1.1: Pericyte markers and their expression in other cell types

Pericyte Marker	Shared expression with	References
αSMA	VSMCs, myofibroblast	(Nehls and Drenckhahn, 1991) (Morikawa *et al.*, 2002)
Desmin	Cardiac, skeletal, and smooth muscle	(Nehls, Denzer and Drenckhahn, 1992; Morikawa *et al.*, 2002; Paulin and Li, 2004)
NG2	Neurons, microglia	(Karram, Chatterjee and Trotter, 2005)
CD13	Myeloid Cells	(Favaloro *et al.*, 1988; Crouch and Doetsch, 2018)
PDGFRβ	Neurons, VSMCs	(Lindahl *et al.*, 1997; Lindblom *et al.*, 2003; Winkler, Bell and Zlokovic, 2010)
CD146 (MCAM)	Endothelial cells, VSMCs	(Crisan *et al.*, 2008)
Aminopeptidase A	Myeloid Cells	(Alliot *et al.*, 1999)
Aminopeptidase N	Myeloid Cells	(Alliot *et al.*, 1999)
RGS5	VSMCs	(Li *et al.*, 2004; Mitchell *et al.*, 2008)
Nestin	Neural Stem Cells	(Alliot *et al.*, 1999)
CD44	MSCs, haematopoietic cells, cancer cells,	(Crisan *et al.*, 2008; Senbanjo and Chellaiah, 2017)
CD73	MSCs, tumour cells, endothelial cells, immune cells	(Crisan *et al.*, 2008; Turiello, Pinto and Morello, 2020)
CD90	MSCs, T immune cells, neurons fibroblasts	(Crisan *et al.*, 2008; Sauzay *et al.*, 2019)
CD105	MSCs, endothelial cells, tumour cells	(Crisan *et al.*, 2008; Kauer *et al.*, 2019)
Tbx-18	VSMCs, atrial cardiac muscle	(Guimarães-Camboa *et al.*, 2017)

αSMA= alpha smooth muscle actin, NG2- neural/glial antigen 2, PDGFRβ= platelet derived growth factor β, RGS5= Regulator of G Protein Signalling 5, Tbx-18= T-box transcription factor 18, VSMC= vascular smooth muscle cell, MSC=mesenchymal stem/stromal cell

Pericytes also play key roles in the formation and regulation of the blood-brain barrier (BBB) and are an integral part of the neurovascular unit (NVU). The NVU is made of brain parenchymal cells; neurons, interneurons, microglia, and astrocytes interacting with various vascular cell types including pericytes which regulate cerebral blood flow due to alterations to neuronal activity. Brain pericyte dysfunction has also been shown to cause many neurological diseases ranging from traumatic brain injury, Alzheimer's disease, stroke and others (Cheng *et al.*, 2018). In stroke, ischemia causes pericytes

to release matrix metalloproteinases (MMPs) which degrade the endothelial tight junctions of the BBB increasing its permeability.

Pericytes are also abundant in the heart vasculature and play an important role in the maintenance of cardiac homeostasis. Under physiological conditions, cardiac pericytes regulate vascular permeability, the delivery of trophic factors and the production and storage of pro-coagulation factors (Avolio *et al.*, 2015). In CVDs such as MI, atherosclerosis, and vascular calcification, pericytes may also contribute to disease pathology. It has been shown using a rat model of ischaemia reperfusion in the heart that pericyte contraction blocked 40% of capillaries after vessel occlusion and reduced capillary diameter by 67% (O'Farrel *et al.*, 2017). Pericytes may play a role in atherosclerosis progression as lipid accumulation within plaques may cause pericytes to be recruited into the atherosclerotic lesion (Summerhill and Orekhov, 2019). Furthermore, angiogenesis from the vasa vasorum has been shown to precede atherosclerotic plaque development with neovascularisation of microvessels being associated with plaque rupture. Pericytes may also contribute to vascular calcification directly through their innate ability to differentiate into osteoblasts and chondrocytes (Summerhill and Orekhov, 2019).

Mesenchymal Stem/Stromal Cells

Mesenchymal stem/stromal cells (MSCs) are multipotent cells characterized by 1) their ability to adhere to plastic cell culture, 2) their ability to undergo trilineage differentiation to osteoblasts, chondrocytes, and adipocytes and 3) the expression of MSC markers; CD105, CD90 and CD73 and lack CD45, CD19, CD14 CD11b, CD34, CD79α and HLA-DR *in vitro* (Dominici *et al.*, 2006). MSCs were first identified in cell cultures from bone marrow by Arnold Caplan, who first coined the term "MSC" (Caplan, 1991). However, for many years the *in-situ* counterpart to MSCs remained elusive until 2008 when MSCs were shown to reside in the perivascular wall of small (pericytes) and large (adventitial) vessels (Crisan *et al.*, 2008; Corselli *et al.*, 2012). Human pericytes were identified as $CD146^+$ $NG2^+$ $PDGFR\beta^+$ and lacking haematopoietic, endothelial, and myogenic markers by flow cytometry (Crisan *et al.*, 2008). CD34+ human adventitial cells from adipose tissue, lacking expression of CD146, CD45 and CD31, were subsequently identified as another origin of MSCs in

large vessels (Corselli *et al.*, 2012). MSCs can therefore be derived from perivascular cells from almost any vascularised tissues. MSCs are also a major focus in the field of regenerative medicine and have been utilised in thousands of clinical trials (Gomez-Salazar *et al.*, 2020). One key feature of MSCs is that they can retain certain properties from the vascularised tissue from which they were isolated *in vivo* and that even within the same tissue different populations of MSCs may display altered functional properties. For example, in the skeletal muscle, PDGFRβ^{+} PDGFRα^{-} cells are myogenic whereas PDGFRβ^{+} PDGFRα^{+} perivascular cells are fibrogenic and adipogenic (Jensen *et al.*, 2018). Furthermore, MSCs expressing the ROR2 receptor are more chondrogenic than ROR2^{-} counterparts. Both pericytes and adventitial cells can be separated based on the expression of aldehyde dehydrogenase (ALDH) with a ALDH^{bright} subsets possessing a more "primitive transcriptional profile" than ALDH^{dim} subsets (Hardy *et al.*, 2017). CD10^{+} perivascular cells are osteoprogenitors lacking adipogenic and other differentiation potentials (Ding *et al.*, 2020).

In summary, cells resident within the blood vessels help to maintain cardiovascular homeostasis and as a response to changes in their cellular environment may contribute to CVD pathogenesis. One family of molecules are important in the maintenance of homeostasis, development of cardiovascular disease and in MSC biological function is the family of platelet-derived growth factors (PDGFs).

Platelet Derived Growth Factors and Receptors

Signalling between the PDGF family of ligands and their PDGF receptors (PDGFR) play a role in the development of the cardiovascular system, response to injury and in disease processes. Numerous cell types including endothelial cells, platelet cells, neurones and macrophages can express members of the PDGF family. PDGFs are also involved in MSC biology *in vitro* in the regulation of growth and migration. There are five PDGF ligands, four homodimers, PDGFA, PDGFB, PDGFC, PDGFD and a heterodimer, PDGFAB. These five ligands bind to three receptors, PDGFRα, PDGFRβ and PDGFRαβ (Andrae, Gallini and Betsholtz, 2008). Several PDGF/PDGFR binding interactions have been shown *in vivo* and *in vitro* (Figure 1.2A).

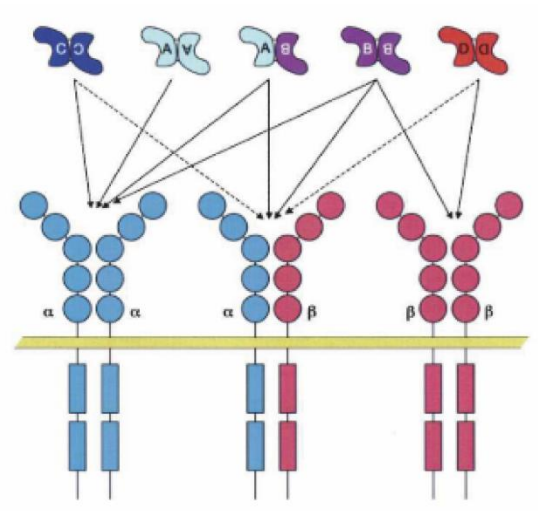

Figure 1.2: PDGF/PDGFR receptor interactions *in vivo* and *in vitro*.

There are 5 platelet derived growth factor (PDGF) ligands; A, B, AB, C and D which may selectively bind to 2 PDGF receptors made of α and β subunits. PDGFC binds to both PDGFR α and PDGFRαβ. PDGFA selectively binds to PDGFRα. PDGFAB can bind to PDGFRαβ and PDGFRα. PDGFB can bind to all 3 receptors. PDGFD binds to PDGFRαβ PDGFRβ. Taken from (Andrae, Gallini and Betsholtz, 2008).

Binding to PDGFRα can be achieved by PDGFA, PDGFB, PDGFAB and PDGFC. PDGFRβ can be bound by both PDGFB and PDGF-D. Finally, the PDGFRαβ can be bound by PDGFs B, AB, and C. One important aspect of the structure of PDGF structure is the presence of the PDGF retention motifs on PDGFA and PDGFB.

This allows regulation of the PDGF tissue distribution by binding to extracellular matrix components. The c-terminal protein motif of PDGFB and PDGFA is negatively charged due to the presence of basic amino acid residues. PDGFC and PDGFD do not contain this structure. Active splicing of PDGFA and active processing of PDGFB can occur and is cell type dependent meaning that both ligands can be released from cells in their soluble forms (Andrae, Gallini and Betsholtz, 2008).

PDGF-mediated activation of PDGFRs causes the monomeric dimers to assemble and increases the receptors tyrosine kinase activity (Heldin and Westermark, 1999). This in turn causes phosphorylation of substrates, engaging signalling cascades driving cellular responses, for example, cell proliferation and migration (Tallquist and Kazlauskas, 2004). After PDGFRs are activated, they are then taken into the cells and degrade resulting in the cessation of signalling. Of particular importance in cardiovascular development health and disease is the interaction between PDGFB and PDGFRβ due to its involvement in the cellular communication between endothelial cells and pericytes.

PDGFB/PDGFRβ Signalling

Signalling between PDGFB and PDGFRβ plays a key role in angiogenesis, during development of the cardiovascular system, its growth and as a response to injury. The first steps in angiogenesis are the degradation of the shared basement membrane by MMP's and the detachment of pericytes from endothelium due to VEGF -A. At this point VEGF-A also causes endothelial cell proliferation and migration which begin to form the new blood vessel developing within a tissue. However, this newly sprouting vessel is fragile and unstable requiring proper pericyte coverage. During the sprouting phase endothelial cells release PDGFB which is retained on the cell surface and extracellular matrix. This is made possible by the presence of the c-terminal protein motif of PDGFB which interacts with heparin sulfate proteoglycans of the extracellular matrix creating a chemotactic gradient, limiting the range of action and tissue distribution of PDGFB. PDGFRβ^{+} pericytes interact with PDGFB retained in the extracellular matrix and pericellular space. This interaction causes their pericyte proliferation and migration to the site of the newly forming capillary. Angiogenesis is also activated in various injury models such as heart injury. Angiogenesis as a response to hypoxic injury in the heart triggers neovascularisation in the infarct and peri infarcted area to reduce infarct size and promote re-oxygenation of damaged tissue. Both PDGFB and PDGFRβ have been shown to be highly expressed in the heart post-MI (Zymek *et al.*, 2006). Inhibition of PDGFB/PDGFRβ signalling impairs vessel maturation and reduced pericyte coverage on newly sprouting vessels (Zymek *et al.*, 2006). As such signalling between PDGFB and PDGFRβ is essential in the damaged heart.

PDGFB also plays an important role in MSC biology and function causing cell growth, migration and proliferation *in vitro* (Caplan, 1991). Co-culture of MSC precursors with endothelial cells showed that endothelial released PDGFB can enhanced cell proliferation and also induce their differentiation into a SMC/ pericyte fate(Hirschi *et al.*, 1999). PDGFB was also shown to be a potent regulator of bone marrow MSC progenitor migration using chemotaxis (Fiedler *et al.*, 2002). Enhanced migration and proliferation of MSCs was also observed in human adipose derived MSCs *in vitro* (Kang *et al.*, 2005). PDGFB may also modulate the behaviour of transplanted MSCs. Indeed, overexpression of PDGFB in human bone marrow MSCs via a lentiviral vector enhances their migratory and proliferative capacities in restoring blood flow in a mouse

model of hindlimb ischemia (Sondergaard *et al.*, 2009). In a rabbit model of ligament injury, transplanted MSCs transfected with PDGFB increased the healing responses such as collagen deposition and angiogenesis(Li, Jia and Yu, 2007). Furthermore, PDGFB released from transplanted MSCs in a paracrine manner to promote angiogenesis as shown in a rodent model of hind limb ischemia (Bortolotti *et al.*, 2015). PDGFB may also modulate the cell fate of MSCs *in vitro*. Early studies indicated that PDGFB administration did not enhance osteochondrogenic differentiation of bone marrow MSCs *in vitro* (Cassiede *et al.*, 1996). However, later PDGFB was shown to selectively enhanced the osteogenic capacity of adipose-derived MSCs over those from the bone marrow *in vitro* (Hung *et al.*, 2015).

PDGFB/ PDGFRβ signalling is therefore essential to cardiac development, repair and in the modulation of MSC function *in vitro* and *in vivo.*

Mouse models of PDGFB/PDGFRβ Signalling

Animal models of human disease have been the backbone of many areas of scientific research. Much of the mechanistic insight regarding the role of PDGFB/PDGFRβ signalling comes from studies utilising genetically modified mouse models.

In 1994, the first genetically altered mouse models were developed to understand the effect of PDGFB and PDGFRβ *in vivo*. Germline ablation of PDGFB in *pdgfb*$^{-/-}$ mice results in perinatal lethality with late embryonic mice showing haemorrhaging and dilation of major blood vessels as well as severe developmental defects in the kidney (Levéen *et al.*, 1994). Similar renal defects were observed in *pdgfrb*$^{-/-}$ mice which also die prior to birth and exhibit severe haemorrhaging (Soriano, 1994). Later renal defects in both models were shown to be due to an absence of mesangial cell and pericytes due to failure to recruit PDGFRβ^{+} progenitors (Lindahl *et al.*, 1998). Furthermore, both models exhibit myocardial hypoplasia, underdevelopment of the left and right ventricles and dilated coronary vessel structure (Van Den Akker *et al.*, 2008). *Pdgfb*$^{-/-}$ mice were also found to be pericyte deficient in the brain and develop microaneurysms which ruptured at late gestation (Lindahl *et al.*, 1997). Both *pdgfb*$^{-/-}$ and *pdgfrb*$^{-/-}$ exhibit endothelial hyperplasia and abnormal brain vascular morphology (Hellström *et al.*, 2001). These early models proved to be essential in understand fundamental role of PDGFB/PDGFRβ in pericyte and VSMCs recruitment during blood vessel

development and in the development of the placenta and epididymis (Hellström *et al.*, 1999; Ohlsson *et al.*, 1999; Basciani *et al.*, 2004).

Other models investigating PDGFB/PDGFRβ signalling have also since been established and studied in various areas of research. *Pdgfb*$^{+/-}$ heterozygotes develop diabetic retinopathy with a 30% depletion in retinal pericytes and reduced capillary number (Hammes *et al.*, 2002). Double transgenic *pdgfb*$^{+/-}$ *pdgfrb*$^{+/-}$ mice have reduced pericytes coverage and exhibit progressive pericyte loss in the brain in aging (Vanlandewijck *et al.*, 2015). *Pdgfrb*$^{redeye/redeye}$ mice, possessing a mutation in position +2 of intron 6 resulting in partial splicing of the *pdgfrb* gene, exhibit impaired pericyte recruitment, increase vascular permeability and leakage and retinal neurodegeneration (Jadeja *et al.*, 2013). Transgenic overexpression of PDGFB causes emphysema accompanied by localised fibrotic lesions in the lung (Hoyle *et al.*, 1999). Cardiac specific over expression of PDGFB caused a similar phenotype with focal accumulation of fibrosis in the ventricular myocardium and cardiac hypertrophy (Gallini *et al.*, 2016). Similarly, hepatic overexpression of PDGFB induces liver fibrosis (Czochra *et al.*, 2006) Overexpression of PDGFB in the retina promotes pericyte, endothelial cell, astrocyte and microglial proliferation (Seo *et al.*, 2000). Another interesting model used to study alterations in PDGFB/ PDGFRβ signalling is the PDGFRβ$^{F7/F7}$ mouse which has 7 missense mutations in the PDGFRB gene which reduces cardiac pericyte number during development but does not affect kidney pericytes to the same extent (Tallquist, French and Soriano, 2003). This mutation disrupts residues and signal transduction pathways; residue 578 (Src), residue 715 (Grb2), residues 739 and 750 (PI3K), residue 770 (RasGAP), residue 1008 (SHP-2), switching the tyrosine to phenylalanine, and residue 1020 (PLCγ), changing tyrosine to isoleucine(Montagne *et al.*, 2018). These mice also have a reduced pericyte number in the brain and skeletal muscle (Nikolakopoulou *et al.*, 2017; Methner *et al.*, 2019)

Thus, transgenic mouse models have provided invaluable insight into the role of PDGFB and PDGFRβ in pericyte biology and function, angiogenesis, and fibrotic injury.

The *Pdgfb*$^{ret/ret}$ mutant mouse model

Due to the perinatal lethality of both the PDGFB and PDGFRβ knockout mice, it is difficult to determine how altering PDGFB/PDGFRβ signalling in adult mice may disrupt cardiovascular homeostasis. The *pdgfb*^{ret} mutant mouse model, where the PDGFB retention motif has been deleted, survive into adulthood and are an ideal candidate model to study altered PDGFB/PDGFRβ signalling.

Pdgfb^{ret} mutant mice were first created by the laboratory of Professor Christer Betsholtz generating a germline mutant using mouse embryonic stem cells. To accomplish this, a loxP-flanked PGK-neo cassette was inserted into intron 5 as well as a stop codon/HindIII site into exon 6 of the pdgfb gene. Heterozygous mutants were generated and bred with protamine-Cre mice to delete the PGK-neo cassette which generated the pdgfb^{ret} (retention motif knockout, RET KO) allele (Lindblom *et al.*, 2003). As previously noted, the c-terminal protein motif of PDGFB through binding to heparin sulfate proteoglycans (HSPGs) regulated PDGFB tissue distribution in the extracellular matrix (ECM). This interaction is important during cell migration and spatial distribution of secreted growth factors, for example during angiogenesis. Consequently, *pdgfb*$^{ret/ret}$ mice have reduced pericyte coverage of the microvasculature. Since their generation, *pdgfb*$^{ret/ret}$ mice have been studied in a variety of biological settings. Prior to the start of my project, the effect of this mutation had been described in several tissues and at differing stages of development.

The effects of the *pdgfb*^{ret} mutation were first reported during embryonic development. At embryonic day (E) 15.5 *pdgfb*$^{ret/ret}$ defective investment of pericytes into the walls of the microvasculature was observed. At E15.5 *pdgfb*$^{ret/ret}$ mice, had around a 50% depletion in pericyte coverage and abnormal brain capillary structure (Lindblom *et al.*, 2003). Subsequent characterisation also revealed reduced pericyte coverage and vascular leakage at in E11.5 *pdgfb*$^{ret/ret}$ embryos. However, unlike both PDGFB and PDGFRβ null mutants, no vascular haemorrhaging was observed in the brain at developmental later stages E12.5 and E14.5 (Lindblom *et al.*, 2003). A great number of studies have investigated the role of *pdgfb*^{ret} mutation in the adult brain.

Armulik and collaborators investigated the importance of pericytes in the regulation of the blood brain barrier using *pdgfb*$^{ret/ret}$ mice (Armulik *et al.*, 2010). They found that reduced pericyte coverage led to leakage of the BBB in the brains of adult pdgfb$^{ret/ret}$

mice. They observed that changes in permeability were due to increased endothelial transcytosis and through regulation of specific genes in endothelial cells involved in the BBB function (Armulik *et al.*, 2010). This also results in altered of cholesterol homeostasis in the brain of *pdgfb*$^{ret/ret}$ mice (Saeed *et al.*, 2014). However, further studies on *pdgfb*$^{ret/ret}$ mice have shown that the pericyte deficiency does not influence the transport of small molecules and drugs such as diazepam, oxycodone and paliperidone (Mihajlica, Betsholtz and Hammarlund-Udenaes, 2018b, 2018a). Implying that BBB barrier function against xenobiotic compounds is preserved in a pericyte deficient state.

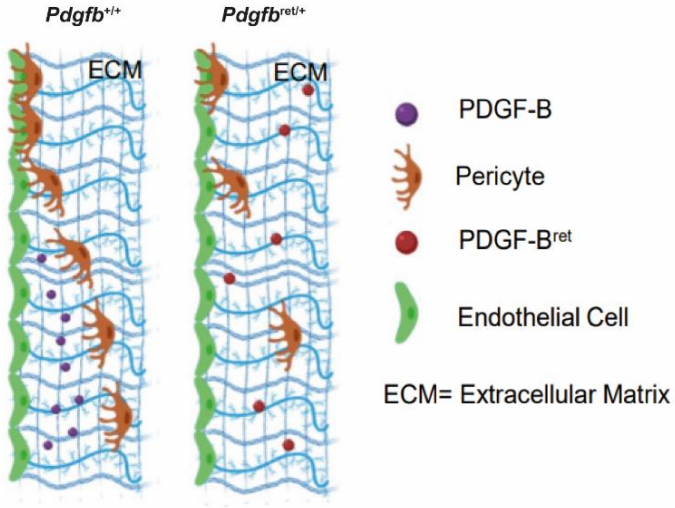

Figure 1.3: PDGFB/PDGFRβ signalling in *pdgfb*$^{+/+}$ and *pdgfb*$^{ret/ret}$ mice in angiogenesis.

During normal angiogenesis PDGFB is released and retained in the pericellular space and extracellular matrix by the action of the PDGFB retention motif. This means pericytes are recruited to newly forming vessel and when in place, pericytes allow vessels to mature and maintain their structural integrity. In *pdgfb*$^{ret/ret}$ mice the deletion of the PDGFB retention motif alters tissue distribution of the PDGFBret protein. This in turn impairs pericyte recruitment to newly forming vessels (Lindblom *et al.*, 2003).

Pdgfb$^{ret/ret}$ mice have been used as a model for the human condition of idiopathic basal ganglia calcification (IBGC) as they were found to develop vascular-associated brain calcification that progresses in size with age (Keller *et al.*, 2013). IBGC is a neurodegenerative disorder in which bilateral calcification of the basal ganglia occurs. In humans, mutations in PDGFB and PDGFRβ have been identified in families with IBGC (Keller *et al.*, 2013). In *pdgfb*$^{ret/ret}$ mice, calcium phosphate nodules in the pons, thalamus and midbrain increased in size between 2 and 12 months. Outside of the brain other aspects of the *pdgfb*^{ret} mutant physiology have been assessed.

Raines and collaborators investigated the hepatic system of *pdgfb*$^{ret/ret}$ mutant mice due to the fact the microvasculature plays an important role in insulin signalling. They investigated the permeability of the vasculature of the liver, skeletal muscle, and heart via injection of dextran (Raines *et al.*, 2011). Under homeostatic conditions vascular permeability can be defined as the vascular sieving of small molecules and solutes. However, in pathological conditions disruption of the vascular barrier enhances vessel permeability resulting in the leakage of large molecules into tissue, oedema and inflammatory processes (Claesson-Welsh, 2015). No change in vascular permeability was observed in the skeletal muscle although permeability of the heart increased after 24 hours. The largest increase in vascular permeability was observed in the liver. However, they saw no difference in hepatic stellate cell, which are modified pericyte-like cells, coverage of the liver microvasculature between control (*pdgfb*$^{+/+}$ and *pdgfb*$^{ret/+}$ littermates) and *pdgfb*$^{ret/ret}$ mice. They also found that *pdgfb*$^{ret/ret}$ mice also had enhanced glucose homeostasis and insulin clearance from the circulation. In the same study, they observed that in obese *pdgfb*$^{ret/ret}$ mice (*pdgfb*^{ret} mice crossed with leptin deficient mice) reduced PDGFB signalling enhanced insulin action and glucose levels to were the same as controls (Raines *et al.*, 2011).

Kidney structure was altered in *pdgfb*$^{ret/ret}$ mutant mice during development and after birth (Lindblom *et al.*, 2003). At E17.5 there is a reduction in the number of mesangial cells in the kidneys of *pdgfb*$^{ret/ret}$ mice leading to malformation of the glomerular capillaries. Later examination of the kidneys at 1 month of age describes how this deficiency in mesangial cell number and glomerular malformations had normalized. However, at 6 months of age *pdgfb*$^{ret/ret}$ mice have a large accumulation of extracellular matrix and collagen and have excessive amounts of albumin in their urine at 3 months of age (Lindblom *et al.*, 2003).

Retinal defects were also described in *pdgfb*$^{ret/ret}$ mice. The eyes of *pdgfb*$^{ret/ret}$ mice were smaller and around 10% had white ocular defects such as the degeneration of photoreceptors, invasion of retinal pigment epithelial cells and fibrosis (Lindblom *et al.*, 2003). The vasculature of the eye was also malformed and disorganised with vascular mural cells detached and forming cellular sheets on the retinal surface. A subsequent study showed that these structural deterioration was progressive starting at postnatal day (P) 10 with vascular abnormalities and followed by photoreceptor death, glial cell

activation and gliosis and other abnormalities by P28 (Genové, Mollick and Johansson, 2014).

Despite extensive study in the brain and other tissues and the severe phenotype exhibited by PDGFB and PDGFRβ knockout mice in the heart, only one study has briefly examined the effect of the *pdgfb*^{ret} mutation in the heart. In this study, they interpreted the development of eccentric hypertrophy in the hearts of male *pdgfb*$^{ret/ret}$ mice that progressed from 10 to 20 weeks (Nystrom *et al.*, 2006). However, no follow up beyond this time point was performed and the effects of sex in *pdgfb*$^{ret/ret}$ mice were not established.

Preclinical Cardiovascular Imaging *in vivo*

Techniques to image the cardiovascular system in patients is common practice in the diagnosis and treatment for many conditions. Although many imaging systems were initially conceived for use in patients, the technology has been altered and refined for research purposes on animal models of disease. Today, preclinical imaging *in vivo* has become a cornerstone of cardiovascular research.

Ultrasound Imaging

High frequency ultrasound is one technique which has been widely used in preclinical studies for cardiovascular research. Ultrasound waves are high frequency sound waves which cannot be heard by the human ear (>20,000Hz). In preclinical imaging the frequency of ultrasound waves produced by an ultrasound probe can vary from 15MHz to 80MHz (Foster, Hossack and Adamson, 2011). In imaging both humans and animals, ultrasound waves are produced by a probe which propagate through the tissue, are reflected, and acquired by a transducer. This allows either 2-dimensional (2D) or 3D images to be acquired. In echocardiography, 2D cross sectional images can be acquired in real time on an ultrasound scanner. Areas of high echogenicity are shown as high echoes (bright white) than areas of lower echogenicity. In cardiac scanning in mice, parasternal images are acquired because a rodent's heart is anatomically more vertical than humans (Moran *et al.*, 2013). Several imaging

modalities are available to assess different aspects of cardiac structure and function *in vivo*.

2D Brightness-mode (B-mode) images are shown in greyscale on an ultrasound scanner. In this modality a cine-loop can be acquired and by defining left ventricular cavities, systolic and diastolic function can be assessed (Moran *et al.*, 2013). Motion-mode (M-mode) is another imaging modality but is instead, a singular point of ultrasound data selected from a B-mode image (Moran *et al.*, 2013). This singular point of ultrasound data is displayed over time and using automatic boundary detection algorithms, the diameter of ventricular and atrial cavities as well as myocardial wall thickness can be measured.

Speckle tracking echocardiography (STE) is a relatively novel cardiac imaging technique which can be utilised to measure cardiac strain. A “speckle” is an artefact caused by an interference pattern which is formed by interference from echoes which are out with the capabilities of the ultrasound system to detect (Moran *et al.*, 2013). Each area of the myocardium can produce a speckle pattern which is unique, however, myocardial motion may cause this to change (Moran *et al.*, 2013). STE techniques are utilised to measure strain which is an indicator of tissue deformation. Preselected regions of the myocardium are tracked across time and the displacement between these two regions is measured. This data can allow assessment of regional as well as global systolic and diastolic changes to cardiac function. STE strain analysis can be utilised to detect early regional changes in cardiac function prior to the onset of global dysfunction. Echocardiography has wide spread applications and is utilised to assess rodent models of dilated cardiomyopathy and MI, as well as the effects of pharmaceutical compounds on cardiac function (Schnelle *et al.*, 2018; Moran and Thomson, 2020; Kryukov *et al.*, 2021).

Positron Emission Tomography/Computed Tomography Imaging

Positron emission tomography (PET) was first used in medical imaging of brain tumours using sodium iodide in the 1950s and 1960s (Nutt, 2002). PET is a highly sensitive imaging technique scanning which through the detection of positron emissions from radiotracer binding in an organ or tissue. A PET scanner is equipped with two photon detectors which can detect the photons produced by an emitted

positron colliding with an electron. Two of the most widely used radiotracers in PET imaging are ^{18}F-fluordeoxyglucose (^{18}F-FDG), used in imaging glucose metabolism and ^{18}F-Sodium fluoride (^{18}F-NaF) which binds to hydroxyapatite deposition (Nutt, 2002). Since the 60s, the applications of PET scanning have grown, and micro-PET scanners have been developed for use in preclinical imaging. PET imaging is often combined with CT allows localisation of radiotracer activity within a given organ or tissue.

During a CT scan, a patient or animal is placed upon a motorised table which moves them into the CT scanner. Unlike convention X-ray machines, CT scanners use a motorized x-ray source that rotates around the subject in a spiral manner. CT imaging uses serial x-rays to provide cross-sectional imaging of a whole organism, organ or tissue in 3D (Brenner, Hall and Phil, 2007). Clinically, CT scans have been utilised for diagnostic purposes such as in injury caused by trauma to bone, tumour imaging and imaging of coronary artery calcification (Jung, 2021). Micro CT scanners have been developed to obtain *in vivo* imaging of rodents and to image organs *ex vivo*. Furthermore, micro PET and CT scans have been combined into hybrid micro PET/CT scanners which enable functional imaging of biological processes combined with information regarding the anatomical location of radiotracer activity (Jan *et al.*, 2006).

^{18}F-NaF is a commonly used radiotracer initially used in bone imaging; however, this can be also used to measure microvascular calcification. When combined with CT scan, the use of ^{18}F-NaF can distinguish between macroscopic vascular calcification and microscopic vascular calcification and as such can distinguish between stable and unstable plaque formation (Joshi *et al.*, 2014). Indeed, recently whole body and *ex-vivo* PET/CT imaging using ^{18}F-NaF has been previously performed to characterize the progression of atherosclerosis and microcalcification of the aorta of *Apoe*$^{-/-}$ mice fed an atherogenic diet (MacAskill *et al.*, 2020).

Both echocardiography and PET/CT imaging are invaluable research tools to allow structural and functional assessment of the cardiovascular system in preclinical models of CVD.

Summary and Project Outline

I have introduced the importance of the role of blood vessels and their cellular constituents in health and disease. PDGFB/PDGFRβ signalling is important not only for cardiovascular development and disease but also in MSC biology *in vitro.* *Pdgfb*$^{ret/ret}$ mice have altered PDGFB/PDGFRβ signalling, survive into adulthood, exhibit brain vascular calcification and early changes to left ventricular structure. However, whether ectopic extracerebral calcification occurs in other organs or tissues in *pdgfb*$^{ret/ret}$ mice is not known and whether this mutation differently affects cardiac function in aging male and female mice has not been studied. Finally, the effect on the *pdgfb*^{ret} mutation on MSCs *in vitro* has also not been established.

Using state-of-the-art imaging techniques, PET/CT, and cardiac ultrasound, combined with MSC *in vitro* assays I aimed to investigate the role of the *pdgfb*^{ret} mutation in cardiac homeostasis.

Hypothesis

The *pdgfb*^{ret} mutation induces ectopic extracerebral vascular calcification and leads to alterations to left ventricular structure and decline in heart function in aging male and female mutant mice. The *pdgfb*^{ret} mutation induces changes to MSC osteogenic differentiation potential *in vitro*.

Aims

Identify ectopic extracerebral vascular calcification in pdgfb$^{ret/ret}$ mice.

Determine the effect of the *pdgfb*^{ret} mutation on cardiac structure and function.

Assess *pdgfb*^{ret} mutant MSC osteogenic potential *in vitro.*

Chapter 2: Materials and Methods

Ethics Statement

All experiments were carried out according to the University of Edinburgh Animal Welfare and Ethical Review Body, UK Home Office Animal (Scientific Procedures) Act 1986 and with Directive 20101/63/EU of the European Parliament.

Animals

Mice were bred in the animal facility at the Centre of Regenerative Medicine, Edinburgh. Animals were housed under a 12-hour light/12-hour dark cycle mimicking circadian rhythm and fed a chow diet and water *ad libitum.* To undergo ultrasound and PET/CT experiments, mice were transferred to the Chancellor's Building (LF2) Animal Facility, Edinburgh. In LF2, mice were housed under a 12-hour light/12-hour dark cycle mimicking circadian rhythm. Animals were fed a chow diet and water *ad libitum.*

Pdgfb$^{ret/ret}$ mice were created by deletion of the PDGFB retention motif. This was done through targeting a loxP-flanked PGK-neomycin cassette into intron5 and a premature stop codon/ HindIII site into exon 6 of the *pdgfb* gene in mouse embryonic stem cells (Figure 2.1A, Lindblom *et al.*, 2003). This allowed generation of the *pdgfb*^{ret} allele (Figure 2.1B, Lindblom *et al.*, 2003). The *pdgfb*^{ret} mouse line was maintained by breeding of male and female heterozygous (*pdgfb*$^{ret/+}$) mice on the C57BL6/J background. Due to previously reported fertility issues exhibited by female *pdgfb*$^{ret/ret}$ mice, they were not utilised for breeding (Lindblom *et al.*, 2003). *Pdgfb*$^{+/+}$ and *pdgfb*$^{ret/+}$ littermate mice were used in all experiments with *pdgfb*$^{ret/ret}$ mice.

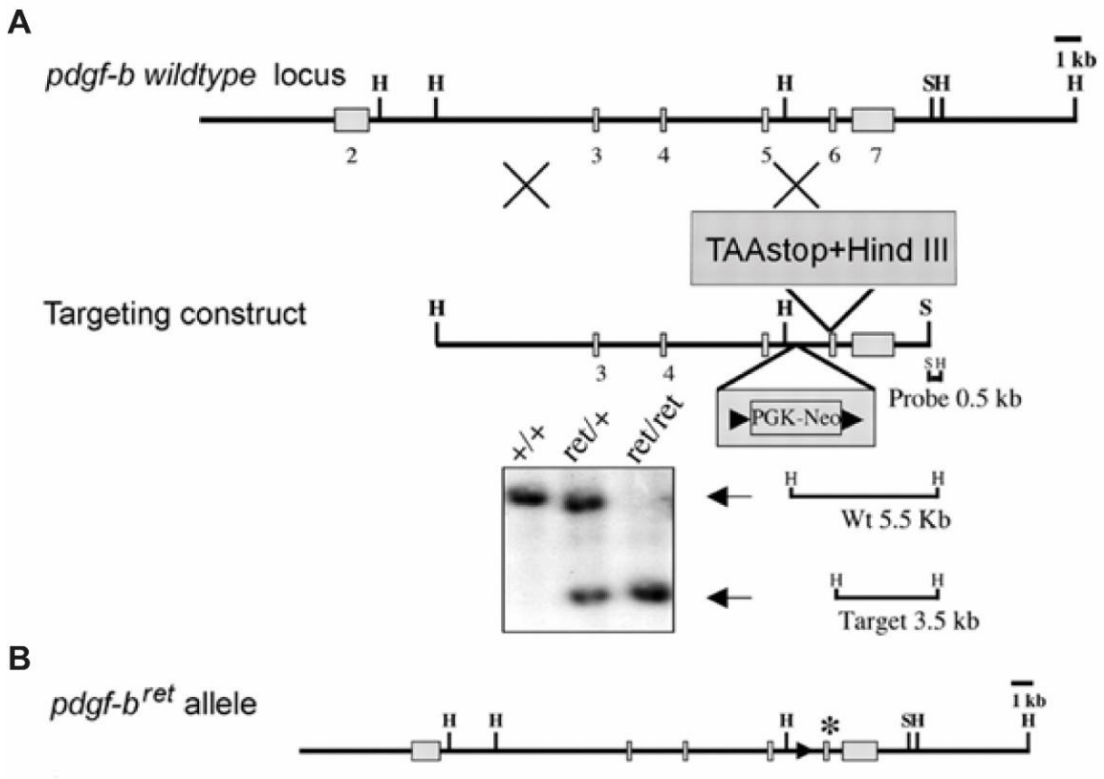

Figure 2.1: Generation of *pdgfb*$^{ret/ret}$ mice.

Generation of the *pdgfb*^{ret} allele targeting loxP-flanked PGK-neomycin cassette into intron5 and a premature stop codon/ HindIII site into exon 6 of the *pdgfb* gene (**A**). Schematic view of the *pdgfb*^{ret} allele (**B**). Taken from Lindblom *et al.*, 2003.

DNA Extraction

Mice were genotyped by polymerase chain reaction (PCR). DNA samples (ear clippings) from postnatal *pdgfb*$^{+/+}$, *pdgfb*$^{ret/+}$, and *pdgfb*$^{ret/ret}$ mice were taken at postnatal day 14 and frozen at -20^{o}C or DNA extraction was immediately performed using the REDExtract-N-AmpTM Tissue PCR Kit (Sigma-Aldrich, Massachusetts, USA). For DNA extraction, frozen samples were thawed and placed in a solution consisting of 100µL of extraction solution and 25µL of tissue preparation solution. Samples were incubated at 55^{o}C in a shaking incubator for 10mins and transferred to a stationary incubator heated to 95^{o}C for 3mins. 100µL of neutralisation solution was then added to each sample.

Genotyping

PCR was used to identify *pdgfb*$^{+}$ and *pdgfb*^{ret} alleles in DNA samples. Separate PCRs were performed to independently detect *pdgfb*$^{+}$ and *pdgfb*^{ret} alleles. Information regarding primer sequences for the detection of each allele are given in Table 2.1. For each allele, 4µL of each DNA sample was added to 16uL of PCR mix (Table 2.2). DNA and PCR mix were then placed in the PCR machine, the program cycle was selected and left until completion (Table 2.3). Upon completion samples were run on a 1.5% agarose gel in 1xTAE buffer (Invitrogen, Massachusetts, USA) for 90mins at 115V. Samples were run alongside a molecular weight ladder (EasyLadderI) with bands at 100, 250, 500, 1000 and 1500 base pairs to allow identification of amplified products.

Table 2.1: Primer details

Allele	Primer sequences	Amplified Product Size (base pairs)
pdgfb^{+}	Forward: CATGCTGCCTTGTAATCCGTTC Reverse: CGGCGGATTCTCACCGT	340
pdgfb^{ret}	Forward: CTCGGGTGACCATTCGGTAA Reverse: TCTAAGTCACAGCCAGGGAGTAGC	212

Table 2.2: PCR MIX

PCR Mix Constituents	Volume per sample
REDExtract-N-Amp PCR Reaction Mix	10µL
Forward Primer	1µL
Reverse Primer	1µL
dH_2O	4µL

Table 2. 3:PCR Program

Temperature (^{o}C)		Number of Cycles	Cycle Duration
94		1	5min
94		35	30s
63			40s
72			1min
72		1	4min
10		1	Infinite hold

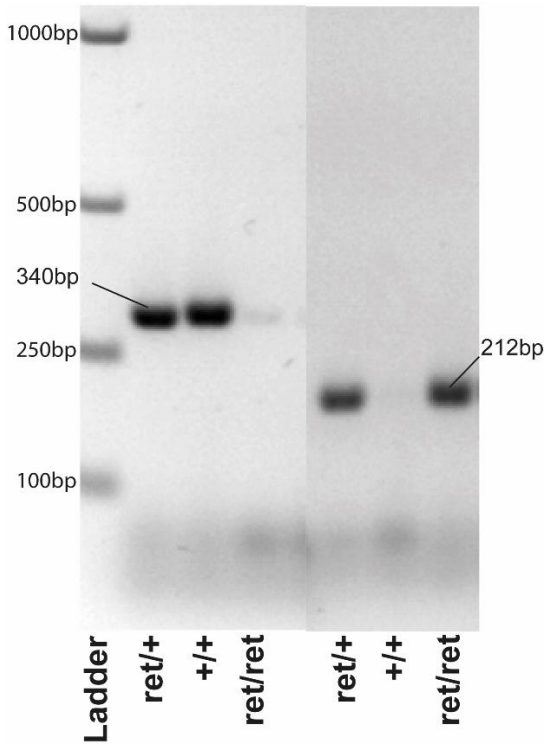

Figure 2.2: Example of pdgfbret genotyping

The *pdgfb*$^{+}$ band (340bp) is present in DNA samples from both *pdgfb*$^{+/+}$ (+/+) and *pdgfb*$^{ret/+}$ (ret/+) mice but absent in samples from *pdgfb*$^{ret/ret}$ (ret/ret) mice. The *pdgfb*^{ret} band (212bp) is present in DNA samples from ret/+ and ret/ret mice and absent from +/+ samples. bp=base pairs. Gel images were provided by Diana Sa da Bandeira.

Echocardiography Imaging Procedure

Echocardiography was performed on adult mice using Vevo 770 and 3100 High Frequency Ultrasound biomicroscopes (FUJIFILM, VisualSonics.Inc, Amsterdam, The Netherlands) with an RMV707B centre frequency 20MHz probe or MX550D centre frequency 40MHz probe. Both male and female *pdgfb*$^{+/+}$, *pdgfb*$^{ret/+}$ and *pdgfb*$^{ret/ret}$ mice were scanned at 3, 6, 9 and 12 months of age ±14 days. Prior to scanning, mice were anaesthetised via inhalation of 4% isoflurane (Merial Animal Health Limited) in medical oxygen (BOC Medical, Manchester, UK). Onset of anaesthesia was determined prior to scanning by loss of pedal withdrawal reflex. Mice were transferred to a heat plate to maintain core body temperature at 37^{o}C, placed in the supine position and limbs were taped down to sensory leads. Anaesthesia was continually monitored and maintained by 1-2% isoflurane through inhalation via a nose cone. Body temperature was monitored using a rectal probe. Thoracic hair was removed using a commercially

available electric shaver and depilatory cream. Aqueous ultrasound solution (Aquasonic 100, Parker Laboratories INC) was applied to the abdomen to allow readings to be taken. The ultrasound probe was placed in a conformation which allowed parasternal long axis (PSLAX) electrocardiogram (ECG)-gated Kilohertz Visualization (EKV) gated and B-mode cine loops over several cardiac cycles to be acquired. Post-processing was then performed to reconstruct an image containing more data frames than could be acquired in real time. From B-mode view the m-mode cursor was placed mid cavity tracing across the left ventricular posterior and anterior walls. After scanning, mice were transferred to recovery cages on a heated plate until consciousness had been regained. Analysis of ultrasound data was completed using Visualsonics Vevo 770 V3.0.0 and VevoLab software (FUJIFILM, VisualSonics.Inc, Amsterdam, The Netherlands).

EKV and M-mode Analysis

Analysis of EKV cine loops were performed using Visualsonics Vevo 770 V3.0.0 and VevoLab 3100 software (FUJIFILM VisualSonics.Inc, Amsterdam, The Netherlands). From EKV cine loops, 2D images of the left ventricle during end-diastole (Figure 2.3A) and end-systole (Figure 2.3B) were selected and endocardial and epicardial areas were manually defined. Endocardial and epicardial major axis were also delineated. M-mode continuous images from a particular point on the myocardial wall were selected from B-mode cine loops and the diameter of endocardial wall was traced over diastole and systole (Figure 2.3C, Table 2.4). From these measurements a host of structural and functional cardiac parameters were calculated by image analysis software (Table 2.5).

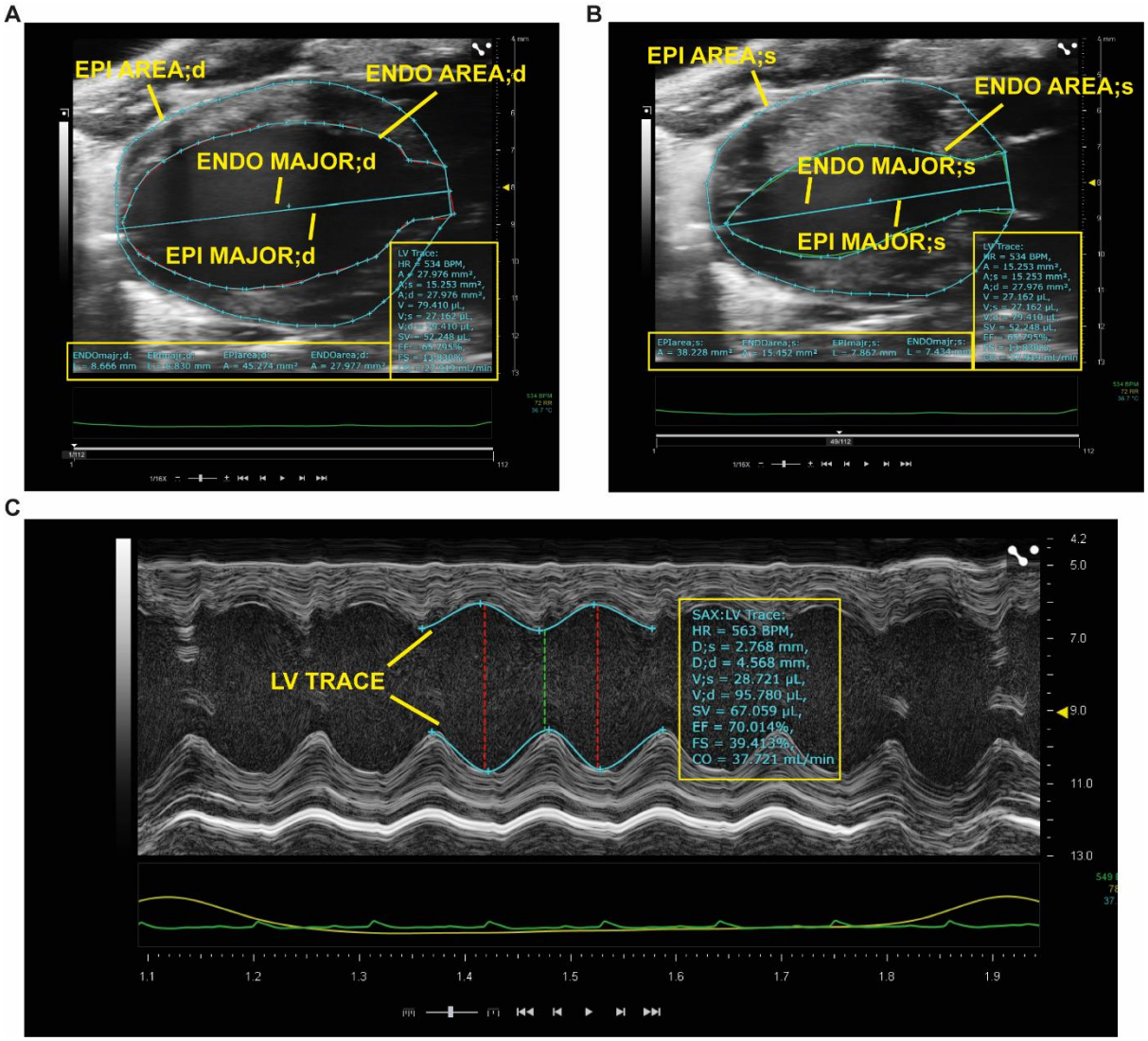

Figure 2.3: Example EKV and M-mode Image Analysis.

Example images of parasternal long axis EKV and m-mode analysis. An example of direct measurements taken during end-diastole (**A**) and end-systole (**B**) of endocardial boundaries. On both images endocardial (ENDO AREA;d, ENDO AREA;s) and epicardial areas (EPI AREA;d,, EPI AREA;s) are defined. The endocardial (ENDO MAJOR d, ENDO MAJOR;s) and epicardial (EPI MAJOR;d, EPI MAJOR;s) majors are the distance between the base and apex of the endocardium and epicardium respectively. Example of m-mode analysis highlighting the LV trace (blue line) of the endocardial wall over several cardiac cycles (**C**). Yellow boxes indicate measurements and functional parameters calculated by analysis.

Table 2 4: Echocardiography Measurements

Measurements	Unit	Image Type
Endocardial Major; d	mm	EKV
Endocardial Major; s	mm	EKV
Endocardial Area; d	mm^2	EKV
Endocardial Area; s	mm^2	EKV
Epicardial Major; d	mm	EKV
Epicardial Major; s	mm	EKV
Epicardial Area; d	mm^2	EKV
Epicardial Area; s	mm^2	EKV
LV Endocardial Trace	N/A	M-Mode

d= diastole s=systole LV= left ventricle

Table 2. 5: Structural and Functional Parameters and Equations

Parameter	Unit	Equation
Wall Thickness (T)	mm	$\frac{\sqrt{\frac{LV\ Area\ Epicardial\ Border;d}{\pi}} - \sqrt{\frac{LV\ Area\ Endocardial\ Border;d}{\pi}}}{\sqrt{\frac{LV\ Area\ Endocardial\ Border;d}{\pi}}}$
LV Mass	mg	$1.05 \text{ x } (\frac{5}{6} \text{ x } LVAEPI \text{ x } (LVL;d + \text{T}) - (\frac{5}{6} \text{ x } LVAEND \text{ x } LVL;d)$
Stroke Volume	µL	$Left\ Ventricular\ Vol;d - Left\ Ventricular\ Vol;s$
Cardiac Output	µL/min	$Stroke\ Volume\ x\ Heart\ Rate$
Fractional Area Change	%	$\frac{Left\ Ventricular\ Area;d - Left\ Ventricular\ \ Area;s}{Left\ Ventricular\ Area;d} x100$
Ejection Fraction	%	$\frac{Left\ Ventricular\ \ Stroke\ Volume}{Left\ Ventricular\ \ volume;d} x100$
Fractional Shortening	%	$\frac{LVID,d - LVID;s}{LVID;d}\ x100$

LVAEPI= Epicardial area, LVAEND= endocardial area, LVL= Left ventricle length,

LVID; d= diastolic left ventricular internal diameter LVID; s= systolic left ventricular internal diameter

Speckle Tracking Analysis

Analysis of speckle tracking echocardiography (STE) was performed using VevoLab3100 (FUJIFILM VisualSonics.Inc, Amsterdam, The Netherlands) software using the strain analysis feature STE can be utilised to calculate cardiac parameters as well as visualise strain in 2D over the course of several cardiac cycles. Figure 2.4A highlights an example from a 12-month *pdgfb*$^{+/+}$ mouse of a B-mode video of the left ventricle in PSLAX view with endocardial and epicardial borders defined (Figure 2.4A, yellow box). From this output, cardiac and strain parameters can be calculated (Figure 2.4A, blue box, Table 2.6). Furthermore, in the example image radial strain over 3 cardiac cycles is shown overlapped with m-mode images of the left ventricle and visualisation of radial strain values with positive strain shown in red and negative strain values shown in blue (Figure 2.4A, green box). Similarly, longitudinal strain over 3 cardiac cycles has been shown overlapped with m-mode images of the left ventricle with visualisation of strain patterns shown below (Figure 2.4A, red box). Radial and longitudinal strain from *pdgfb*$^{+/+}$ and *pdgfb*$^{ret/ret}$ were also visualised in 3D over 3 cardiac cycles (Figure 2.4B). Example 3D images show differences in the pattern of radial and longitudinal strain between *pdgfb*$^{+/+}$ and *pdgfb*$^{ret/ret}$ mice.

Table 2.6: Speckle Tracking Echocardiography Equations

Parameter	Unit	Equation
Strain (S)	%	$S = \frac{\Delta L}{L0} = \frac{L - L0}{L0}$
Strain Rate (SR)	1/ms	$SR = S/(\Delta t) = (\Delta \mathrm{L}/\mathrm{L0})/\Delta \mathrm{t}) = (\Delta \mathrm{L}/\Delta \mathrm{t})/\mathrm{L0} = \Delta \mathrm{V}/\mathrm{L0}$
Global Longitudinal Strain (GLS)	%	$GLS = \frac{LES - LED}{LED}$

ΔL= absolute change in length, L0= baseline length, ΔV=velocity gradient of segment, Δt=change in time, L_{ED}=original length of the LV contour in diastole L_{ES}= original length of the LV contour in systole

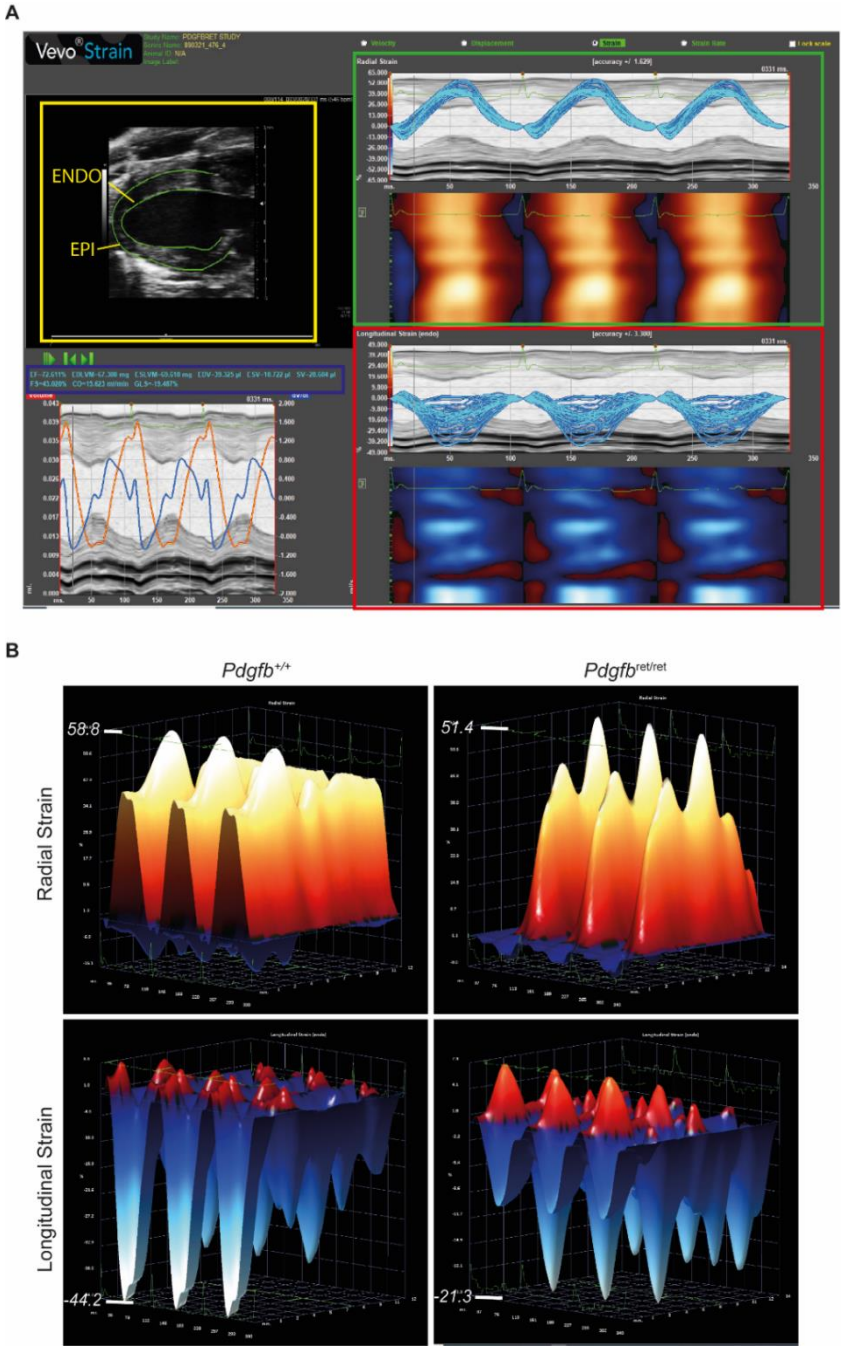

Figure 2.4: Example of Strain output and 3D Strain Visualisation

(**A**) *Pdgfb*$^{+/+}$ example of strain output of strain measured across the endocardium from VevoLab 3100 analysis software. Highlighted are B-mode images of the heart with endocardial (ENDO) and epicardial (EPI) images defined (yellow box). Cardiac parameters can be calculated from B-mode images (blue box). Visualisation of radial (green box) and longitudinal (red box) strain over 3 cardiac cycles. (**B**) 3D visualisation of radial (top panels) and longitudinal (bottom panels) strain in *pdgfb*$^{+/+}$ and *pdgfb*$^{ret/ret}$ mice are shown and highlight differential strain patterns in *pdgfb*$^{+/+}$ and *pdgfb*$^{ret/ret}$ mice. Peak strain values are annotated and highlighted on each 3D visualisation.

Segmental Strain Analysis

Both radial (Figure 2.5A) and longitudinal strain (Figure 2.5B) can be visualised and quantified using the time to peak analysis parameter on Vevo3100 software. Segmental strain analysis was performed to investigate differences in strain across 6 points of the endocardium; the posterior basal (Post(B)), posterior mid (Post(M)) posterior apical (Post(A)), anterior basal (Ant(B)), anterior mid (Ant(M)) and anterior apical (Ant(A)) regions (Figure 2.5). This function can also be utilised to calculated radial and longitudinal strain rate, displacement, and velocity. All these parameters can be visualised over time and values for strain and time to peak strain (T2Pk,) are given (Figure 2.5). T2Pk is the time from the R-Wave (baseline) to when the maximum peak is reached for each of 6 segments of the left ventricular wall. This can be calculated for velocity, displacement, strain, or strain rate, depending on which parameter is selected. I next performed analysis to evaluate longitudinal and radial strain on the posterior and anterior endocardial wall as well as on the base, mid and apical regions. This was done by combining the average values of the posterior and anterior segments listed previously. To do this the mean radial and longitudinal strain values across the posterior and anterior segments were manually calculated. Using the reverse strain function on VevoLab software both reverse longitudinal and radial strain could be calculated for left ventricular segments. Reverse strain can be used to evaluate diastolic function of the left ventricle. Ventricular dyssynchrony was determined from longitudinal and radial strain using established measures; maximum opposing wall delay between the earliest and the latest segment; time-to peak variation, defined as the standard-deviation of time-to-peak over all 6 segments; and standard-deviation of time-to-peak corrected for the r-r interval (Yu *et al.*, 2007; Mor-Avi *et al.*, 2011; Bauer *et al.*, 2013).

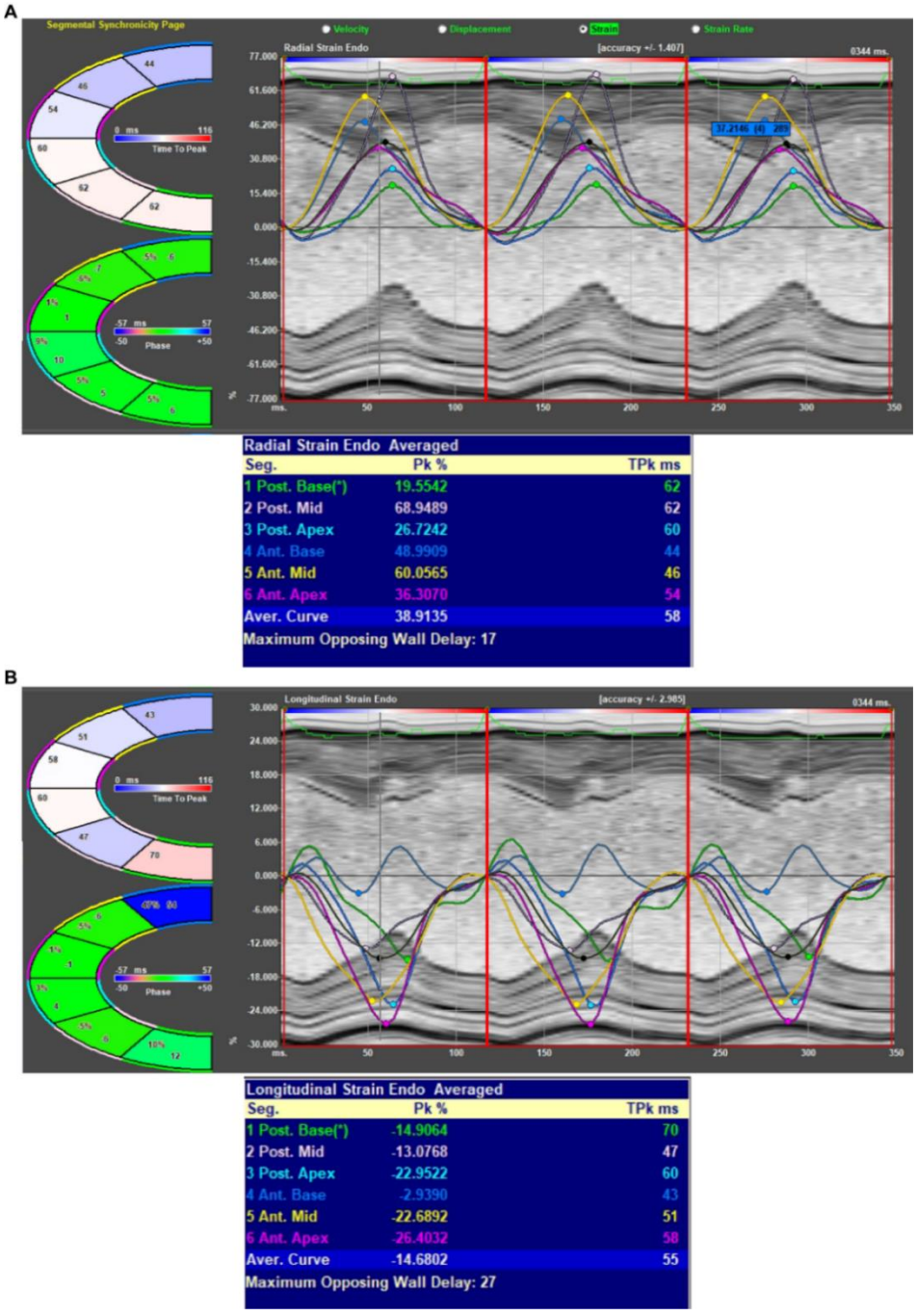

Figure 2.5: Example of Time to Peak Strain Analysis

Example of time to peak analysis output of from the hearts of *pdgfb*$^{+/+}$ mice using VevoLab Software, visualising strain over 6 segments of the endocardium; 6 points of the endocardium; the posterior basal (Post. Base, green line), posterior mid (Post. Mid), white line) posterior apical (Post. Apical, cyan line), anterior basal (Ant. Base, blue line), anterior mid (Ant. Mid, yellow line) and anterior apical (Ant. Apex, pink line) regions. The average radial and longitudinal strain curve values are also shown and quantified. Radial (**A**) and longitudinal (**B**) strain is shown over 3 cardiac cycles overlapped with m-mode images with segmental strain (Pk%) and time to peak (Tpk ms) values. Segmental strain rate, displacement and velocity can also be calculated.

Table 2.7:Ultrasound Strain Parameters

Parameter	Definition	Reference
Longitudinal Strain	Measurement of left ventricular deformation (base to apex) of the cardiac wall and describes a systolic shortening of left ventricular chamber length.	(Smiseth *et al.*, 2016)
Radial Strain	Measurement of deformation along the chamber wall in a radial or perpendicular direction to the wall which describes a systolic thickening of the ventricle.	(Smiseth *et al.*, 2016)
Strain Rate	The amount of strain during systolic contraction within a certain time of a specific orientation.	(Smiseth *et al.*, 2016)
Reverse Strain	Describes a diastolic lengthening of left ventricular chamber length.	(Ersbøll *et al.*, 2014)
Reverse Strain Rate	The amount of strain during diastolic relaxation within a certain time of a specific orientation.	(Ersbøll *et al.*, 2014)
Time to Peak Strain	Length of time it takes for the maximum strain value to be reached during contraction or relaxation.	(Johnson *et al.*, 2019)
Max Wall Delay	The maximal difference in peak velocity at basal and mid segments in opposing ventricular walls.	(Gorcsan *et al.*, 2010)
Standard Deviation of Time to Peak Strain	Derived from myocardial deformation recorded using tissue data in the longitudinal direction, has recently been proposed as an index of ventricular dyssynchrony.	(Yu *et al.*, 2007)
Velocity	The speed of the left ventricular wall motion from baseline position during the cardiac cycle.	(Dandel *et al.*, 2009)
Displacement	The distance the left ventricular wall moves from its baseline position during the cardiac cycle.	(Dandel *et al.*, 2009)

Positron Emission Tomography/ Computed Tomography (PET/CT)

In PET/CT experiments, 12-month-old (±2 weeks) male and female *pdgfb*$^{+/+}$, *pdgfb*$^{ret/+}$ and *pdgfb*$^{ret/ret}$ mice were utilised. Prior to PET scans, mice were anaesthetised via inhalation of 1.5-2.5% isoflurane (50/ 50 oxygen/nitrous oxide, 1 l/min). Mice were weighed prior to scanning. A 60min PET scans was performed immediately after injection of ^{18}F-NaF via the femoral artery or tail vein. PET data was acquired using a micro-PET/CT animal scanner (nanoPET/CT, Mediso, Hungary). A CT scan was acquired for attenuation correction. A further CT scan was obtained after administration of the contrast agent consisting of a 1:3 mix of Mvivo Au and

FenestraVC (Medilumine, Montreal, Canada). After the CT scan, animals were sacrificed, and tissues were harvested. Using Mediso's iterative Tera-Tomo 3D reconstruction algorithm, scans were reconstructed. This included point spread correction, and the following settings: 4 iterations, 6 subsets, full detector model, low regularization, spike filter on, voxel size 0.4 mm and 400–600 keV energy window. Scans were analysed using PMOD 3.8 software (PMOD technologies, Switzerland). Volumes of interest (VOIs) were manually drawn around the heart, both kidneys, the descending aorta whole brain and calcified brain regions on non-contrast and contrast CT images. Time activity curves were generated. For PET scans the average ^{18}F-NaF binding from 30-60 mis after tracer had reached equilibrium was quantified as standardized uptake values (SUVs) calculated as concentration in the VOI divided by the injected dose by animal weight. SUVmax values were calculated by taking the average of the 5 highest SUV values within a given VOI. The SUV ratio (background to tissue ratio) was calculated by taking the PET activity of a background reference VOI placed in the bifurcation of the vena cava and dividing by the given PET activity of a defined VOI. On CT scans the average CT values within a VOI were calculated alongside the Hot Average CT values which are the average of the 5 highest CT values within a given VOI.

Tissue Collection

After PET/CT scans, animals were culled, hearts were immediately weighed after gentle blotting of tissue paper and placed in phosphate-buffered saline (PBS). Due to radioactivity all tissues were stored a lead lined fridge overnight in PBS at 4^{O}C. Afterwards each limb was dissected, muscle and connective tissue was removed. Tibia length was measured after PET/CT scans using a ruler.

Mesenchymal Stem/Stromal Cell Culture

At around 3 months (12 weeks±2weeks), *pdgfb*$^{+/+}$, *pdgfb*$^{ret/+}$ and *pdgfb*$^{ret/ret}$ mice were sacrificed and tissues including heart, kidney, skeletal muscle and large coronary blood vessels, were harvested separately. Tissues were cut into smaller pieces in PBS containing 10% foetal calf serum and1% penicillin-streptomycin (FCS/PBS/PS,

GIBCO) on ice. Tissues were incubated with a collagenase mix consisting of collagenases type I, II and IV (0.5 mg/ml, Sigma-Aldrich, Massachusetts, USA) in the water bath at 37°C, shaking at 160 rpm for 45 min. Tissues were further mechanically dissociated between two slides and centrifuged for 10 min at 2000 rpm at 4°C. The supernatant was removed, cell pellets were re-suspended in PBS/FCS/PS and red blood cell lysis buffer (Stem Cell Technologies, Cambridge, UK) for 12 min at room temperature (RT). Cells were centrifuged for 10 min at 2000 rpm. After removing the supernatant, cells were re-suspended in 10% FCS/PBS/PS and passed through a 70 µm cell strainer. Cells pellets centrifuged for 10 min at 2000 rpm and resuspended in 20% FCS and 1%PS in DMEM high glucose medium containing Glutamax (GIBCO, ThermoFisher, UK) and cultured in uncoated 6-well plates until around 70-85% confluent. Cells were next split into either T25 or T75 flasks until passage 3 and utilised for osteogenesis assays.

Osteogenesis Assays

At passage 3, cells were counted for each tissue and seeded in a 24-well plate at a density of 40,000 cells/well in control media (10%FCS/1%PS in DMEM) or osteogenic media (10%FCS/1%PS in DMEM containing 0.1µm dexamethasone, 50µM ascorbate-2-phosphate and10mM β-glycerophosphate) (Langenbach and Handschel, 2013). Three technical replicates were used for control and osteogenic conditions. Media was changed 3 times per week. At 7 and 14 days of differentiation assay, cells were fixed in 4% PFA, washed 3 times with PBS and stained with Alizarin Red (Sigma-Aldrich, Massachusetts, USA) for 15 min at RT. Cells were then washed 3 times in PBS and imaged using a brightfield microscope (Zeiss Axio Observer, Carl Zeiss Vision, UK).

We next harvested the differentiated cells and controls and analysed the content using a spectrophotometer. In short, PBS was removed from the wells and 10% acetic acid was added. Plates were then placed on shaker for 30 min and the cell monolayer was gently scraped from each well and placed in separate 1.5ml eppendorfs and vortexed vigorously for 30 sec. Cell suspensions were then incubated at 85°C for 10 mins and placed on ice for 5 mins. Cell suspensions were centrifuged for 15 mins at 14,000xg. 1mM ammonium hydroxide was added to each suspension, then vortexed and 50 µl

of each added to separate wells in a 96 wells plate. Optical density (OD450) values were measured using an Omega FLUOStar plate reader (Omega, BMG Labtech, UK).

Statistical Analysis

Statistical analyses were performed using GraphPad Prism V6.0 (GraphPad Software, California, USA). For each data set normality was determined using Shapiro-Wilk distribution test. All error bars given are standard error of mean (SEM). Differences were considered significant at p-values of less than 0.05. Details of each statistical test used is given in each figure legend independently.

Chapter 3: The effect of the *Pdgfb*^{ret} mutation on Vascular Calcification

Introduction

In simple terms, vascular calcification is the active deposition of calcium-phosphate complexes within the vasculature which may occur due to aging and in CVD (Giallauria *et al.*, 2013). As such, it is sometimes known as "vascular aging" and can be conceptualised as "arterial stiffness'. Calcification can occur throughout the body as a response to necrotic inflammation and may lead to the rupture of atherosclerotic plaques causing MI (Joshi *et al.*, 2014). With such a high proportion of the aging population developing vascular calcification, there is a great need to study and understand the signalling pathways involved so that treatments can be developed.

Vascular calcification can be categorised into two phases: early initial microcalcification and late stage macrocalcification (Wang *et al.*, 2018). Microcalcification is associated with active inflammatory processes during atherosclerosis and is induced though the activity of inflammatory cytokines activating osteogenic differentiation of cells and mineralisation of the extracellular matrix (Joshi *et al.*, 2014). The presence of microvascular calcification is associated with unstable atherosclerotic plaques liable to rupture and cause thrombotic occlusion of the vessel lumen leading to MI (Joshi *et al.*, 2014). Macrovascular calcification is end stage calcification and may be thought of as a healing process or physiological defence as the body attempts to isolate and stabilise injured or damaged tissue. Furthermore, the presence of macrocalcification in plaques is associated with more stable plaque phenotype with a reduced risk of rupture (Shioi and Ikari, 2018). It is also important to note that calcification of organs and tissues may also occur in a variety of pathological conditions setting and is not exclusive to blood vessels and may also occur in the heart valves and kidney (Proudfoot, 2019).

Signalling by PDGFs is involved in vascular calcification through modulation of inflammatory cytokines, IL-1 and IL-6 and mediation of oxidative stress (Ouyang *et al.*, 2018). PDGFs may also modulate phenotypic switching of VSMCs, and other influence the phenotype of vascular cell types, to become pro-calcifying osteoblast-like cells which may contribute to vessel calcification (Sameer Bardeesi *et al.*, 2017).

However, *in vivo* studies investigating the role of PDGFB/PDGFRβ in the development of vascular calcification are lacking.

Pdgfb$^{ret/ret}$ mice, have a hypomorphic version of *pdgfb* allele and develop macroscopic, vessel-associated calcifications around the pons, midbrain, medulla and hypothalamus regions of the brain (Keller *et al.*, 2013). Alongside mutations in *PDGFRB* gene, loss of function mutations in the *PDGFB* gene have been shown to lead to idiopathic basal ganglia calcification (IBGC) in humans and *pdgfb*$^{ret/ret}$ mice model this condition closely. In IBGC patients, males develop a greater level of calcification than females (Nicolas *et al.*, 2015). IBGC is characterised by calcifications in or around the cerebral microvasculature (Betsholtz and Keller, 2014). In mice the extent of calcifications linked to the level of endothelial, rather than neuronal, release of PDGFB. These calcifications begin to develop at 4 months and are present at 12 months of age. However, whether *pdgfb*$^{ret/ret}$ mice develop micro- or macrocalcification out with the brain in the coronary vasculature, heart or kidneys at 12 months of age has not been yet established. I wished to investigate whether ectopic vascular calcification was exclusive to the brain in *pdgfb*$^{ret/ret}$ mice and hypothesised that due to the germline nature of the *pdgfb*^{ret} mutation in conjunction with the factor that PDGFB is released by all endothelial cells, other tissues would develop calcified lesions. I also wished to understand whether sex played a role in the extent of calcification like in IBGC patients.

Hypothesis

"*Pdgfb*$^{ret/ret}$ mice develop ectopic calcification throughout the vasculature and that the extent of calcification may be sex-dependent"

Aims

1. Identify areas of ectopic vascular calcification in *pdgfb*^{ret} mutant mice.
2. Compare the extent of vascular calcification between male and female *pdgfb*$^{+/+}$, *pdgfb*$^{ret/+}$and *pdgfb*$^{ret/ret}$ mutant mice.

Study Design

To address my aims, we performed whole body PET/CT imaging of male and female 12-month-old *pdgfb*$^{+/+}$, *pdgfb*$^{ret/+}$ and *pdgfb*^{ret} mutant mice using ^{18}F-NaF and a vascular contrast agent. Mice were scanned at 12 months old as previous studies identified high levels of calcification in their brains at this time point using micro-CT, magnetic resonance imaging, and histological analysis (Keller *et al.*, 2013). I reasoned calcium deposition in other tissues may be present at this timepoint. ^{18}F-NaF is a well-characterised radiotracer, which binds to hydroxyapatite crystals, and was initially used in the radiochemical imaging of bone (Blau, Ganatra and Bender, 1972). ^{18}F-NaF uptake occurs when OH- ions present in hydroxyapatite are exchanged with ^{18}F- ions which form fluorapatite (Blau, Ganatra and Bender, 1972). ^{18}F-NaF is utilised clinically to identify and image vascular calcification in conditions such as aortic valve calcification or atherosclerotic coronary artery disease(Dweck *et al.*, 2014; Fletcher *et al.*, 2021). Use of ^{18}F-NaF along with CT imaging can distinguish between macro- and microvascular calcification, making it particularly useful in imaging active disease progression and end-stage disease (MacAskill *et al.*, 2020). By using a gold particle-based vascular contrast agent, we were able to visualise organs and blood vessels in live mice to identify potential differences to vascular structure. Male and female mice were used to identify any sex differences in the extent of calcification. The number of mice per group are details in Table 3.1, however, due to external factors only 2 female *pdgfb*$^{ret/ret}$ mice were utilised in our studies (See Chapter 7: General Discussion).

Table 3.1: Number of mice scanned using PET/CT imaging.

Genotype	Sex		Total
	Male	Female	
Pdgfb$^{+/+}$	3	3	6
Pdgfb$^{ret/+}$	4	3	7
Pdgfb$^{ret/ret}$	4	2	6

Results

The anatomical location and the extent of brain calcification are variable but only present in *pdgfb*$^{ret/ret}$ mice.

To confirm the presence of calcification within the brains of our cohort of *pdgfb*$^{ret/ret}$ mice, I first examined non-contrast CT images from both male and female *pdgfb*$^{+/+}$, *pdgfb*$^{ret/+}$ and *pdgfb*$^{ret/ret}$ mice. CT images of the skull in the transverse, axial and sagittal planes of each mouse are shown in white contrasting with the lower grey signal of soft brain tissue within and around the skull (Figure 3.1A, B, C). On CT images, white indicates high CT signal and higher density of the tissue being imaged. Indeed, as previously reported (Keller *et al.*, 2013), macroscopic brain calcification was not present in any of *pdgfb*$^{+/+}$ (Figure 3.1A) or *pdgfb*$^{ret/+}$ (Figure 3.1B) mice analysed and this was true for both males and females. Brain calcification was exclusive to *pdgfb*$^{ret/ret}$ mice (Figure 3.1C), but the extent and anatomical location of calcification observed was highly variable. The most common pattern of calcification observed, in 3/6 *pdgfb*$^{ret/ret}$ mice was exhibited bilateral thalamic calcification accompanied by calcification localised around the pons (Figure 3.1C, Figure 3.2A, B). All the mice exhibiting this pattern were males suggesting the extent of calcification may be determined by sex.

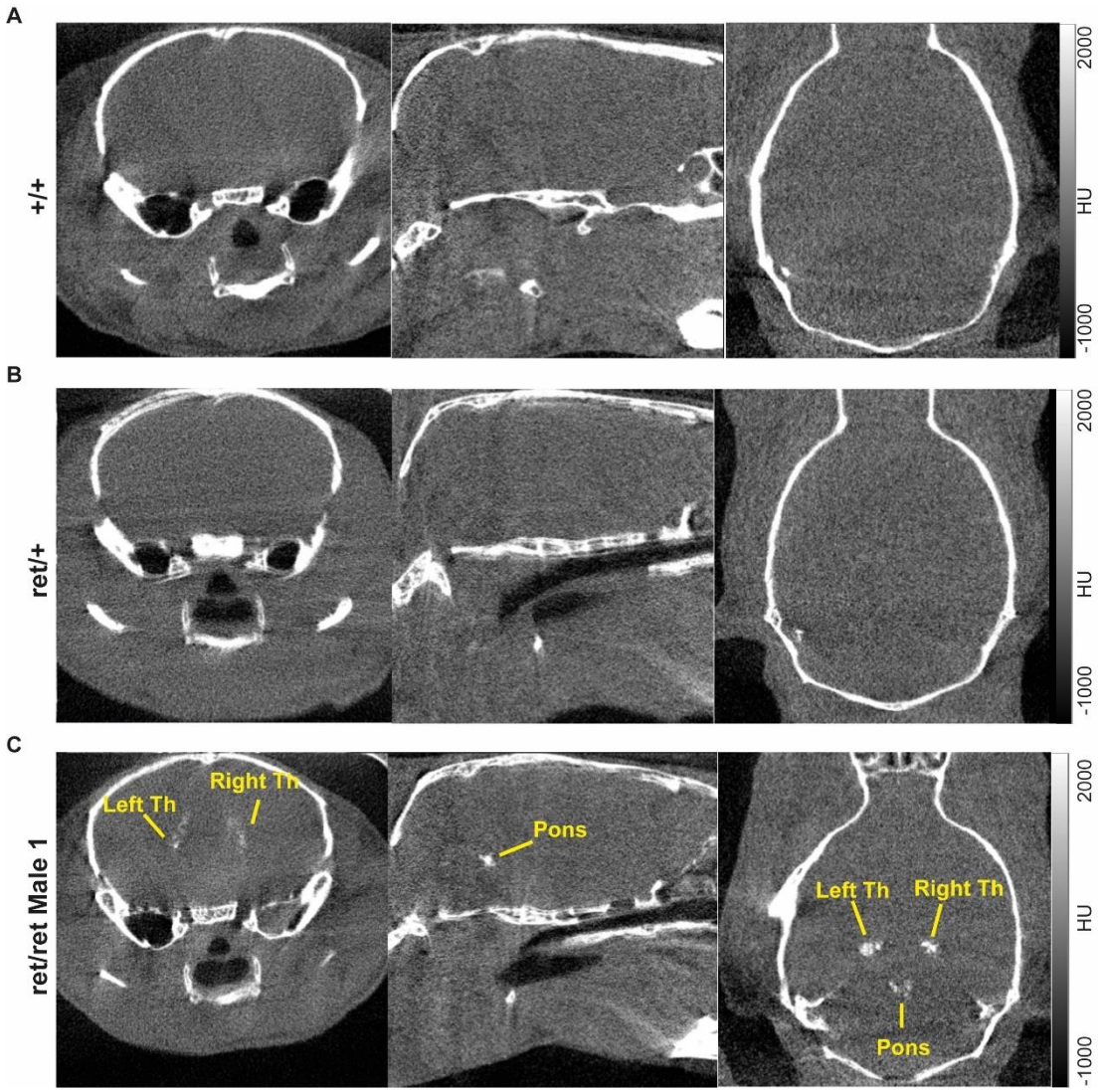

Figure 3.1: Confirmation of brain calcification in *pdgfb*$^{ret/ret}$ mice.

Examples of non-contrast CT images of the brains of *pdgfb*$^{+/+}$ (+/+, **A**), *pdgfb*$^{ret/+}$ (ret/+, **B**) mice and of one male *pdgfb*$^{ret/ret}$ (ret/ret, **C**) mouse shown in axial (left), sagittal (middle) and coronal (right) planes. Neither male or female *pdgfb*$^{+/+}$ or *pdgfb*$^{ret/+}$ mice exhibit any cerebral macroscopic calcification. The most common calcification phenotype in *pdgfb*$^{ret/ret}$ mice is bilateral thalamic calcification and calcification in the pons region. Images were analysed using PMOD 4.2 software. HU= Hounsfield units; Th=thalamus

A further two *pdgfb*$^{ret/ret}$ mice, one male and one female, exhibited a very small area of calcification around the pons absent of any thalamic calcification (Figure 3.2 C, D). One female *pdgfb*$^{ret/ret}$ mouse did not exhibit macrovascular calcification in any brain region (Figure 3.2E).

Examination of non-contrast CT images suggests that calcification is exclusive to *pdgfb*$^{ret/ret}$ mice, however, the extent of calcification shows high levels of interindividual variation. Furthermore, brain calcification is confined to the thalamus and pons regions with no calcification observed out with these areas.

To corroborate these observations and quantify the extent of calcification, I utilised volume of interest (VOI) analysis to select the regions of the brain in all genotypes, *pdgfb*$^{+/+}$, *pdgfb*$^{ret/+}$ and *pdgfb*$^{ret/ret}$, corresponding to the thalamic and pons regions. This facilitated quantification of the CT signal in non-contrast CT images of the whole brain, pons and left and right thalamus regions. This produced values for the average CT signal. Standard values for CT signal vary in literature but in soft tissue may range from -100 to 120 Hounsfield units (HU). Firstly, quantification of the whole brain CT signal did not reveal any significant differences in the average CT signal for combined groups of male and female *pdgfb*$^{+/+}$, *pdgfb*$^{ret/+}$ and *pdgfb*$^{ret/ret}$ mice (Figure 3.3A, $p>0.05$). In each group the average whole brain CT signal was around 100HU, *pdgfb*$^{+/+}$ (99.59HU), *pdgfb*$^{ret/+}$ (101.5HU) and *pdgfb*$^{ret/ret}$ (100.3HU) falling within the range of soft tissue. When groups of male mice were examined alone no differences were found in the average or hot average CT signal in the whole brain (Figure 3.3B, E, $p>0.05$). Examination of female mice independently revealed that the average CT signal in the whole brain was significantly higher in *pdgfb*$^{ret/+}$ than *pdgfb*$^{+/+}$ mice, although average CT values for both groups fall within the range of soft tissue so this would not indicate the presence of macroscopic calcification (Figure 3.3C, $p<0.05$). Due to the small group size, no statistical analyses could be performed to compare female *pdgfb*$^{ret/ret}$ mice with the other groups, however, the average CT signal seems comparable to *pdgfb*$^{+/+}$ and *pdgfb*$^{ret/+}$ mice.

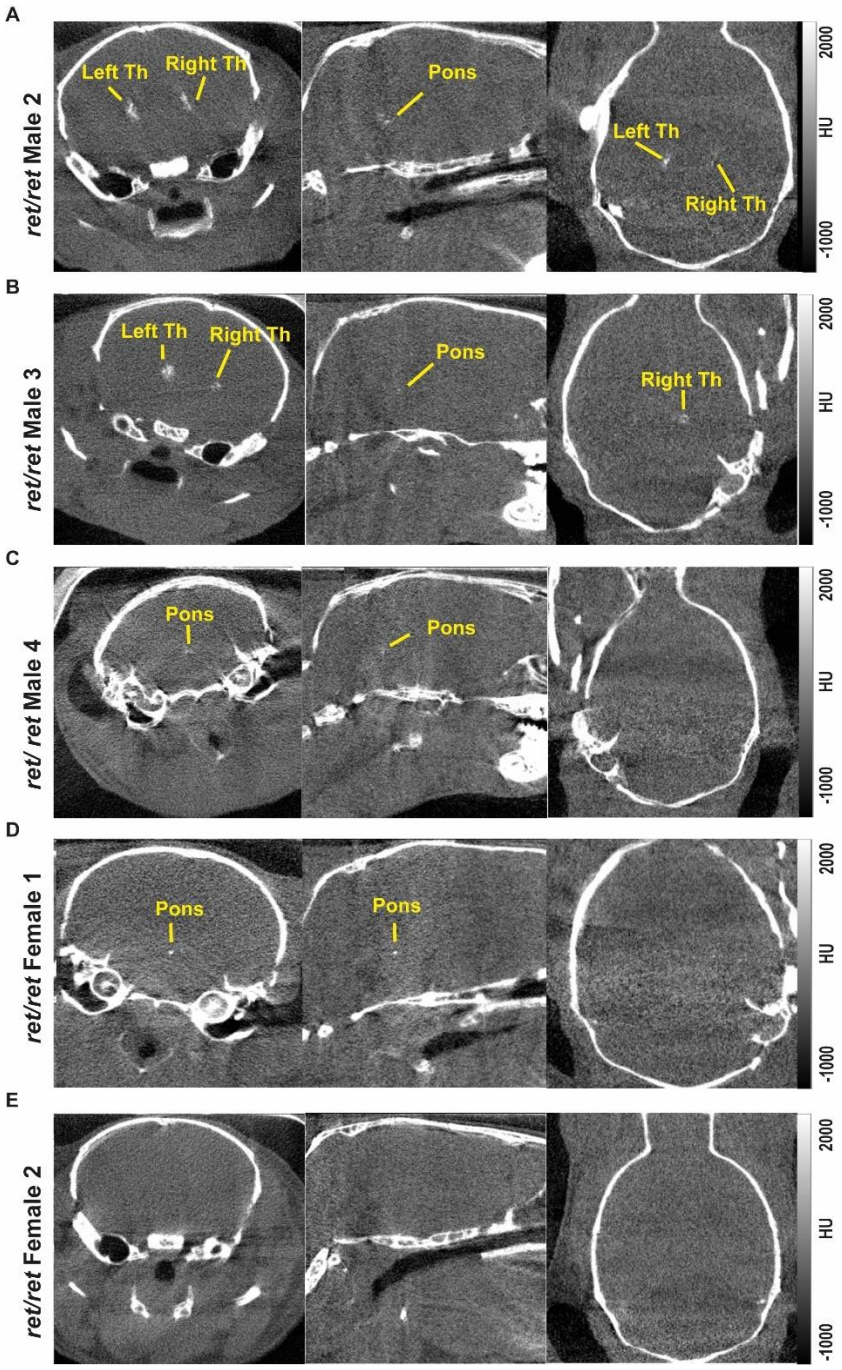

Figure 3.2: *Pdgfb*$^{ret/ret}$ mice exhibit variable levels of calcification in their brains.

Examination of all *pdgfb*$^{ret/ret}$ (ret/ret) brains reveals that the anatomical location and level of macroscopic calcification detected on non-contrast CT images varied significantly on an individual basis. Bilateral macroscopic calcification associated with the thalamus was detected in one male *pdgfb*$^{ret/ret}$ mouse with macroscopic calcification detected around the pons (**A**). The second individual displayed bilateral calcification around the thalamus and around the pons area (**B**). Two *pdgfb*$^{ret/ret}$ mice, one male (**C**) and one female (**D**) exhibited a very small amount of calcification around the pons area lacking any thalamic calcification. The final female *pdgfb*$^{ret/ret}$ mouse did not exhibit any evidence of macroscopic calcification (**E**). Images were analysed using PMOD 4.2 software. HU= Hounsfield units; Th=Thalamus

Next, the CT signal for each brain region was calculated. No significant differences were observed in the average CT values for the pons region across genotypes, in the *pdgfb*$^{ret/ret}$ group we can observed variation in data distribution indicating that some mice in this group have pons calcification (Figure 3.3D, p>0.05). This is evident when we divide groups into male and females. Although no significant differences in the average CT signal were observed between male *pdgfb*$^{+/+}$, *pdgfb*$^{ret/+}$ and *pdgfb*$^{ret/ret}$ mice, we can clearly observe large variation in male *pdgfb*$^{ret/ret}$ indicating variable levels of pons calcification (Figure3.3E, p>0.05). There was no difference in the average CT signal from the pons region between female *pdgfb*$^{+/+}$ and *pdgfb*$^{ret/+}$ mice and female *pdgfb*$^{ret/ret}$ mice exhibited a similar value for the average CT signal (Figure 3.3F, p>0.05). Next, both left and right thalamic regions were examined. In combined groups of male and female mice, a significant increase in average CT signal in the left thalamus was observed between *pdgfb*$^{ret/ret}$ mice and *pdgfb*$^{+/+}$ mice (Figure 3.3G, p<0.05). No difference as observed between *pdgfb*$^{ret/+}$ mice and *pdgfb*$^{+/+}$ and *pdgfb*$^{ret/ret}$ mice in left thalamus signal for combined groups (Figure 3.3G, p>0.05). When split into groups of male and females no significant differences in the average CT signal in the left thalamus was observed across any genotype (Figure 3.3 H, I, p>0.05). No difference in right thalamic average CT signal was observed for combined groups or for groups of males and females independently (Figure 3.3J, K, L, p>0.05). However, within the male *pdgfb*$^{ret/ret}$ cohort large variation was observed which indicates the presence of macroscopic calcification in the right thalamus in some but not all male *pdgfb*$^{ret/ret}$ mice (Figure 3.3K).

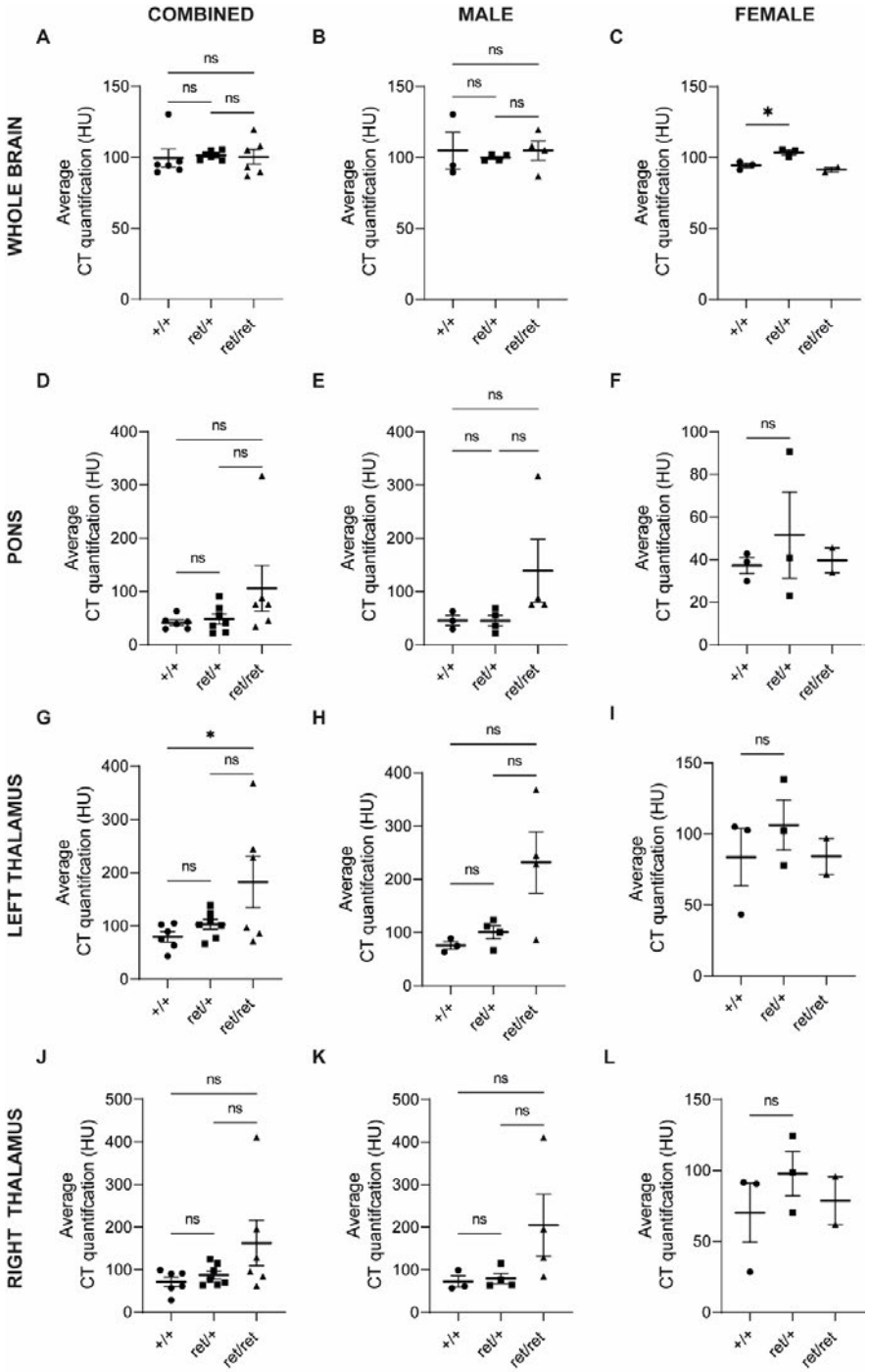

Figure 3.3: Quantification of CT signal indicates regional brain calcification differences in *pdgfb*$^{ret/ret}$ mice.

Volume of interests (VOIs) were used to quantify the average CT signal in the whole brain (**A**, **B**, **C**), pons (**D**, **E**, **F**), left (**G**, **H**, **I**) and right thalamus (**J**, **K**, **L**) areas in *pdgfb*$^{+/+}$ (+/+), *pdgfb*$^{ret/+}$ (ret/+) and *pdgfb*$^{ret/ret}$ (ret/ret) mice. Values for combined male and female (left row), males alone (middle row) and females (left row) are shown. Analysis was performed using PMOD 4.2 software. HU= Hounsfield units. Data shown as mean±SEM. One-Way ANOVA with Tukey's post-hoc test ns= not significant *p<0.05

The hot average CT signal defined as the average of the 5 highest CT values within a defined VOI, is useful in determining whether some macroscopic calcification in large tissue regions as measuring the average CT signal these differences may be lost due to regions of low signal. The hot average signal was not found to be significantly altered in the whole brain for the combined sex group, male group or female groups (Figure 3.4A, B, C, $p>0.05$). Although in the male cohort a greater variation in hot average CT signal was observed. The hot average CT signal was also not significantly changed in the pons region across genotypes although variation in data distribution in the *pdgfb*$^{ret/ret}$ group was observed further indicating heterogeneity in the presence of calcification (Figure 3.4D, $p>0.05$). This large variation may be accounted for by the fact that not all *pdgfb*$^{ret/ret}$ mice in our cohort exhibit macroscopic calcification around the pons and that some calcified nodules may be denser than others. This may indicate more advanced calcification in this region in certain *pdgfb*$^{ret/ret}$ mice. Next, I quantified the hot average CT signal in the right and left thalamic regions of the brain. The hot average CT signal was significantly greater in *pdgfb*$^{ret/ret}$ vs *pdgfb*$^{+/+}$ mice in the left thalamic region (Figure 3.4G, $p<0.05$). Male *pdgfb*$^{ret/ret}$ mice also had a significantly greater hot average CT signal compared with *pdgfb*$^{ret/+}$ mice; however, no differences were observed between *pdgfb*$^{+/+}$ vs *pdgfb*$^{ret/+}$ or *pdgfb*$^{ret/ret}$ mice (Figure3.4H, $p>0.05$). No difference in the hot average CT signal was observed between male *pdgfb*$^{+/+}$ and *pdgfb*$^{ret/+}$ mice or *pdgfb*$^{ret/+}$ mice and *pdgfb*$^{ret/ret}$ mice in the left thalamus (Figure 3.4H, $p>0.05$). No difference in the hot average signal from the less thalamus was detected in the female cohort (Figure 3.4I, $p>0.05$). Quantification of the hot average CT signal of the right thalamus did not reveal significant differences across groups of combined sex, males, or females (Figure 3.4J, K, L $p>0.05$).

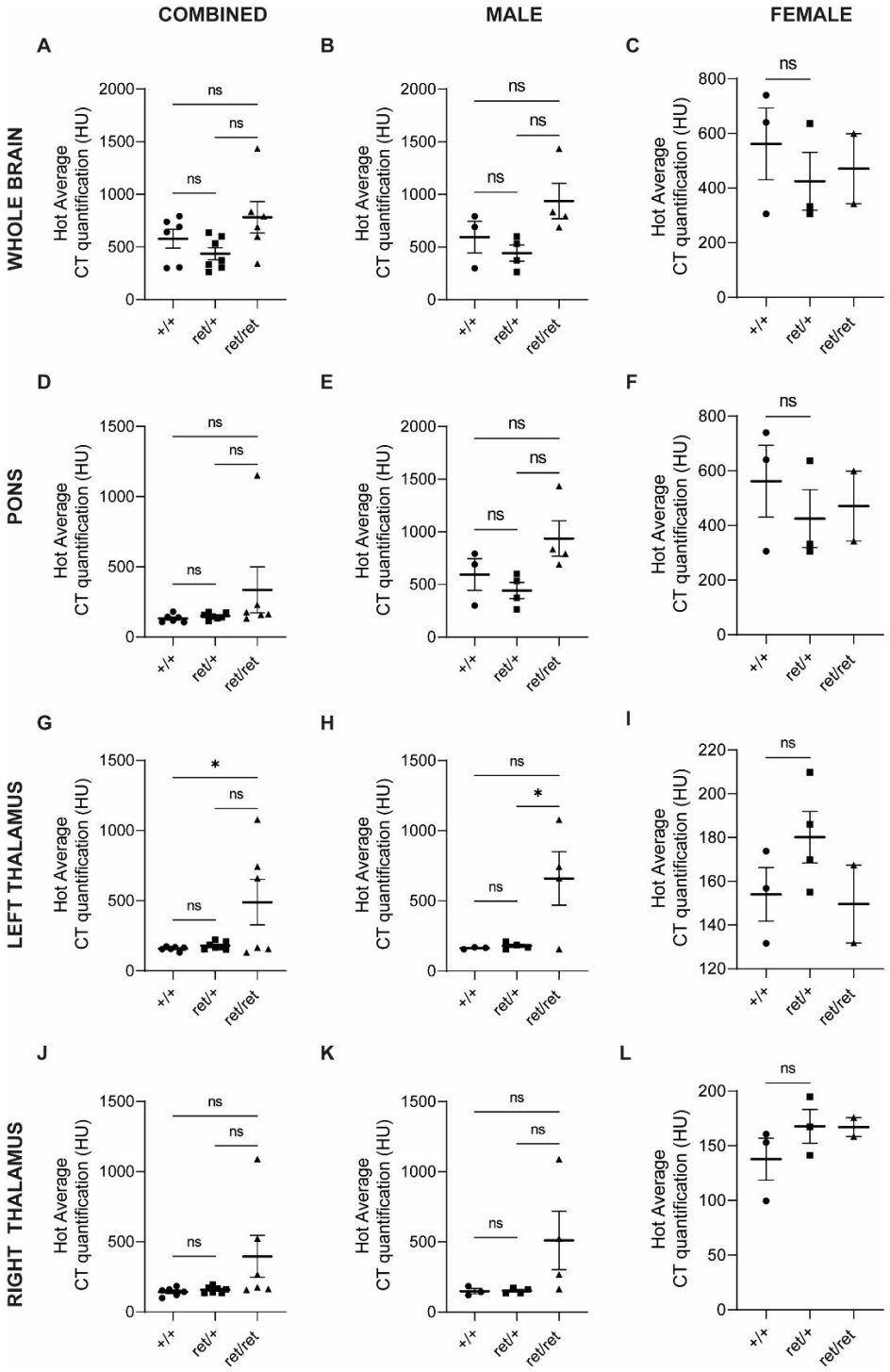

Figure 3.4: Quantification of hot average CT values in *pdgfb*$^{+/+}$, *pdgfb*$^{ret/+}$ and *pdgfb*$^{ret/ret}$ mice.

VOIs quantification of hot average CT values in the whole brain (**A**, **B, C**), pons (D**, E, F**), left (**G**, **H**, **I**) and right thalamus (**J**, **K**, **L**) areas in *pdgfb*$^{+/+}$ (+/+), *pdgfb*$^{ret/+}$ (ret/+) and *pdgfb*$^{ret/ret}$ (ret/ret) mice. The hot average is defined as the average signal intensity of the 5 highest intensity pixels within a regional VOI. Values for combined male and female (left row), males alone (middle row) and females (left row) are shown. Analysis was performed using PMOD 4.2 software. HU= Hounsfield units. Data shown as mean±SEM. One-Way ANOVA with Tukey's post-hoc test ns= not significant *p<0.05

Although greater variation was observed in the male *pdgfb*$^{ret/ret}$ group with the average of both measurements being greater than *pdgfb*$^{+/+}$ and *pdgfb*$^{ret/+}$ groups.

In summary, no male or female *pdgfb*$^{+/+}$ and *pdgfb*$^{ret/+}$ mice exhibit any macroscopic brain calcification on CT images, which was confirmed by regional and whole brain CT quantification. Three out of 4 male *pdgfb*$^{ret/ret}$ mice exhibit bi-thalamic and pons calcification. One male and one female *pdgfb*$^{ret/ret}$ mouse exhibited a small amount of calcification surrounding the pons and a last female had no identifiable calcification on CT images. To detect areas of microscopic calcification I next examined whole body PET scans.

No microscopic calcification in the brain was detected in *pdgfb*$^{ret/ret}$ mice.

^{18}F-NaF, has been shown to have a greater binding propensity for microscopic rather than macroscopic calcification and as such is useful in assessing progressive calcification or active disease (Moss *et al.*, 2020). *Pdgfb*$^{+/+}$, *pdgfb*$^{ret/+}$ and *pdgfb*$^{ret/ret}$ mice underwent PET scans using ^{18}F-NaF. On images obtained from PET scans areas of high ^{18}F-NaF tracer uptake are shown ranging from yellow to red indicating low to high signal, for example in bones. PET images displaying the average signal of the last 30 minutes of the scan are shown as this allows the ^{18}F-NaF radiotracer to move throughout the body and bind to areas of calcification. These images can then be overlaid with CT images to distinguish the anatomical location of PET signal.

I next examined imaging data from PET scans of the brains of *pdgfb*$^{+/+}$, *pdgfb*$^{ret/+}$ and *pdgfb*$^{ret/ret}$ mice. Images captured of the average signal over the last 30 minutes were combined and overlaid with non-contrast CT scans from *pdgfb*$^{+/+}$, *pdgfb*$^{ret/+}$ and *pdgfb*$^{ret/ret}$ mice (Figure 3.5A, B, C). Examination of these images did not indicate the uptake of ^{18}F-NaF within the brains of *pdgfb*$^{+/+}$ and *pdgfb*$^{ret/+}$ mice and indeed high ^{18}F-NaF uptake is confined to the skulls. This was also the case in *pdgfb*$^{ret/ret}$ mice, even in those individuals which exhibited high levels of macroscopic calcification detected by CT (Figure 3.5C). To confirm this, I quantified the ^{18}F-NaF signal within the brain using VOIs given in standard uptake values (SUV). ^{18}F-NaF signal in the whole brain was not significantly different in groups of combined males and female *pdgfb*$^{+/+}$, *pdgfb*$^{ret/+}$ and *pdgfb*$^{ret/ret}$ mice (Figure 3.6A, $p>0.05$). This was also the case when males and females were examined separately (Figure 3.6B, C $p>0.05$).

Average SUV values for ^{18}F-NaF uptake in the pons was unchanged in in the combined sex group or females (Figure 3.6 D, F, $p>0.05$). I did, however, observed greater average SUV values in male *pdgfb*$^{+/+}$ mice versus both *pdgfb*$^{ret/ret}$ and *pdgfb*$^{ret/+}$ male mice (Figure 3.6B, $p<0.05$). Left (Figure 3.6 G, H, I) and right thalamic (Figure 3.6 J, K, L) regions were unchanged in terms of their average SUV values, and this was true for combined groups of mice and also male and female mice separately. The next parameter I examined was SUVmax for the ^{18}F-NaF signal. Like the hot average CT signal, SUVmax is the average of the highest 5 SUV values within a predefined VOI. In combined male and female *pdgfb*$^{+/+}$, *pdgfb*$^{ret/+}$ and *pdgfb*$^{ret/ret}$ mice no significant difference was observed SUVmax values in the whole brain (Figure 3.6A) and pons (Figure 3.6D, $p>0.05$). The same was observed for SUVmax values for males and female separately in the whole brain (Figure 3.7B, C) and pons (Figure3.7E, $p>0.05$). In the left thalamus *pdgfb*$^{ret/+}$ mice were observed to have a significantly greater SUVmax when compared to *pdgfb*$^{+/+}$ and *pdgfb*$^{ret/ret}$ mice perhaps suggesting the presence of microcalcification in this region in these animals (Figure 3.7G, $p<0.05$). When divided into males and females however no differences where observed and large variation SUVmax in the male *pdgfb*$^{ret/+}$ group was observed (Figure 3.7H, I, $p<0.05$). This could suggest that the *pdgfb*$^{ret/+}$ males examined in this study may develop microcalcification. No difference in SUVmax was found in the right thalamus in the combined, male or female groups (Figure 3.7J, KL, $p>0.05$).

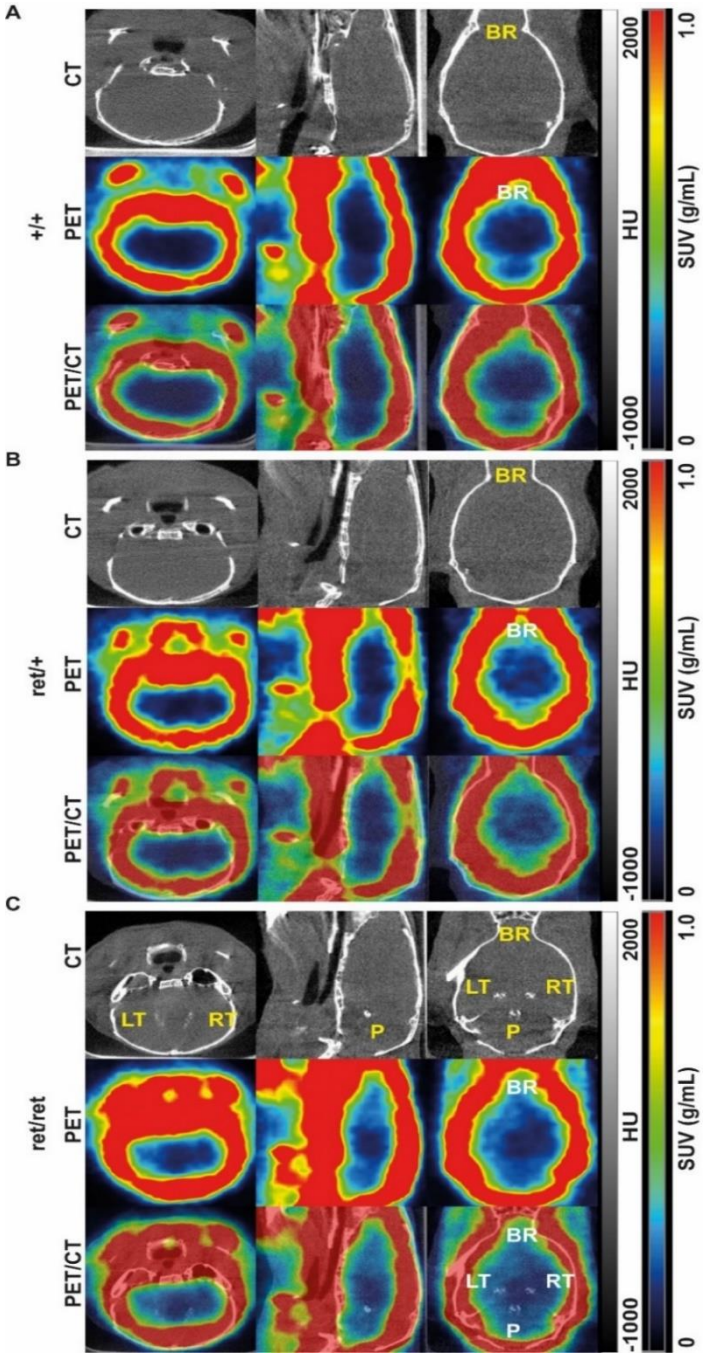

Figure 3.5: PET imaging of ^{18}F-NaF activity in the brains on *pdgfb*$^{ret/ret}$ mice.

Example CT images (top), PET images (middle) and PET/CT images combined in axial (left), sagittal (middle) and coronal (right) planes. PET and PET/CT images show the average ^{18}F-NaF signal taken over the last 30 minutes of the scan centred around the skull and brains (BR) of *pdgfb*$^{+/+}$ (+/+, A), *pdgfb*$^{ret/+}$ (ret/+, **B**) and *pdgfb*$^{ret/ret}$ mice (ret/ret, **C**). Representative images are from male mice. Images do not reveal any PET signal within the skulls of *pdgfb*$^{+/+}$ or *pdgfb*$^{ret/+}$ mice (**A**, **B**). Images show high ^{18}F-NaF uptake into the skulls as expected but no PET signal was detected in the brains of *pdgfb*$^{ret/ret}$ mice even those which had high levels of macroscopic calcification in the pons (P) and left (LT) and right thalamus (RT, **C**). HU- Hounsfield units SUV- standard uptake values.

The standard uptake values ratio (SUVR) is degree of radiotracer uptake in a region, in this case the brain compared with that in a given reference region. In this case this the VOI reference region was the bifurcation of the vena cava as this region would not be expected to have active calcification as measured by ^{18}F-NaF uptake. I next calculated the SUVR the whole brain, pons and thalamus regions in combined groups of male and females, and males and females separately. The SUVR in the whole brain was significantly higher in *pdgfb*$^{+/+}$ mice than *pdgfb*$^{ret/+}$ mice in the combined sex cohort, however, no difference was observed between any other genotypes (Figure 3.8A, $p<0.05$). When groups of male and females were examined independently, no difference was observed in their SUVR values in the whole brain although SUVR was higher in *pdgfb*$^{+/+}$ groups (Figure 3.8B, C, $p>0.05$). No difference was observed in the SUVR derived from the pons region in combined groups, males and females (Figure 3.8D, E, F $p>0.05$). In the combined groups of male and female mice alone, no significant changes in SUVR values in the left thalamus were found (Figure 3.8G, $p>0.05$). In the male cohort, *pdgfb*$^{ret/+}$ mice had significantly greater SUVR compared with *pdgfb*$^{ret/ret}$ mice (Figure 3.8H, $p<0.05$). No significant differences in the SUVR values in combined, male or female cohorts were observed (Figure 3.8J, K, L, $p<0.05$). Taken together, SUV values for the brain and smaller brain regions suggest that there is little active calcification in the brain of *pdgfb*$^{+/+}$ and *pdgfb*$^{ret/ret}$ mice, however, there is an increase in *pdgfb*$^{ret/+}$ mice, perhaps representing active disease in the left thalamus. Next, I examined other organs in these mice to determine the presence of macro or microscopic calcification out with the brain.

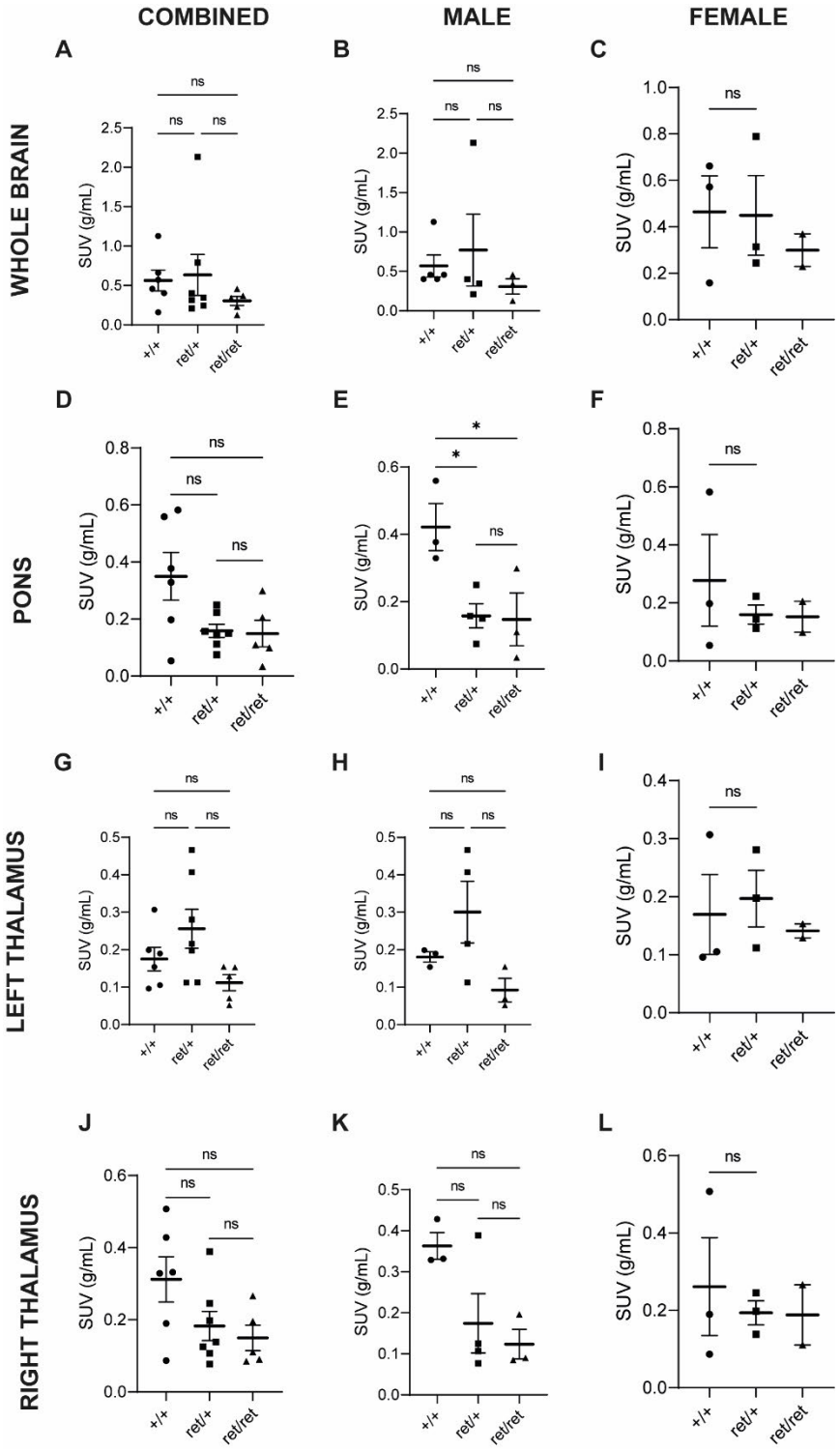

Figure 3.6: Quantification of average SUV values of ^{18}F-NaF activity in the brain.

Quantification of average standard uptake values (SUV) from the brain (**A**, **B**, **C**), pons (**D**, **E**, **F**) left thalamus (**G**, **H**, **I**) and right thalamus (**J**, **K**, **L**) in combined groups and single sex groups of male and female *pdgfb*$^{+/+}$, (+/+) *pdgfb*$^{ret/+}$ (ret/+)and *pdgfb*$^{ret/ret}$ (ret/ret) mice. Data shown as mean±SEM. One-Way ANOVA with Tukey's post-hoc test or Kruskal-Wallis test. ns= not significant *p<0.05. Images were analysed using PMOD 4.2 software.

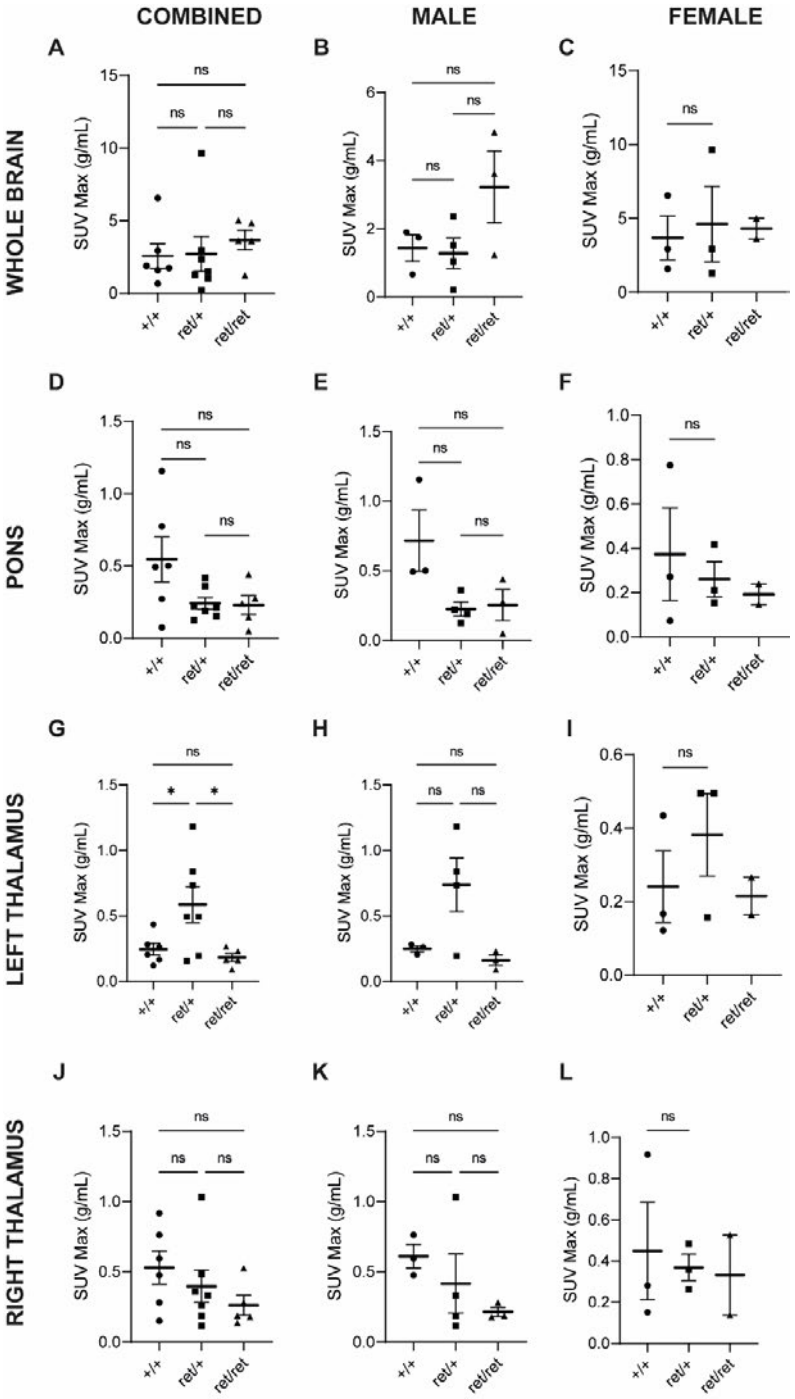

Figure 3.7: Quantification of SUVmax values in the brain.

Quantification of average SUVmax values from the brain (**A**, **B**, **C**), pons (**D**, **E**, **F**) left thalamus (**G**, **H**, **I**) and right thalamus (**J**, **K**, **L**,) in combined groups and single sex groups of male and female *pdgfb*$^{+/+}$, (+/+) *pdgfb*$^{ret/+}$ (ret/+) and *pdgfb*$^{ret/ret}$ (ret/ret) mice. Data shown as mean±SEM. One-Way ANOVA with Tukey's post-hoc test or Kruskal-Wallis test. ns= not significant *p<0.05. Images were analysed using PMOD 4.2 software.

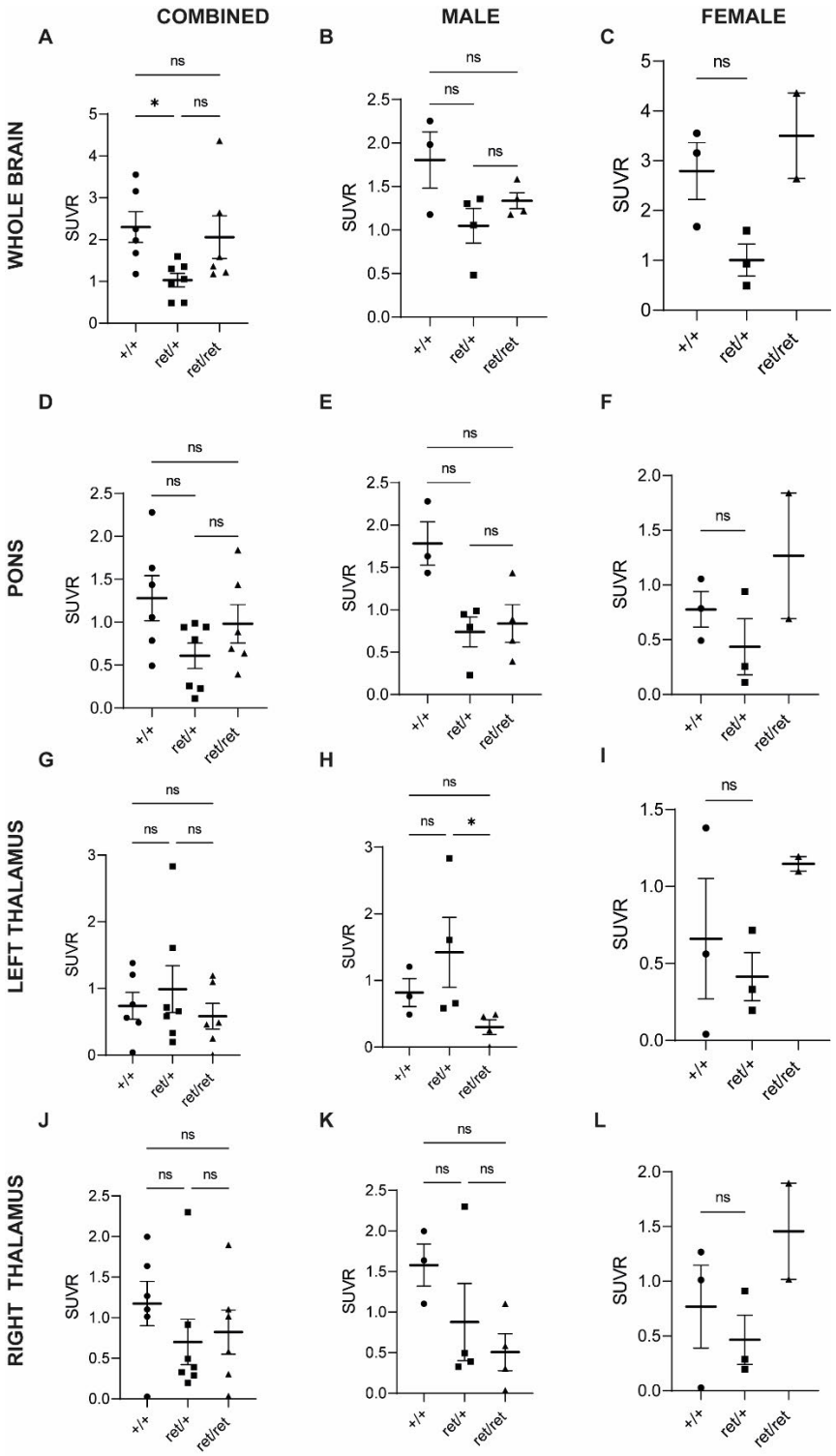

Figure 3.8: SUVR was higher in the left thalamus in male *pdgfb*$^{ret/+}$ mice.

Standard uptake values ratio (SUVR) from the whole brain (**A**, **B**, **C**), pons (**D**, **E**, **F**) left thalamus (**G**, **H**, **I**) and right thalamus (**J**, **K**, **L**,) in combined groups and single sex groups of male and female *pdgfb*$^{+/+}$,(+/+) *pdgfb*$^{ret/+}$ (ret/+)and *pdgfb*$^{ret/ret}$ (ret/ret) mice. Data shown as mean±SEM. One-Way ANOVA with Tukey's post-hoc test or Kruskal-Wallis test. ns= not significant *p<0.05. Images were analysed using PMOD 4.2 software.

Pdgfb$^{ret/ret}$ mice did not develop macroscopic calcification in any heart region.

Next, I examined non-contrast CT images of the hearts of *pdgfb*$^{+/+}$, *pdgfb*$^{ret/+}$ and *pdgfb*$^{ret/ret}$ mice for the presence of macroscopic calcification in any regions of the heart. Examination of non-contrast CT images did not show any macroscopic calcification in *pdgfb*$^{+/+}$, *pdgfb*$^{ret/+}$ or *pdgfb*$^{ret/ret}$ mice (Figure 3.9 A, B, C). When groups of males and females were combined no difference in the average CT signal from was observed (Figure 3.9D $p>0.05$). In the male group and increase in the average CT signal was observed in *pdgfb*$^{+/+}$ vs both *pdgfb*$^{ret/+}$ and *pdgfb*$^{ret/ret}$ mice, however, this fell within the values for soft tissue (-100 to 120HU) which would not indicate the presence of macroscopic calcification (Figure 3.9E, $P<0.05$). No difference in the average CT values were observed in female mice (Figure 3.9F). The hot average CT values from the heart remained unchanged across all genotypes in the combined sex cohort and when divided into groups of males and females (Figure 3.9 G, H, I $p>0.05$). Both quantification and examination of CT images of the heart indicates that macroscopic calcification is absent in my cohort of 12-month-old *pdgfb*$^{ret/ret}$ mice.

No evidence of microcalcification was detected in the hearts of *pdgb*$^{ret/ret}$ mice.

Low ^{18}F-NaF activity was observed in the hearts of *pdgfb*$^{+/+}$ (Figure 3.10 A), *pdgfb*$^{ret/+}$ (Figure 3.10B) and *pdgfb*$^{ret/ret}$ mice (Figure 3.10C). In the top panel non-contrast CT images are shown, the middle panel shows PET scans, and the bottom panel shows PET/CT scan overlays (Figure 3.10). The average SUV values over the last 30 minutes of the scan in *pdgfb*$^{+/+}$, *pdgfb*$^{ret/+}$ and *pdgfb*$^{ret/ret}$ were measured and showed no difference between genotypes in combined and single sex groups (Figure 3.11A, B, C, $p>0.05$). Although examination of data distribution in the male cohort showed a greater variability in data distribution than in the hearts of *pdgfb*$^{ret/+}$ and *pdgfb*$^{ret/ret}$ mutants than *pdgfb*$^{+/+}$ mice. SUVMax values, average of the 5 highest SUV values, were also unchanged between each genotype in the combined and male and female cohorts (Figure 3.11 D, E, F $p>0.05$).

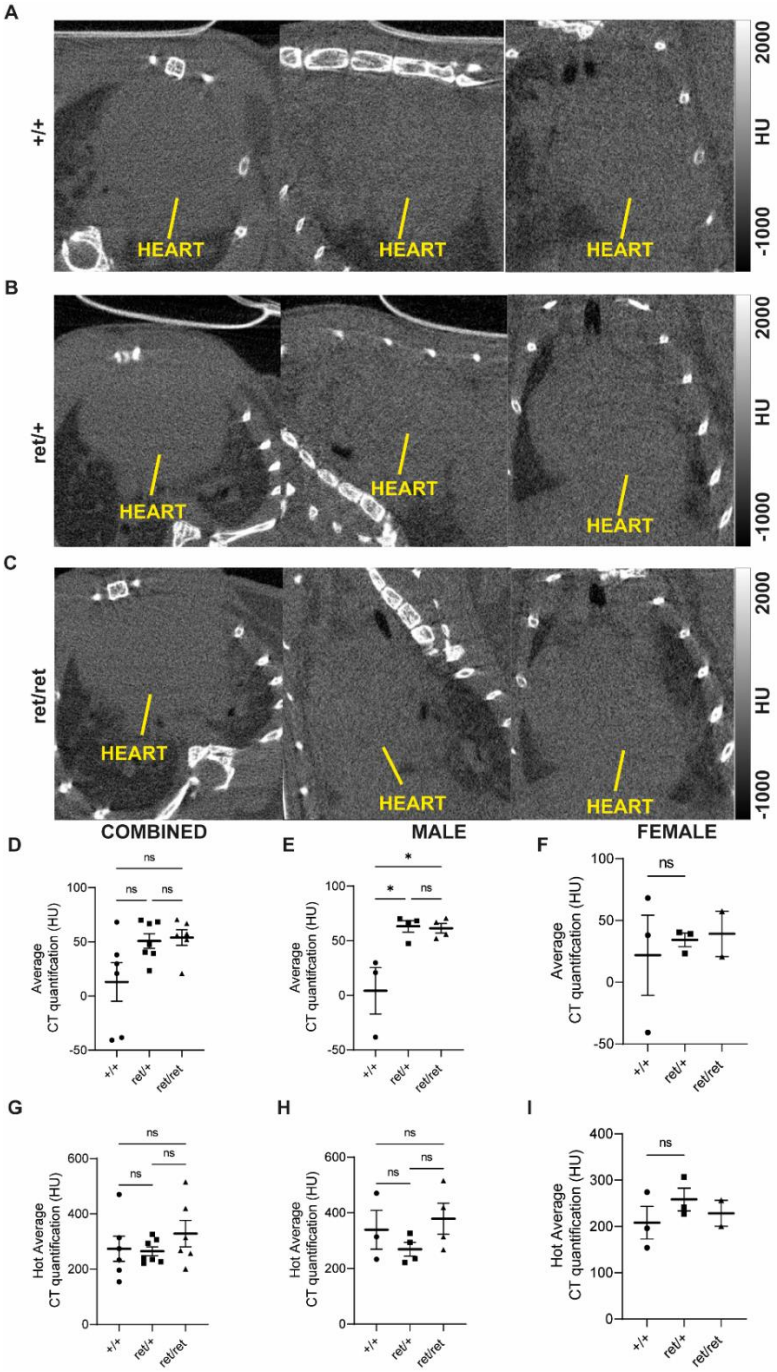

Figure 3.9: CT imaging and quantification did not reveal macroscopic calcification in the hearts of *pdgfb*$^{+/+}$, *pdgfb*$^{ret/+}$ and *pdgfb*$^{ret/ret}$ mice.

Example non-contrast CT images shown in axial (left), sagittal (middle) and coronal (right) planes of the heart in *pdgfb*$^{+/+}$ (+/+, **A**), *pdgfb*$^{ret/+}$ (ret/+, **B**) and *pdgfb*$^{ret/ret}$ (ret/ret, **C**) mice. No macroscopic calcification was detected in the hearts of any mice scanned. Quantification of the average CT values for both sexes combined (**D**), males (**E**) and females (**F**) are shown. Hot average CT values in the hearts for males and females combined(**G**), males alone (**H**) and females alone (**I**) were calculated. Analysis was performed using PMOD 4.2 software. HU= Hounsfield units. Data shown as mean±SEM. One-Way ANOVA with Tukey's post-hoc test or Kruskal-Wallis test. ns= not significant, *p<0.05.

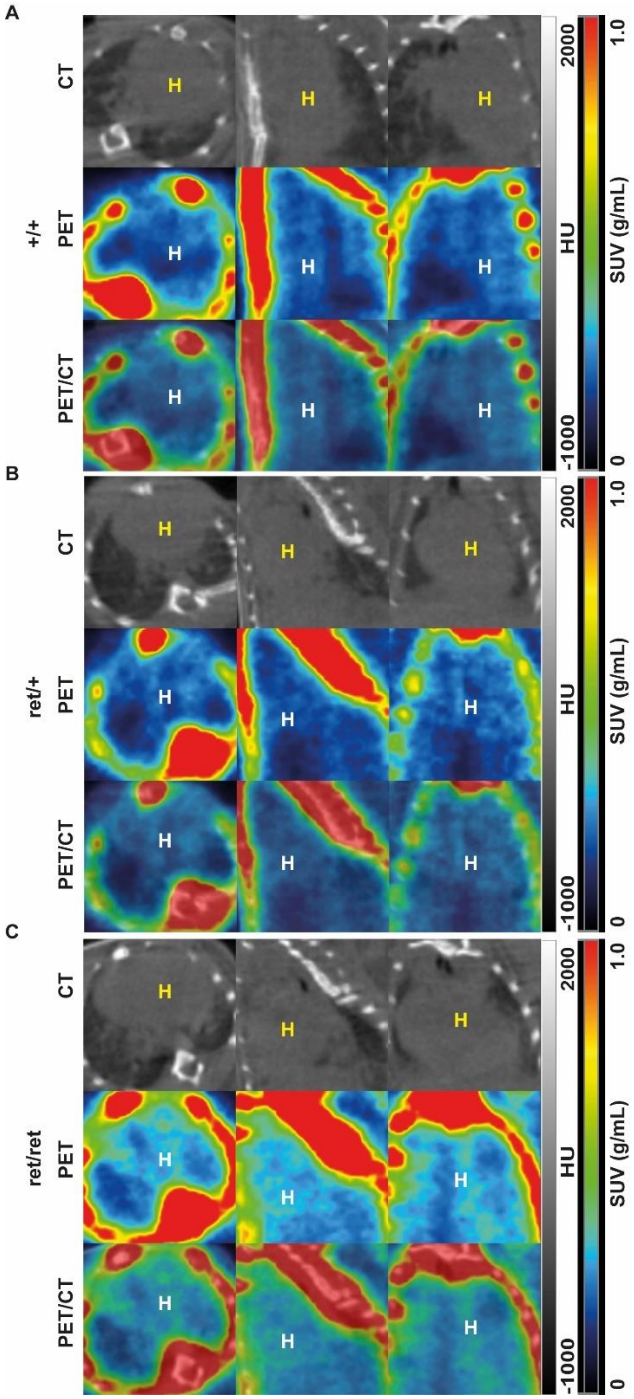

Figure 3.10: Low ^{18}F-NaF uptake was observed in the hearts of *pdgfb*$^{+/+}$, *pdgfb*$^{ret/+}$ and *pdgfb*$^{ret/ret}$ mice.

Example PET/CT overlayed images in axial (left), sagittal (middle) and coronal (right) views of the average ^{18}F-NaF and CT signals taken over the last 30 minutes of the scan of heart of *pdgfb*$^{+/+}$ (+/+, **A**), *pdgfb*$^{ret/+}$ (ret/+, **B**) and *pdgfb*$^{ret/ret}$ mice (ret/ret, **C**). Images show the heart (H) with high PET signal in the bones of the rib cage and spine. Low ^{18}F-NaF signal was detected the area corresponding with the heart shown on PET/CT images.

The SUVR was significantly higher in *pdgfb*$^{+/+}$ mice versus *pdgfb*$^{ret/+}$ mice in the combined cohort (Figure 3.11G, $p<0.05$). Although not significant SUVR was also greater for the hearts of *pdgfb*$^{+/+}$ mice compared to *pdgfb*$^{ret/ret}$ mice (Figure 3.11G). This suggests a greater level of ^{18}F-NaF uptake in the heart in *pdgfb*$^{+/+}$ mice compared with mutant mice which may indicate the development of microcalcification. When divided into groups of males and females no difference in the SUVR was observed in either male or female cohorts, however, the same trend of reduced SUVR in the hearts of male and female *pdgfb*$^{ret/+}$ and *pdgfb*$^{ret/ret}$ mice compared with *pdgfb*$^{+/+}$ mice was observed. This may suggest the active calcifying processes in the hearts of *pdgfb*$^{+/+}$ mice. This data indicates no active microcalcification is present in the hearts of *pdgfb*$^{ret/ret}$ mice.

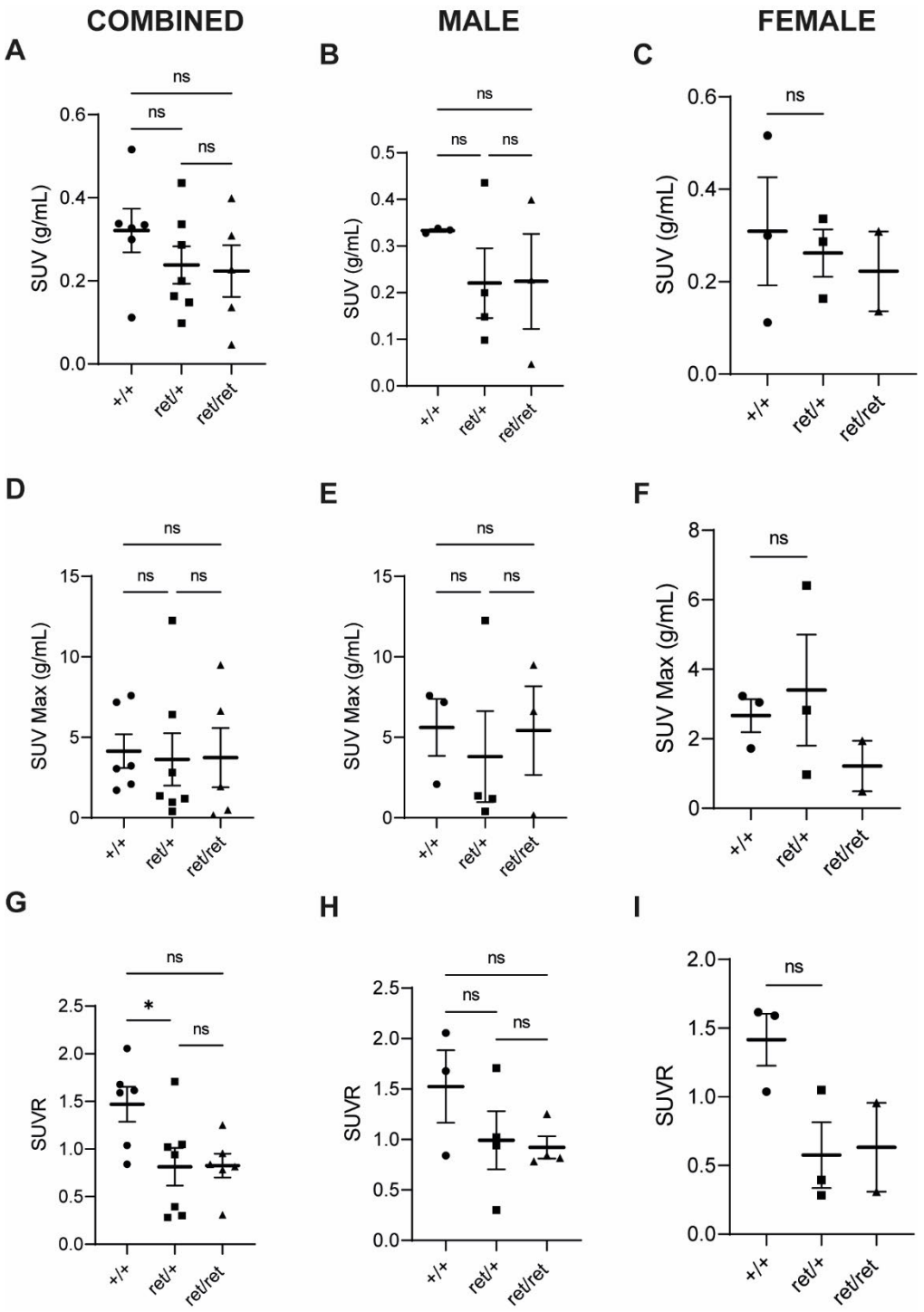

Figure 3.11: SUVR in the heart was greater in *pdgfb*$^{+/+}$ mice.

Quantification of average SUV, (**A**, **B**, **C**) SUVmax (**D**, **E**, **F**) and SUVR (**G**, **H**, **I**) values in the heart in combined groups, males and female *pdgfb*$^{+/+}$, *pdgfb*$^{ret/+}$ and *pdgfb*$^{ret/ret}$ mice. Data shown as mean±SEM. One-Way ANOVA with Tukey's post-hoc test, Kruskal-Wallis test or unpaired t-test. ns= not significant. Images were analysed using PMOD 4.2 software.

Contrast-enhanced CT imaging enabled visualisation of the aorta.

Next in my analysis, I assessed and the presence of macroscopic calcification in two regions of the aorta: the aortic arch region and the descending portion of the thoracic aorta. In non-contrast CT images, it is difficult to clearly distinguish each portion of the aorta. Therefore, the descending thoracic aorta was further visualised using contrast enhanced CT with a gold-particle based contrast agent (Figure 3.12). While this identifies the descending thoracic aorta, no obvious differences were observed between *pdgfb*$^{+/+}$ (Figure 3.12A), *pdgfb*$^{ret/+}$ (Figure 3.12B) and *pdgfb*$^{ret/ret}$ (Figure 3.12C) mice in terms of aortic structure. Contrast CT images allowed VOIs to be defined, overlayed and adjusted to non-contrast enhanced CT images for quantification. However, in the presence of the contrast, quantification cannot be performed, due to possible interference between the agent and the CT signal. Macroscopic calcification was not detected in descending thoracic aorta as average CT values (Figure 3.12 D, E, F) and hot average CT values (Figure 3.12 G, H, I) did not differ significantly in combined or in individual sex cohorts ($p>0.05$). Similarly, I used contrast enhanced CT to allow visualisation of the aortic arch in *pdgfb*$^{+/+}$ (Figure 3.13A), *pdgfb*$^{ret/+}$ (Figure 3.13B) and *pdgfb*$^{ret/ret}$ (Figure 3.13C) mice. Quantification of the average (Figure 3.13 D, E, F) and hot average (Figure 3.13 G, H, I) of CT values in all cohorts did not reveal any significant differences, supporting the absence of macroscopic calcification in each of the groups. In summary, evidence from the examination of CT images alongside quantification suggests that the aorta of *pdgfb*$^{ret/ret}$ mice do not contain advanced calcified plaques. I next analysed PET images to determine the presence of active microcalcification in *pdgfb*$^{+/+}$, *pdgfb*$^{ret/+}$ and *pdgfb*$^{ret/ret}$ mice in the descending portion of the thoracic aorta and aortic arch.

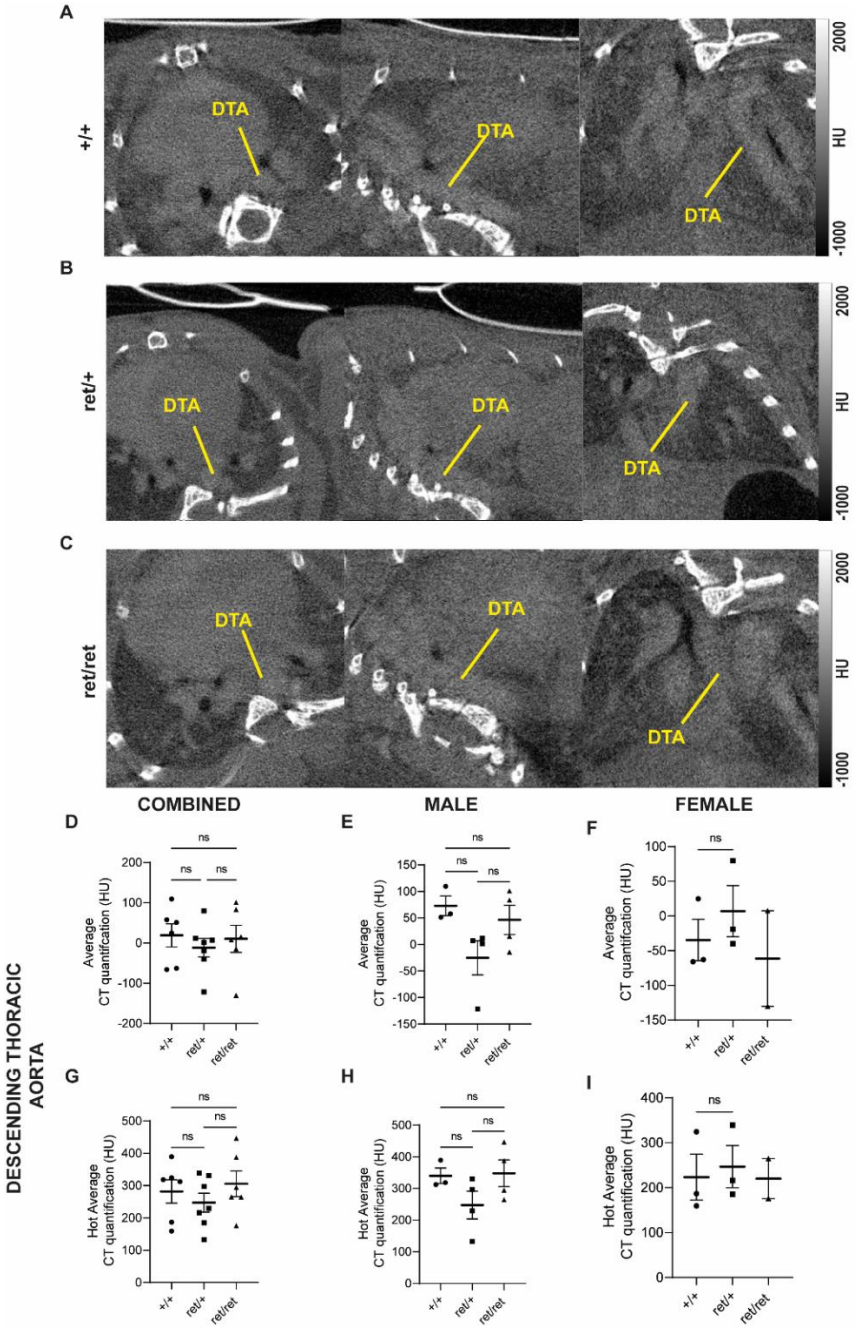

Figure 3.12: Visualisation of the descending thoracic aorta (DTA) using contrast CT.

Contrast enhanced CT images in axial (left), sagittal (middle) and coronal (right) views of the descending thoracic aorta (DTA) in *pdgfb*$^{+/+}$ (+/+, **A**), *pdgfb*$^{ret/+}$ (ret/+, **B**) and *pdgfb*$^{ret/ret}$ mice (ret/ret, **C**). Use of the gold nanoparticle-based contrast agent allowed clear visualisation of the aorta found in close proximity running between the spinal cord and the heart. Examination of contrast CT images did not reveal any obvious morphological differences in aortic structure between +/+, ret/+ and ret/ret mice. Quantification of the average (**D**, **E**, **F**) and hot average (**G**, **H**, **I**) of CT values of the aortic arch in non-contrast CT images independent of the sex of the animals. Analysis was performed using PMOD 4.2 software. HU= Hounsfield units. Data shown as mean±SEM. One-Way ANOVA with Tukey's post-hoc test, Kruskal-Wallis test or unpaired t-test ns= not significant.

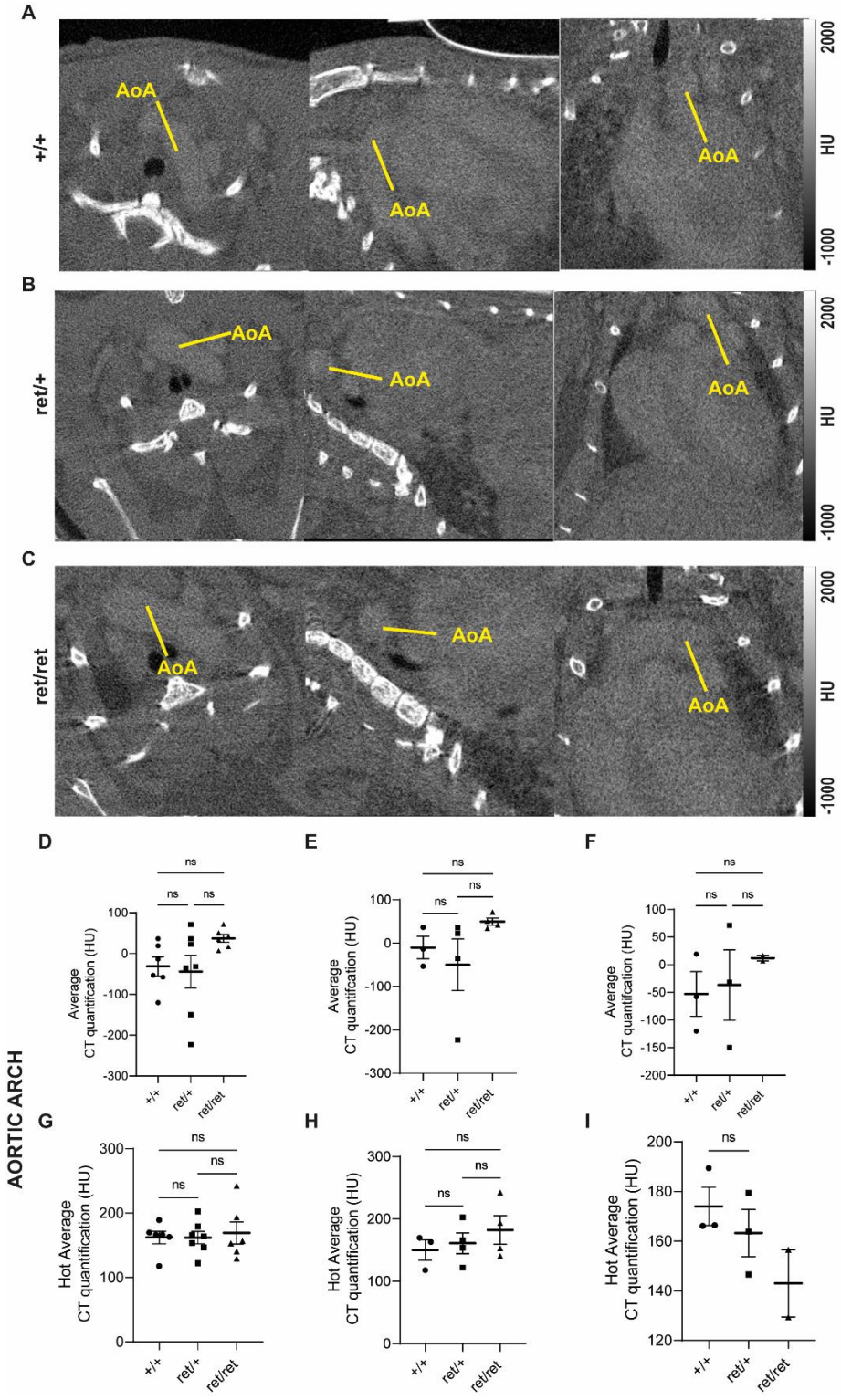

Figure 3.13: Visualisation of the aortic arch (AoA) using contrast CT and CT quantification.

Contrast enhanced CT images of the aortic arch (AoA) in *pdgfb*$^{+/+}$ (+/+, **A**), *pdgfb*$^{ret/+}$ (ret/+, **B**) and *pdgfb*$^{ret/ret}$ mice (ret/ret, **C**). Quantification of the average (**D**, **E**, **F**) and hot average (**G**, **H**, **I**) CT signal of the aortic arch in non-contrast CT images in combined and individual sex groups. Analysis was performed using PMOD 4.2 software. HU= Hounsfield units. Data shown as mean±SEM. One-Way ANOVA with Tukey's post-hoc test, Kruskal-Wallis test or unpaired t test. ns= not significant.

$Pdgfb^{+/+}$ mice exhibit higher ^{18}F-NaF signal in the aorta that $pdgfb^{ret}$ mutant counterparts.

Using contrast CT images overlayed with PET images showing the thoracic cavity I was able to select VOIs corresponding to the descending thoracic aorta (Figure 3.14) and the aortic arch (Figure 3.16). Examination of CT, PET, and PET/CT combined images of the thoracic cavity in $pdgfb^{+/+}$, $pdgfb^{ret/+}$ and $pdgfb^{ret/ret}$ mice did not show high ^{18}F-NaF activity in the areas corresponding with the descending thoracic aorta or aortic arch (Figure 3.14 A, B, C, Figure 3.16 A, B, C). I confirmed this by quantifying ^{18}F-NaF signal in these regions. Indeed, quantification of the ^{18}F-NaF signal over the last 30 mins of the PET scan showed no difference in the SUV (Figure 3.15, A, B, C), SUVmax (Figure 3.15, D, E, F) or SUVR (Figure 3.15, G, H, I) values in the descending thoracic aorta. This was true for the combined sex groups, in cohorts of males and females, however although not significant, there was a trend where SUV and SUVR were higher in $pdgfb^{+/+}$ mice vs $pdgfb^{ret/+}$ mice or $pdgfb^{ret/ret}$ littermates. This trend was maintained in the male cohort but was less apparent in females. Quantification of SUV values in the aortic arch followed a similar trend. In the combined cohort both SUV and SUVR values in the aortic arch were significantly higher in $pdgfb^{+/+}$ mice versus $pdgfb^{ret/+}$ mice (Figure 3.17, A, G $p<0.05$). Although not significant, both SUV and SUVR values were greater in the aortic arch of $pdgfb^{+/+}$ mice than $pdgfb^{ret/ret}$ mice (Figure 3.17, A, G, $p>0.05$). In the combined cohort no difference in the SUVmax values were found in combined cohorts, in males or in females (Figure 3.17, D, E, F, $p>0,05$). Interestingly, in males and females the trend in SUVmax values was reversed with male $pdgfb^{+/+}$ mice having higher SUVmax values than their $pdgfb^{ret}$ mutant littermates and female $pdgfb^{+/+}$ having lower SUVmax values than littermates. However, a greater number of female mice should be scanned to fully evaluate this observation. Quantification of PET signal in the aorta suggests that $pdgfb^{+/+}$ mice may begin to develop microcalcifications in the aortic arch, however, this was not observed in $pdgb^{ret/+}$ and $pdgb^{ret/ret}$ littermates.

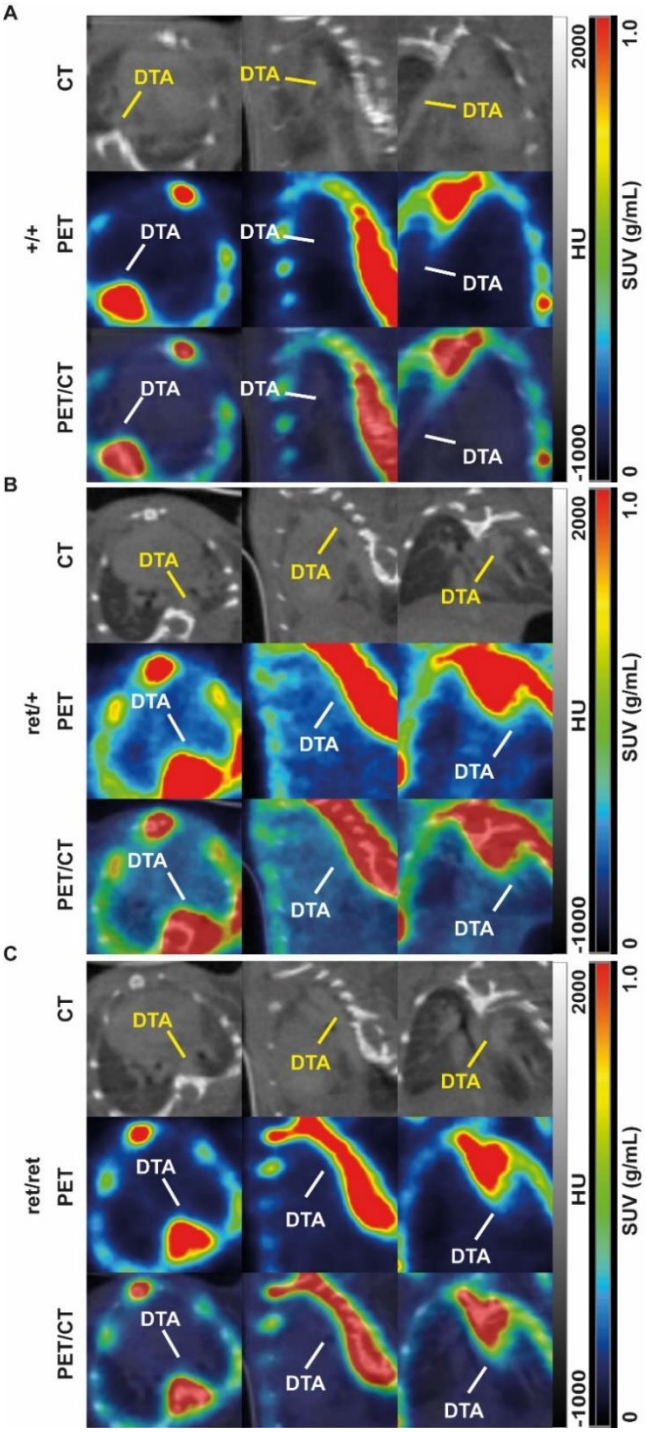

Figure 3.14: No microcalcification was observed in the descending thoracic aorta of *pdgfb*$^{+/+}$, *pdgfb*$^{ret/+}$ and *pdgfb*$^{ret/ret}$ mice.

Example of a contrast CT (top), PET (middle) and PET/CT (bottom) images combined in axial (left), sagittal (middle) and coronal (right) views. PET and PET/CT images show the average ^{18}F-NaF signal taken over the last 30 mins of the scan centred rib cage and thoracic cavity. Within the thoracic cavity the descending thoracic aorta (DTA) was identified but radiotracer activity was low in the DTA in *pdgfb*$^{+/+}$ (+/+, **A**), *pdgfb*$^{ret/+}$ (ret/+, **B**) and *pdgfb*$^{ret/ret}$ mice (ret/ret, **C**). HU- Hounsfield units SUV- standard uptake values.

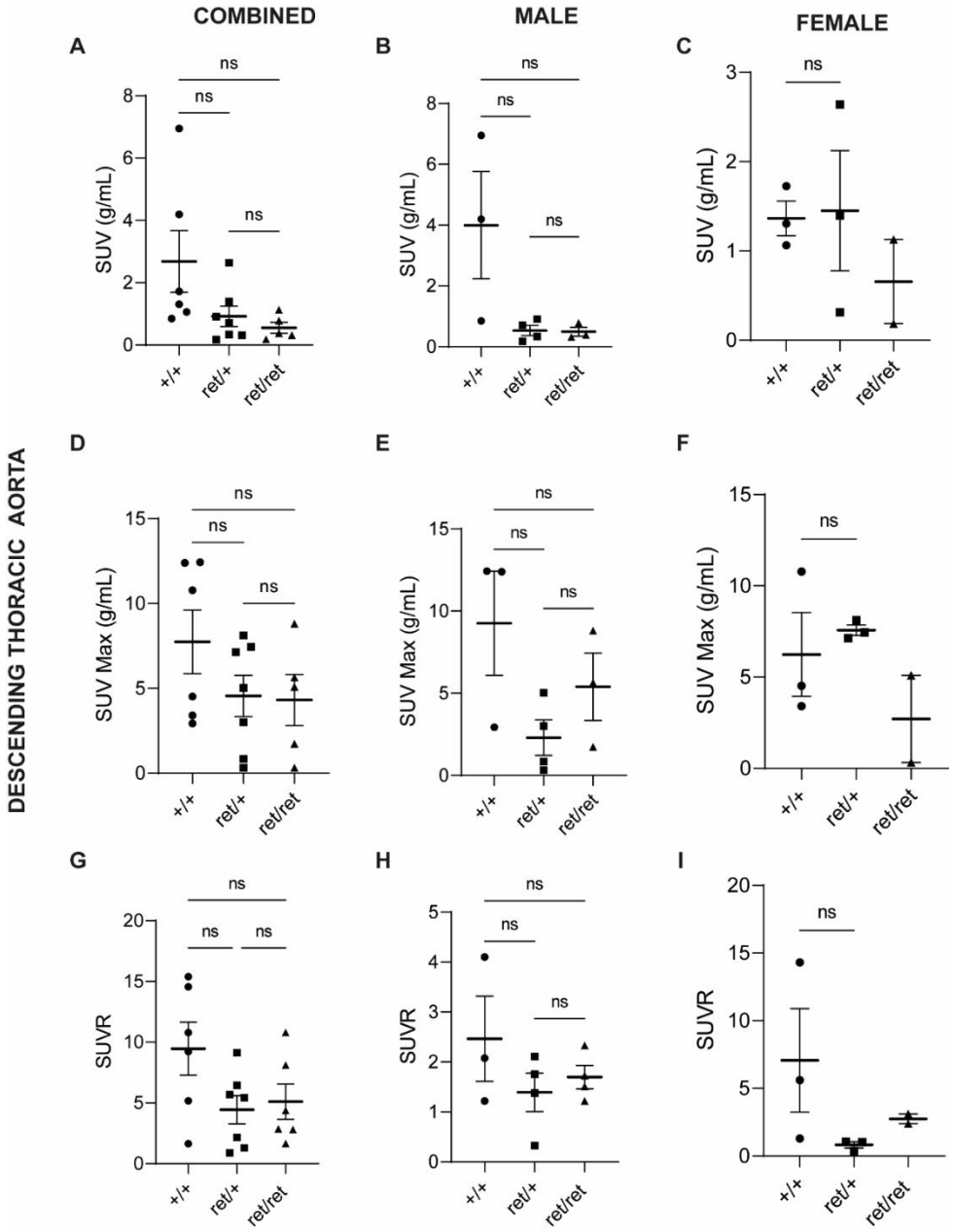

Figure 3.15: No difference in ^{18}F-NaF signal intensity or uptake in the descending thoracic aorta of *pdgfb*$^{+/+}$, *pdgfb*$^{ret/+}$ and *pdgfb*$^{ret/ret}$ mice was found.

Quantification of average SUV, (**A**, **B**, **C**), SUVmax (**D**, **E**, **F**), and SUVR (**G**, **H**, **I**) values in the descending thoracic aorta in combined and males and female groups, *pdgfb*$^{+/+}$ (+/+), *pdgfb*$^{ret/+}$ (ret/+) and *pdgfb*$^{ret/ret}$ (ret/ret) mice. Data shown as mean±SEM. One-Way ANOVA with Tukey's post-hoc test, Kruskal-Wallis test or unpaired t-test. ns= not significant. Images were analysed using PMOD 4.2 software.

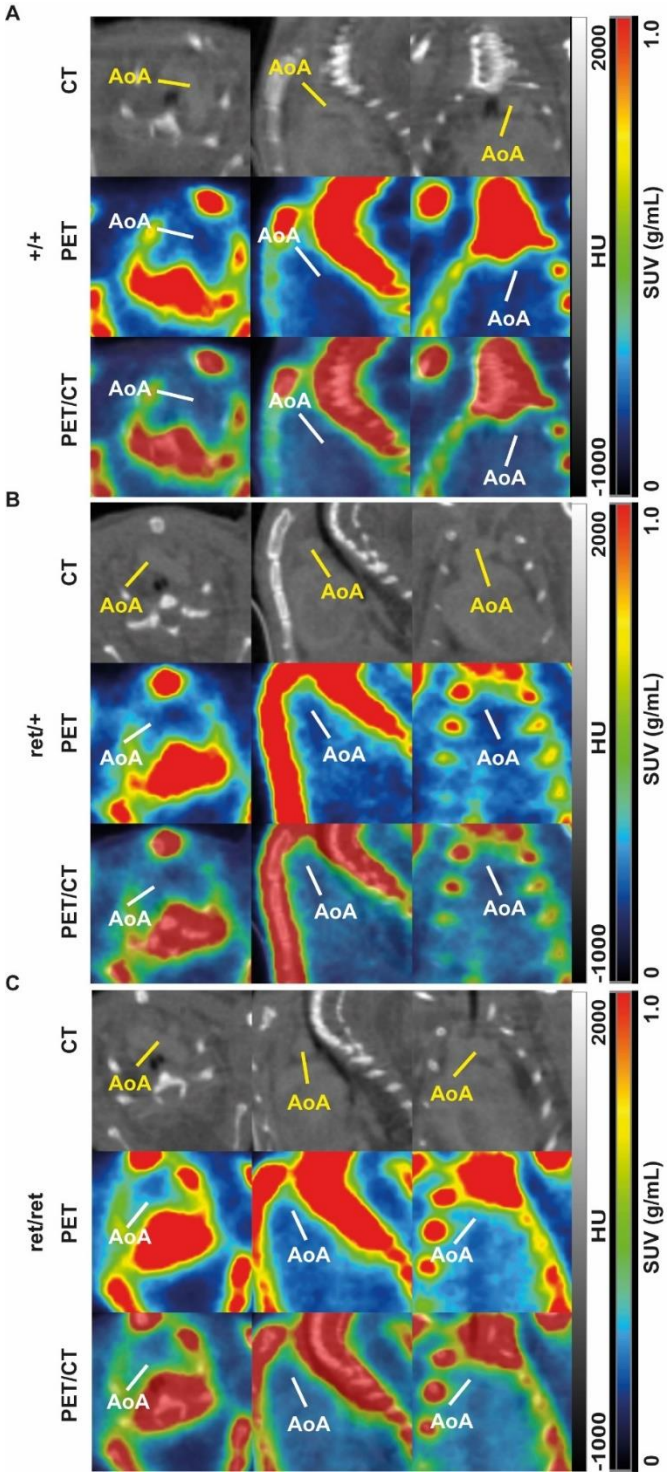

Figure 3.16: No microcalcification was observed in the aortic arch (AoA) of *pdgfb*$^{+/+}$, *pdgfb*$^{ret/+}$ and *pdgfb*$^{ret/ret}$ mice.

Example of a contrast CT (top), PET (middle) and PET/CT (bottom) images combined in axial (left), sagittal (middle) and coronal (right) views. PET and PET/CT images show the average ^{18}F-NaF signal taken over the last 30 mins of the scan centred rib cage and thoracic cavity. Within the thoracic cavity the aortic arch (AoA) was identified. Radiotracer activity was low in the DTA in *pdgfb*$^{+/+}$ (+/+, **A**), *pdgfb*$^{ret/+}$ (ret/+, **B**) and *pdgfb*$^{ret/ret}$ mice (ret/ret, **C**). HU- Hounsfield units SUV- standard uptake values.

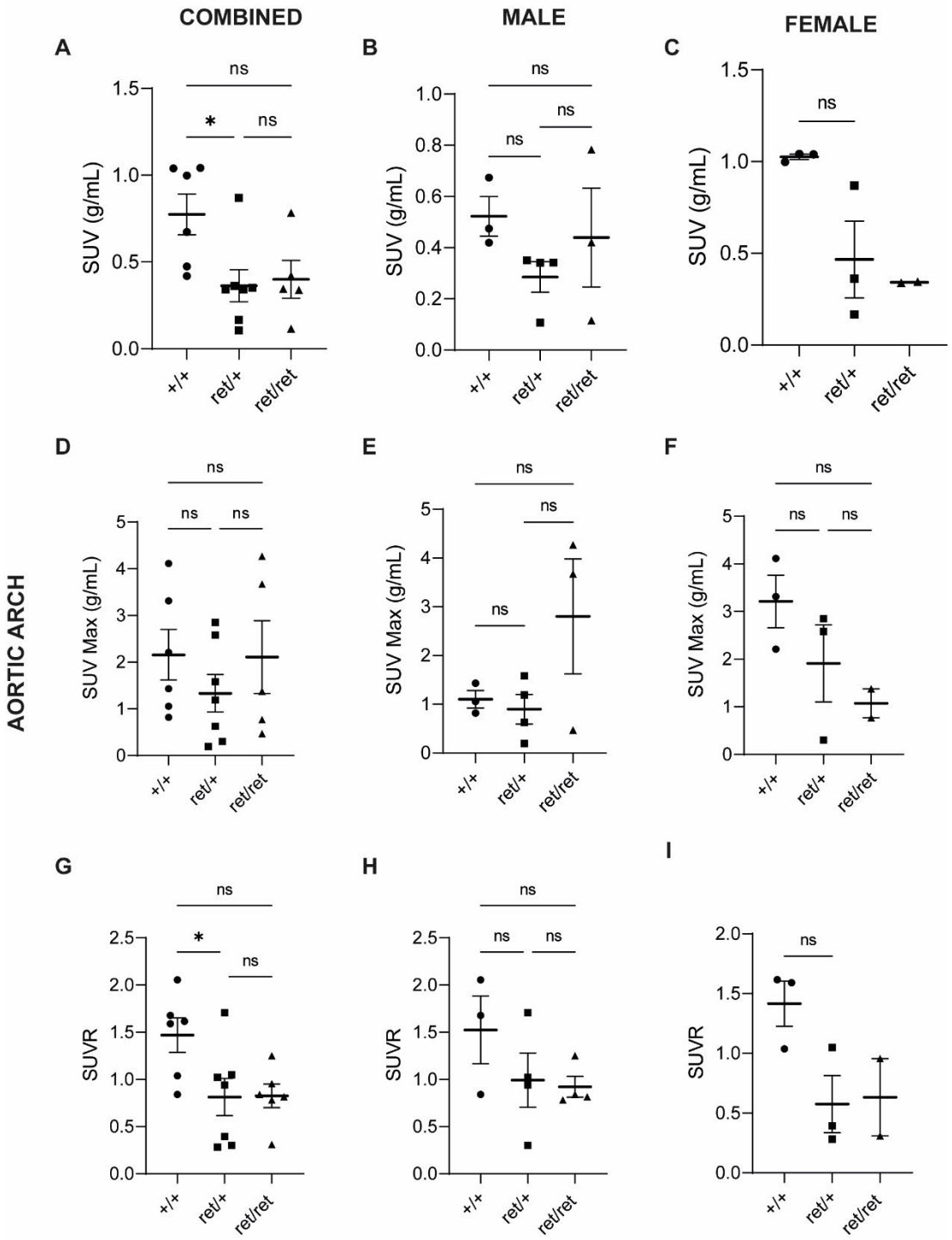

Figure 3. 17: ^{18}F-NaF signal intensity and uptake was greater in the aortic arch of *pdgfb*$^{+/+}$ mice.

Quantification of average SUV, (**A**, **B**, **C**) SUVmax (**D**, **E**, **F**) and SUVR (**G**, **H**, **I**) values in the descending thoracic aorta in combined groups, males and female *pdgfb*$^{+/+}$ (+/+), *pdgfb*$^{ret/+}$ (ret/+) and *pdgfb*$^{ret/ret}$ (ret/ret) mice. Data shown as mean±SEM. One-Way ANOVA with Tukey's post-hoc test, Kruskal-Wallis test or unpaired t-test. ns= not significant. Images were analysed using PMOD 4.2 software.

No macroscopic calcification was identified in the kidneys of *pdgfb*$^{ret/ret}$ mice.

The final tissues I examined were the kidneys in pdgfb$^{+/+}$, pdgfb$^{ret/+}$ and pdgfb$^{ret/ret}$ mice. One previous study reported that *pdgfb*$^{ret/ret}$ mice develop glomerulosclerosis and kidney dysfunction by 3 months of age (Lindblom *et al.*, 2003). However, whether this leads to calcification at a later timepoint is unknown. Non-contrast CT scans of kidneys allowed identification of the kidneys but did not reveal any evidence of macrovascular calcification as shown by low CT signal in *pdgfb*$^{+/+}$ (Figure 3.18A), *pdgfb*$^{ret/+}$ (Figure 3.18B) and *pdgfb*$^{ret/ret}$ (Figure 3.18C) mice. To confirm this, I quantified the CT signal in both the left and right kidneys. Quantification of average CT signal in the left kidney did not reveal any significant differences in combined groups of males and female mice and CT values fell within the normal range (-100 to 120 HU) for soft tissue (Figure 3.19A, $p>0.05$). In the male and female cohorts no significant differences or obvious trends in the average CT values were observed between genotypes (Figure 3.19B, C $p>0.05$). The average CT signal in the right kidney was unchanged between *pdgfb*$^{+/+}$, *pdgfb*$^{ret/+}$ and *pdgfb*$^{ret/ret}$ mice in the combined sex cohort and although the average CT signal was higher in *pdgfb*$^{ret/ret}$ mice vs *pdgfb*$^{+/+}$ or *pdgfb*$^{ret/+}$ littermates. However, this remains within the range of values for normal tissue (Figure 3.19A, $p>0.05$). This trend was observed in both male and female cohorts but no significant differences in the average CT signal between groups were found (Figure 3.19B, C $p>0.05$). The hot average CT value quantification further confirmed these observations. They followed a similar trend, but no significant difference in either value in the left (Figure 3.19 D, E, F) or right kidney (Figure 3.19 G, H, I) for combined, male or female cohorts was found ($p>0.05$). In summary, no macroscopic calcification could be observed in the kidneys of *pdgfb*^{ret} mutant mice as confirmed by quantification of CT images. Moreover, the ^{18}F-NaF radiotracer is excreted via the kidneys, and thus, the PET signal in this region could not be quantified. Taken together, data from PET/CT imaging suggests that macroscopic calcification is only present in the brains of *pdgfb*$^{ret/ret}$ mice.

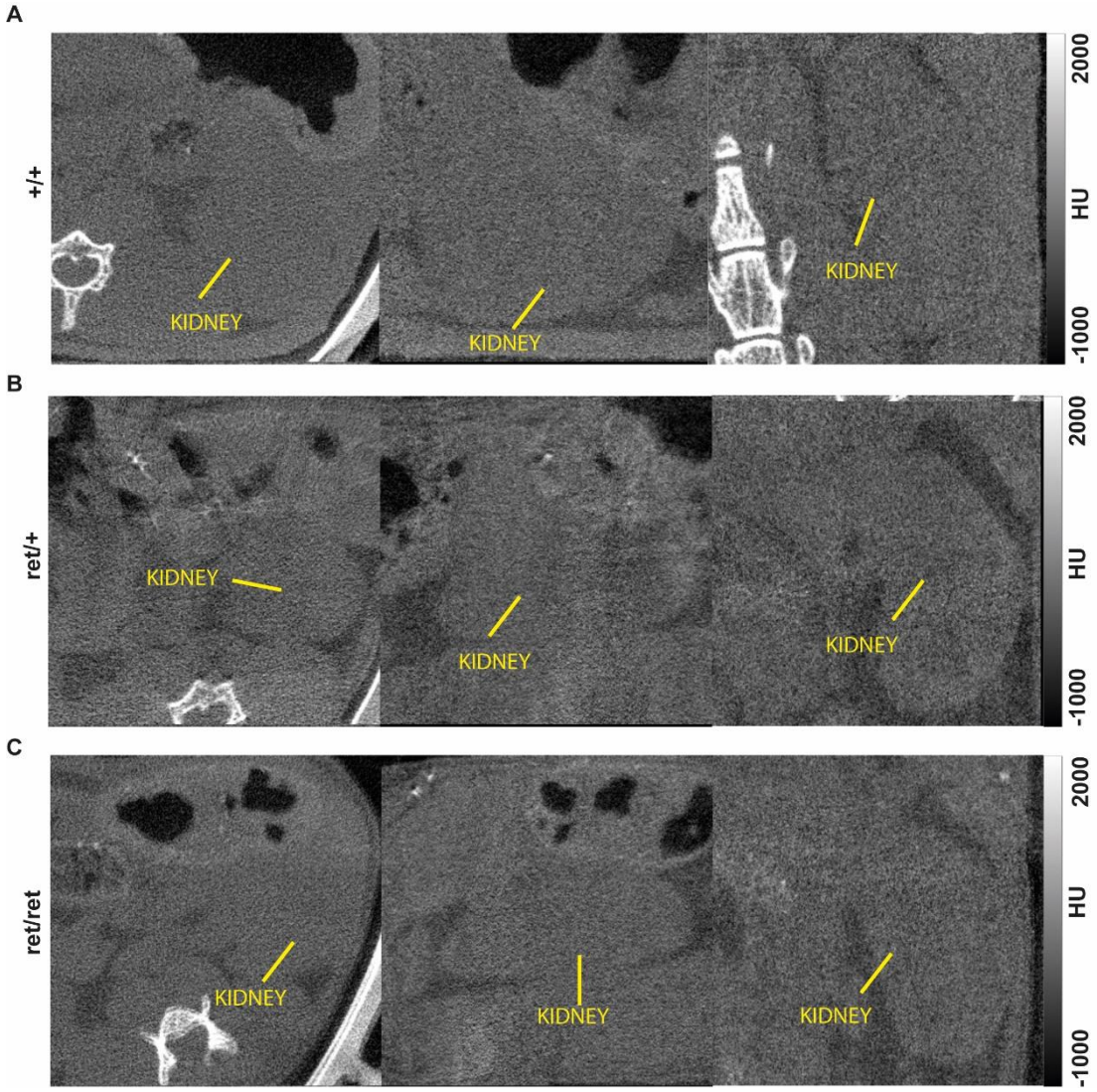

Figure 3.18: No renal macroscopic calcification was detected in *pdgfb*$^{+/+}$, *pdgfb*$^{ret/+}$ and *pdgfb*$^{ret/ret}$ mice.

Representative example of non-contrast CT images of the kidneys of *pdgfb*$^{+/+}$ (+/+, **A**) and *pdgfb*$^{ret/+}$ (ret/+, **B**) and *pdgfb*$^{ret/ret}$ (ret/ret, **C**) mice did not reveal any evidence of macroscopic calcification. HU-Hounsfield units

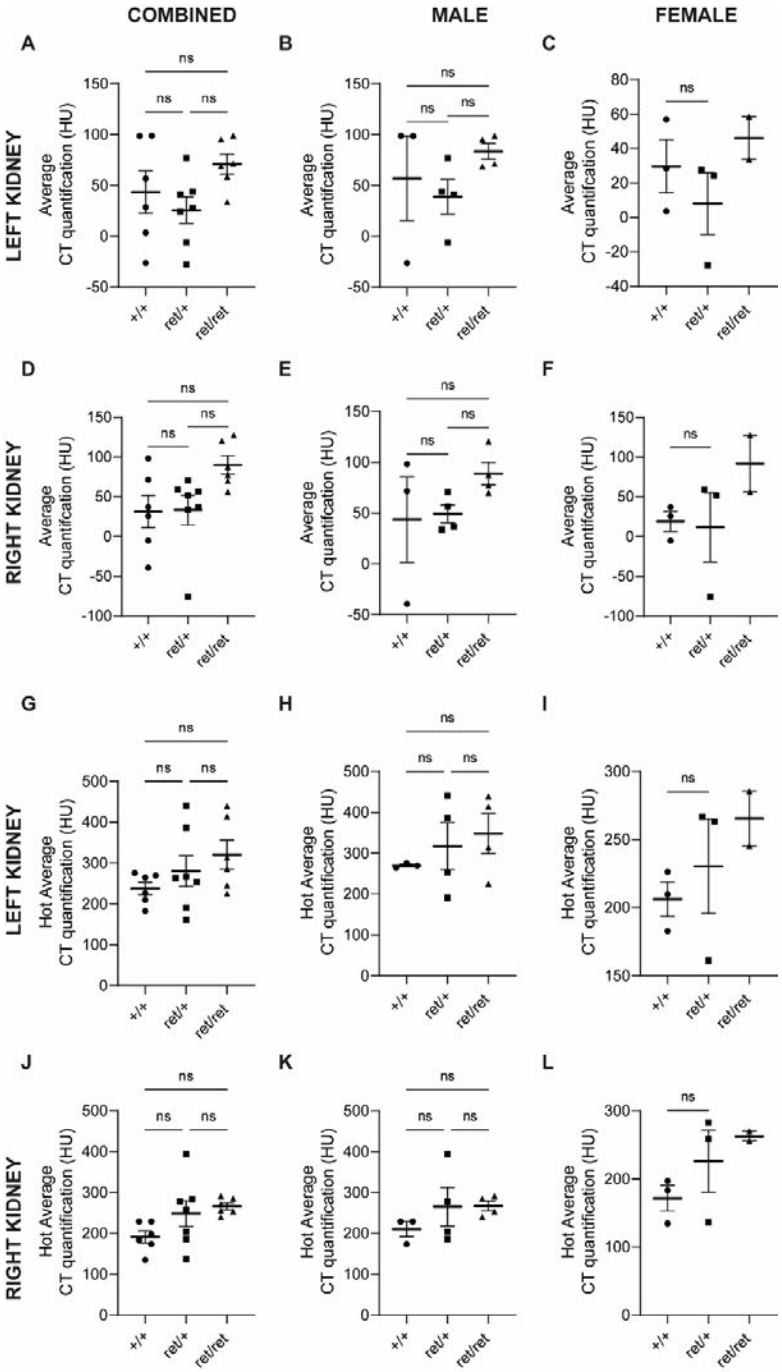

Figure 3. 19: The CT signal quantification confirms the absence of renal macroscopic calcification in *pdgfb*$^{+/+}$, *pdgfb*$^{ret/+}$ and *pdgfb*$^{ret/ret}$ mice.

Quantification of the average CT signal for the left (**A**, **B**, **C**) and right kidney (**D**, **E**, **F**). The hot average CT signal for the left (**G**, **H**, **I**) right and right kidneys (**J**, **K**, **L**). Analysis was performed using PMOD 4.2 software. HU= Hounsfield units Data shown as mean±SEM. One-Way ANOVA with Tukey's post-hoc test, ns= not significant

Discussion

In this chapter I aimed to determine whether *pdgfb*$^{ret/ret}$ mice develop ectopic calcified lesions out with the brain, in the heart, aorta and kidneys. I also wished to assess whether the extent of calcium deposition was sex dependent.

Pdgfb$^{ret/ret}$ regional macroscopic brain calcification shows high interindividual variability.

Pdgfb$^{ret/ret}$ mice develop microvascular associated calcifications over the course of 12 months as shown by MRI scans and histological analysis (Keller *et al.*, 2013). However, whether this causes macro calcification in the brain and whether this is sex-dependent was not explored. More importantly whether this mutation also causes calcifications in other tissues and organs such as the aorta, heart or kidneys had not yet been established. Whole body PET/CT imaging was utilised with the objective to detect micro and macroscopic calcifications in the brain, heart, aorta, and kidney in male and female *pdgfb*$^{ret/ret}$ mice. I observed that brain calcification was absent in *pdgfb*$^{+/+}$ and *pdgfb*$^{ret/+}$ mice. This corroborates previous findings demonstrating this phenotype only occurs in *pdgfb*$^{ret/ret}$ mice not in *pdgfb*$^{+/+}$ and *pdgfb*$^{ret/+}$ littermates (Keller *et al.*, 2013). However, this phenotype is not observed in all PDGFB or PDGFRβ mutant mice. *Pdgfb*$^{+/-}$ or *pdgfrb*$^{+/-}$ heterozygous mice as well as double *pdgfb*$^{+/-}$ *pdgfrb*$^{+/-}$ mutant mice do not develop brain calcification at 12-14 months (Vanlandewijck *et al.*, 2015). Furthermore *pdgfrb*$^{redeye/redeye}$ mice, have a 75% reduction in pdgfrb mRNA but do not develop brain calcification (Vanlandewijck *et al.*, 2015). More recently, tamoxifen-induced endothelial-specific deletion of the *pdgfb* gene in in 2 month old *pdgfb*^{iECKO} mice was shown to cause progressive pericyte loss in the brain from 4 to 18 months of age followed by an increase in the permeability of the blood brain barrier (Vazquez-Liebanas *et al.*, 2022). However, unlike in *pdgfb*$^{ret/ret}$ mice, tamoxifen deletion of *pdgfb* in adult mice did not result in the development of brain microcalcification (Vazquez-Liebanas *et al.*, 2022). This may suggest that exposure to PDGFB levels during embryonic development may be a key factor in developing brain calcifications in adults. This is further supported by the fact that *pdgfb* null mutant mice rescued to adulthood by transgenic re-expression of *pdgfb* in the

endothelium, develop calcified brain lesions similar to *pdgfb*$^{ret/ret}$ mice (Keller *et al.*, 2013).

An unexpected observation I made was that the anatomical location of the brain calcification in *pdgfb*$^{ret/ret}$ was highly variable. The most common calcified phenotype I observed in *pdgfb*$^{ret/ret}$ mice, which were all male, was present in both left and right thalamic regions and in the pons region (3/6 mice). The second most common phenotypic profile was of a small region of pons calcification exhibited by one male mouse and one female mouse (2/6 mice). The second *pdgfb*$^{ret/ret}$ female in my cohort did not exhibit any macroscopic calcification in any region of the brain. These differences in regional calcification within *pdgfb*$^{ret/ret}$ mice has not been previously observed. It had been previously reported that *pdgfb*$^{ret/ret}$ mice develop microvessel associated calcifications in areas corresponding to the basal forebrain, pons, medulla and both left and right thalamus starting at 4 months (Keller *et al.*, 2013). A later study also showed variation in calcification load in *pdgfb*$^{ret/ret}$ mice, however no differences in terms of anatomical location was described (Zarb *et al.*, 2019). To the best of my knowledge, we are the first to describe the presence of pons calcification without any thalamic calcification in *pdgfb*$^{ret/ret}$ mice. The pons was the common site of calcification and observed in most *pdgfb*$^{ret/ret}$ mice (5/6) in my cohort. The fact that thalamic calcification is absent in two mice suggests that pons calcification precludes thalamic calcification or could be due to interindividual variation. Pontine calcifications, absent of thalamic calcification, is rare occurrence in humans however case reports in humans have been published (Stamelou *et al.*, 2013). Pontine calcification may occur after severe brain trauma and is also associated with the presence of brain tumours and arteriovenous malformations (Saito *et al.*, 2005; Kumar *et al.*, 2011). Indeed, single cells analysis of cerebral BBB endothelial cells from *pdgfb*$^{ret/ret}$ mice absent pericyte contact has shown up-regulation of genes associated with venous endothelial cells have altered expression of growth factors and regulatory proteins (Mäe *et al.*, 2021). Furthermore, endothelial cells present in leakage points in the BBB of *pdgfb*$^{ret/ret}$ mice were also observed to display an arteriolar shifted identity (Mäe *et al.*, 2021). As such it may be that shift in endothelial cell phenotype acquiring more arterio-venous characteristics may be a contributary factor in the onset of pontine calcification. Bi-thalamic calcification is a hallmark of IBGC in humans and occurs in individuals with mutations in PDGFB, PDGFRB and

SLC20A2A. Thalamic calcification may also occur naturally in aging but also in individuals suffering from lead or carbon monoxide poisoning, radiation, viral infection and also trauma (Renard *et al.*, 2014). Differences in thalamic calcification and pons calcification or why one area may be more greatly affected than other has not fully been explored. Calcifications in both areas are vessel associated beginning in the blood vessel wall and then expanding to encompass and affect surrounding tissue. However, why one area would be affected to a greater extent than the other is not known. However, one possible reason may be differences in blood vessel density in each brain region. Indeed, mapping of microvessels in the human brain has shown that the area containing the thalamus has a greater vessel density and differential vessel orientation than in the pons (Kubíková *et al.*, 2018). This could suggest that areas with greater vessel density are more likely to calcify. Different molecular pathways could also drive pons or thalamic calcification. For example, a large multicentre trial in individuals with PFBC absent of mutations in PDGFRB, PDGFB and SLC20A2A showed that mutations in the MYORG gene was associated with central pontine calcification which is not typically present in other genetic PFBC cases (Zeng *et al.*, 2021) . However, whether the *pdgfb*$^{ret/ret}$ mice have altered MYORG signalling is unknown.

Regional differences in calcification may also be accounted for by the fact that tissue distribution of the PDGFBret protein is non-uniform with an altered chemotactic gradient which may vary from individual to individual. As previously stated, microcalcification of the brain may be a consequence of PDGFB deficiency during embryonic brain development, however, the exact mechanism driving brain calcification in adult *pdgfb*$^{ret/ret}$ mice is not fully understood. Initially it was thought that brain areas lacking pericytes may be more susceptible to calcification, however, histological analysis showed that susceptible calcified areas showed a high level of CD13+ pericyte coverage compared with less susceptible brain regions (Vanlandewijck *et al.*, 2015). Further analysis of calcified lesions, identified the presence of osteoblast-like and osteoclast-like cells both around and inside of calcified regions in the brain of *pdgfb*$^{ret/ret}$ mice (Zarb *et al.*, 2019). Whether the precursors of these cells in *pdgfb*$^{ret/ret}$ mice are pericytes is unknown but both pericytes and endothelial cells have been shown to differentiate into mesenchymal calcifying cells and may be viable precursor candidates.

The role of sex on *pdgfb*$^{ret/ret}$ brain calcification could not be determined.

I wished to understand whether the extent of calcification in *pdgfb*$^{ret/ret}$ mice is sex-dependent, however, due to small number of female *pdgfb*$^{ret/ret}$ mice this could not be determined. All *pdgfb*$^{ret/ret}$ males in my study exhibited some brain calcification. Three of four males scanned showed bi-thalamic and regional pons calcification and one male was lacking thalamic calcification and exhibited only a small region of calcification surrounding the pons. Out of the 2 *pdgfb*$^{ret/ret}$ females scanned, only one showed evidence of macrocalcification in the pons region. In my cohort, preliminary observations suggest that on average, male *pdgfb*$^{ret/ret}$ mice appeared to show a greater extent of calcification than females. This would reflect what has been previously seen in IBGC in humans (Nicolas *et al.*, 2015). Studies assessing the phenotype of *pdgfb*$^{ret/ret}$ mice have not specifically looked at whether this phenotype is sex dependent and typically do not differentiate between male and female mice. A recent paper released by Keller and collaborators using MRI imaging showed interindividual variation in the extent of thalamic calcification in 6 individual *pdgfb*$^{ret/ret}$ mice of mixed genders, aged 8-12 months (Zarb *et al.*, 2019). However, unlike my present study, all mice (6/6) examined, exhibited bilateral thalamic calcification. They did not observe differences in the area of brain calcification between male and female *pdgfb*$^{ret/ret}$ mice although the number of *pdgfb*$^{ret/ret}$ mice scanned was relatively small (3 males/3 females) and as such may not be enough to provide conclusive evidence. In summary, no definitive conclusions could be drawn regarding the role of sex on macroscopic brain calcification in *pdgfb*$^{ret/ret}$ mice. In future investigations, a greater number of both male and female *pdgfb*$^{ret/ret}$ mice should be scanned to determine whether the anatomical location of brain calcification is related to sex. Histological analysis of brain sections using calcification markers should also be performed to confirm these findings in future studies. Investigation of the number of pericytes, osteoclast-like and osteoblast-like cells found surrounding and within calcified lesions could also be performed to determine whether sex influences this. Indeed, oestrogen has been shown to modulate inflammation in the brain (Vegeto, Benedusi and Maggi, 2008) and as such, may be protective or reduce the extent of calcification in female *pdgfb*$^{ret/ret}$ mice.

Microscopic calcification was not detected in the brains of *pdgfb*$^{ret/ret}$ mice.

Use of the radioactive ^{18}F-NaF isotope which binds more effectively to active microvascular calcification can distinguish between microcalcification and macrocalcification when used in conjunction with CT scans, did not show significant differences in the average signal in the whole brain, left thalamus, right thalamus, and pons areas between *pdgfb*$^{+/+}$ and *pdgfb*$^{ret/ret}$ brains. Interestingly, *pdgfb*$^{ret/+}$ mice exhibited greater ^{18}F-NaF activity in the left thalamus. This may indicate the presence of microvascular calcification in this region which could develop into macrovascular calcified nodules like those observed in *pdgfb*$^{ret/ret}$ mice. In addition, SUVR was greater in male *pdgfb*$^{ret/+}$ mice than male *pdgfb*$^{ret/ret}$ mice suggesting a higher ^{18}F-NaF activity. One hypothesis may be that having one copy of the *pdgfb*^{ret} allele may cause brain calcification to develop at a slower rate than in *pdgfb*$^{ret/ret}$ mice. It could also occur since exposure to the PDGFBret protein during development even at a reduced dosage may cause calcification at a later time point. This hypothesis could be tested by performing scans in *pdgfb*$^{ret/+}$ mice at 18 and 24 months of age to further assess the extent of brain calcification with aging.

No evidence of ectopic macrovascular calcification was detected in the hearts in *pdgfb*$^{ret/ret}$ mice.

One of my primary aims was to investigate whether calcification was limited to the brain or also present in the heart, aorta, and kidneys in *pdgfb*$^{ret/ret}$ mice to give greater insight into the role of PDGFB/PDGFRβ signalling in the development of vascular calcification *in vivo.* In addition to exploring the heart, I was also able to visualise and accurately localise the PET signal to the aortic arch and to the descending thoracic aorta by overlaying this with contrast CT images. In the heart, macrovascular calcification was not detected in *pdgfb*$^{ret/ret}$ mice by examination of non-contrast CT scans and by quantification of the CT signal. By overlaying the PET and CT images, I measured ^{18}F-NaF activity in the heart in combined and individual male and female groups. Although SUV and SUVmax values remained unchanged, I did observe that *pdgfb*$^{+/+}$ mice had a greater amount of ^{18}F-NaF activity as shown by an increase SUVR when compared to *pdgfb*$^{ret/+}$ and *pdgfb*$^{ret/ret}$ mice. This may indicate that *pdgfb*$^{+/+}$ mice

are beginning to develop early microscopic calcifications due to aging, however, the location of microcalcification in the heart could not be identified as ^{18}F-NaF signal was low on each of the PET scans. This data suggests that *pdgfb*$^{ret/+}$ and *pdgfb*$^{ret/ret}$ mice do not develop heart calcifications at least by 12 months. Histological analysis should be performed in future studies to determine the anatomical location of microvascular calcification within the heart. Analysis of PET/CT scans do not present evidence of micro or macroscopic calcification in the hearts of *pdgfb*$^{ret/+}$ and *pdgfb*$^{ret/ret}$ mice.

High ^{18}F-NaF activity was observed in the aortic arch of *pdgfb*$^{+/+}$ mice but was reduced in *pdgfb*^{ret} mice.

Vascular calcification of coronary arteries is highly prevalent in patients with heart disease and is associated with major events such as MI. It is also highly prevalent in the elderly and occurs as part of the normal aging. Microcalcifications are associated with unstable plaques and may rupture whereas macroscopic vascular calcification is associated with healing and end-stage processes. In both male and female *pdgfb*$^{ret/ret}$ mice, no evidence of macroscopic calcification was observed in the aortic arch or in the descending thoracic aorta. This was also the case for *pdgfb*$^{ret/+}$ and *pdgfb*$^{+/+}$ littermates. Similar results were found via microCT imaging of the thoracic cavity of *pdgfb*$^{ret/ret}$ mice by Keller and collaborators who also observed the absence of any macroscopic calcified lesions in major blood vessels (Zarb *et al.*, 2019). Furthermore, they also measured the calcification propensity of *pdgfb*$^{ret/ret}$ mouse serum which was found to be the same as age matched control animals (*pdgfb*$^{+/+}$ and *pdgfb*$^{ret/+}$ mice). This was done using a nanoparticle-based assay that can detect the formation of transformation of spherical calcipotriene particles into a crystalline conformation (Pasch *et al.*, 2012). However, I did observe a significantly higher average ^{18}F-NaF signal in the aortic arch of *pdgfb*$^{+/+}$ mice compared with *pdgfb*$^{ret/+}$ littermates which was also greater than *pdgfb*$^{ret/ret}$ mice although not significant. This suggests active calcifying process in these mice possibly due to aging. This trend was also observed when mice were divided based on their gender, although no significant differences were found between the 2 groups. However, I did not measure the calcification propensity of the serum of mice in my cohort. Due to the presence of high ^{18}F-NaF activity in *pdgfb*$^{+/+}$ and not *pdgfb*$^{ret/+}$ mice, it may be that the exposure to the PDGFBret

protein in embryonic vessel development does not exacerbate calcification of the arteries in later adult life. However, measurement of serum PDGFB levels in *pdgfb*^{ret} mutant mice should be performed to confirm this. This may be due to the fact that increased secretion of PDGFB into the circulation in aging mice and has been shown to drive reduction of bone mass and arterial stiffening (Santhanam *et al.*, 2021). Another possibility is that perhaps *pdgfb*$^{ret/ret}$ mutant mice may be protected from microvascular calcification due to their altered blood vessel structure. *Pdgfb*$^{ret/ret}$ mice have altered aortic structure having less VSMC layers, a bigger vessel diameter as well disorganised pulmonary vascular muscularisation (Nystrom *et al.*, 2006; Tannenberg *et al.*, 2018). These changes were shown to be protective in hypoxic-induced pulmonary remodelling as *pdgfb*$^{ret/ret}$ mice did not develop pulmonary hypertension (Tannenberg *et al.*, 2018). This further suggest that *pdgfb*$^{ret/+}$ or *pdgfb*$^{ret/ret}$ mice may be protected against coronary vessel calcification. A recent study used transgenic *Ldlr*$^{-/-}$ *pdgfb*$^{ret/ret}$ fed on a high fat diet to promote atherosclerotic plaque development (Tillie *et al.*, 2021). The authors found that, compared with control mice, *Ldlr*$^{-/-}$ *pdgfb*$^{ret/ret}$ mice had more stable plaques and were protected from plaque rupture, intraplaque haemorrhage as well as microvessel loss, although the plaque size did increase (Tillie *et al.*, 2021). This was due to variety of protective vascular and metabolic effects. Perhaps *pdgfb*$^{ret/ret}$ mice may be protected from microvascular calcification of blood vessels in a similar way.

Pdgfb$^{ret/ret}$ mice do not develop kidney calcification.

The final organ in which I wished to examine for the presence of macroscopic calcification was the kidneys. Previous studies investigating the kidneys of *pdgfb*$^{ret/ret}$ mice showed inhibited mesangial cell recruitment and delayed embryonic glomerular development which was corrected 1 month after birth (Lindblom *et al.*, 2003). However, by 6 months of age, glomerulosclerosis and excessive matrix deposition was present in these *pdgfb*$^{ret/ret}$ mice with increased albuminuria (Lindblom *et al.*, 2003). No macroscopic calcification was detected using CT scans in the left or right kidneys of *pdgfb*$^{+/+}$, *pdgfb*$^{ret/+}$ and *pdgfb*$^{ret/ret}$ mice in my study. Since the ^{18}F-NaF radiotracer is excreted through the kidneys, the presence of microvascular calcification could not be determined. These scans suggest that calcification in *pdgfb*$^{ret/ret}$ mice is

restricted to the brain; however, further studies should be performed in a greater number of mice for confirmation.

Future Work

Contrary to my hypothesis, *pdgfb*$^{ret/ret}$ mice did not develop ectopic calcifications in their aorta, heart, and kidney at 12 months of age. I also found variability in the region of the brain calcifications in which brain calcifications were found. I was also unable to determine sex-specific differences in calcification in *pdgfb*$^{ret/ret}$ mice.

To further confirm and reinforce my findings a greater number of mice should be scanned using whole body PET/CT imaging. This would allow the extent of interindividual variation within the *pdgfb*$^{ret/ret}$ cohort in terms of brain calcification to be further understood. Histological analysis using calcification markers; alcian blue, alizarin red and von kossa which mark different stages in the calcification process could also be employed to track calcification progression in different brain regions. These markers could also be utilised in the aortic arch and hearts mice to localise the site of calcification and ^{18}F-NaF signal. Autoradiography is a technique where histological sections of tissues are treated with a radioactive isotope which binds to localised targets sites, in this case ^{18}F-NaF which will bind to calcium in hydroxyapatite deposition (Griem-Krey *et al.*, 2019). Using this technique, areas of calcification within tissues such as the aorta and heart may be identified. However, this requires that several fully sectioned aortas and hearts are stained and analysed to detect the areas possibly affected. The uncontrolled expression of PDGFB in mutant mice may also account for variation in regional brain calcification in my cohort of *pdgfb*$^{ret/ret}$ mice. In the future, specific antibodies, or other small molecules such macrocyclic peptides, tagged with a fluorescent reporter, which can bind to the soluble PDGFBret protein could be developed to allow distribution of this ligand in the pericellular and extracellular space to be visualised on histological brain sections. PDGFBret protein expression could also be tested by dissection and isolating specific brain areas such as the thalamus and pons. QPCR or western blots could then be performed for PDGFB. This may indicate whether interindividual variation is due the PDGFBret protein being more highly expressed in certain areas of the brain in some *pdgfb*$^{ret/ret}$ mice. This may partially account for the heterogeneity observed in my cohort.

The role of sex in *pdgfb*$^{ret/ret}$ mice on calcification could also be further studied by increasing the number of female mice. My preliminary observations from CT scans of 2 female *pdgfb*$^{ret/ret}$ mice indicate very low levels of calcification. Oestrogen is vascular protective and may also modulate inflammation in the brain (Vegeto, Benedusi and Maggi, 2008). It may be interesting to use immunofluorescent staining for oestrogen receptors in the brain of male and female *pdgfb*$^{ret/ret}$ mice as this may reveal whether oestrogen receptor expression is protective against brain calcification.

Why calcification only occurs in the brain of *pdgfb*$^{ret/ret}$ mice is unclear. One suggestion may be that 12 months may not enough time for calcified lesions to develop in other tissues in *pdgfb*$^{ret/ret}$ mice. Longer term follow-up of these mice, beyond 12 months, may show increased calcification. This would be particularly important as vascular calcification is most common in elderly patients and aging mice may more accurately reflect the human condition. Another suggestion to account for lack of ectopic calcification out with the brain may be due to tissue specificity in the effects of *pdgfb*^{ret} mutation. This may affect pericyte coverage of blood vessels in some organs more than others during development. Therefore, studies during embryonic development using in *pdgfb*$^{ret/ret}$ mice might give information regarding the extent and degree to which the vascular development of other organs are affected. This could be done on sections from various tissues by quantifying pericyte coverage of various vessel types using pericyte markers via immunohistochemistry.

Conclusion

In summary, results from this chapter show that *pdgfb*$^{ret/ret}$ mice develop variable levels of macrocalcification in their brains but not the heart, kidney, and aorta. This study provides essential information for scientific community working in the field of the brain by confirming that *pdgfb*$^{ret/ret}$ mutant mice can be exclusively used to study brain calcification.

Chapter 4:
The effect of the *Pdgfb*^{ret} mutation on Cardiac Structure and Function in Aging

Introduction

In this chapter I aimed to explore the effects of the *pdgfb*^{ret} mutation on cardiac structure and function in aging in male and female mice. As previously discussed PDGFB is essential in cardiac development, angiogenesis and is also involved in cardiovascular disease. However, very little is known about the effects of the *pdgfb*^{ret} mutation in the heart.

The *pdgfb*^{ret} mutation alters the range of action of PDGFB resulting in impaired pericyte recruitment during angiogenesis. This in turn leads to alterations in both microvascular and large vessel structure (Lindblom *et al.*, 2003; Nystrom *et al.*, 2006). Mutations in PDGFB in mice have been described to greatly influence the developing cardiovascular system (Hellström *et al.*, 1999). PDGFB and PDGFRβ germline knockout (KO) mice die perinatally due to severe haemorrhaging with altered vasculature structure (Van den Akker *et al.*, 2008). This is due to lack of pericyte/VSMC coverage of the vasculature resulting in leaky and unstable vessels. Both PDGFB and PDGFRβ KO mice also develop cardiac abnormalities, exhibiting dilation of coronary blood vessels and alterations to cardiac structure. Deletion of PDGFB and PDGFRβ manifests in underdevelopment of the left and right ventricles with sparse and disorganised arrangement of trabecular blood vessels (Van Den Akker *et al.*, 2008). Interestingly, cardiac specific overexpression of PDGFB in transgenic mice is not lethal; however, these mice did develop a hypertrophic heart and had increased collagen deposition around cardiomyocytes and the intramyocardial branches of coronary arteries (Gallini *et al.*, 2016).

Similarly, *pdgfb*^{ret} mice survive into adulthood but it is yet to be established whether they develop any cardiovascular pathology. To date only one study interpreted their results using echocardiographic assessment as the development of eccentric hypertrophy at 10 to 20 weeks of age in male *pdgfb*$^{ret/ret}$ mice. Eccentric hypertrophy is defined as increase in size of the heart cavity and decrease in the thickness of the ventricular walls (Simone, 2004). Whether changes to heart structure and function that were exhibited by *pdgfb*$^{ret/ret}$ mutant mice are truly adaptive and not pathological in

nature is yet to be fully understood. Indeed, in the setting of human disease early changes in cardiac structure can be adaptive but may preclude a reduction in cardiac function and subsequent CVD. Therefore, further experimentation is necessary to fully understand the effects of the *pdgfb*^{ret} mutation on the heart.

Sex is a major factor influencing cardiac structure. In healthy individuals, women have smaller heart size and left ventricular mass than men of the same age and race which translates to a reduced cardiac output and stroke volume(de Simone *et al.*, 1991; Levy *et al.*, 2010). The difference in left ventricular mass begins at puberty as males developed a greater left ventricular mass with increases in both the size of the chamber and wall thickness(De Simone *et al.*, 1995). This indicates a role for sex hormones in the sexual dimorphism observed between males and females at baseline. However, the mechanism underlying these differences are not completely understood. As previously stated, rodent cardiac development closely models that of humans and indeed rodents display sex differences in myocardial structure and function. For example, cardiomyocytes from male rats have been observed to have stronger contractile properties than those of females however these differences are reduced with age. In humans aging evokes an increase in wall thickness and septal diameter in males and females however only males develop an increase in left ventricular diameter (Grandi *et al.*, 1992). Aging also causes a loss of myocardial mass in males but not in females which has been attributed to compensatory hypertrophy (Olivetti *et al.*, 1995). However, diastolic function was shown to decrease in both males and females with age (Grandi *et al.*, 1992).

Sex and age are important factors influencing cardiac structure and function in humans and rodents under normal conditions, but their role in determining the cardiac structure and function of *pdgfb*$^{ret/ret}$ mutant mice is unknown.

Hypothesis

Male and female *pdgfb*^{ret} mutant mice have altered cardiac structure and function in aging.

Aims

1. Assess cardiac structure and function in young male and female *pdgfb*^{ret} mutant mice at 3 months of age.
2. Determine the effect of aging on cardiac structure and function in *pdgfb*^{ret} mutant mice.

Study Design

To address these aims, I utilised high resolution 2D echocardiography to assess cardiac structure and function of *pdgfb*$^{+/+}$, *pdgfb*$^{ret/+}$ and *pdgfb*$^{ret/ret}$ mice (Figure 5.1). In my study, each group was split into males and females to identify any potential sex differences in cardiac development. Ultrasound scans were performed on groups of 3-, 6-, 9- and 12-month-old mice (Table 5.1). However, due to an unforeseen issue some mice had to be culled prior to the end of the study and the same individual mice were not always used at each time point. For details of statistical analysis and complete methodology see Chapter 2: Materials and Methods. Body weight, heart weights and tibia length were also measured at 12 months after culling mice.

Table 4.1: Number of mice used in echocardiography experiments.

Age (months)	Sex	Genotype		
		pdgfb$^{+/+}$	*pdgfb*$^{ret/+}$	*pdgfb*$^{ret/ret}$
3	Male	5	5	4
	Female	6	4	4
	Total	**11**	**9**	**8**
6	Male	5	5	4
	Female	7	6	3
	TOTAL	**12**	**11**	**7**
9	MALE	6	5	4
	FEMALE	6	5	4
	TOTAL	**12**	**10**	**8**
12	Male	4	5	4
	Female	6	5	4
	TOTAL	**10**	**10**	**8**

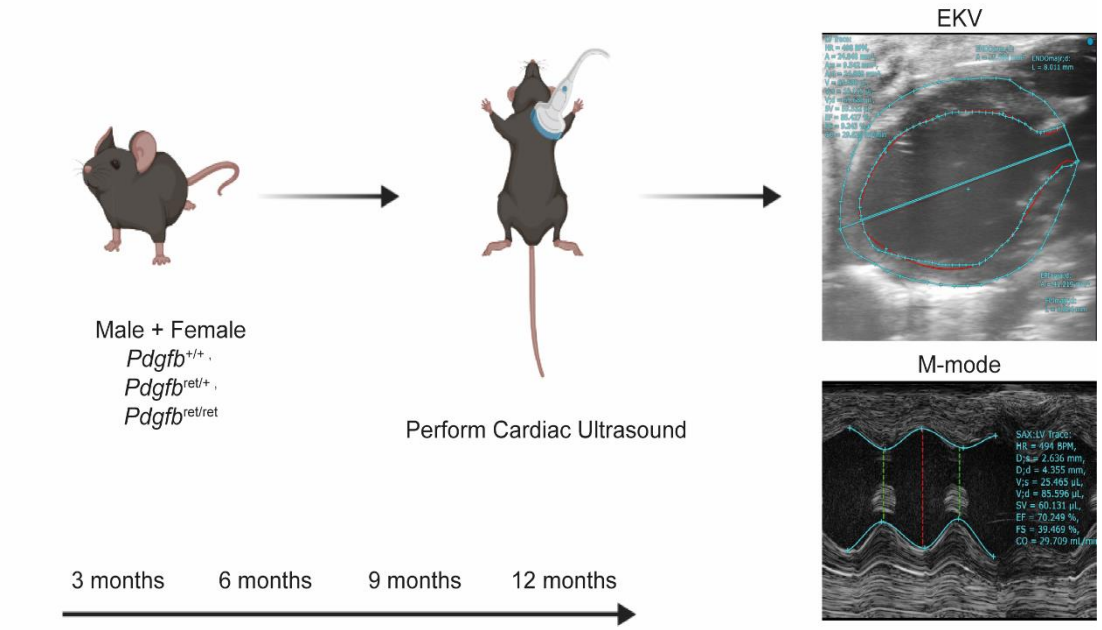

Figure 4. 1: *Pdgfb*^{ret} mutant Echocardiography Study

Mice were separated into males and females, and then into groups depending upon genotype, *pdgfb*$^{+/+}$, *pdgfb*$^{ret/+}$ and *pdgfb*$^{ret/ret}$. Each group of mice underwent cardiac echocardiography at 3, 6, 9 and 12 months of age. ECG-Kilohertz gated volts (EKV) and m-mode 2D images were analysed using VevoLab 3100 software and results collated and quantified. After scans mice were culled then body weight, tibia length and heart weight were measured.

Results

Pdgfb$^{ret/ret}$ mice exhibit left ventricular dilation at 3 months of age.

Upon initial examination of EKV images, *pdgfb*$^{ret/ret}$ mice showed an increase left ventricular endocardial area when compared to both *pdgfb*$^{+/+}$ and *pdgfb*$^{ret/+}$ littermates during end-diastole and to a lesser extent end-systole (Figure 4.2A, B), consistent with dilation.

Left ventricular end diastolic area (LVEDA) was significantly increased in male *pdgfb*$^{ret/ret}$ mice compared to both *pdgfb*$^{+/+}$ and *pdgfb*$^{ret/+}$ mice (Figure 4.3A, *p<0.05, **p<0.01) and was also significantly increased in the female *pdgfb*$^{ret/ret}$ cohort compared to *pdgfb*$^{+/+}$ mice (Figure 4.3A, *p<0.05). This indicates the presence of cardiac dilation in both male and female *pdgfb*$^{ret/ret}$ mice. Interestingly no difference was observed between female *pdgfb*$^{ret/+}$ and *pdgfb*$^{+/+}$ and *pdgfb*$^{ret/ret}$ mice, with some less pronounced left ventricular dilation (Figure 4.3A, p>0.05). This was not observed in male *pdgfb*$^{ret/+}$ mice as their LVEDA was the same as *pdgfb*$^{+/+}$ littermates (Figure 4.3A, p<0.05). The mean LVESA appears slightly increased in both male and female *pdgfb*$^{ret/ret}$ mice compared to both *pdgfb*$^{+/+}$ and *pdgfb*$^{ret/+}$ mice, but there was no significant effect of genotype on left ventricular systolic area (Figure 4.3B, p>0.05). The next parameter examined was left ventricular mass (LV mass), as estimated by ultrasound based on LV areas. At 3 months, LV mass was significantly increased in female *pdgfb*$^{ret/ret}$ mice compared to female *pdgfb*$^{+/+}$ mice (Figure 4.3C, *p<0.05); however, no differences were observed in the male group although the data follows a similar trend as for females (Figure 5.3C, p>0.05). Wall thickness was unchanged between *pdgfb*$^{+/+}$, *pdgfb*$^{ret/+}$ and *pdgfb*$^{ret/ret}$ at 3 months of age in the male or female cohort (Figure 4.3D, p>0.05). These findings show that, at 3 months of age, both male and female *pdgfb*$^{ret/ret}$ mice exhibit left ventricular dilation with females exhibiting further changes to the left ventricular mass, consistent with hypertrophy. To determine whether these changes led to alterations to cardiac function, I next examined functional parameters.

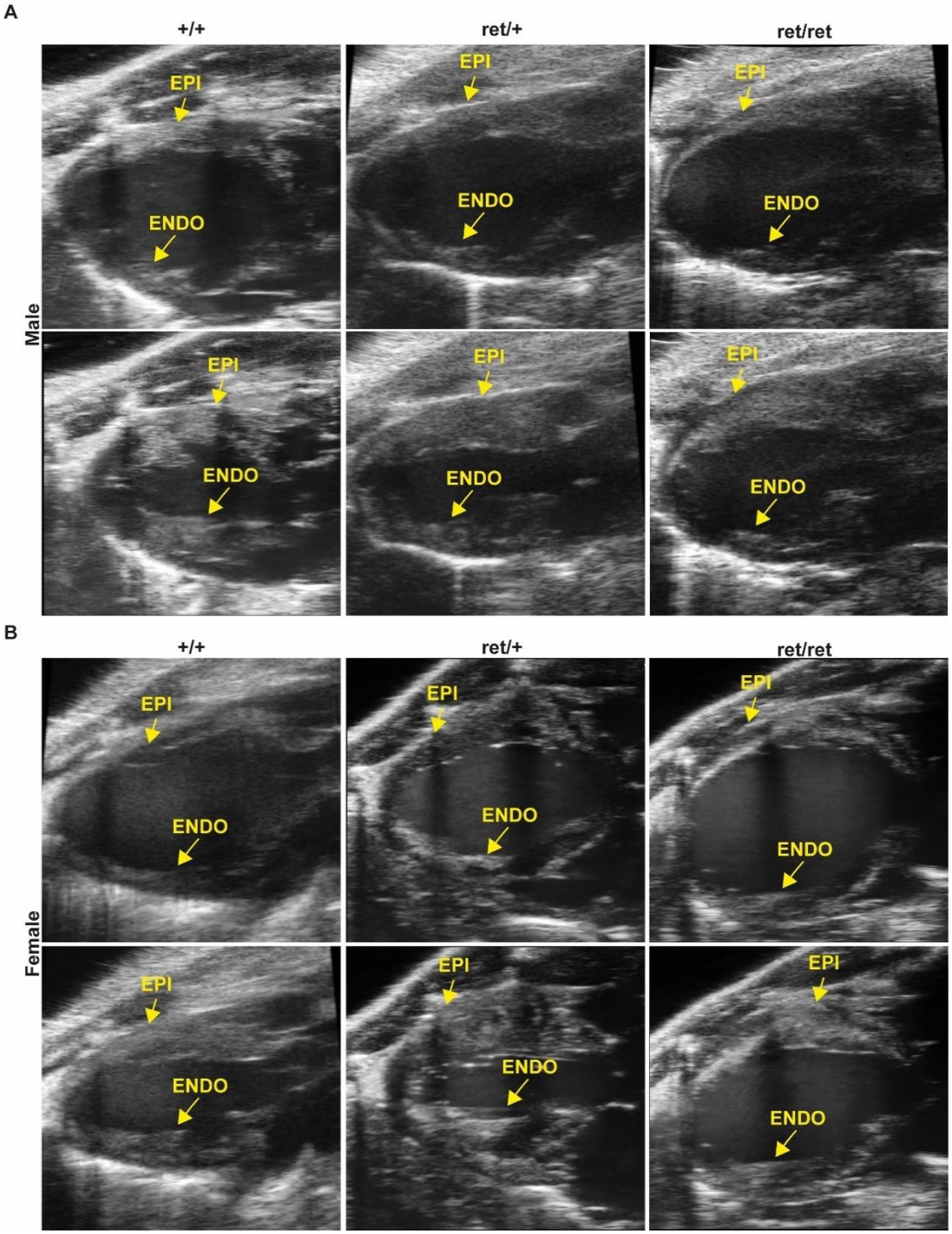

Figure 4.2: PSLAX EKV images showing left ventricular dilation at 3 months of age in male and female *pdgfb*$^{ret/ret}$ mice.

Example of EKV images of the left ventricle during diastole (top panels) and systole (bottom panels) in male (**A**) and female (**B**) *pdgfb*$^{+/+}$ (+/+), *pdgfb*$^{ret/+}$ (ret/+) and *pdgfb*$^{ret/ret}$ (ret/ret) mice. Both the endocardial (ENDO) and epicardial (EPI) boundaries are highlighted (arrows). EKV images show an example of cardiac dilation in male and female *pdgfb*$^{ret/ret}$ mice that is most pronounced during diastole but also present in systole.

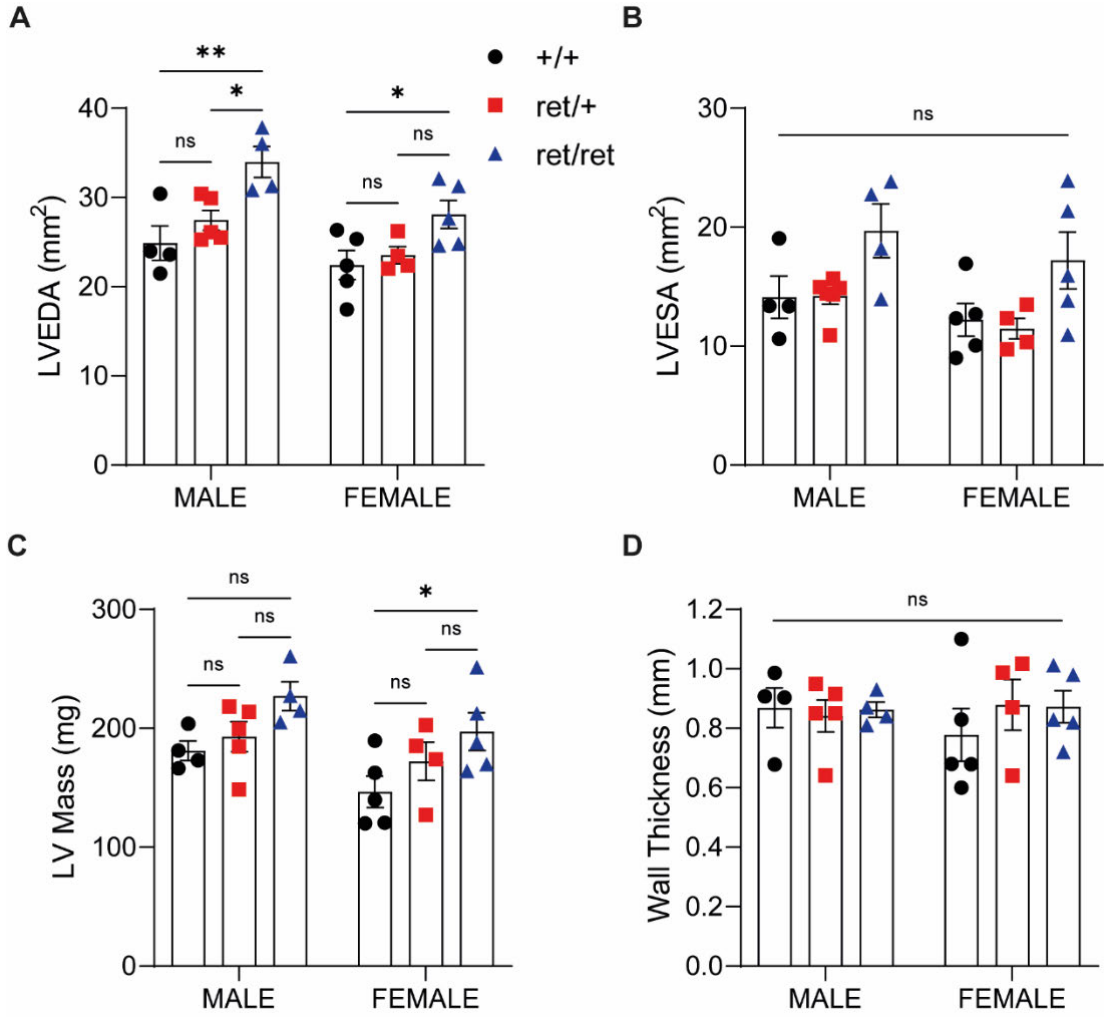

Figure 4. 3: Male and female *pdgfb*$^{ret/ret}$ mice exhibit structural changes to the heart at 3 months of age.

Quantification and analysis of PSLAX EKV images was performed to assess changes to left ventricular structure in 3-month-old male and female *pdgfb*$^{+/+}$ (+/+, black circles), *pdgfb*$^{ret/+}$ (ret/+, red squares) and *pdgfb*$^{ret/ret}$ (ret/ret, blue triangles) mice. Structural parameters: left ventricular end-diastolic area (LVEDA, **A**), left ventricular end-systolic area (LVESA, **B**), left ventricular mass (LV mass, **C**) and left ventricular wall thickness were measured (**D**). Data was analysed using VevoLab software; n=4-6/group. All data shown as mean±SEM. p-values determined by two-way ANOVA with Tukey's multiple comparison. *p<0.05, **p<0.001, ns=not significant

Male *pdgfb*^{ret} mice have increased cardiac output at 3 months of age.

I next investigated whether changes in cardiac structure caused changes to cardiac function in *pdgfb*$^{ret/ret}$ mice. CO was significantly higher in *pdgfb*$^{ret/ret}$ males compared

with their *pdgfb*$^{+/+}$ counterparts (Figure 4.4A, **p<0.01) whereas no differences were observed between genotypes in the female mice (p>0.05). SV, although appearing to increase, was not significantly altered in male *pdgfb*^{ret} mutant mice (Figure 5.4B, p>0.05). In contrast, SV was significantly higher in female *pdgfb*$^{ret/+}$ mice compared to *pdgfb*$^{+/+}$ females (Figure 4.4B, p>0.05, *p<0.05).

Contractile function is not impaired in 3-month-old *pdgfb*^{ret} mice.

At 3 months of age, both FAC (Figure 4.4C) and EF (Figure 4.4D) were unchanged in both males and females *pdgfb*^{ret} mice compared to *pdgfb*$^{+/+}$ littermates (p>0.05). These data show that *pdgfb*^{ret} mutant mice do not exhibit any changes to cardiac contractile function.

Female *pdgfb*$^{ret/ret}$ mice exhibit cardiac structural changes, not observed in male mice, at 6 months of age

Both male and female *pdgfb*$^{+/+}$, *pdgfb*$^{ret/+}$ and *pdgfb*$^{ret/ret}$ mice underwent ultrasound scans at 6 months of age and EKV images were acquired. LVEDA (Figure 4.5A) nor LVESA (Figure 4.5B) were similar between genotypes in both the male and female cohorts (p>0.05). Wall thickness was also not significantly altered in any of the groups which was also previously observed at 3 months (Figure 4.5C, p>0.05). LV mass was significantly greater in *pdgfb*$^{ret/ret}$ mice from the female cohort whereas no difference in LV mass was observed in male mice (Figure 4.5D, p>0.05).

No alterations to cardiac function were observed in either sex at 6 months of age in *pdgfb*^{ret} mutant mice

At 6 months of age CO (Figure 4.6A) and SV (Figure 4.6B) were similar between the groups (p>0.05). Furthermore, no changes in cardiac contractility measured by FAC (Figure 4.6C) or EF (Figure 4.6D) were observed between genotype in either sex (p>0.05).

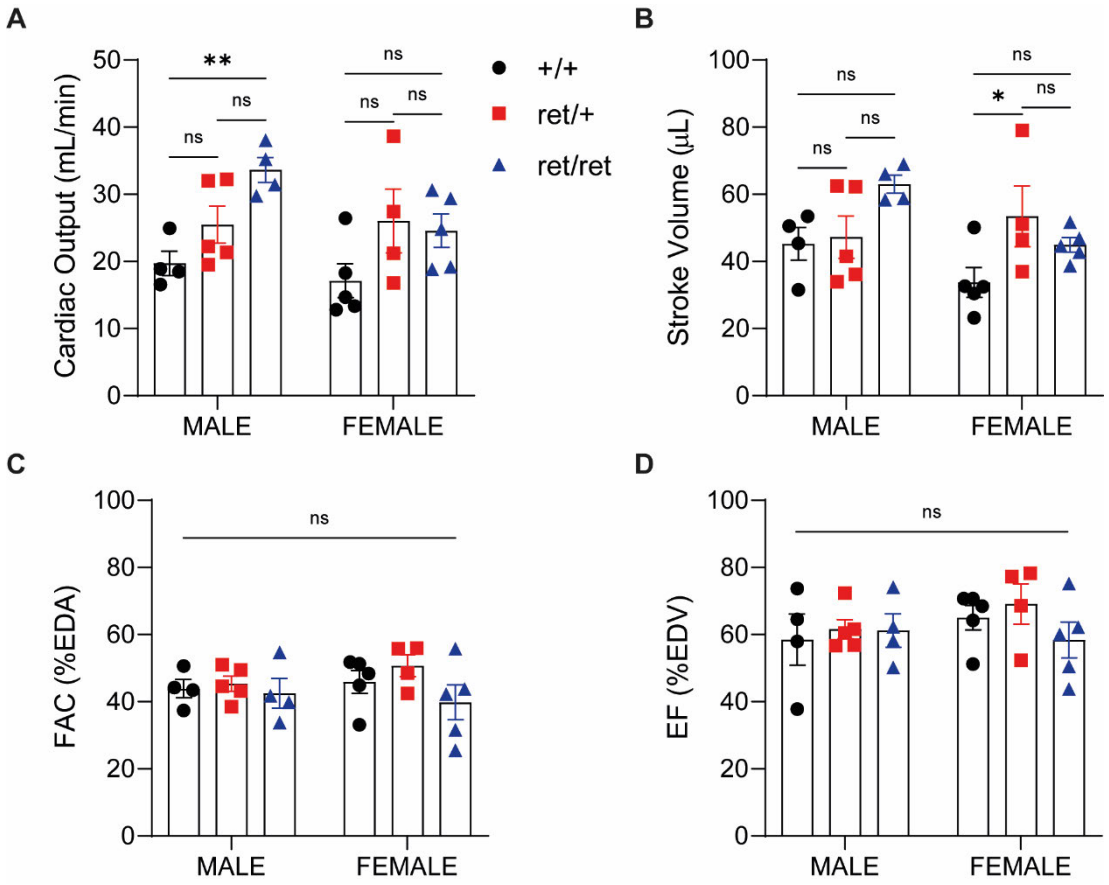

Figure 4.4: *Pdgfb*^{ret} mutant mice exhibit increased cardiac output and stroke volume at 3 months of age.

Parameters relating to left ventricular function and contraction were analysed for 3-month-old *pdgfb*$^{+/+}$ (+/+, black circles), *pdgfb*$^{ret/+}$ (ret/+, red squares) and *pdgfb*$^{ret/ret}$ (ret/ret, blue triangles) mice. Cardiac output (**A**) and stroke volume (**B**) were measured as well as contractile parameters fractional area change (FAC, **C**) and ejection fraction (EF, **D**). Data was analysed using VevoLab software; n=4-6/group. All data shown as mean±SEM and p-values were determined by two-way ANOVA with Tukey's multiple comparison. *p<0.05, **p<0.001, ns=not significant.

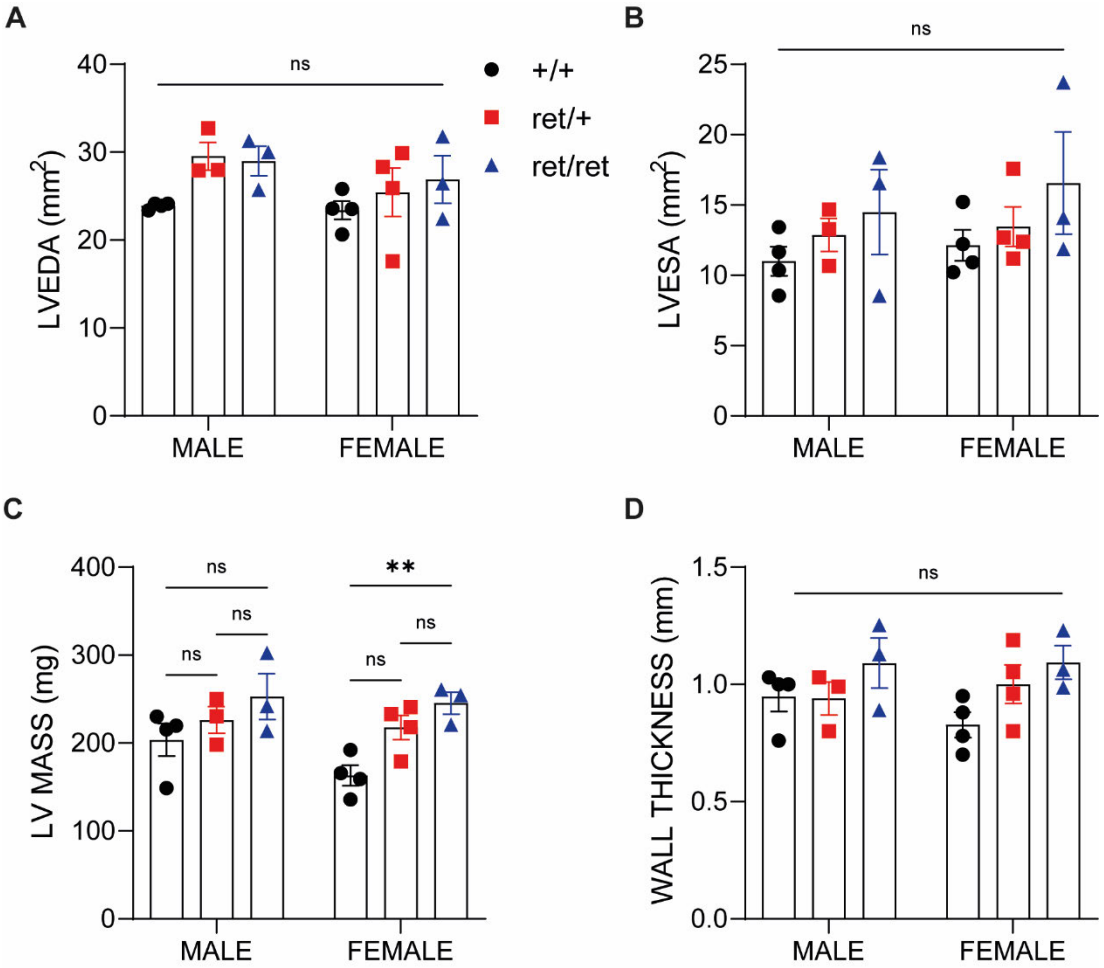

Figure 4.5: Female, not male, *pdgfb*$^{ret/ret}$ mice exhibit structural changes to the left ventricle at 6 months of age.

Analysis of left ventricular structural parameters in 6-month-old male and female *pdgfb*$^{+/+}$ (+/+, black full circles), *pdgfb*$^{ret/+}$ (ret/+, red squares) and *pdgfb*$^{ret/ret}$ (ret/ret, blue triangles) mice; left ventricular end-diastolic area (LVEDA, **A**), left ventricular end-systolic area (LVESA, **B**), left ventricular mass (LV mass, **C**) and left ventricular wall thickness (**D**). Data was analysed using VevoLab software. All data shown as mean±SEM. n=3-7/group, p-values were determined by two-way ANOVA with Tukey's multiple comparison. **p<0.001, ns=not significant

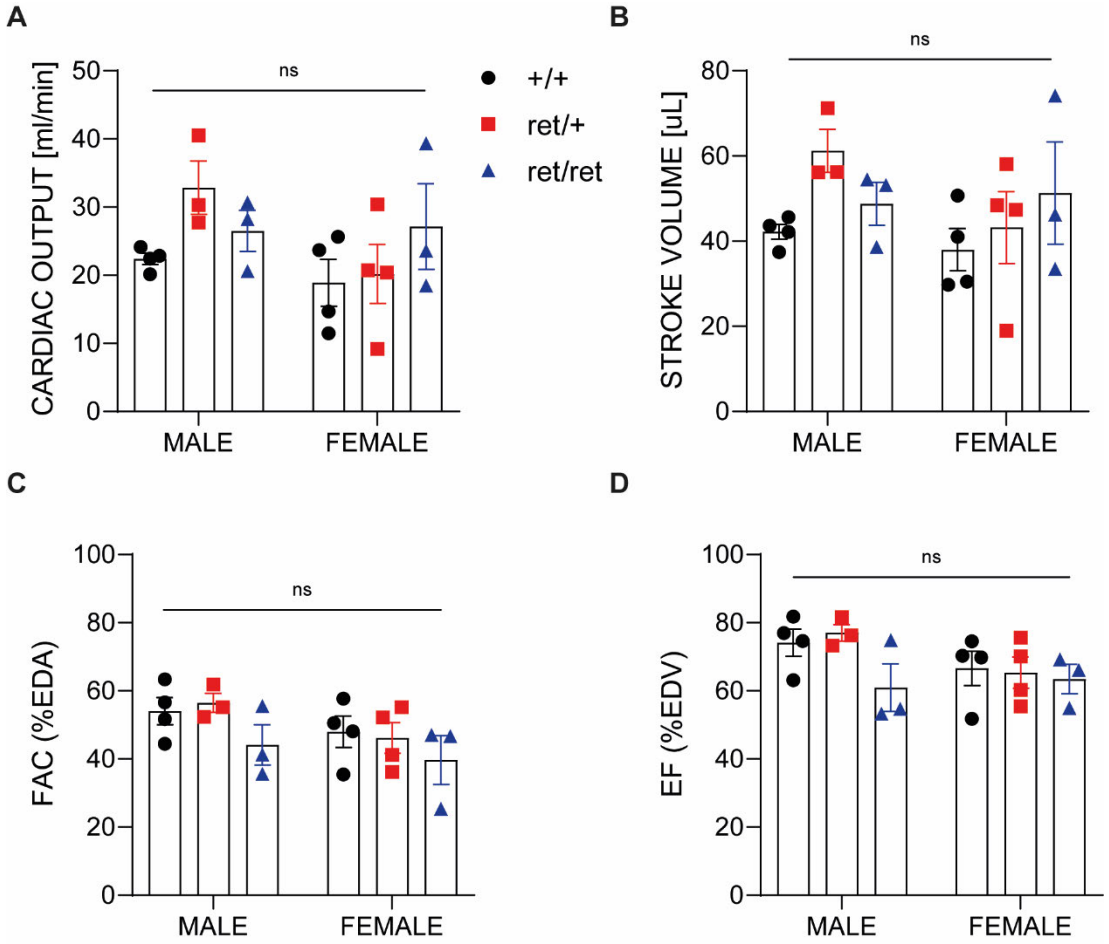

Figure 4.6: No differences in cardiac function were observed in male or female *pdgfb*^{ret} mutant mice at 6 months of age.

Analysis of left ventricular functional parameters in 6-month-old male and female *pdgfb*$^{+/+}$ (+/+, black circles), *pdgfb*$^{ret/+}$ (ret/+, red squares) and *pdgfb*$^{ret/ret}$ (ret/ret, blue triangles) mice; cardiac output (**A**), stroke volume (**B**) fractional area change (FAC, **C**) and ejection fraction (EF, **D**). Data was analysed using VevoLab software. All data shown as mean±SEM. n=3-7/group, p-values were determined by two-way ANOVA with Tukey's multiple comparison. ns=not significant

Female pdgfb$^{ret/ret}$ mice exhibit left ventricular dilation at 9 months

To further evaluate the *pdgfb*^{ret} mutant mice cardiac phenotype with age, cardiac structure was assessed at 9 months of age in both male and female cohorts. LVEDA was significantly higher in female *pdgfb*$^{ret/ret}$ mice compared to female *pdgfb*$^{ret/+}$ mice, however no difference was observed between any of genotypes in the male group (Figure 4.7A, *p<0.05, p>0.05). LVESA was also unchanged between genotypes in both the male and female groups (Figure 4.7B, p>0.05). No differences in wall thickness (Figure 4.7C) or LV mass (Figure 4.7D) were observed between any groups at 9 months of age (p>0.05).

Cardiac function was unchanged at 9 months of age in *pdgfb*^{ret} mutant mice.

At 9 months of age, both CO (Figure 4.8A) and SV (Figure 4.8B) were unchanged between the groups (p>0.05). Cardiac contractility as measured by FAC (Figure 4.8C) and EF (Figure 4.8D) was unchanged at 9 months of age in both sexes and groups examined (p>0.05).

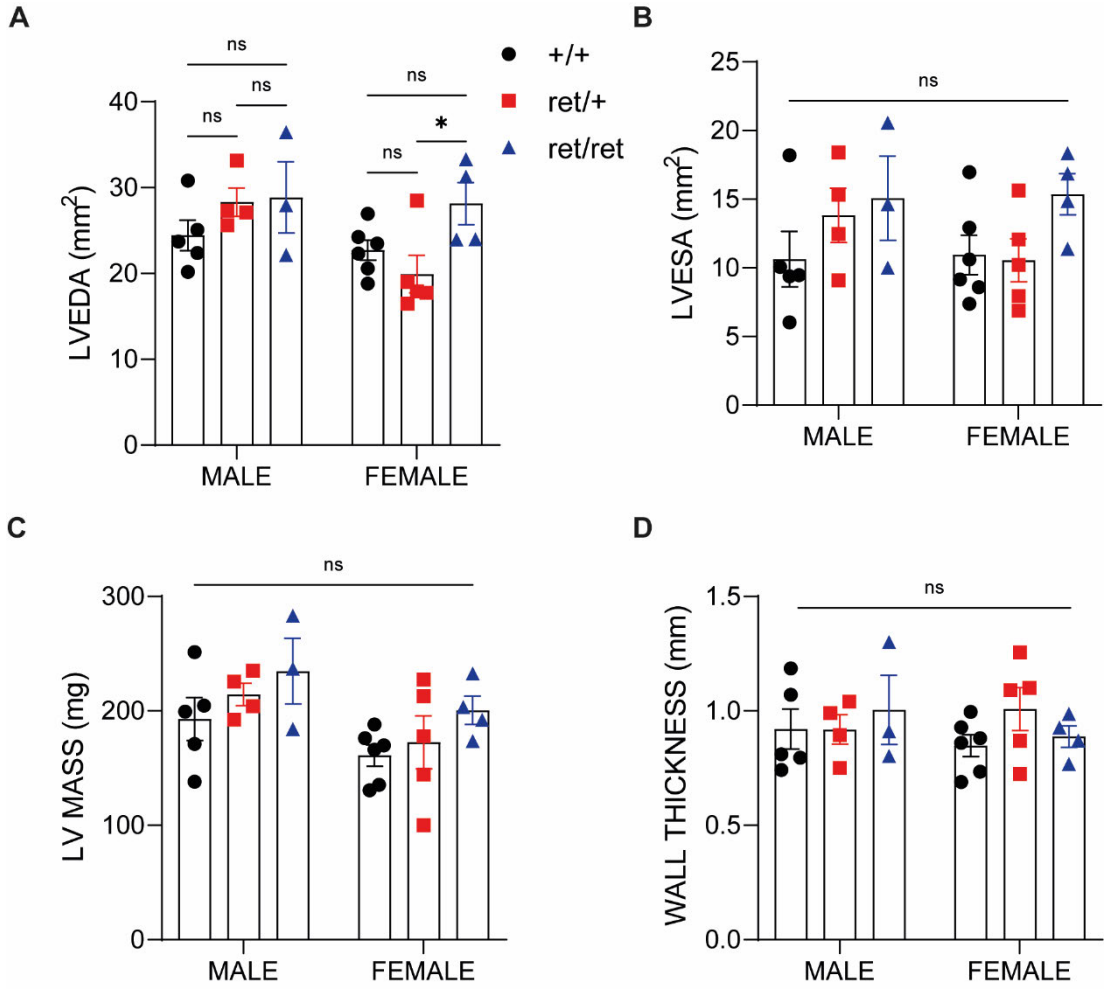

Figure 4.7: Female *pdgfb*$^{ret/ret}$ mice exhibit a differential cardiac phenotype than male *pdgfb*$^{ret/ret}$ mice at 9 months of age.

Left ventricular end-diastolic area (LVEDA, **A**), left ventricular end-systolic area (LVESA, **B**), left ventricular mass (LV mass, **C**) and left ventricular wall thickness (**D**) measured in 9-month-old male and female *pdgfb*$^{+/+}$ (+/+, black circles), *pdgfb*$^{ret/+}$ (ret/+, red squares) and *pdgfb*$^{ret/ret}$ (ret/ret, blue triangles) mice. Data was analysed using VevoLab software. All data shown as mean±SEM. n=3-7/ group, p-values were determined by two-way ANOVA with Tukey's multiple comparison. *p<0.05, ns=not significant.

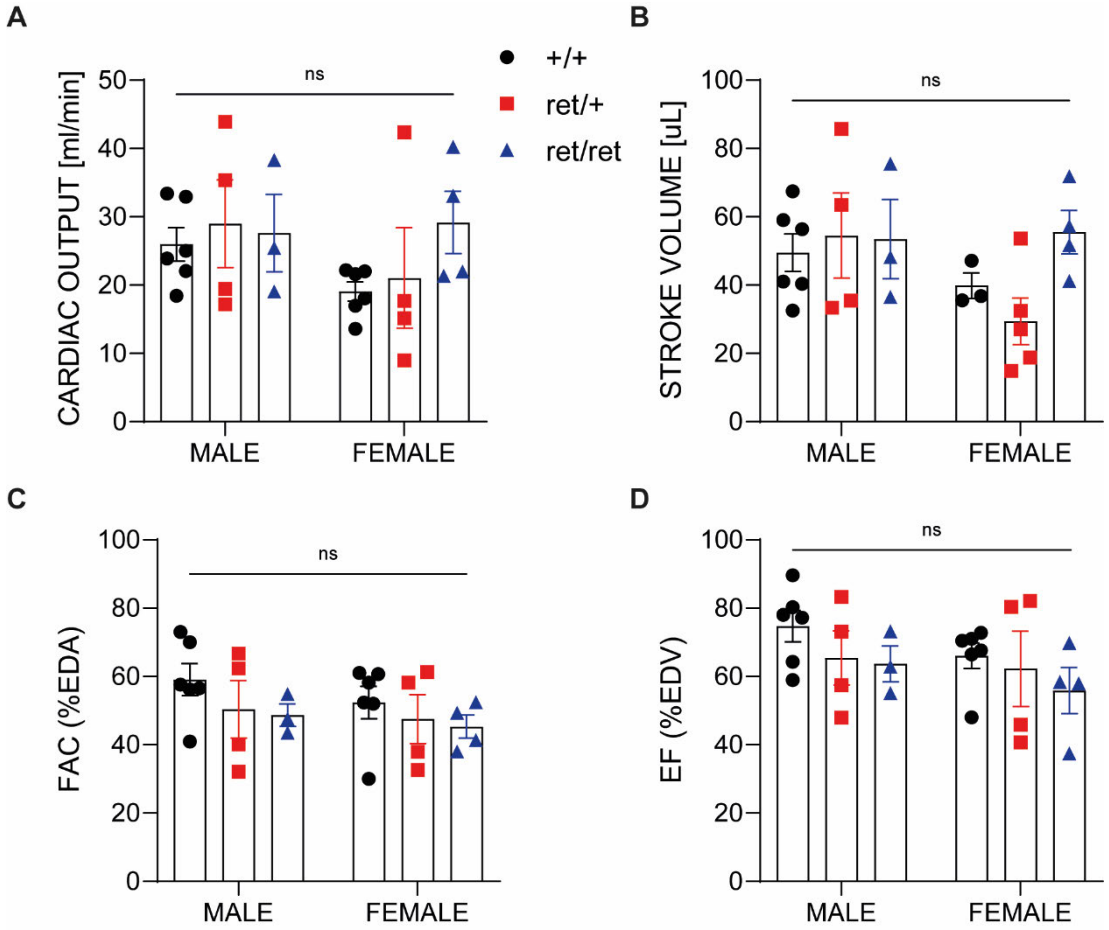

Figure 4.8: Changes to cardiac function are absent in male and female *pdgfb*^{ret} mutant mice at 9 months of age.

Cardiac output (**A**), stroke volume (**B**), fractional area change (FAC, **C**) and ejection fraction (EF, **D**) measured in 9-month-old *pdgfb*$^{+/+}$ (circles, white bar), *pdgfb*$^{ret/+}$ (ret/+, red squares) and *pdgfb*$^{ret/ret}$ (ret/ret, blue triangles) mice. Data was analysed using VevoLab software. All data shown as mean±SEM. p-values determined via two-way ANOVA with Tukey's multiple comparison. ns=not significant

At 12 months, changes to cardiac structure in *pdgfb*^{ret} mice are resolved.

The final ultrasound scans were performed at 12 months of age in male and female *pdgfb*$^{+/+}$, *pdgfb*$^{ret/+}$ and *pdgfb*$^{ret/ret}$ mice. Both LVEDA (Figure 4.9A) and LVESA (Figure 5.9B) were similar between each group and sex ($p>0.05$). LV mass (Figure 4.9C) and wall thickness (Figure 5.9D) were unchanged at 12 months of age in any of the genotype groups or sexes ($p>0.05$). CO and SV were also similar between genotypes in either sex at 12 months of age (Figure 4.10A, B, $p>0.05$). Both FAC and EF were also unchanged at this time point (Figure 4.10C, D, $p>0.05$).

M-mode imaging reveals no changes to fractional shortening in *pdgfb*^{ret} mutant mice.

M-mode of the left ventricle over several cardiac cycles were acquired. M-mode images are 2D images which allow visualisation and measurement of left ventricular diameter during diastole (LVDD) and systole (LVSD) over several cardiac cycles (Figure 4.11A) to calculate fractional shortening (FS). No difference in FS was observed at 3 months of age between any genotype in either the male of female cohort (Figure 4.11B, $p>0.05$). This was also found at 6 (Figure 4.11C), 9 (Figure 5.11D) and 12 (Figure 4.11E) months of age ($p>0.05$). This data further supports the fact that the pdgfbret mutation does not affect myocardial contractility at any of the time points measured in our study

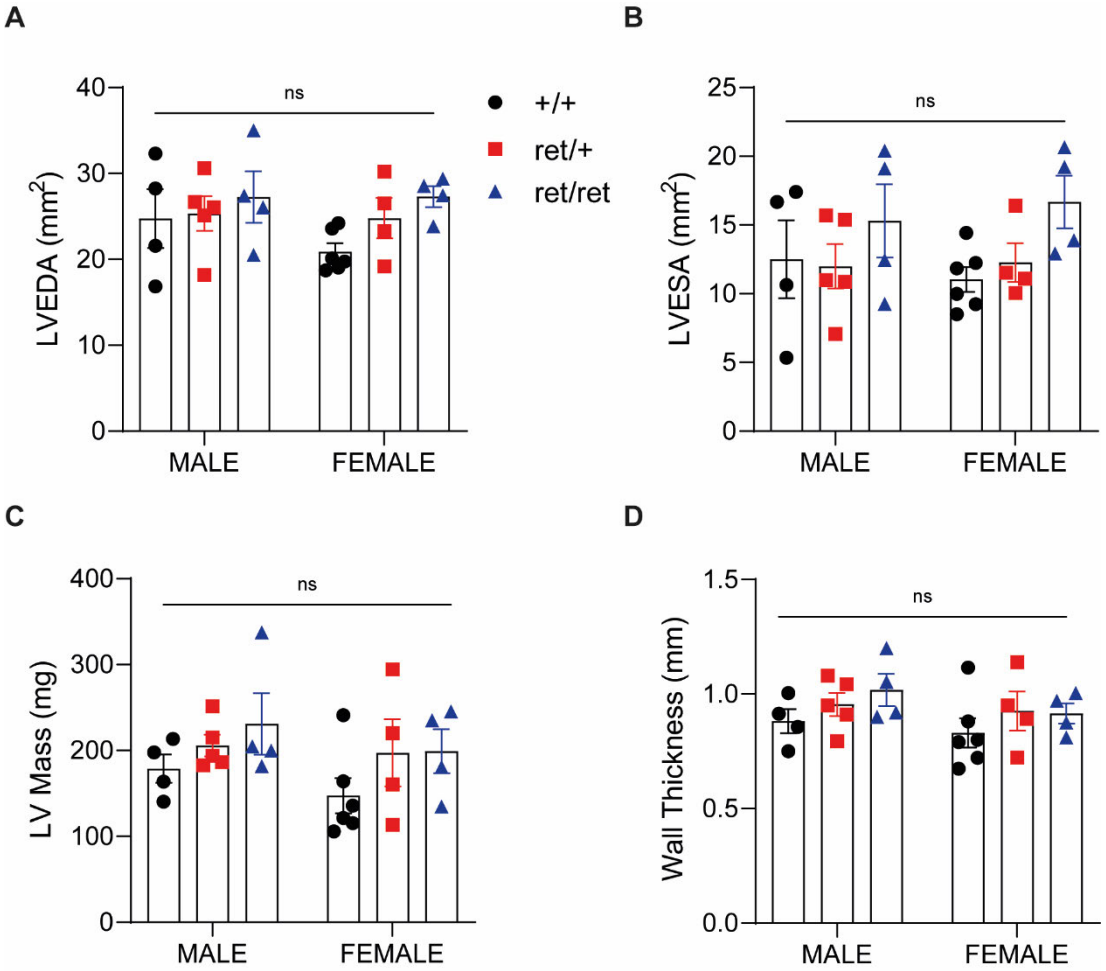

Figure 4.9: Cardiac structure in male or female *pdgfb*^{ret} mutant mice is similar at 12 months of age.

Left ventricular end-diastolic area (LVEDA, **A**), left ventricular end-systolic area (LVESA, **B**), left ventricular mass (LV mass, **C**), and left ventricular wall thickness (**D**) measured in 12-month-old male and female *pdgfb*$^{+/+}$ (+/+, black circles), *pdgfb*$^{ret/+}$ (ret/+, red squares) and *pdgfb*$^{ret/ret}$ (ret/ret, blue triangles) mice. Data was analysed using VevoLab software. All data shown as mean±SEM. p-values were determined by Two-way ANOVA with Tukey's multiple comparison. ns=not significant

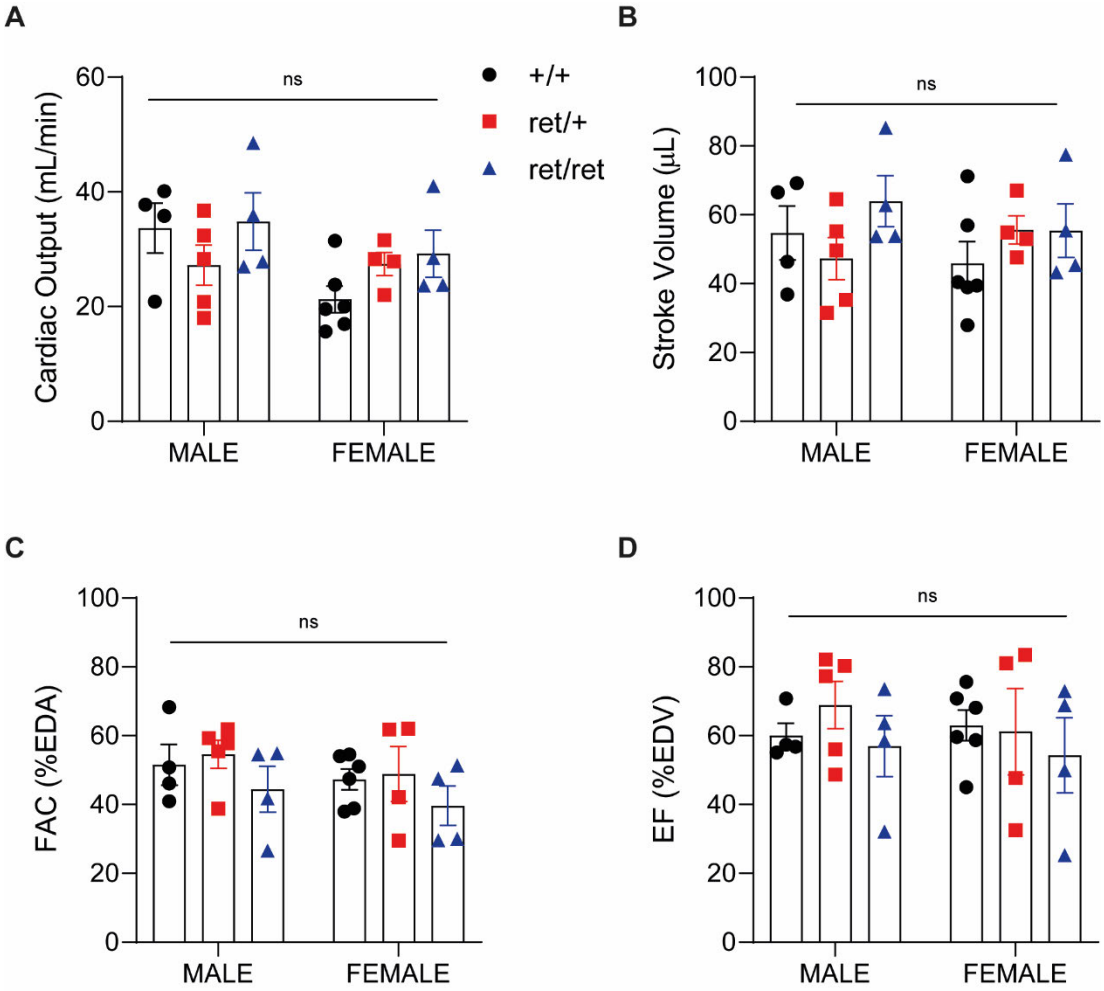

Figure 4.10: Functional parameters are unchanged at 12 months of age in male and female *pdgfb*^{ret} mutant mice.

Cardiac output (**A**), stroke volume (**B**), fractional area change (FAC, **C**) and ejection fraction (EF, **D**) measured in 12-month-old *pdgfb*$^{+/+}$ (+/+, black circles), *pdgfb*$^{ret/+}$ (red squares, ret/+) and *pdgfb*$^{ret/ret}$ (blue triangles, ret/ret) mice. Data was analysed using VevoLab software. All data shown as mean±SEM. Two-way ANOVA with Tukey's multiple comparison. ns=not significant

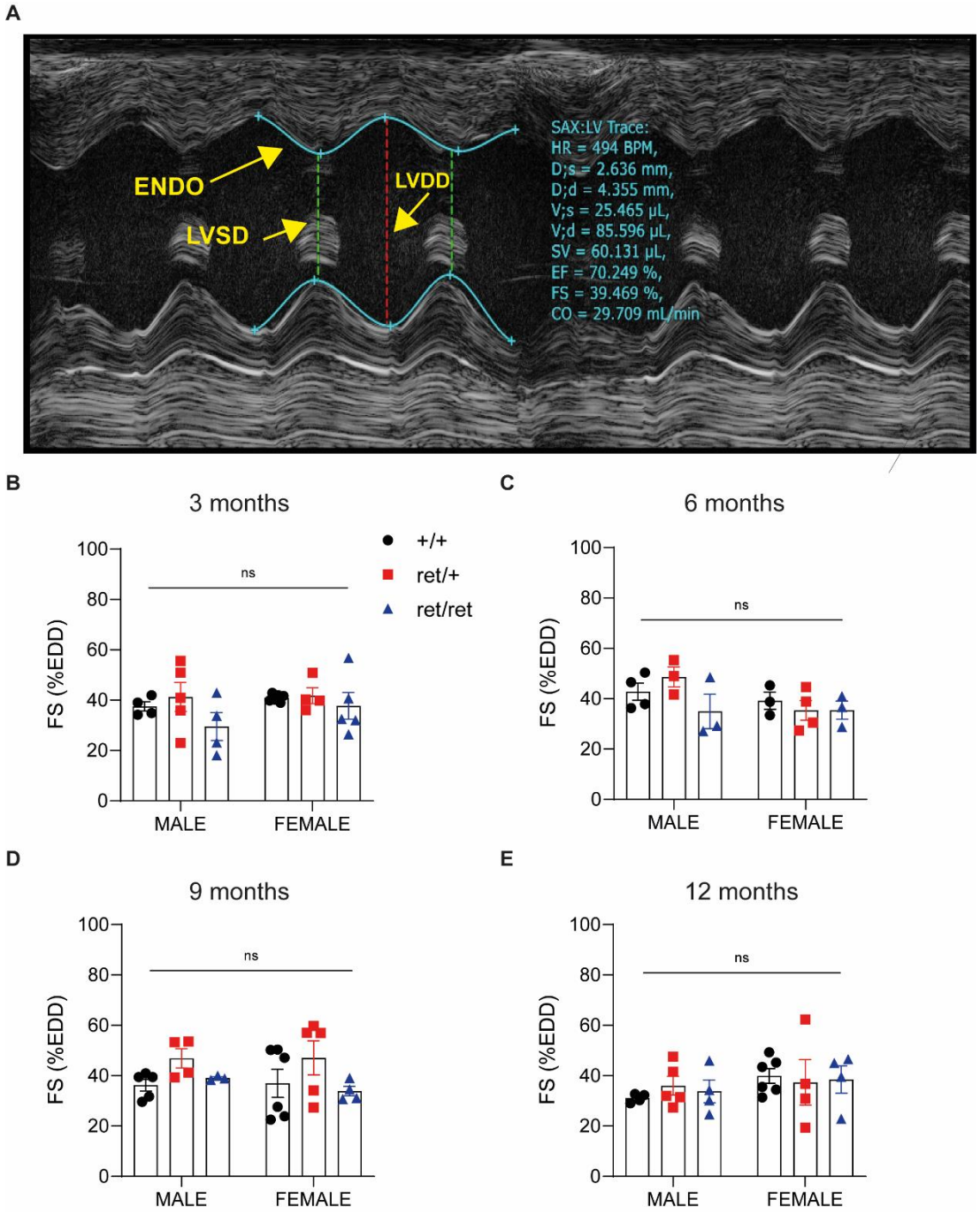

Figure 4.11: Fractional shortening of the left ventricle was unaltered in *pdgfb*^{ret} mutant mice.

Example of a short axis 2D m-mode image from *pdgfb*$^{+/+}$ mice (**A**) highlighting measurements taken to derive fractional shortening (FS). The image shows continuous left ventricular contraction taken over several cardiac cycles. The endocardial wall (ENDO, blue line) is shown. The green line showing left ventricular systolic diameter and the red line indicating left ventricular diastolic diameter. FS was calculated at 3(**B**), 6(**C**), 9(**D**) and 12(**E**)-month time points in male and female *pdgfb*$^{+/+}$ (+/+), *pdgfb*$^{ret/+}$ (ret/+) and *pdgfb*$^{ret/ret}$ (ret/ret) mice. Data shown as mean± SEM, Two-way ANOVA with Tukey's test, ns= not significant n=3-6/group

One year old *pdgfb*$^{ret/ret}$ mice do not exhibit signs of cardiac hypertrophy.

Male *pdgfb*$^{ret/ret}$ mice had significantly lower body weight compared with both *pdgfb*$^{+/+}$ and *pdgfb*$^{ret/+}$ mice (Figure 4.12A, p<0.05). In comparison to females where body weight was similar in all groups (p>0.05). No difference in heart weight was observed in male or female *pdgfb*$^{+/+}$, *pdgfb*$^{ret/+}$ and *pdgfb*$^{ret/ret}$ mice (Figure 4.12B, p>0.05). Heart weight to body weight ratio was significantly higher in male *pdgfb*$^{ret/ret}$ mice compared to *pdgfb*$^{ret/+}$ mice (Figure 4.12C, p<0.001) but remained unchanged in female mice (Figure 4.12C, p>0.05). Heart weight/Tibia length ratio was similar across genotypes in either male or female cohorts (Figure 4.12D, p>0.05)

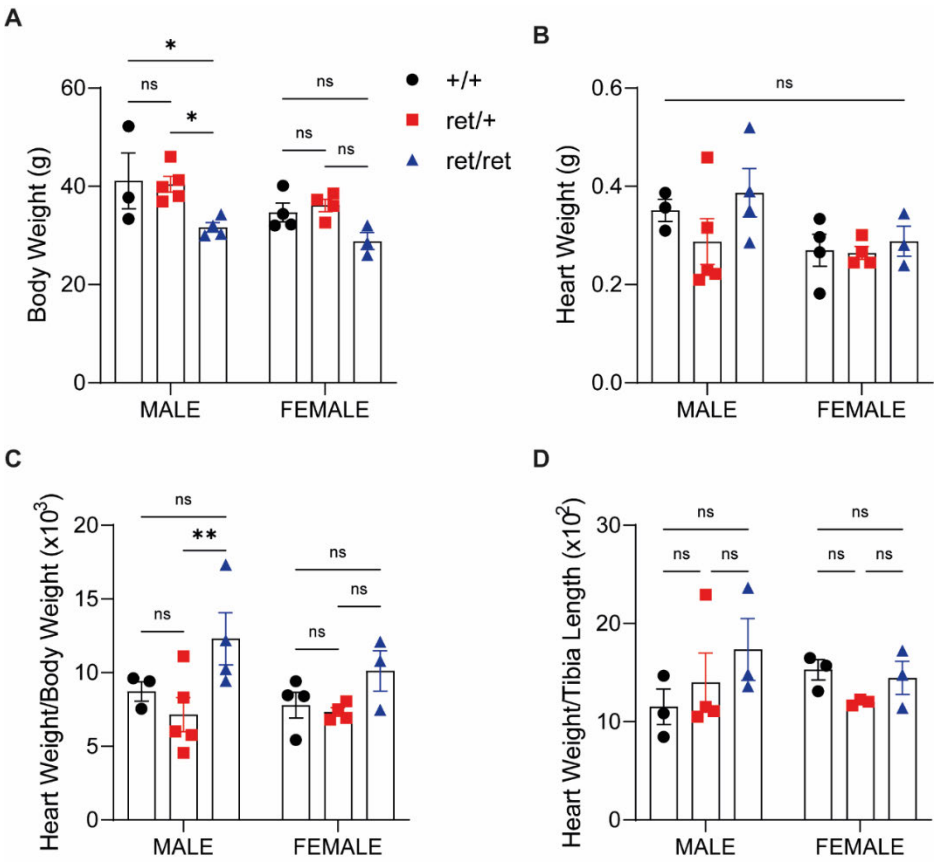

Figure 4. 12: Male *pdgfb*$^{ret/ret}$ mice have reduced body mass but do not exhibit signs of cardiac hypertrophy.

Body weight (**A**), heart weight (**B**), heart weight to body weight ratio (**C**) and heart weight to tibia length ratio (**D**) of male and female *pdgfb*$^{+/+}$, (+/+, black circles) *pdgfb*$^{ret/+}$ (ret/+, red squares) and *pdgfb*$^{ret/ret}$ (ret/ret, blue triangles) mice measured at 12 months of age. Data shown as mean±SEM. n=3-5/group Two-way ANOVA with Tukey's multiple comparison. **p<0.001 *p<0.05 ns=not significant

Male *pdgfb*$^{ret/ret}$ mice have altered cardiac development and function from 3 to 12 months.

After examination of outcomes at each time point, I then examined structural and functional parameters in male and female *pdgfb*$^{+/+}$, *pdgfb*$^{ret/+}$ and *pdgfb*$^{ret/ret}$ mice over the course of my 12-month study. Significant changes to left ventricular structure were observed in male and female *pdgfb*$^{ret/ret}$ mice and I wished to determine whether these changes were retained over time. Values at 3 months were considered as baseline and changes were considered with reference to these for each genotype.

Examination of LVEDA and LVESA in male mice (Figure 4.13A, C) did not reveal any differences between 3 months and any other time point in any of the genotype groups ($p>0.05$). A similar observation was made in the female cohort (Figure 4.13B, D, $p>0.05$). LV mass did not significantly change in the male mice between 3 months and any other time point (Figure 4.13E), nor in the female mice (Figure 4.13F, $p>0.05$). Wall thickness was also not significantly altered from 3 months to any other time point in the study in both male (Figure 4.13G) and female (Figure 5.13H) mice ($p>0.05$). Taken together this data suggests that *pdgfb*$^{+/+}$, *pdgfb*$^{ret/+}$ and *pdgfb*$^{ret/ret}$ mice cardiac structure is not significantly altered during aging.

I next assessed functional parameters over time. CO significantly increased between 3 and 12 months in male *pdgfb*$^{+/+}$ mice (Figure 4.14A, $p<0.05$). For male *pdgfb*$^{ret/+}$ and *pdgfb*$^{ret/ret}$ mice CO did not increase over time. Neither CO nor SV were significantly different between 3 months and any other time point in the female cohort (Figure 4.14B, C, D). Furthermore, contractile parameters, EF (Figure 4.14E, F), FAC (Figure 4.14G, H) and FS (Figure 4.14I, J) did not change significantly between 3 months and any other time point ($p>0.05$) in male or female mice.

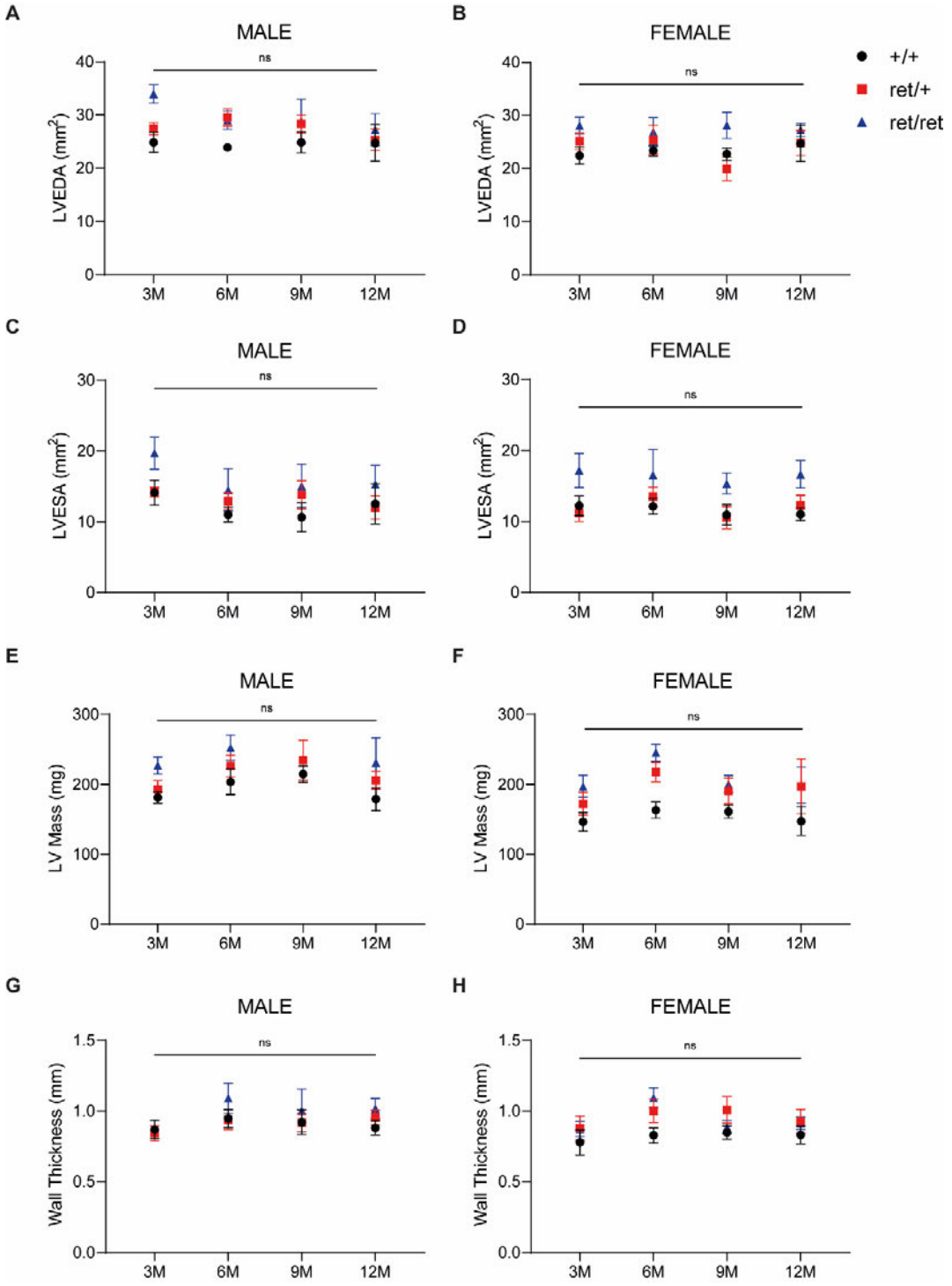

Figure 4.13: Analysis of structural parameters over time in male and female *pdgfb*$^{+/+}$ and *pdgfb*^{ret} mutant mice.

LVEDA (**A**, **B**), LVESA (**C**, **D**), LV mass, (**E**, **F**), wall thickness (**G**, **H**) plotted over each time point for male and female *pdgfb*$^{+/+}$ (black circle,) *pdgfb*$^{ret/+}$ (red square) and *pdgfb*$^{ret/ret}$ mice (blue triangle). All data shown as mean±SEM. Two-way ANOVA with Dunnett's multiple comparison. ns=not significant

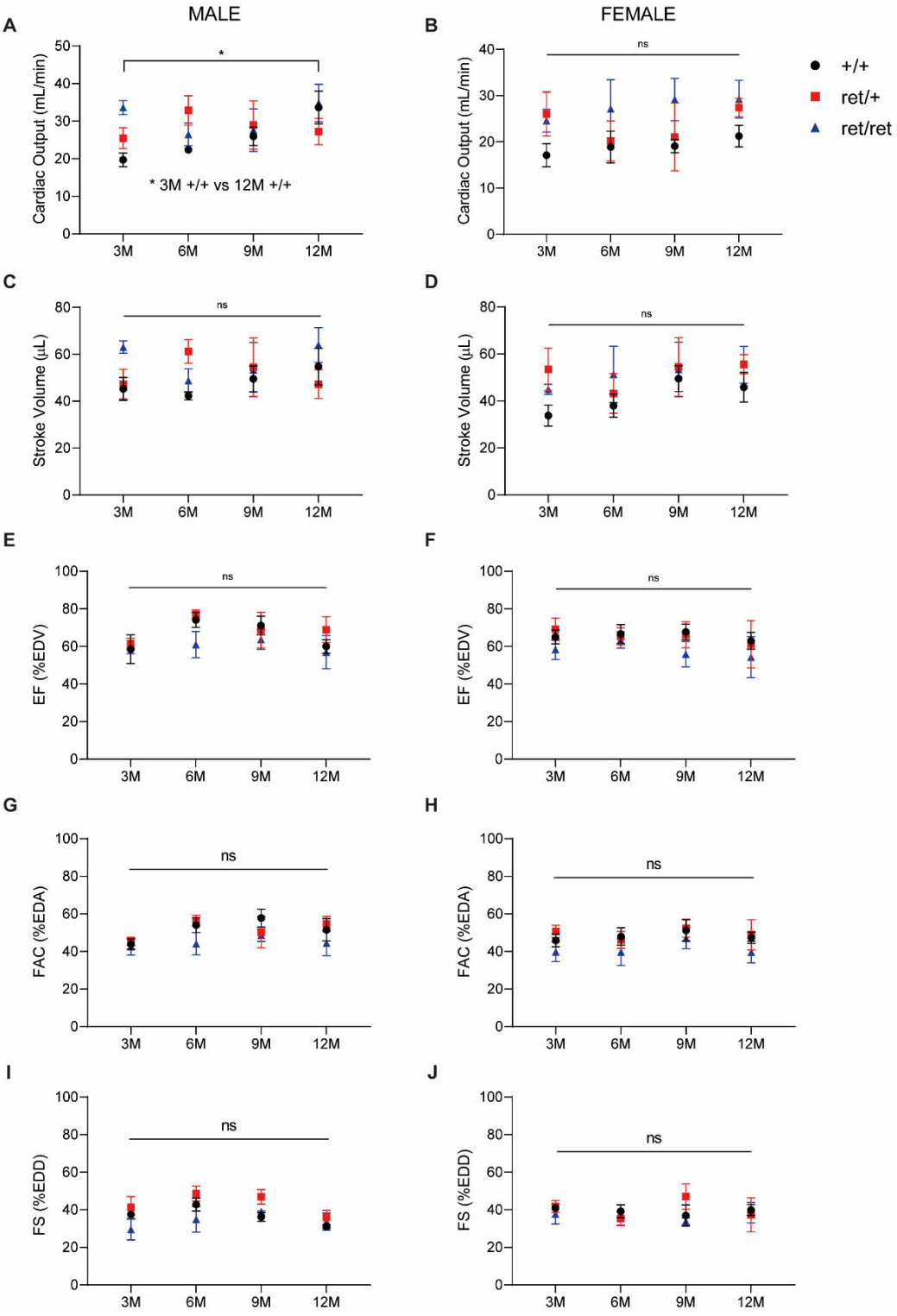

Figure 4.14: Analysis of functional parameters over time in male and female *pdgfb*$^{+/+}$ and *pdgfb*^{ret} mutant mice.

Cardiac output (**A**, **B**), stroke volume (**C**, **D**), ejection fraction, (EF, **E**, **F**), fractional area change (FAC, G, H) and fractional shortening (FS, **I**, **J**) plotted over each time point for male and female *pdgfb*$^{+/+}$ (black circle) *pdgfb*$^{ret/+}$ (red square) and *pdgfb*$^{ret/ret}$ mice (blue triangle). All data shown as mean±SEM. Two-way ANOVA with Dunnett's multiple comparison. *p<0.05 ns=not significant.

Discussion

The main aims of this chapter were to perform echocardiography to assess cardiac structure and function in young male and female *pdgfb*$^{ret/ret}$ mice compared with *pdgfb*$^{+/+}$ and *pdgfb*$^{ret/+}$ littermates and to determine if aging influences structure and function up to 1 year of age. Mutations in *pdgf* have been shown to lead to a variety of cardiovascular pathologies ranging from severe haemorrhaging during embryonic development to cardiac hypertrophy and fibrosis in adult mice. Male and female mice also exhibit changes to cardiac structure and function in aging however, the effect of the *pdgfb*^{ret} mutation on cardiac structure and function in aging male and female mice was not yet described.

Young male and female *pdgfb*$^{ret/ret}$ mice exhibit transient left ventricle dilation.

A major finding based on my experiments is that both male and female *pdgfb*$^{ret/ret}$ mutant mice exhibit left ventricular dilatation at 3 months of age. However, it is key to note that only a small number of mice were scanned in my study due to issues with breeding (see Chapter 7: General Discussion) and as such we were unable to follow the same mice throughout my study. This may introduce variability into our study and lower our ability to detect significant changes. Similar results to mines were reported in male *pdgfb*$^{ret/ret}$ mice (Nystrom *et al.*, 2006) but I me the first to show that female *pdgfb*$^{ret/ret}$ mice exhibit this phenotype. By 12 months however dilation of the left ventricle is resolved indicating that changes are transient. Neither male nor female *pdgfb*$^{+/+}$ an *pdgfb*$^{ret/+}$ exhibit this dilatory phenotype at three months. Over time male and female *pdgfb*$^{+/+}$ and *pdgfb*$^{ret/+}$ mice LVEDA is unchanged from 3 months to any other time point over the course of the experiment. However, male, and female *pdgfb*$^{ret/ret}$ mice over LVEDA decreases between 3- and 6-months although does not significantly differ from any other time point. Ventricular dilation may occur in the setting of volume overload which may pathological or physiological in nature, however, the underlying cause of this phenotype is not fully understood. PDGFB and PDGFRβ KO mouse models exhibit enlarged hearts, dilation of the ventricles and coronary blood vessels but do not survive into adulthood (Levéen *et al.*, 1994; Soriano, 1994). Furthermore, these PDGFB and PDGFRβ KO mice have reduced VSMC and pericyte coverage indicates that structural changes to the left ventricle in young *pdgfb*$^{ret/ret}$ mice may be due to reduced recruitment of VSMC and pericyte progenitors in the formation

of large coronary vessels and ventricles in development. However, it is unclear whether the heart is affected during embryonic and early postnatal development in *pdgfb*$^{ret/ret}$ mice. As such it would therefore be important to analyse early postnatal and embryonic heart development and function. Confocal imaging data from the Crisan lab, has suggested that the embryonic aorta formed properly in *pdgfb*$^{ret/ret}$ mid-gestation mouse embryos (Sa da Bandeira et al, in preparation) and further preliminary histological and immunohistology analysis in a small number of embryos found that there were no observable differences in left ventricular structure at E11 or E14 in *pdgfb*$^{ret/ret}$ mice (Jemma Makepeace, unpublished preliminary observations), nor at E18 (Ana Barbosa, unpublished) compared with littermates. However, it would be interesting to repeat these experiments in a greater number of embryos and further explore the embryonic development of *pdgfb*$^{ret/ret}$ mice using embryonic echocardiography to determine whether changes to cardiac function can be detected at this time point. Further scans could then be performed later in neonatal and young postnatal mice to fully characterise the cardiac structure and function of *pdgfb*$^{ret/ret}$ mice. This will give a greater insight into how mutations in the *pdgfb* gene may affect human cardiac development and whether changes to *pdgfb*$^{ret/ret}$ cardiac structure arise from development.

Another potential cause of left ventricular dilation exhibited in *pdgfb*$^{ret/ret}$ mice may be tissue oedema caused by increased vascular permeability due to lack of full pericyte coverage of cardiac microvessels. This may be responsible for the increases in echocardiography measured LV mass observed at 3 months in male and 3 and 6 months in female *pdgfb*$^{ret/ret}$ mice compared with *pdgfb*$^{+/+}$ mice. Previous studies briefly assessed vascular permeability of the hearts of *pdgfb*$^{ret/ret}$ mice using dextran permeability assays which showed an increase in dextran leakage after 24 hours (Raines *et al.*, 2011). However, no information was given regarding the age or sex of the mice utilised. If the vascular permeability is increased in *pdgfb*$^{ret/ret}$ mice differences in LV mass observed between male and female *pdgfb*$^{ret/ret}$ may be due to the actions of oestrogen which is a known vasodilatory molecule and has been shown to increase microvascular permeability in the uterus (Cullinan-Bove and Koos, 1993). Female *pdgfb*$^{ret/ret}$ mice did exhibit a persistent increase in LV mass at 3 and 6 months which was resolved at 9 and 12 months. Since hormonal changes in females are expected to be seen around 7-9 months of age (Brinton, 2012), a reduction in oestrogen levels

at this time may mean that any tissue leakage or oedema is resolved in *pdgfb*$^{ret/ret}$ female mice. This is further supported by the fact that overall heart weight was unchanged in *pdgfb*$^{ret/ret}$ mice compared with littermates at 12 months of age. Therefore, it would be important to assess vascular permeability of the heart using dextran permeability assays at multiple ages to determine whether this changes with age in *pdgfb*$^{ret/ret}$ mice.

Another suggestion may be that microvessel rarefaction may also promote left ventricular dilation. This is commonly observed in patients with heart failure with preserved ejection fraction who also develop left ventricular dilation(Su *et al.*, 2021). This may occur early in *pdgfb*$^{ret/ret}$ mouse development if there are not enough recruited pericytes to stabilise forming vessels. To test this, we could assess blood vessel density in the ventricles of *pdgfb*$^{ret/ret}$ mice on histological sections using immunohistochemistry for CD31, an endothelial cells marker. The number of CD31+ vessels could then be quantified to understand f this is reduced in *pdgfb*$^{ret/ret}$ mice. In conjunction with this marker for pericytes could be utilised to determine whether all vessels have proper pericyte coverage and if this relates to altered heart function.

Left ventricular dilation may also occur in eccentric cardiac hypertrophy which had been was reported in male *pdgfb*$^{ret/ret}$ mice (Nystrom *et al.*, 2006). Eccentric hypertrophy is one of two common hypertrophic responses, the other being concentric hypertrophy. Eccentric hypertrophy involves the thinning of the ventricular wall and increased left ventricular volume and occurs due to volume overload (Simone, 2004). My data show that the structural phenotype displayed by *pdgfb*$^{ret/ret}$ mice at 3 months of age is like that observed in eccentric hypertrophy albeit without thinning of the ventricular wall, as ventricular wall thickness and LV mass was unchanged. Therefore, the phenotype we observed in our study is better described as a dilatory response rather than a hypertrophic response as echocardiography derived wall thickness and LV mass did not change. To further investigate this hypothesis histological analysis of the heart should be performed to assess changes to cardiomyocyte structure. In eccentric hypertrophy, cardiomyocytes in the left ventricle elongate as a response to volume overload. Therefore, analysis of cardiomyocyte cross sectional area with wheat germ agglutin should be performed to identify potential changes to cardiomyocytes in *pdgfb*$^{ret/ret}$ mice. To understand these changes further molecular analysis could be performed. For example, concentric and eccentric hypertrophy have

been shown to have distinct differential underlying molecular pathways in either physiological or pathological settings. For example, one study showed greater atrial natriuretic peptide (ANP), b-type natriuretic peptide (BNP), β-myosin heavy chain (MHC) and α-skeletal actin upregulation in the heart ventricle using a mouse model of aortic band pressure overload versus a chronic swim-training volume overload model (McMullen and Jennings, 2007). ANP and BNP act to reduce cardiac hypertrophy, fibrosis and are anti-inflammatory molecules released under pathological cardiac conditions such as heart failure (Nakagawa, Nishikimi and Kuwahara, 2019; Mezzasoma *et al.*, 2020). Up-regulation of contractile proteins β-MHC and α-skeletal actin is also associated with reduced cardiac function and pathology (Boheler *et al.*, 1991; Krenz and Robbins, 2004). In mice, PDGF signalling is increased in response in pressure overload hypertrophy and cardiomyocyte specific deletion of PDGFRβ results in a more severe hypertrophic response than controls (Chintalgattu *et al.*, 2010). However, whether PDGF signalling is altered in the hearts of *pdgfb*$^{ret/ret}$ mice is unknown but may play a direct role in changes to left ventricular structure.

Dilation of the left ventricle may also occur in the setting of dilated cardiomyopathy which is also characterised by enlargement and dilation of one or both ventricles, and impaired contractility (Weintraub, Semsarian and Macdonald, 2017). However, I observed that contractile parameters such as EF, FAC and FS were unaffected in at any time point in *pdgfb*$^{ret/ret}$ mice. However, EF may also be preserved in heart failure, a syndrome with limited treatments involving microvascular and lymphatic dysfunction (Cuijpers *et al.*, 2020). Indeed, it has been demonstrated that *pdgfb*$^{ret/ret}$ mice have altered lymphatic vessel structure due to defective smooth muscle cell (SMC) recruitment during the formation of lymphatic vessels (Wang *et al.*, 2017). This may also contribute to the alterations observed in *pdgfb*$^{ret/ret}$ mice through increased oedema due to leakage of lymphatic vessels increasing heart weight and left ventricular mass.

At 3 months of age, *pdgfb*^{ret} mice have increased cardiac output.

I next observed that *pdgfb*^{ret} mice have changes in cardiac function related to changes in left ventricular structure at 3 months of age. Male *pdgfb*$^{ret/ret}$ mice had increased CO and female *pdgfb*$^{ret/+}$ mice had increased SV. Both functional parameters are related

to the volume of blood being pumped from the left ventricle with *pdgfb*$^{ret/ret}$ mice pumping more blood from the left ventricle than their *pdgfb*$^{+/+}$ counterparts. Typically, CO or SV increase can be due to numerous physiological changes such increased size of the heart, blood volume and increased contractility of the heart (Singh and Sharma, 2020). However, the most likely cause of increased CO and SV in my study is because endocardial volume is calculated based on changes to LVEDA by the VevoLab software. However, it would be important to assess CO and SV in further experiments. Underlying changes in CO can also occur due to regulation by the nervous system, endocrine system as well as changes in paracrine signalling (King and Lowry, 2019). In addition, increased CO is a feature of the endurance athlete's heart. However, *pdgfb*$^{ret/ret}$ mice have reduced physical performance compared to littermates (Nystrom et al, 2006). In conjunction with my data, this suggests that contractility of the heart is unchanged, and the increased CO and SV exhibited by *pdgfb*$^{ret/ret}$ mice do not confer physiological benefit to heart function and physical performance. Instead, the increase in CO and SV may be due to a systemic increase in blood volume through changes to blood vessel cellular composition or blood vessel number. This may lead to a volume overload response prompting the physiological cardiac changes. To confirm this result, it would be important to directly measure the CO of *pdgfb*$^{ret/ret}$ mice. This could be done using thermodilution which is a direct invasive measurement of cardiac output performed via a surgical procedure where thermocouples are inserted into the jugular veins, right atria and then into the aortic arch (Franco *et al.*, 1999). Other methods of CO measurement may include the use of a flow doppler probe placed over the ascending aorta (Tournoux *et al.*, 2011) .

Blood volume is also determined by the kidney and embryonic *pdgfb*$^{ret/ret}$ mice have mesangial cell (also called renal pericyte-like cells) deficiency which normalizes at 1 month of age (Lindblom *et al.*, 2003). However, at 3 months these mice develop albuminuria and glomerulosclerosis at 6 months which is indicative of kidney dysfunction. This may also account for some of changes we found in the heart structure and function at 3 months of age in our mutants, therefore it would be important to study the role of the kidney and kidney function of *pdgfb*^{ret} mice in a future investigation. Kidney structure and function can could be assessed by renal ultrasound and histological analysis to determine the presence of cardiac pathology.

One recently developed method to measure blood volume and intracardial flow is through micro single positron emission computed tomography (SPECT) imaging. This method may also be used to asses microvascular function (Matsunari, 2020). SPECT imaging works in a similar manner to PET imaging by injection of radioactive tracer into the blood and measuring its activity and uptake (Chatziioannou, 2005).

The fact that female *pdgfb*$^{ret/+}$ mice appear to develop structural and functional changes in my study is interesting as typically these mice have been used as a control group in some published studies investigating the *pdgfb*^{ret} mutation. However, one study showed that *pdgfb*$^{ret/+}$ mice have a reduced pericyte number compare to *pdgfb*$^{+/+}$ mice, although this did not affect the brain vascular function (Mäe *et al.*, 2021). Therefore, it is unclear whether *pdgfb*$^{ret/+}$ mice are comparable with *pdgfb*$^{+/+}$ littermates or may show some differences to blood vessel structure which depending on the vessel location, may impact vascular function. My data suggest that female *pdgfb*$^{ret/+}$ mice develop differently from their male *pdgfb*$^{ret/+}$ counterparts and exhibit some structural changes to the left ventricle at different stages of development.

Male and female *pdgfb*$^{ret/ret}$ mice have altered cardiac structure which is resolved in aging.

Increase in LV mass is associated with cardiac hypertrophy and alongside dilation and abnormal left ventricular geometry are indicators of high risk of cardiovascular event. Numerous studies have shown that sex can play in the onset of cardiovascular conditions with men typically showing symptoms of cardiovascular disease at an earlier age than women (Regitz-Zagrosek and Seeland, 2011). For example, aortic valve disease can lead to eccentric hypertrophy in humans with females having higher short- and long-term survival than men (Chodick et al, 2017). One suggestion is that differences in hormonal profile between male and female mice may influence the cardiac structure in *pdgfb*$^{ret/ret}$ mice. Signalling between oestrogen and its receptors have been shown to be cardioprotective and inhibit cardiac hypertrophy (Pedram et al, 2008). Indeed, many observational studies have highlighted that pre-menopausal woman are protected from CVD due to the fact they develop it later and as previously mentioned post-menopausal women may have a worse short-term prognosis than similarly aged men.

To determine whether the observed changes to cardiac structure would later cause a deterioration in cardiac function and contractility and a pathological phenotype, we performed subsequent scans and analysis of cardiac function at 6, 9 and 12 months. At 6 months, no differences in terms of LVEDA and other structural parameters were observed in male *pdgfb*$^{ret/ret}$ mice when compared to their *pdgfb*$^{+/+}$ and *pdgfb*$^{ret/+}$ counterparts. Female *pdgfb*$^{ret/ret}$ mice displayed a greater LV mass than *pdgfb*$^{+/+}$ littermates as calculated from EKV images but no further changes to structural parameters were observed at this time point. This data suggests that the changes to left ventricular structure observed at 3 months of age are transient and may suggest that male and female *pdgfb*$^{ret/ret}$ mice may be phenotypically different at 6 months of age. However, measurement of LV mass alone from EKV images is not enough to indicate the presentence of cardiac hypertrophy to confirm this, measurement of cardiomyocyte cross sectional area should be performed to understand what is occurring at the cellular level.

Since hormonal changes in females are expected to be seen around 7-9 months of age (Brinton, 2012), we sought to examine both males and females at both 9 and 12 months. We found no difference between LV mass between any genotype in 9-month-old mice of either sex, although female *pdgfb*$^{ret/ret}$ mice had an increase in LVEDA when compared with *pdgfb*$^{+/+}$ littermates. This data highlights subtle differences in development between male and female *pdgfb*$^{ret/ret}$ mice. One hypothesis may be that these changes occur in relation to changes in their hormonal profile. Both mice and rats reach sexual maturity between 3 and 6 months of age and females reach the equivalent of human perimenopause by around 9 months of age where the ovaries begin to reduce production of oestrogen (Brinton, 2012). This may account for the endocardial dilatation seen at 9 months of age in female *pdgfb*$^{ret/ret}$ mice as oestrogen levels may be reduced resulting in the presence of a dilatory phenotype previously observed at 3 months. Furthermore, oestrogen and PDGFB signalling are molecularly intertwined with many studies highlighting the vasculo-protective effects. In rat VSMCs, the most common oestrogen form,17β-oestradiol (E2), was shown to attenuate PDGFB mediated proliferation and cell migration (Kappert *et al.*, 2006). Similarly, E2 treatment also inhibited PDGFB production from porcine endothelial cells in a dose dependent manner and enhanced pericyte: endothelial cell capacity to form

vascular networks *in vitro* (Glinskii *et al.*, 2013). However, the hormonal profile of mice was not tested in our study but should be performed in the future.

Moreover, data from 12-month ultrasound scans reveal no difference in terms of structure and function between males and females of any genotypes, further suggesting that the subtle changes in female *pdgfb*$^{ret/ret}$ mice observed may only be transient. These data do not indicate a pathological phenotype but would rather be physiological or perhaps compensatory adaptations put in place due to the *pdgfb*^{ret} mutation. Despite some differences being observed in cardiac structure in aging at 6 and 9 months old, female *pdgfb*$^{ret/ret}$ mice show no difference to functional parameters at 12 months of age. By this time, female *pdgfb*$^{ret/ret}$ mice exhibit a similar phenotype as their male counterparts. This suggest that oestrogen levels or changes to oestrogen concentration after 9 months of age may play a key role in the manifestation of the cardiovascular phenotype in *pdgfb*$^{ret/ret}$ mice. This also suggest that male *pdgfb*$^{ret/ret}$ mice may be protected through unknown mechanisms, from the development of any adverse cardiac pathology or that changes to left ventricular structure are compensatory in nature. Interestingly, endothelial specific PDGFB ablation in mice produces similar changes to cardiac structure during late embryonic development which also dissipate by 12 months (Bjarnegård *et al.*, 2004). This fact combined by the phenotype observed by *pdgfb*$^{ret/ret}$ mice may indicate that PDGFB released by endothelial cells during development is a key factor in ensuring the heart develops properly but compensatory physiological changes to attenuate these effects may occur during adulthood.

Male and female *pdgfb*^{ret} mutant mice exhibit differential structural and functional development of the heart over 12 months

I then examined changes to cardiac structure and function over time. Compared with initial 3-month measurements no significant changes to LV mass were observed in either male or female mice at any other time point. This further supports the idea that male and female *pdgfb*$^{ret/ret}$ mice do not develop a hypertrophic phenotype, but this should be confirmed with histological analysis of the left ventricle. Indeed, heart mass was not shown to significantly differ between *pdgfb*$^{+/+}$, *pdgfb*$^{ret/+}$ or *pdgfb*$^{ret/ret}$ mice in either the male or female cohort at 12 months of age. Interestingly I also saw that over

time there was no difference in LVEDA between 3 months and any other time point for male and female mice. I also observed that there was no difference in CO over time for *pdgfb*$^{ret/+}$ and *pdgfb*$^{ret/ret}$ mice. However, with age there was a steady increase in CO in male *pdgfb*$^{+/+}$ mice from 3 months to 12 months. I did not observe same change in the female cohort. This may be partly accounted for by the fact that male *pdgfb*$^{ret/ret}$ mice have stunted growth and were significantly smaller at 12 months than *pdgfb*$^{+/+}$ and *pdgfb*$^{ret/+}$ mice and CO is known to positively correlate with body mass and fat free mass (de Simone *et al.*, 2005). However, I did not observe this in female *pdgfb*$^{ret/ret}$ mice. It has been previously reported that in resting adult blood vessels PDGFB expression in endothelial cells is low but may increase in diseased vessels (Raines, 2004). In humans, the amount of circulating growth factors including PDGFB depends upon sex and age. One study showed that males have a higher level of PDGF and other growth factors in their platelet rich plasma than females (Xiong *et al.*, 2017). Another study had contradictory findings with females having higher levels of PDGFB and other factors in plasma than males. They also found that younger individuals had higher concentrations of both PDGFB and PDGFAB in their plasma than older individuals (Evanson *et al.*, 2014). Therefore, differences in PDGFB levels in aging male and female *pdgfb*$^{ret/ret}$ mice could account for some of the phenotypic differences I observed.

Future Work

Due to the small numbers in our study future investigations should be performed in a greater number of *pdgfb*$^{ret/ret}$ mice if breeding allows. In the study I examined cardiac structure and function of *pdgfb*^{ret} mutant mice until 12 months of age, however, perhaps by studying these mice over a greater time course beyond 12 months of age, they develop a more pronounced cardiac phenotype or signs of cardiac pathology. As previously stated, CVDs typically affect the elderly population but can begin to manifest in middle aged individuals. By 12 months of age, no obvious signs of cardiac pathology were observed. In future studies longevity could be investigated at 18 and 24 months or perhaps longer to determine the onset of any cardiac pathology. C57Bl/6 wild-type mice develop increased diastolic dysfunction and left ventricular hypertrophy by 35 months of age (Dai and Rabinovitch, 2009). However, whether *pdgfb*$^{ret/ret}$ mice

develop a pathological hypertrophic phenotype in advanced aging is unknown. The fact that the early dilatory like changes to left ventricular structure are ameliorated by 12 months of age may also suggest that these mice are protected in some way for the development of an adverse cardiac pathology. Another recent study has shown that *ldlr*$^{-/-}$*pdgfb*$^{ret/ret}$ mice fed a high cholesterol diet appear to be protected in the setting of atherosclerosis due to the development of stable rather than unstable atherosclerotic plaques (Tillie *et al.*, 2021). In my study, I have demonstrated the effect of the *pdgfb*^{ret} mutation on cardiac structure and function. However, the molecular basis for these physiological changes is not understood. In future investigations it could be important to analyse these mice at the molecular level to better understand the underlying processes involved in transient changes to cardiac structure and function at 3 months of age and what processes lead to the amelioration of these changes with aging. To evaluate this question further, I would perform RNA sequencing on the hearts of both male and female *pdgfb*$^{+/+}$ and pdgfb$^{ret/ret}$ mice at 3 months of age when cardiac changes are most pronounced and 12 months of age when cardiac function is unchanged when compared to *pdgfb*$^{+/+}$ mice. This analysis may also reveal differential regulation of molecular pathways in male and female mice. This may reveal changes to other molecules, which may inhibit further cardiac dilation or any pathways which regulate changes to left ventricular structure. Molecular analysis may also reveal novel molecules which could be targeted by pharmacological agents in the setting of human CVD to inhibit the onset of cardiac hypertrophy or dilatation. Over the course of the study, male and female mice displayed differences in the cardiac phenotype exhibited with differences in left ventricular mass and LVEDA observed at 6 and 9 months of age in male and female *pdgfb*$^{ret/ret}$ mice. These differences may in part be due to in E2 signalling which has been described to regulate the signalling of PDGFB, PDGFA and other growth factors. Alongside the previously proposed molecular analysis of the hearts of *pdgfb*$^{ret/ret}$ male and female mice, it would be important to measure oestrogen blood concentration. In females, oestrogen levels can vary significantly due to changes in the oestrous cycle. Furthermore, around 9 months of age, there is a drop in oestrogen levels in female mice (Brinton, 2012). To investigate this further, I would like to perform genetic and molecular analysis of male and female *pdgfb*$^{ret/ret}$ mice specifically to check the expression of oestrogen and androgen receptors in the heart and vasculature in both endothelial cells and perivascular cells which may vary between male and female *pdgfb*$^{+/+}$ and *pdgfb*$^{ret/ret}$ mutant mice. A reduced oestrogen

receptor expression was found in vessels from post-menopausal females compared with pre-menopausal women and androgen receptor expression is expected to be reduced with falling testosterone expression in aging males (Connelly *et al.*, 2022). Therefore, changes not only to hormone levels but also their receptor expression may be a factor involved in regulating the cardiac phenotype of *pdgfb*$^{ret/ret}$ mice.

Conclusion

In conclusion, left ventricular dilatation was observed at 3 months of age in *pdgfb*$^{ret/ret}$ mice with male and female mice. These changes appear to be transient and are ameliorated by 12 months of age with male and female mice exhibiting no phenotypic differences at this time point. These results also suggest that the *pdgfb*^{ret} mutation does not lead to an adverse cardiac phenotype by 12 months of age in male or female mice.

Chapter 5: The effect of the *Pdgfb*^{ret} mutation on Cardiac Strain

Introduction

In chapter 4, I characterised the effects of the *pdgfb*^{ret} mutation on cardiac structure and function. Using 2D echocardiography and subsequent analysis of EKV and M-mode images, I observed that changes in cardiac structure were more pronounced at 3 months of age in *pdgfb*$^{ret/ret}$ mice and appeared to dissipate at later time points. By 12 months of age no differences were observed between genotypes indicating that the differences observed between earlier time points do not progress and lead to cardiac dysfunction at least by 12 months of age.

Speckle tracking echocardiography (STE) has been utilised both pre-clinically and in patients for early detection of cardiac dysfunction (Geyer *et al.*, 2010). One meta-analysis of 2597 subjects found that "normal" global longitudinal strain values varied between -15.9 to -22.1%, circumferential strain ranged from -20.9 to -27.8% and global radial strain ranged from 35.1 to 59% (Yingchoncharoen *et al.*, 2013). However, due to a number of variables, these values may differ and as such a value of around -20% for global longitudinal strain may be expected in healthy individuals (Lang *et al.*, 2015). In humans, STE has been used to diagnose and evaluate a range of pathological conditions such as left ventricular hypertrophy, aortic stenosis and ischaemic heart disease (Collier et al, 2017). In pathological conditions typically these values may be reduced as contractility of the left ventricle is impaired. STE can also be utilised to determine whether the treatments for such conditions are working and improving cardiac function. In the setting of cardiac injury STE has been found to have a major role in predicting patient prognosis post-MI and the development of heart failure (Tomoaia *et al.*, 2019). STE also can be used to define the extent of scar formation and to identify the presence of viable myocardial tissue (Tarascio *et al.*, 2017). One benefit of strain imaging is that it can be used in the accurately assess diastolic function which can prove to be difficult in heart failure patients with preserved ejection fraction and normal systolic function using echocardiography modalities (Choudhury *et al.*, 2017).

STE has been utilised to evaluate cardiac function and myocardial strain in several pre-clinical studies in rodent models of CVD. Induction of pressure overload through

aortic constriction saw a reduction in global longitudinal strain one week post-surgery and dyssynchrony of the heart after 7 weeks (Bauer *et al.*, 2013). Interestingly, changes to global longitudinal strain due to aortic constriction preceded any differences observed in fractional shortening (Bauer *et al.*, 2013). Similarly, in a mouse model of type 1 diabetes, changes to myocardial strain and stress were observed at 1 week post-diabetes onset, whereas, changes in functional parameters measured using conventional 2D echocardiography were not detected until 6 weeks post-diabetes onset (Shepherd *et al.*, 2016). STE was also utilised to illustrate the cardio-protective effects of APPL1 (an insulin and adiponectin mediator) in mice fed on high fat diet (Park *et al.*, 2013).

More recently, STE has also been used to study cardiovascular aging in rodents. De Lucia and colleagues evaluated aging in male C57BL/6 mice over the course between 6 and 20 months. (De Lucia *et al.*, 2019). They observed that segmental strain deteriorated with age and found STE detected changes to systolic and diastolic function at a younger age than conventional echocardiography methods (De Lucia *et al.*, 2019). STE has also recently been used to evaluate cardiac function relating to age dependent remodelling of the extracellular matrix (Grilo *et al.*, 2020).

To detect early cardiac changes caused by the *pdgfb*^{ret} mutation, I utilised STE to measure myocardial strain and stress in aging *pdgfb*$^{+/+}$, *pdgfb*$^{ret/+}$ and *pdgfb*$^{ret/ret}$ mice.

Hypothesis

Early changes in cardiac structure and function lead to increased myocardial strain in aging *pdgfb*^{ret} mutant mice

Aims

1. Identify any differences in cardiac function by STE in aging between *pdgfb*$^{+/+}$, *pdgfb*$^{ret/+}$ and *pdgfb*$^{ret/ret}$ mice.
2. Assess changes in myocardial stress, deformation, and motion, during aging.

Study Design

In this study STE was performed on combined groups of male and female *pdgfb*$^{+/+}$, *pdgfb*$^{ret/+}$ and *pdgfb*$^{ret/ret}$ mice at 6, 9 and 12 months of age (Figure 5.1, Table 5.1). Strain analysis of B-mode images was performed, and structural and functional cardiac measurements were acquired. Further measurements relating to global and segmental myocardial stress and strain were also acquired using VevoLab software. Longitudinal strain refers to lengthening and shortening of the left ventricular wall and radial strain indicates the forces of systolic contraction. Displacement and velocity reflect myocardial motion and may indicate the passive movement of the myocardium during the cardiac cycle but may also highlight impaired ventricular motion due to the presence of cardiovascular disease. The reverse strain mode also allowed analysis of diastolic dysfunction.

Table 5. 1: Number of mice used in STE experiments.

Genotype	Number of mice scanned		
	Age		
	6 months	9 months	12 months
pdgfb$^{+/+}$	8	8	8
pdgfb$^{ret/+}$	5	4	4
pdgfb$^{ret/ret}$	4	3	3

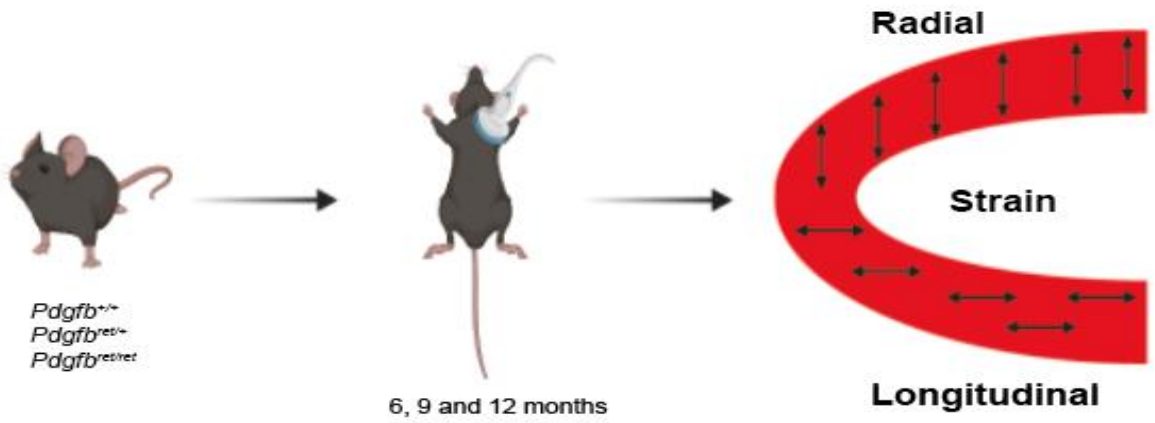

Figure 5. 1: Myocardial strain imaging of *pdgfb*^{ret} mutant mice.

Pdgfb$^{+/+}$, *pdgfb*$^{ret/+}$ and *pdgfb*$^{ret/ret}$ mice were scanned using cardiac ultrasound and PSLAX B-mode images were acquired. Analysis of radial and longitudinal myocardial strain parameters was performed at 6, 9 and 12 months of age.

Results

Assessment of cardiac parameters reveals left ventricular dilation in *pdgfb*$^{ret/ret}$ mice at 6 months of age.

From STE, peak global longitudinal strain (GLS) a measurement of the average strain across the endocardial wall and an indicator of systolic function was obtained. No differences were observed in GLS between *pdgfb*$^{+/+}$, *pdgfb*$^{ret/+}$ and *pdgfb*$^{ret/ret}$ at 6, 9 or 12 months (Figure 5.2A) suggesting that the overall systolic function is maintained in aging. Ejection fraction (EF_{Strain}) as calculated by STE was also unchanged between groups at any time point (Figure 5.2). The EF to GLS ratio, which has been used clinically as an indicator of myocardial thickening, did not differ between groups at any time point (Figure 5.2C, $p>0.05$) (Pagourelias *et al.*, 2017). At 6 months of age, both EDV (Figure 5.2D) and ESV (Figure 5.2E) were significantly greater in *pdgfb*$^{ret/ret}$ than *pdgfb*$^{+/+}$ and *pdgfb*$^{ret/+}$ littermates ($p<0.05$), however, no significant differences in these structural parameters were detected beyond this time point at 9 and 12 months of age.

The end diastolic left ventricular mass (EDLVM, Figure 5.2F) and the end systolic left ventricular mass (ESLVM, Figure 5.2G) were similar at 6, 9 and 12 months. Cardiac output (CO_{Strain}) was significantly higher in *pdgfb*$^{ret/ret}$ mice than *pdgfb*$^{+/+}$ ($p<0.05$) and *pdgfb*$^{ret/+}$ mice ($p<0.001$) at 6 months of age (Figure 5.2G). In 9-month-old mice, CO_{Strain} was significantly higher in *pdgfb*$^{ret/ret}$ than in *pdgfb*$^{+/+}$ mutants ($p<0.05$), whereas no difference was observed between *pdgfb*$^{ret/+}$ mice and any other genotype. CO_{Strain} was not significantly different between any genotype at 12 months ($p>0.05$). Stroke volume (SV_{Strain}) was significantly higher in 6 months old *pdgfb*$^{ret/ret}$ than *pdgfb*$^{+/+}$ mice at similar age (Figure 5.2I, $p<0.05$). No difference was observed in SV_{Strain} at any other time point between genotypes (Figure 5.2I, $p>0.05$).

Taken together this data shows that *pdgfb*$^{ret/ret}$ mice have changes to left ventricular structure at 6 months of age which are transient and do not persist at 12 months of age. Although the cohort of mice examined is different, this mirrors results previously shown in Chapter 4.

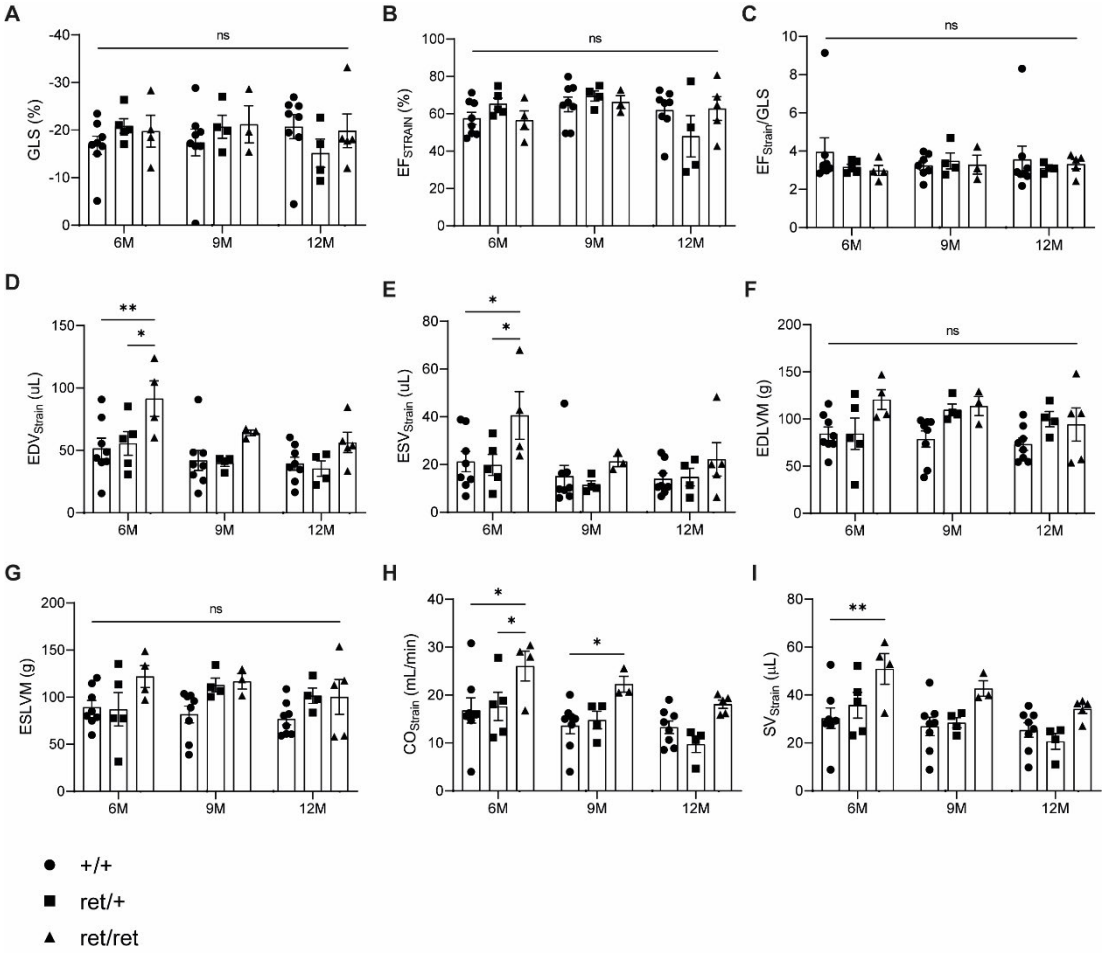

Figure 5. 2: Assessment of cardiac parameters using STE confirms left ventricular dilation in *pdgfb*$^{ret/ret}$ mice.

Cardiac parameters were calculated at 6-, 9- and 12-months using speckle tracking echocardiography (STE) in *pdgfb*$^{+/+}$ (+/+, circles), *pdgfb*$^{ret/+}$ (ret/+, squares), and *pdgfb*$^{ret/ret}$ (ret/ret, triangles) mice. Functional contractile measurements systolic global longitudinal strain (GLS, **A**), Ejection fraction (EF$_{Strain}$, **B**) were calculated by STE strain Vevo software. EF$_{Strain}$/GLS ratio (**C**). Cardiac structural parameters; end diastolic volume (EDV$_{Strain,}$ **D**); end systolic volume (ESV$_{Strain}$, **E**); end-diastolic left ventricular mass (EDLVM, **G**) and end systolic left ventricular mass (ESLVM, **H**) were determined. Functional parameters cardiac output (CO$_{Strain}$) and stroke volume (SV$_{Strain}$) were evaluated. Images were analysed using VevoLab 3100 software. Data shown as mean±SEM. Two-way ANOVA with Tukey's multiple comparisons *p<0.05, **p<0.001 ns=not significant. n=3-8/group.

No difference in radial or longitudinal strain on the posterior or anterior wall was detected in *pdgfb*^{ret} mutant mice.

I next performed analysis to evaluate longitudinal and radial strain on the posterior and anterior endocardial wall as well as on the base, mid and apical regions (Figure 5.3A). At 6 months of age, no differences were observed in longitudinal (Figure 5.3B) or radial strain (Figure 5.3E) on either the anterior or posterior wall between *pdgfb*$^{+/+}$, *pdgfb*$^{ret/+}$ and *pdgfb*$^{ret/ret}$ mice ($p>0.05$). Similarly, no differences in longitudinal strain or radial were observed at 9 months (Figure 5.3C, F) or 12 months of age between groups (Figure 5.3D, G).

No difference in radial or longitudinal strain on the basal, mid or apical endocardial wall was detected *in pdgfb*^{ret} mutant mice.

Longitudinal and radial strain across the basal, mid and apical segments of the endocardial wall was then manually calculated. No differences were observed in longitudinal strain at 6 (Figure 5.3H), 9 (Figure 5.3I) or 12 (Figure 5.3J) months of age between genotypes ($p>0.05$). No differences in radial strain were observed at 6 (Figure 5.3K), 9 (Figure 5.3L) or 12 (Figure 5.3M) months of age ($p>0.05$).

Segmental longitudinal strain or strain rate were similar between groups.

No differences in longitudinal strain were observed across any endocardial segment at 6 (Figure 5.4A), 9 (Figure 5.4C) and 12 (Figure 5.4E) months. Similarly, no difference between genotypes in strain rate across any segment was observed at 6 (Figure 5.4B), 9 (Figure 5.4D) and 12 (Figure 5.4F) months of age.

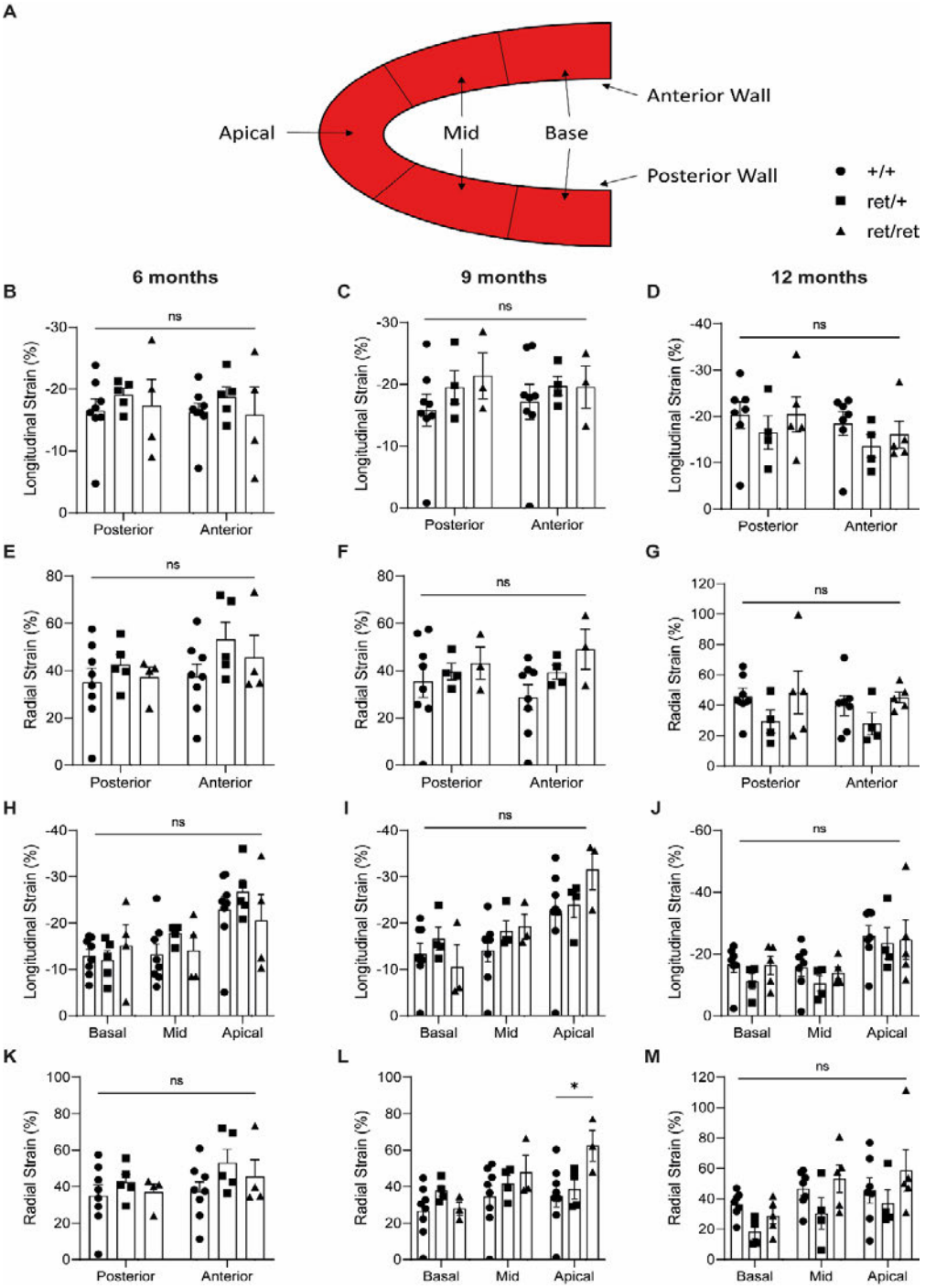

Figure 5. 3: Radial Strain on the apical region of the heart was higher in *pdgfb*$^{ret/ret}$ mice at 9 months of age.

Average myocardial strain across the anterior and posterior wall and in in the apical, middle (mid) and basal (base) segments of the left ventricle (**A**). Longitudinal strain on the posterior and anterior walls of at 6 (**B**), 9 (**C**) and 12 (**D**) months of age in *pdgfb*$^{+/+}$, *pdgfb*$^{ret/+}$ and *pdgfb*$^{ret/ret}$ mice. Radial strain across the anterior and posterior walls at 6 (**E**), 9 (**F**) and 12 (**G**) months of age. Longitudinal strain on base, mid and apical segments of the wall at 6 (**H**), 9 (**I**) and 12 (**J**) months. Radial strain on the base, mid and apical segments at 6 (**K**), 9 (**L**) and 12 (**M**) months. Data shown as mean±SEM. Two-way ANOVA with Tukey's multiple comparisons *p<0.05, ns=not significant. n=3-8/group.

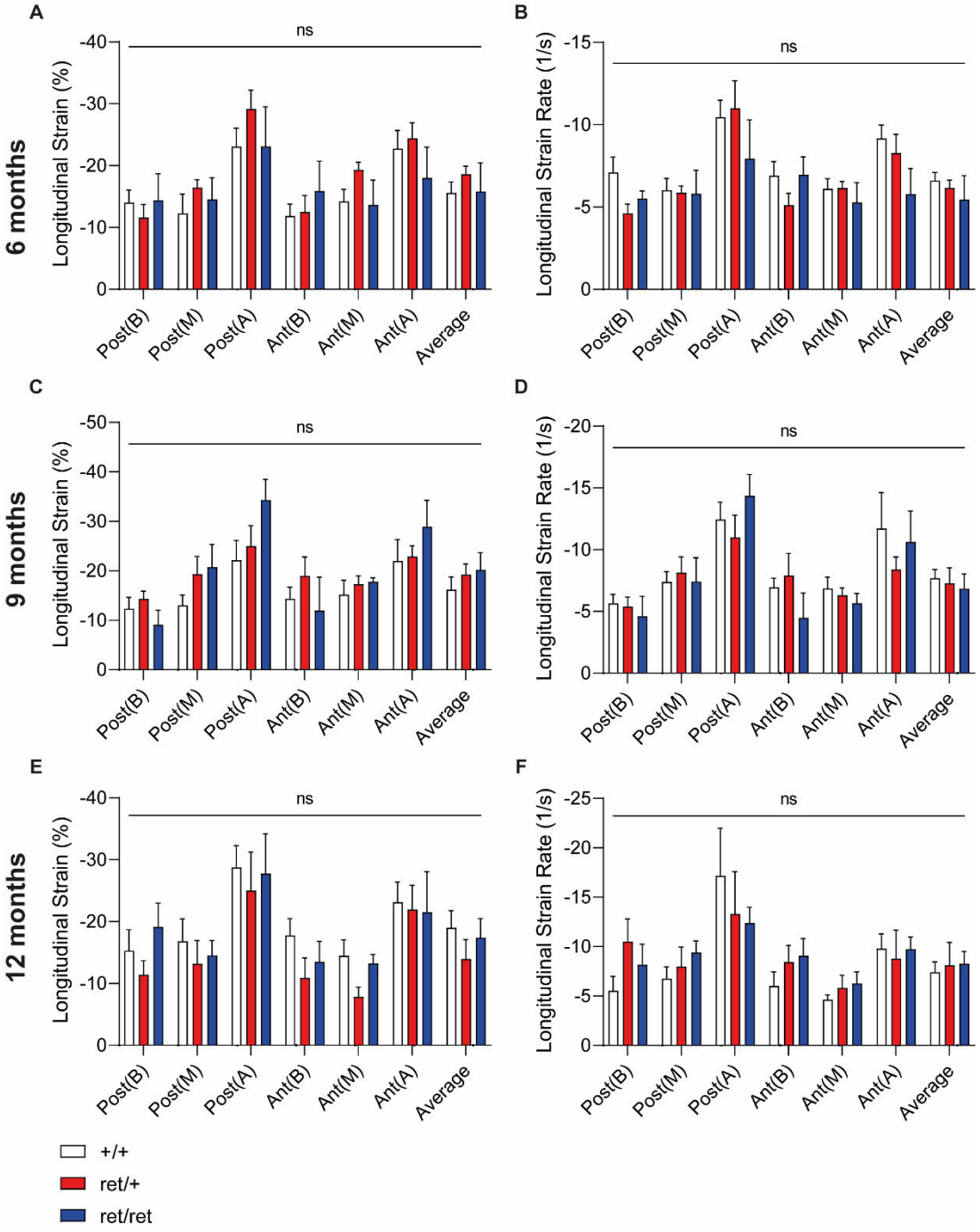

Figure 5.4: Longitudinal strain and strain rate did not change in *pdgfb*$^{ret/ret}$ mice.

Longitudinal strain and strain rate were calculated at 6 (**A**, **B**), 9 (**C**, **D**) and 12 (**E**, **F**) months of age for each segment of the myocardium in *pdgfb*$^{+/+}$ (white bar), *pdgfb*$^{ret/+}$ (red bar) and *pdgfb*$^{ret/ret}$ (blue bar) mice. The myocardium was divided into six segments: the posterior base (Post(B)), posterior mid (Post (M)), posterior apical (Post(A)), anterior base (Ant(B)), anterior mid (Ant(M)) and anterior apical (Ant(A)) segments. The average of all points on the strain and strain rate curves was calculated. Images were analysed using VevoLab 3100 software. Data shown as mean±SEM. Two-way ANOVA with Tukey's multiple comparisons. ns=not significant. n=3-8/group.

Segmental radial strain and strain rate differs between *pdgfb*$^{+/+}$ and *pdgfb*$^{ret/ret}$ mice at 6 and 9 months.

Segmental radial strain and strain rate were evaluated in *pdgfb*$^{+/+}$, *pdgfb*$^{ret/+}$ and *pdgfb*$^{ret/ret}$ mice. At 6 months, no difference in segmental radial strain rate was observed (Figure 5.5A), however, a reduction in Post(M) strain rate was observed between *pdgfb*$^{+/+}$ and *pdgfb*$^{ret/ret}$ mice ($p<0.05$, Figure 5.5B). At 9 months, radial strain in the Post(A) and Ant(A) regions were observed (Figure 5.5C, $p<0.05$). No differences to segmental radial strain rate were observed at 9 months of age (Figure 5.5D). At 12 months, no differences in radial strain (Figure 5.5E) and radial strain rate (Figure 5.5F) were observed between genotypes.

Post(A) segmental time to peak (TTP) strain decreased at 9 months of age in *pdgfb*$^{ret/ret}$ mice.

Segmental Time to peak (TTP) strain as was evaluated in *pdgfb*$^{+/+}$, *pdgfb*$^{ret/+}$ and *pdgfb*$^{ret/ret}$ mice at 6, 9 and 12 months of age. TTP strain can be used as an indicator of dyssnchrony and may be altered in disease settings and in aging. I observed no changes in either segmental longitudinal (Figure 5.6A) or radial (Figure 5.6B) TTP strain at 6 months between groups ($p>0.05$). At 9 months longitudinal TTP strain on the Post(B) region was significantly lower in *pdgfb*$^{ret/ret}$ mice compared with *pdgfb*$^{+/+}$ mice (Figure 5.6C). No difference in segmental radial TTP strain was observed (Figure 5.6B). At 12 months of age neither longitudinal (Figure 5.6E) nor radial (Figure 5.6F) segmental strain was significantly different between groups ($p>0.05$).

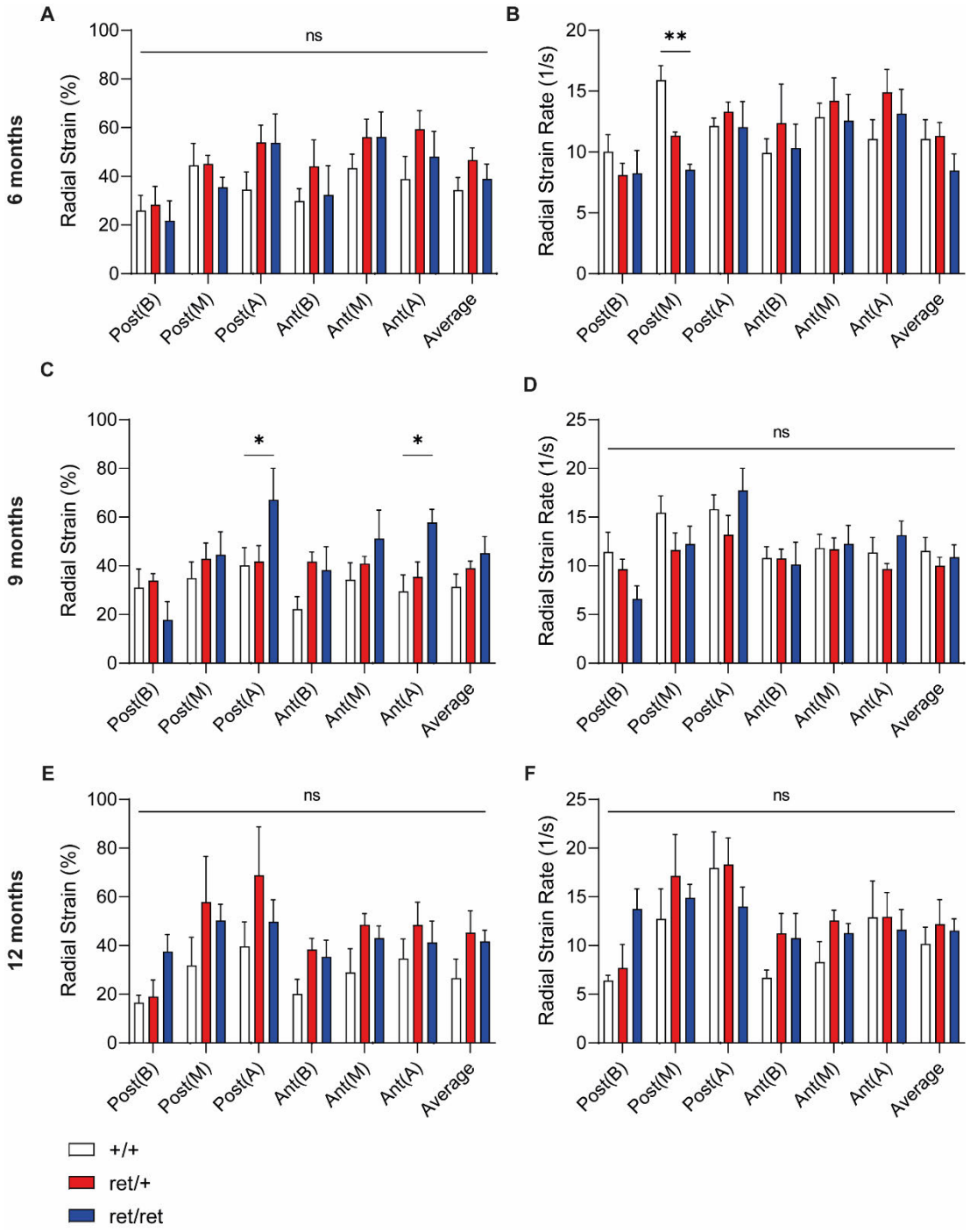

Figure 5.5: In *pdgfb*$^{ret/ret}$ mice radial strain and strain rate was significantly higher in the apical regions of the heart at 9 months of age.

Radial strain and strain rate were calculated at 6 (**A**, **B**), 9 (**C**, **D**) and 12 (**E**, **F**) months of age for each segment of the myocardium in *pdgfb*$^{+/+}$ (white bar), *pdgfb*$^{ret/+}$ (red bar) and *pdgfb*$^{ret/ret}$ (blue bar) mice. The myocardium was divided into six segments: the posterior base (Post(B)), posterior mid (Post (M)), posterior apical (Post(A)), anterior base (Ant(B)), anterior mid (Ant(M)) and anterior apical (Ant(A)) segments. The average of all points on the strain and strain rate curves was calculated. Images were analysed using VevoLab 3100 software. Data shown as mean±SEM. Two-way ANOVA with Tukey's multiple comparisons. *p<0.05 **p<0.01 ns=not significant. n=3-8/group.

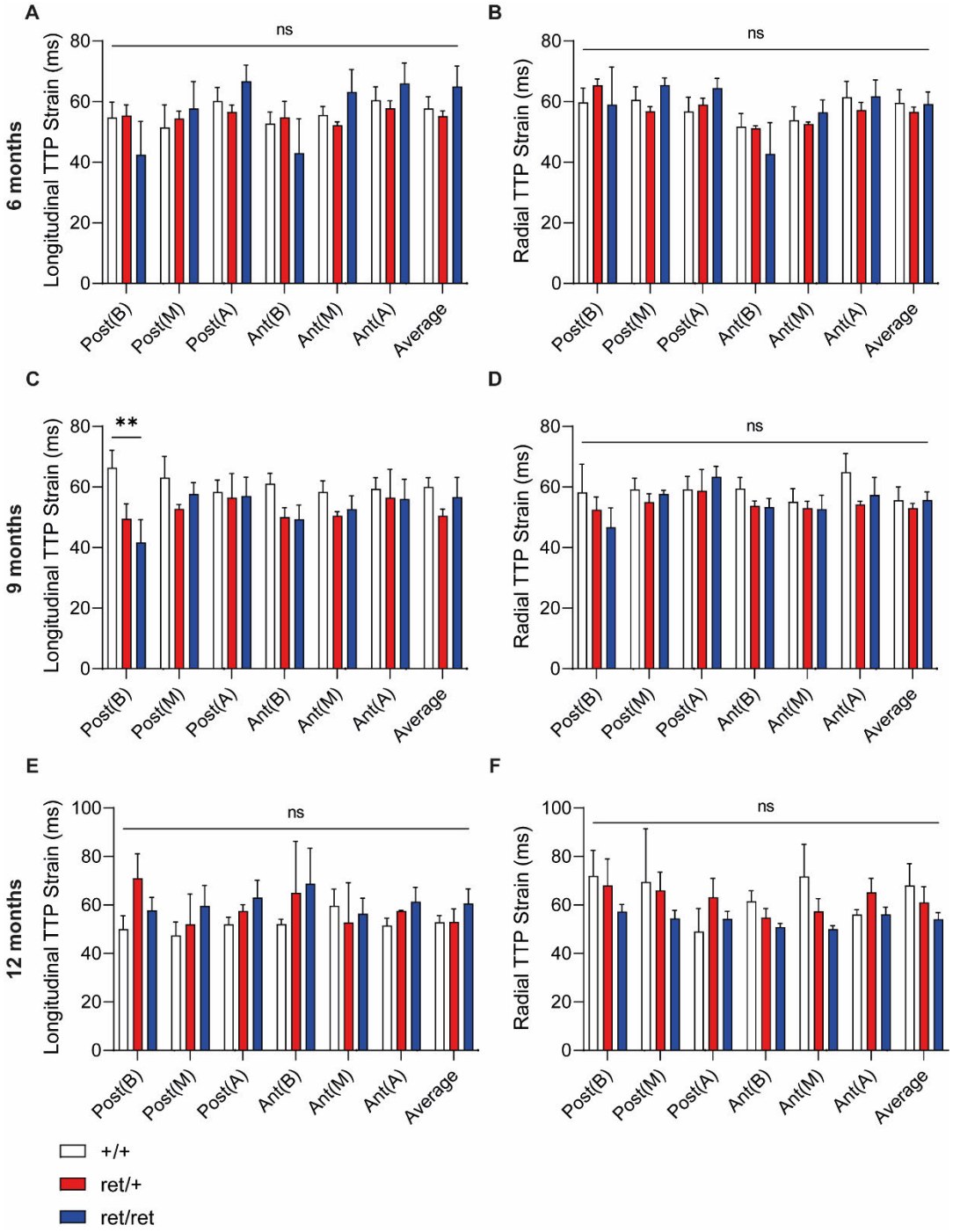

Figure 5.6: Longitudinal time to peak strain was lower on the posterior base segment of the myocardium in 9-month-old *pdgfb*$^{ret/ret}$ mice.

Longitudinal and radial time to peak strain were calculated at 6 (**A**, **B**), 9 (**C**, **D**) and 12 (**E**, **F**) months of age for each segment of the myocardium in *pdgfb*$^{+/+}$ (white bar), *pdgfb*$^{ret/+}$ (red bar) and *pdgfb*$^{ret/ret}$ (blue bar) mice. The myocardium was divided into six segments: the posterior base (Post(B)), posterior mid (Post (M)), posterior apical (Post(A)), anterior base (Ant(B)), anterior mid (Ant(M)) and anterior apical (Ant(A)) segments. The average of all points on the longitudinal and radial TTP strain curves was calculated. Images were analysed using VevoLab 3100 software. Data shown as mean±SEM. Two-way ANOVA with Tukey's multiple comparisons. **p<0.01 ns= not significant n=3-8/group.

Changes to diastolic function were evaluated using the reverse strain function.

Using the reverse strain function on VevoLab software both reverse longitudinal and radial strain could be calculated. Reverse strain can be used to evaluated diastolic function of the left ventricle. At 6 months, no changes in were observed in segmental reverse longitudinal strain (Figure 5.9A) or strain rate (Figure 5.7B, $p>0.05$) between groups. At 9 months, reverse longitudinal strain rate was not significantly altered between groups (Figure 5.7C, $p>0.05$). Reverse longitudinal strain rate on the Post(A) region was significantly greater between *pdgfb*$^{ret/ret}$ mice than both *pdgfb*$^{+/+}$ and *pdgfb*$^{ret/+}$ mice ($p<0.05$, $p<0.001$, Figure 5.7D). At 12 months, neither reverse longitudinal segmental strain (Figure 5.7E) nor strain rate (Figure 5.7F) was changed between groups ($p>0.05$).

Changes to reverse radial strain rate were detected at 9 and 12 months of age.

Reverse segmental radial strain (Figure 5.8A) and strain rate (Figure 5.8B) was unchanged between groups at 6 months of age ($p>0.05$). At 9 months, segmental reverse radial strain was unchanged between groups (Figure 5.8C, ($p>0.05$)). Reverse radial strain rate on the Ant(A) segment was significantly higher in *pdgfb*$^{ret/ret}$ mice than *pdgfb*$^{+/+}$ mice (Figure 5.8D). At 12 months, reverse segmental radial strain was unchanged between groups (Figure 5.8E). Reverse radial strain rate was significantly higher for *pdgfb*$^{+/+}$ mice on the Post(B) region than *pdgfb*$^{ret/+}$ and *pdgfb*$^{ret/ret}$ mice.

No left ventricular dyssnchrony was detected in *pdgfb*$^{ret/ret}$ mice.

Next, I wished to evaluate whether early alterations to cardiac structure and function may cause left ventricular dyssynchrony in *pdgfb*$^{ret/ret}$ mice. I evaluated 4 parameters which are indicators of left ventricular dyssynchrony, mean TTP, maximum opposing wall delay, standard deviation of TTP and standard deviation of TTP divided by the R-R interval. These parameters were evaluated for both longitudinal (Figure 5.9) and radial (Figure 5.10) strain. No difference any of the longitudinal dyssynchrony parameters were observed at 6(Figure 5.9 A-D), 9 (Figure 5.9 E-H) and 12 (Figure 5.9 I-L) months. Similarly, no differences were detected at 6 (Figure 5.10A-D), 9 (Figure 5.10E-H) and 12 (Figure 5.10I-L) months for the evaluation of radial dyssynchrony.

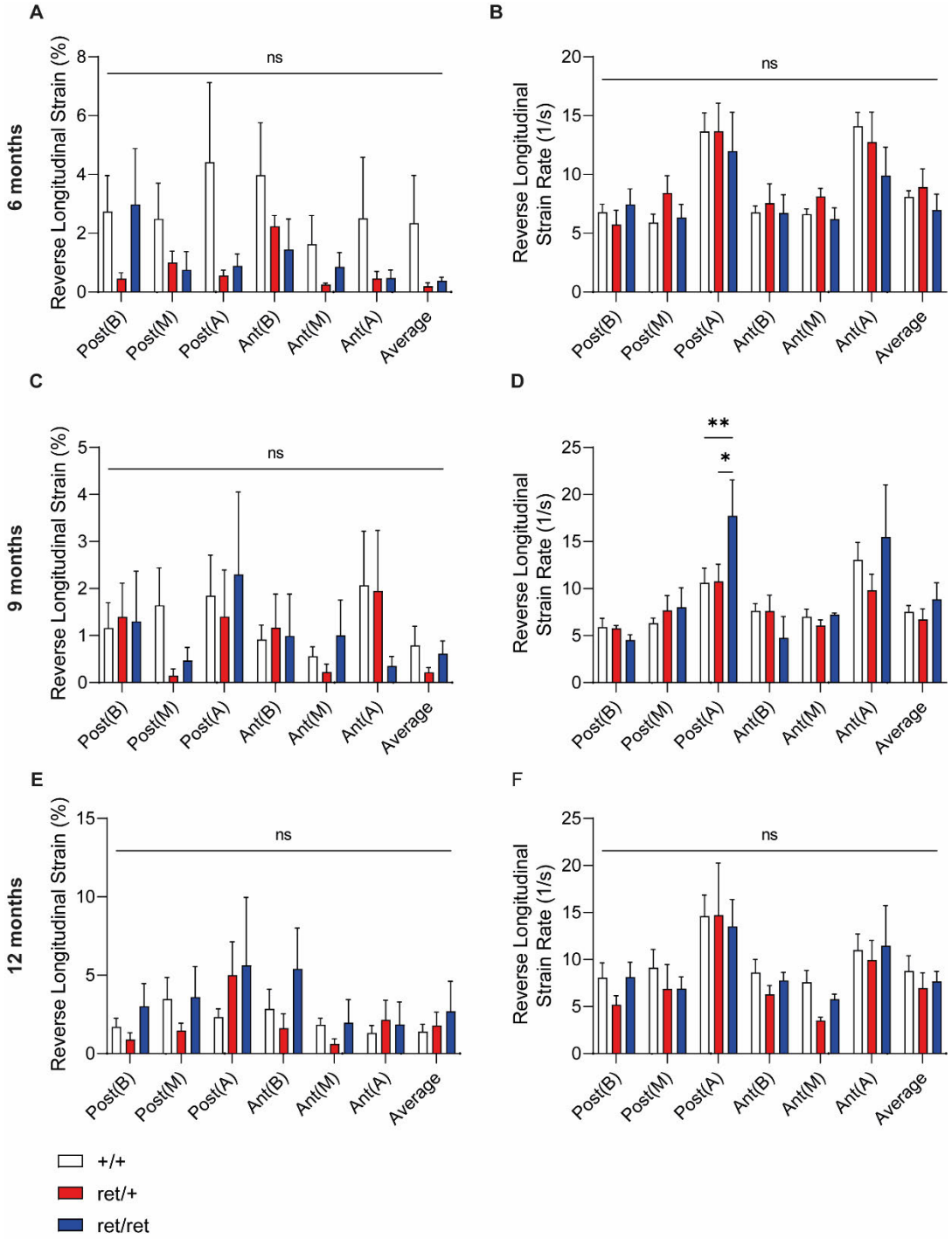

Figure 5.7: Segmental reverse longitudinal strain and strain rate were greater on the posterior apical segment of the myocardium in 9-month-old *pdgfb*$^{ret/ret}$ mice.

Reverse longitudinal strain and strain rate were calculated at 6 (**A**, **B**), 9 (**C**, **D**) and 12 (**E**, **F**) months of age for each segment of the myocardium in *pdgfb*$^{+/+}$ (white bar), *pdgfb*$^{ret/+}$ (red bar) and *pdgfb*$^{ret/ret}$ (blue bar) mice. The myocardium was divided into six segments: the posterior base (Post(B)), posterior mid (Post (M)), posterior apical (Post(A)), anterior base (Ant(B)), anterior mid (Ant(M)) and anterior apical (Ant(A)) segments. The average reverse longitudinal strain and strain rate was also calculated. Images were analysed using VevoLab 3100 software. Data shown as mean±SEM. Two-way ANOVA with Tukey's multiple comparisons. *p<0.05 **p<0.01 ns=not significant. n=3-8/group.

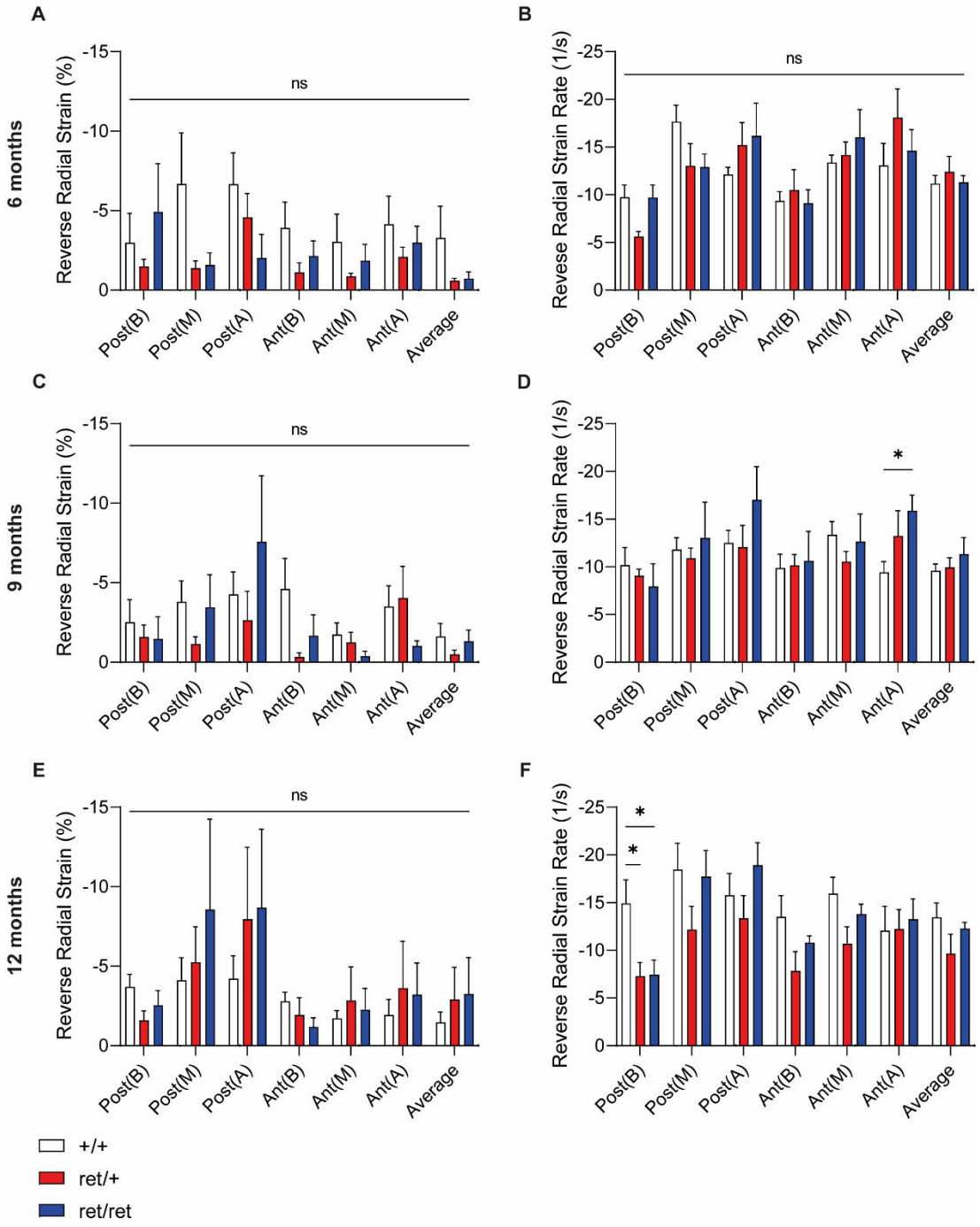

Figure 5.8: Reverse radial strain rate was greater *pdgfb*$^{+/+}$mice than *pdgfb*$^{ret/+}$ and *pdgfb*$^{ret/ret}$ mice at 9 and 12 months of age.

Reverse radial strain and strain rate were calculated at 6 (**A**, **B**), 9 (**C**, **D**) and 12 (**E**, **F**) months of age for each segment of the myocardium in *pdgfb*$^{+/+}$ (white bar), *pdgfb*$^{ret/+}$ (red bar) and *pdgfb*$^{ret/ret}$ (blue bar) mice. The myocardium was divided into six segments: the posterior base (Post(B)), posterior mid (Post (M)), posterior apical (Post(A)), anterior base (Ant(B)), anterior mid (Ant(M)) and anterior apical (Ant(A)) segments. The average reverse radial strain and strain rate were also calculated. Images were analysed using VevoLab 3100 software. Data shown as mean±SEM. Two-way ANOVA with Tukey's multiple comparisons. *p<0.05 ns=not significant. n=3-8/group.

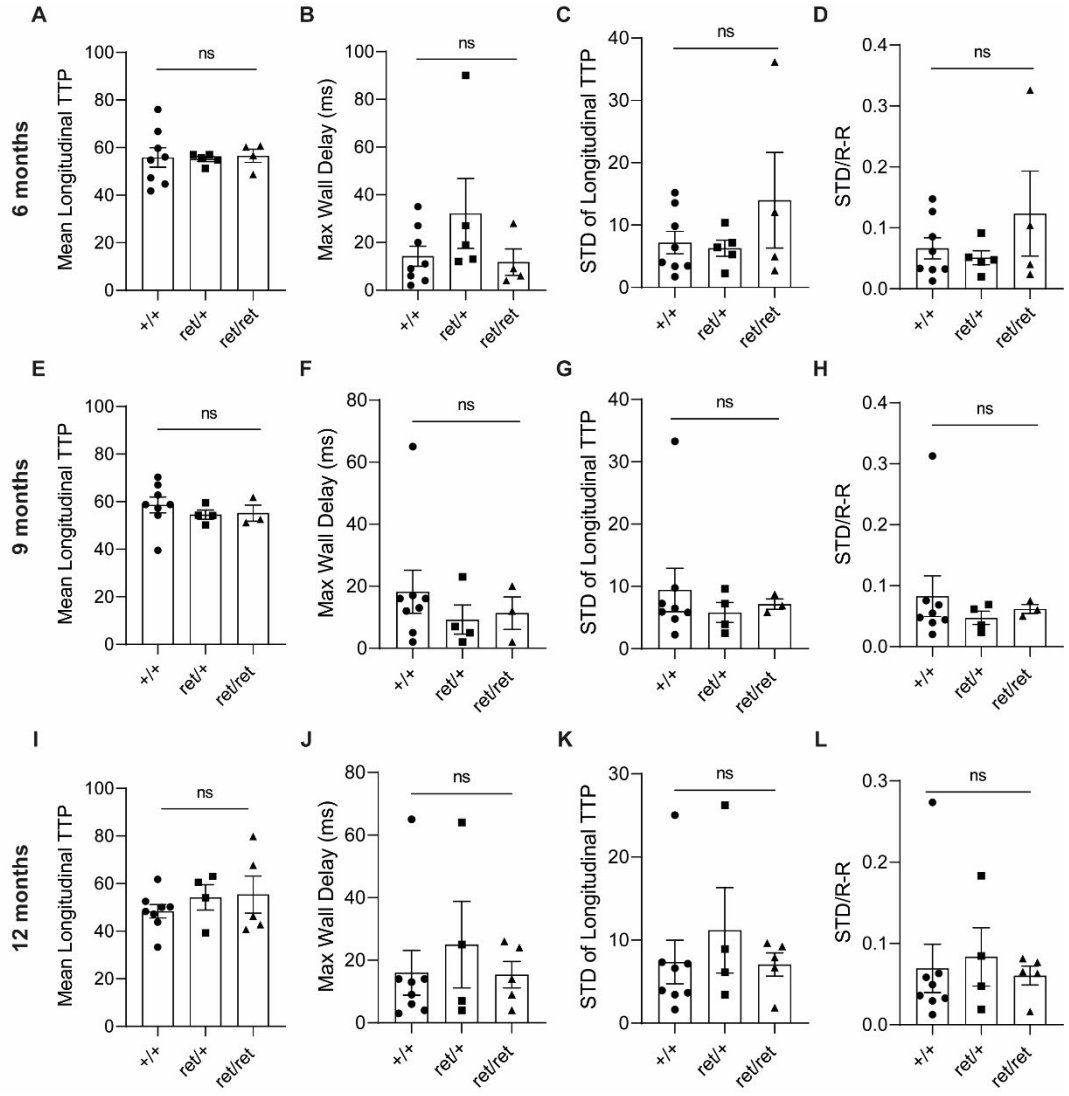

Figure 5.9: Longitudinal dyssynchrony was not detected in *pdgfb*$^{ret/ret}$ mice.

Parameters associated with left ventricular dyssynchrony were determined for *pdgfb*$^{+/+}$ (white bar, circles) *pdgfb*$^{ret/+}$ (red bar squares) and *pdgfb*$^{ret/ret}$ mice (blue bar, triangles) at 6, 9 and 12 months of age. For longitudinal strain, these were the mean longitudinal time to peak (TTP) strain (**A**, **E**, **I**), maximum opposing wall delay (Max Wall Delay, **B**, **F**, **J**), standard deviation (STD) of TTP strain (**C**, **G**, **K**) and the STD of TTP strain/R-R interval (STD/R-R, **D**, **H**, **L**) were determined. Data shown as mean±SEM. Two-way ANOVA with Tukey's multiple comparisons. ns=not significant. n=3-8/group.

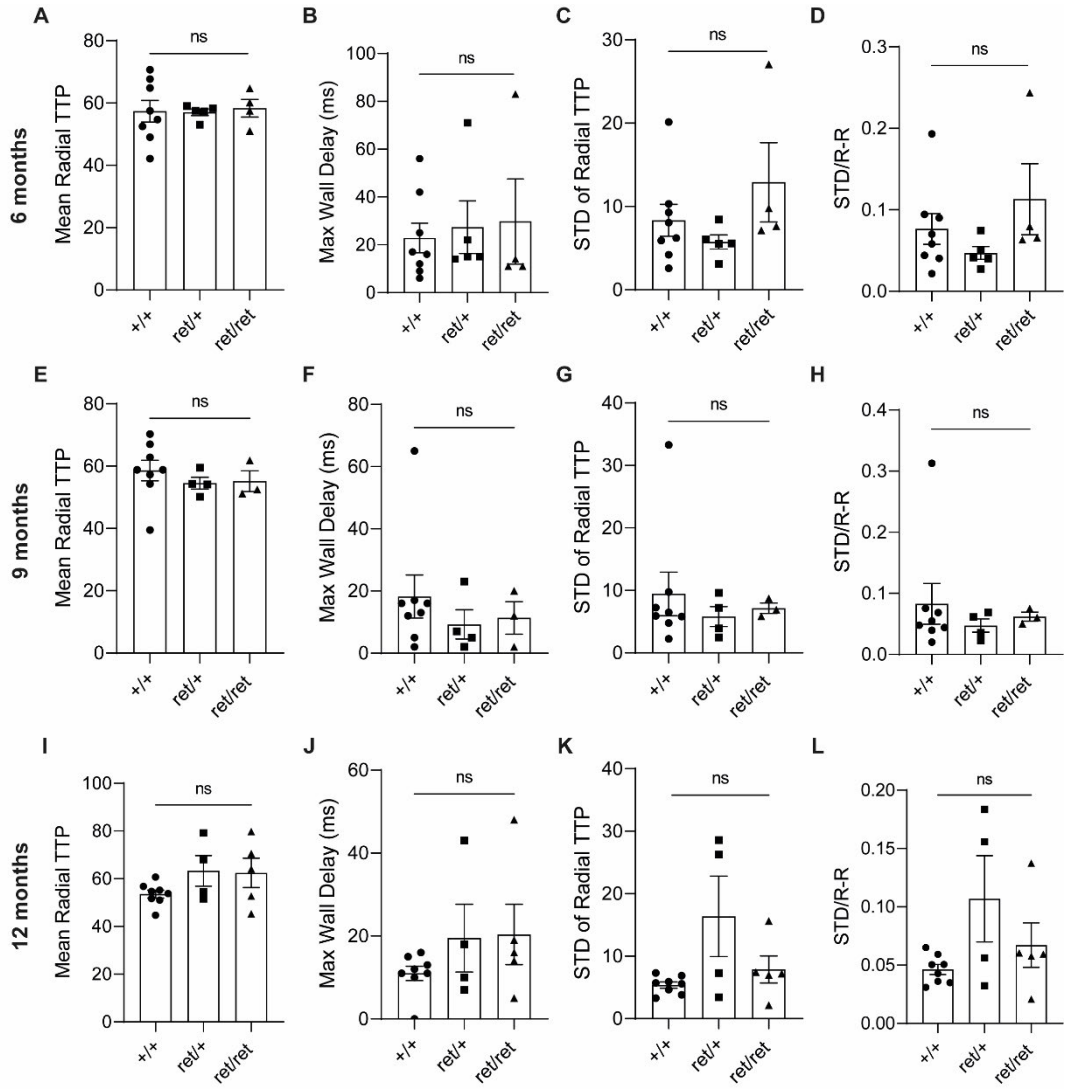

Figure 5.10: Radial dyssynchrony was not detected in *pdgfb*$^{ret/ret}$ mice.

Left ventricular radial dyssynchrony was assessed in *pdgfb*$^{+/+}$ (white bar, circles) *pdgfb*$^{ret/+}$ (red bar squares) and *pdgfb*$^{ret/ret}$ mice (blue bar, triangles) at 6, 9 and 12 months of age. For radial strain, these were the mean radial time to peak (TTP) strain (**A**, **E**, **I**), maximum opposing wall delay (Max Wall Delay, **B**, **F**, **J**), standard deviation (STD) of TTP strain (**C**, **G**,**K**) and the STD of TTP strain/ R-R interval (STD/R-R, D,H,L) were determined. Data shown as mean±SEM. Two-way ANOVA with Tukey's multiple comparisons. ns=not significant. n=3-8/group.

Posterior base radial velocity was increased in *pdgfb*$^{ret/ret}$ mice at 12 months.

Segmental velocity can indicate the movement of the myocardium during the cardiac cycle and changes to segmental velocity may indicate impaired ventricular contraction. I measured radial and longitudinal velocities at 6, 9 and 12 months of age in *pdgfb*$^{+/+}$, *pdgfb*$^{ret/+}$ and *pdgfb*$^{ret/ret}$ mice. At both 6 and 9 months of age, no significant difference in segmental longitudinal (Figure 5.11 A, C) or radial (Figure 5.11 B, D) velocities was observed ($p>0.05$). At 12 months of age no significant difference in segmental longitudinal velocity was observed. Posterior base radial velocity was significantly higher in *pdgfb*$^{ret/ret}$ mice compared with *pdgfb*$^{ret/+}$ mice at 12 months of age ($p<0.05$).

Transient changes to longitudinal and radial displacement were detected in *pdgfb*^{ret} mutant mice at 9 months of age.

Segmental displacement is another indicator of the movement of the myocardium and may change in some pathological conditions. At 6 months, segmental longitudinal (Figure 5.12 A) and radial (Figure 5.12 B) displacement were unchanged between *pdgfb*$^{+/+}$, *pdgfb*$^{ret/+}$ and *pdgfb*$^{ret/ret}$ mice ($p<0.05$). At 9 months of age, longitudinal displacement of the posterior and anterior base was significantly greater in *pdgfb*$^{ret/+}$ mice than *pdgfb*$^{+/+}$ mice (Figure 5.12 C, $p<0.05$). At 9 months of age, radial displacement was greater in the posterior mid and anterior basal segments in *pdgfb*$^{ret/ret}$ mice compared with *pdgfb*$^{+/+}$ mice (Figure 5.12 D, $p<0.05$). at 12 months, no differences in longitudinal (Figure 5.12E) or radial displacement (Figure 5.12F) were observed ($p<0.05$).

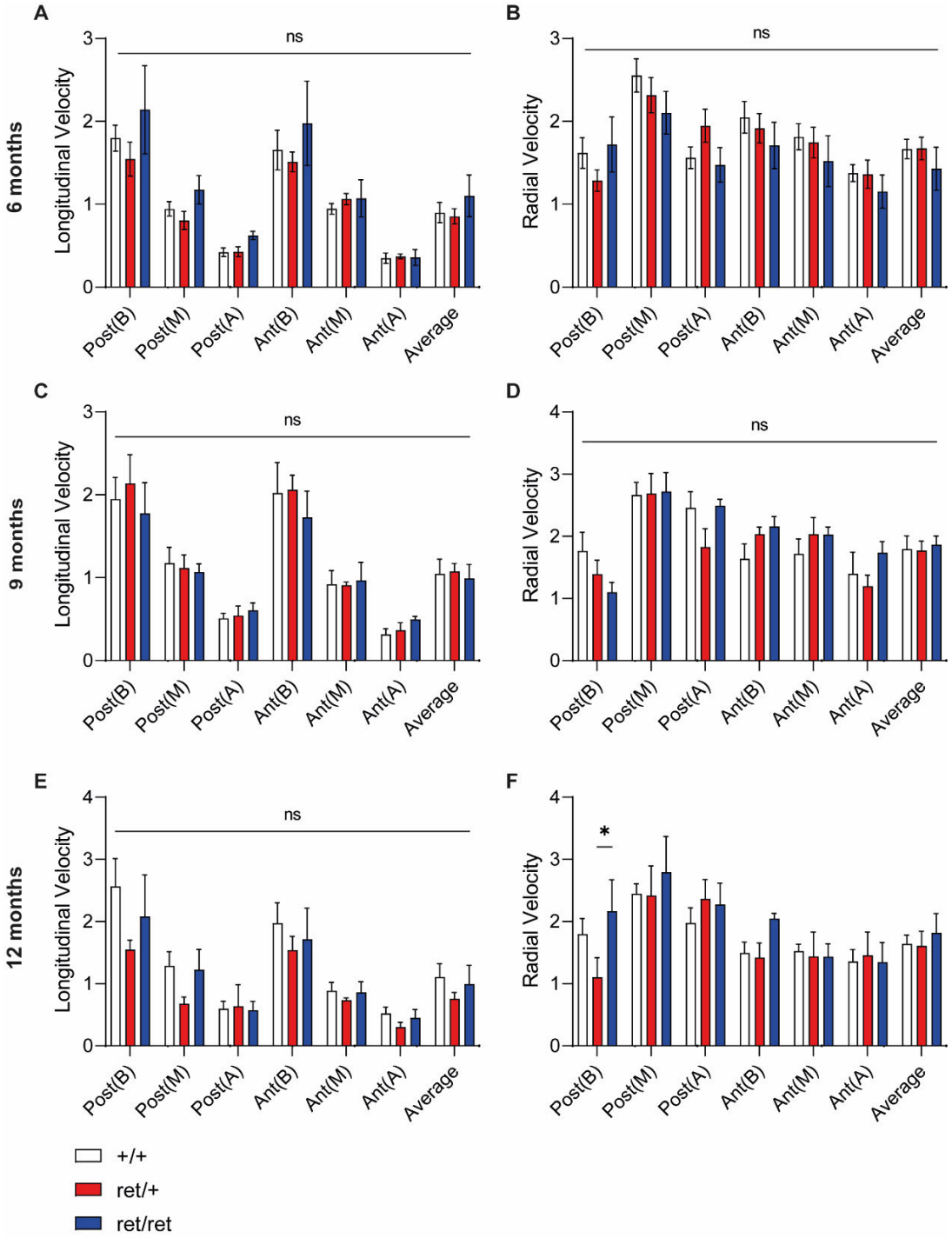

Figure 5. 11: Myocardial segmental velocity was altered in *pdgfb*$^{ret/ret}$ mice at 12 months.

Longitudinal and radial velocities were calculated for 6 (**A**, **B**), 9 (**C**, **D**) and 12 (**E**, **F**) month old *pdgfb*$^{+/+}$ (white bar), *pdgfb*$^{ret/+}$ (red bar) and *pdgfb*$^{ret/ret}$ (blue bar) mice. The myocardium was divided into six segments: the posterior base (Post(B)), posterior mid (Post (M)), posterior apical (Post(A)), anterior base (Ant(B)), anterior mid (Ant(M)) and anterior apical (Ant(A)) segments. The average longitudinal and radial velocities were also calculated. Images were analysed using VevoLab 3100 software. Data shown as mean±SEM. Two-way ANOVA with Tukey's multiple comparisons. *p<0.05 ns=not significant. n=3-8/group.

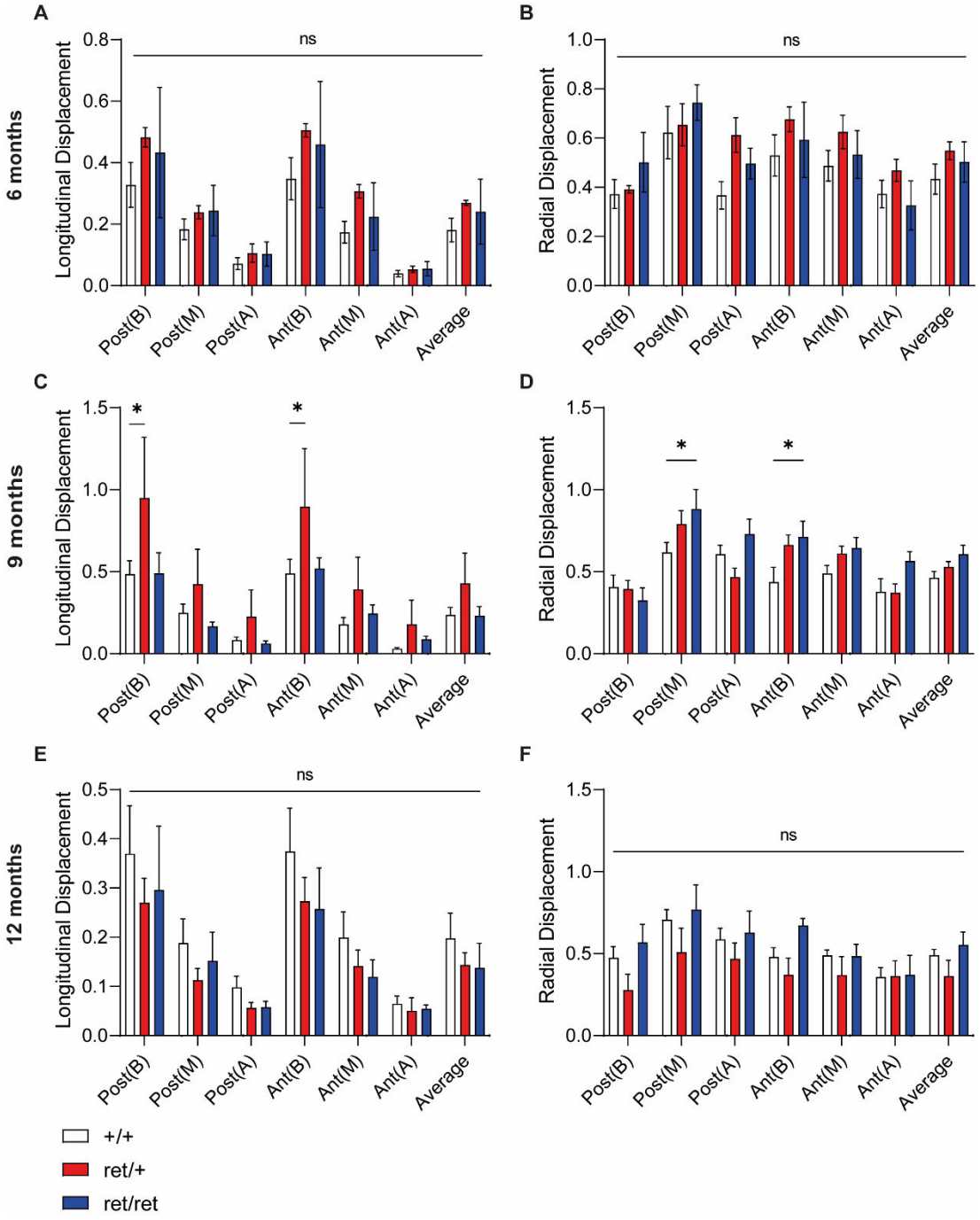

Figure 5.12: Segmental displacement was altered in *pdgfb*^{ret} mutant mice at 9 months.

Longitudinal and radial displacement were calculated for 6 (**A**, **B**), 9 (**C**, **D**) and 12 (**E**, **F**) month old *pdgfb*$^{+/+}$ (white bar), *pdgfb*$^{ret/+}$ (red bar) and *pdgfb*$^{ret/ret}$ (blue bar) mice across six myocardial segments: the posterior base (Post(B)), posterior mid (Post (M)), posterior apical (Post(A)), anterior base (Ant(B)), anterior mid (Ant(M)) and anterior apical (Ant(A)) segments. The average longitudinal and radial displacement were also calculated. Images were analysed using VevoLab 3100 software. Data shown as mean±SEM. Two-way ANOVA with Tukey's multiple comparisons. *p<0.05 ns=not significant. n=3-8/group.

Discussion

This chapter follows on from chapter 4, which evaluated the effects of the *pdgfb*^{ret} mutation on influencing cardiac structure and function. From chapter 4, my results suggest that early changes to cardiac structure and function at 3 months were ameliorated in *pdgfb*$^{ret/ret}$ mice by 12 months of age and no obvious cardiac pathology could be detected. In this chapter I utilised STE to evaluate cardiac structure in function *pdgfb*$^{+/+}$, *pdgfb*$^{ret/+}$ and *pdgfb*$^{ret/ret}$ mice at 6, 9 and 12 months of age. Several studies have shown that STE is superior in terms of early detection of cardiac pathologies and subtle changes to cardiac function when compared to 2D conventional echocardiography. As such, I aimed to further evaluate the cardiac phenotype of *pdgfb*^{ret} mutant mice using this methodology to look for undetected or subtle signs of cardiac pathology. The main finding from our results is that although overall systolic function is maintained over time, we do see changes to segmental and regional systolic and diastolic strain parameters in *pdgfb*$^{ret/ret}$ mice beginning at 9 months that may preclude a change in overall heart function at a later age. Furthermore, we also confirm that *pdgfb*$^{ret/ret}$ mice have altered to left ventricular structure at 6 months of age.

Early left ventricular dilation does not cause global impairment of systolic function in *pdgfb*$^{ret/ret}$ mice.

Cardiac parameters, like those examined in Chapter 4, were determined using STE method. I observed that at 6 months of age, both EDV and ESV were significantly greater in *pdgfb*$^{ret/ret}$ mice compared with *pdgfb*$^{+/+}$ and *pdgfb*$^{ret/+}$ littermates. In the previous chapter, this was not observed, which may indicate that in the evaluation of left ventricle dilation, STE may be more sensitive than conventional 2D echocardiography. However, at both 9 and 12 months of age no differences in EDV and ESV were observed which combined with unchanged left ventricular mass confirms previous findings from chapter 4 that *pdgfb*$^{ret/ret}$ mice develop transient cardiac dilatation and resolves over time. However, we did not assess the underlying cause of these changes. However, the cause of this is still unknown. As previously discussed, one stimulus that may cause an increase in left ventricular volume is blood volume overload. This is observed in eccentric cardiac hypertrophy with thinning of the

left ventricular wall. This may be occurring in *pdgfb*$^{ret/ret}$ mice due to systemic changes to large and micro- blood vessel structure. However, due to lack of changes to left ventricular wall thickness I do not believe that *pdgfb*$^{ret/ret}$ mice develop hypertrophy although this should be confirmed with histological analysis. Indeed Nystrom and collaborators postulated that structural changes to systemic microvessels may drive early cardiac changes in *pdgfb*$^{ret/ret}$ male mice, however, they did not test this hypothesis (Nystrom *et al.*, 2006). As previously stated in chapter 4, measurement of blood volume and intracardial could be done via SPECT imaging. This novel technique would be interesting to utilise in *pdgfb*$^{ret/ret}$ mice to determine whether microvascular dysfunction may be involved in changes in heart structure in aging.

EF_{Strain}, a common indicator of systolic function was not significantly altered at any time point between *pdgfb*$^{+/+}$, *pdgfb*$^{ret/+}$ and *pdgfb*$^{ret/ret}$ mice. Furthermore, GLS, which was found to be a better predictor than EF of all-cause mortality and major cardiovascular event (Kalam, Otahal and Marwick, 2014), was not different between groups at any time point. EF/GLS ratio, used to diagnose cardiac amyloidosis and as an indicator of thickening of the myocardium (Pagourelias *et al.*, 2017) was unchanged at any time point, further suggesting that the cardiac dilation response observed in *pdgfb*$^{ret/ret}$ mice does not involve an increase in ventricular wall thickness. Taken together, these data indicate that the global systolic contractile function of the heart is not adversely affected by early cardiac structural changes elicited by the *pdgfb*^{ret} mutation over 12 months.

I observed that CO_{Strain} and SV_{Strain} were significantly increased at 6 months of age in *pdgfb*$^{ret/ret}$ compared with both *pdgfb*$^{+/+}$ and *pdgfb*$^{ret/+}$ mice. I also observed an increase in CO_{Strain} at 9 months of age between *pdgfb*$^{ret/ret}$ mice and *pdgfb*$^{+/+}$ littermates. These findings indicate that cardiac function is altered in response to left ventricular dilation due to the *pdgfb*^{ret} mutation. However, this was not shown in chapter 4 at 6 months of age. Together this data supports my previous findings of transient changes left ventricular dilatation and the absence of cardiac pathology in *pdgfb*$^{ret/ret}$ mutant mice. It also suggests that STE should be used alongside conventional 2D echocardiography in pre-clinical studies, to confirm findings and fully characterise changes to the heart.

Segmental systolic function and diastolic function were altered at 9 months of age in *pdgfb*^{ret} mutant mice.

Analysis of global strain values did not reveal any obvious changes to overall systolic cardiac function; therefore, I next evaluated segmental myocardial strain across different regions of the left ventricular wall. First, I wished to evaluate on larger segments of the posterior, anterior ventricular wall and then basal, mid and apical segments. I did not observe any differences in radial or longitudinal strain across either the posterior or anterior wall between any genotypes at any time point (Figure 5.3 B-G). Surprisingly there was an increase in radial strain across the apical segments between *pdgfb*$^{+/+}$ and *pdgfb*$^{ret/ret}$ mice at 9 months but not at 12 months (Figure 5.3 L). This may suggest hyperkinetic changes to the myocardium in *pdgfb*$^{ret/ret}$ mice and that alterations to regional systolic function compared with *pdgfb*$^{+/+}$ mice may underlie the physiological adaptations to the *pdgfb*^{ret} mutation.

Segmental longitudinal strain and strain rate did not differ between genotypes at any time point in my study (Figure 5.4). However, examination of segmental radial strain and strain rate did reveal some differences in *pdgfb*$^{ret/ret}$ mice (Figure 5.5). Increases in radial strain on the posterior apical and anterior apical myocardium were observed in *pdgfb*$^{ret/ret}$ mice compared with *pdgfb*$^{+/+}$ mice at 9 months of age (Figure 5.5 C). Using Vevolab software, the left ventricle was further separated into the posterior base (Post(B)), posterior mid (Post (M)), posterior apical (Post(A)), anterior base (Ant(B)), anterior mid (Ant(M)) and anterior apical (Ant(A)) segments. Radial strain rate was significantly decreased in posterior mid region at 6 months of age (Figure 5.5 B). By 12 months, no differences in these parameters were observed. Taken together, these changes suggest that regional systolic contractile function is differentially regulated than the lengthening of the myocardium in *pdgfb*$^{ret/ret}$ mice (Figure 5.5 E, F). The effects of aging has been shown to lead to decrease in global and regional longitudinal and radial strain (De Lucia *et al.*, 2019). Another study has shown subtle and distinct differences in regional strain values between ischemic and non-ischemic cardiomyopathies, observing a pattern of “apical sparing” and “basal worsening” in non-ischaemic patients (Zuo *et al.*, 2020). However, in my study, changes in 9 months in *pdgfb*$^{ret/ret}$ mice were mostly due to the apical radial strain, whereas basal and mid areas appeared to be less affected, suggesting that aging provokes distinct cardiac adaptations in *pdgfb*$^{ret/ret}$ mice which were not observed in *pdgfb*$^{+/+}$ mice in aging.

Segmental diastolic function was altered at 9 and 12 months of age

Using the reverse strain modality, deformation of the left ventricle during diastole was measured by determining segmental reverse longitudinal and radial strain and strain rate (Figure 5.7+5.8). Several segmental strain and strain rate parameters were altered in *pdgfb*$^{ret/ret}$ mice suggesting that early changes to cardiac structure causes altered segmental diastolic function. These changes were prevalent in *pdgfb*$^{ret/ret}$ mice at 9 and 12 months and as such, are the first indication of altered cardiac function in *pdgfb*$^{ret/ret}$ mice at 12 months of age. Diastolic dysfunction has been shown to occur in aging mice at 12 months and then further deteriorate by 20 months (De Lucia *et al.*, 2019). It is unclear however whether these changes are physiological or pathological in nature. However, based upon the results from chapter 4 this may not yet cause an adverse phenotype and further reinforces the need for longer-term aging studies in these mice to identify the potential occurrence of cardiac pathology.

No evidence of left ventricular dyssynchrony in *pdgfb*$^{ret/ret}$ mice.

Ventricular dyssynchrony, can be defined as a difference in timing in ventricular contraction, which may lead to a deterioration in cardiac function and subsequent heart failure. There are many underlying mechanisms of left ventricular dyssnychrony including disruption of electromechanical coupling, regional contractility differences and also the formation of scarring after myocardial injury. Furthermore, previous assessment in aging mice has shown that aging increases left ventricular dyssynchrony at 15 and 20 months of age (De Lucia *et al.*, 2019). In our study, assessment of left ventricular dyssynchrony parameters showed that neither radial nor longitudinal dyssynchrony were present in any genotype (Figures 5.10+ 5.11) at any of the time points evaluated further supporting the idea that *pdgfb*$^{ret/ret}$ mice do not suffer from any severe cardiac pathology by 12 months of age. Follow-up scans beyond this time may reveal if dyssynchrony develops in aging *pdgfb*$^{ret/ret}$ mice and understand whether they develop adverse cardiac pathology.

Future Work

A major limitation of this study is that both male and female mice were grouped together into *pdgfb*$^{+/+}$, *pdgfb*$^{ret/+}$ and *pdgfb*$^{ret/ret}$ groups and as previously shown we did see some differences in cardiac development in male and female *pdgfb*^{ret} mutant mice (Chapter 5). Indeed, a recent study evaluating aging in male and female C57Bl/6J mice aged 2- and 24-months using STE observed a decline in diastolic function in both, male and female mice. However, females mice had better preserved systolic function than males at 24 months. However, due to issues with breeding this was not possible to study these separately (limitations will be expanded upon in Chapter 8: General discussion). It would be important in future experiments to study males and females independently to determine if this affected the cardiac phenotype observed with strain imaging in *pdgfb*$^{ret/ret}$ mice. The fact that males and females are combined may account for some of the changes observed at 9 months of age as these changes may correlate with hormonal changes to oestrogen levels in female *pdgfb*$^{ret/ret}$ mice. Indeed, a recent study performed in c57Bl/6 mice using STE showed that both male and female mice have reduced diastolic function in aging, however, systolic function is maintained in female mice (Zhang *et al.*, 2021). However, analysis from both ultrasound modalities agree that global changes to *pdgfb*$^{ret/ret}$ cardiac structure and function are not present at 12 months of age. However, alterations to regional diastolic strain parameters at 12 months of age suggest that subsequent scans and analysis beyond 12 months should be performed as this may be more reflective of the elderly human population where diseases such as heart failure and dilated cardiomyopathy are more prevalent.

Conclusion

Cardiac strain imaging reveals subtle changes to left ventricular systolic and diastolic function in *pdgfb*$^{ret/ret}$ mice, which were not detected using previous 2D echocardiography modalities. However, the changes observed were mostly transient and most were ameliorated by 12 months of age which highlights differences in cardiac

development and function in *pdgfb*$^{ret/ret}$ mice compared with *pdgfb*$^{+/+}$ and *pdgfb*$^{ret/+}$ counterparts. However, longer aging studies and investigation of sex differences using STE will further clarify the nature of the *pdgfb*$^{ret/ret}$ cardiac phenotype.

Chapter 6:

The effect of the *Pdgfb*^{ret} mutation on MSC Osteogenic Potential *in vitro*

Introduction

In chapter 3, I investigated whether *pdgfb*^{ret} mutation causes extracerebral calcification in multiple organs and tissues *in vivo*. I observed that calcification in the brain of *pdgfb*$^{ret/ret}$ mice showed regional heterogeneity and that calcification was absent in the aorta, coronary vessels, and kidneys. Mesenchymal stem/stromal cells (MSCs) have properties which may implicate them in vascular calcification although their exact contributions are unclear. In this chapter, I aimed to gain a preliminary understanding of how the *pdgfb*^{ret} mutation may affect the functional characteristics of MSCs *in vitro*.

MSCs are the *in vitro* counterpart of pericytes and adventitial cells which can be isolated from any vascularised tissue (Crisan *et al.*, 2008; Corselli *et al.*, 2012). MSCs have been utilized in over 1000 clinical trials for a wide range of diseases and pathological conditions (Gomez-Salazar *et al.*, 2020). According to the International Society for Cellular Therapy, by definition, MSCs adhere to plastic in standard culture conditions; sustain proliferation; undergo tri-lineage differentiation into osteoblasts, chondrocytes, and adipocytes; express the surface antigens CD105, CD90 and CD73 and lack CD45, CD19, CD14 CD11b, CD34, CD79α and HLA-DR (Dominici *et al.*, 2006). Furthermore, PDGFB plays a key role in regulating pericyte and MSC activity *in vivo* and *in vitro.*

One result of the *pdgfb*^{ret} mutation is that pericytes are absent or partially detached from the vasculature as shown in the brain (Lindblom *et al.*, 2003). In certain injury conditions such as in myocardial infarction, pericytes can detach from the existing vasculature, migrate to the site of injury, and contribute to tissue repair and regeneration (Alex and Frangogiannis, 2019; Su *et al.*, 2021). Detachment from endothelial cells and migration may involve phenotypic and functional changes, which may allow pericytes to directly contribute to tissue repair. Indeed, this has been shown in multiple organs such as the heart, kidneys, skeletal muscle, liver, and skin (Birbrair *et al.*, 2014). This led us to hypothesise that the *pdgfb*^{ret} mutation affects MSC behaviour *in vivo.* Partially attached pericytes *in vivo* may phenotypically differ from

those fully attached to blood vessels and possess different biological properties from those in full contact with endothelial cells. Indeed, in *pdgfb*$^{ret/ret}$ mice brain endothelial cells which are not in contact with pericytes have an altered transcriptional profile (Mäe *et al.*, 2021). This in turn may influence the intrinsic biological properties and differentiation potential of MSCs in *pdgfb*^{ret} mutant mice (Figure 6.1).

Although MSCs can be isolated from all vascularised tissues, pericytes are highly heterogeneous with different sub-types being identified in different tissues and each possessing different functional properties (Murray *et al.*, 2017). While human cardiac pericytes expanded in culture were phenotypically like human skeletal muscle pericytes, exhibiting classical MSC markers and morphology, they were not able to differentiate into skeletal myofibers *in vivo* upon skeletal muscle injury nor in culture (Chen *et al.*, 2015). This contrasts with ability of human perivascular MSCs from pancreas, adipose tissue and placenta which all have the ability to differentiate into skeletal muscle fibres upon injury both *in vivo* and *in vitro* (Crisan *et al.*, 2008). Instead, a few cardiac pericytes were able to transdifferentiate into cardiomyocytes in the heart post-MI (Chen *et al.*, 2013). In addition, like pericytes in other tissues, cardiac pericytes were shown possess tri-lineage potential and thus were able to differentiate into bone, cartilage and fat *in vitro* in similar conditions (Chen *et al.*, 2013). Besides tissue of origin, the disease state and aging also play a role in pericyte and MSC phenotype. This difference in pericyte/MSC functional properties and phenotype may also influence their therapeutic properties when isolated for use in stem cell therapy (Cathery *et al.*, 2018). In summary, numerous factors from the environment or niche from which they were derived can affect MSC differentiation potential.

To gain a preliminary understanding of whether MSCs isolated from multiple tissues from *pdgfb*^{ret} mutant mice have altered biological behaviour and differentiation potential we derived MSCs in culture and performed *in vitro* osteogenesis assays.

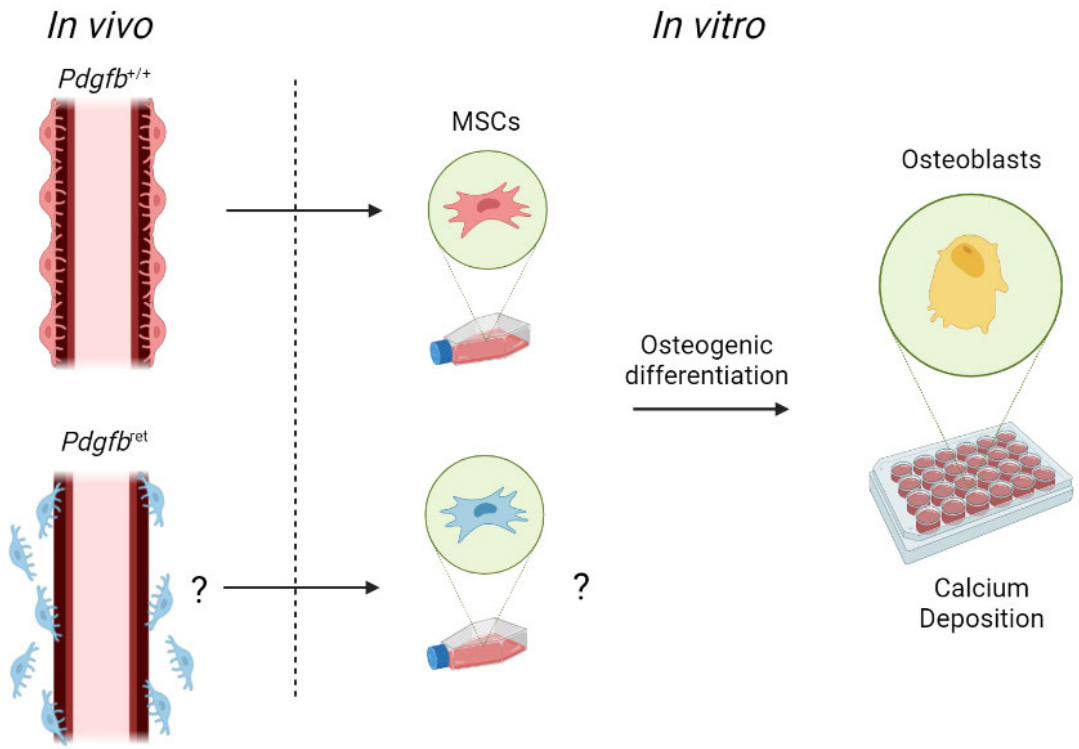

Figure 6.1: Hypothesis: The *Pdgfb*^{ret} mutation affects MSC osteogenic potential *in vitro*.

Due to the *pdgfb*^{ret} mutation, detached or partially attached pericytes (blue) in blood vessels *in vivo*, may phenotypically and functionally differ from those from *pdgfb*$^{+/+}$ mice (red) fully in contact with endothelial cells. Since PDGFB controls osteogenic differential potential of these cells (Cassiede *et al.*, 1996), MSCs isolated from multiple vascularised tissues from *pdgfb*^{ret} mutant mice may have an altered osteogenic differentiation potential.

Hypothesis

MSCs derived from *pdgfb*^{ret} mutant tissues have altered osteogenic differentiation potential *in vitro*

Aims

1. Derive MSC lines from *pdgfb*$^{+/+}$ and *pdgfb*^{ret} mutant cardiac and non-cardiac tissues.
2. Assess the osteogenic differentiation potential of mutant MSCs.

Study Design

MSCs were isolated and cultured from *pdgfb*$^{+/+}$, *pdgfb*$^{ret/+}$ and *pdgfb*$^{ret/ret}$ hearts, coronary vessels, skeletal muscles, and kidneys. MSCs from *pdgfb*$^{ret/+}$ and *pdgfb*$^{ret/ret}$ mice were combined into the *pdgfb*^{ret} mutant group. The number of tissues used at day 7 and 14 of osteogenesis is listed in the Table 6.1 as well as a breakdown of tissues by genotype and the total number of *pdgfb*$^{ret/+}$ and *pdgfb*$^{ret/ret}$ tissues combined.

Table 6.1: Number of tissues used per genotype after 7 and 14 days of osteogenesis.

	Number of tissues							
	Day7				Day 14			
Tissue	+/+	ret/+	ret/ret	ret total	+/+	ret/+	ret/ret	ret total
Heart	6	8	2	10	8	6	2	8
Kidney	7	4	1	5	5	5	0	5
Skeletal Muscle	7	6	1	7	8	3	1	4
Coronary Vessel	9	9	1	10	10	9	2	11

+/+=*pdgfb*$^{+/+}$, ret/+=*pdgfb*$^{ret/+}$, ret/ret=*pdgfb*$^{ret/ret}$, ret total= ret/+ combined with ret/ret

Tissues from *pdgfb*$^{+/+}$ and *pdgfb*^{ret} mutant mice were dissociated and adherent MSCs were cultured and expanded for 3-4 passages prior to osteogenic differentiation (Figure 6.2A). Example images of MSCs isolated from *pdgfb*$^{+/+}$ and *pdgfb*^{ret} mutant coronary vessels show MSCs exhibiting a spindle-like fibroblast morphology and plastic adherence, two classical MSC traits (Figure 6.2B). This was also the case from MSCs isolated from other tissues (data not shown). Next, MSCs isolated from all tissues underwent osteogenic differentiation assays (Figure 6.2C). The osteogenic

differentiation was shown by the presence of alizarin red, a marker of calcium deposition *in vitro*. Optical density measurements were next performed using a spectrophotometer, to quantify the levels of alizarin red.

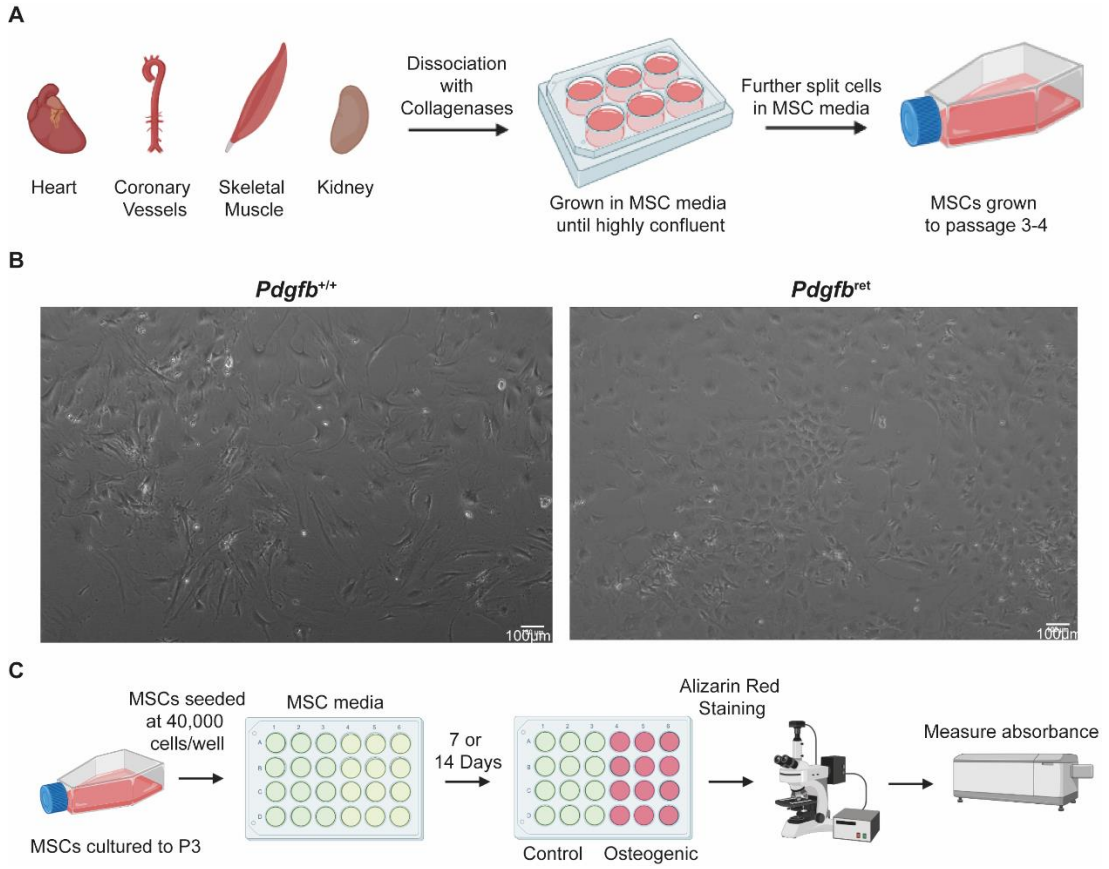

Figure 6.2: MSCs can be derived in vitro, and their osteogenic potential tested from multiple *pdgfb*$^{+/+}$ and *pdgfb*^{ret} mutant tissues.

(**A**) The heart, coronary vessels, skeletal muscle, and kidney of *pdgfb*$^{+/+}$ and *pdgfb*^{ret} mutant mice were harvested and whole tissues were dissociated using a combination of collagenases I, II and IV. Cell suspensions obtained were then seeded and cultured in MSC media in 6-well plates until highly confluent. Cells were then further split and cultured until passage (P) 3 or 4 in T25 (P1) followed by T75 cell culture flasks (P2-P4). (**B**) Example images of coronary vessel-derived MSCs from *pdgfb*$^{+/+}$ (left panel) and *pdgfb*^{ret} mutant mice (right panel) exhibiting classical fibroblast-like morphology. **(C)** At P3 or P4, MSCs were seeded at a density of 40,000 cells/well in a 24-well plate for 24 hours in MSC media. The media was then replaced with either control media or osteogenic media. For each sample, two or three technical replicates were performed. Finally, after 7 or 14 days both control and osteogenic wells were stained with alizarin red, wells were imaged, and optical density was quantified. Scale bar=100µm.

Results

Cardiac MSCs exhibit high levels of heterogeneity in term of their osteogenic potential at 7 and 14 days.

Cardiac MSC lines from both *pdgfb*$^{+/+}$ and *pdgfb*^{ret} mutant hearts were incubated in control or osteogenic media and stained with alizarin red at day 7 and day 14. Alizarin red expression was absent in all wells incubated with the control (non-osteogenic) media. (Figure 6.3A-B, 1st column), This shows that osteogenic differentiation only occurs in the presence of osteogenic compounds present in the osteogenic media and that neither *pdgfb*$^{+/+}$ nor *pdgfb*^{ret} mutant cardiac MSCs can spontaneously differentiate into bone-forming cells. In contrast to controls, a great deal of variation in alizarin red staining was observed in both *pdgfb*$^{+/+}$ and *pdgfb*^{ret} cardiac MSC lines incubated in osteogenic media. Some MSCs exhibited low or no (low/no) osteogenic differentiation, and some had high levels as shown by alizarin red staining of wells. After 7 days of differentiation, we observed both low (Figure 6.3A, middle column) and high amounts of alizarin red deposition (Figure 6.3A, 3rd column) in both *pdgfb*$^{+/+}$ and *pdgfb*^{ret} mutant MSC cultures. This was also the case after 14 days of osteogenic differentiation, where similar results were observed (Figure 6.3B). This data suggests an elevated level of cellular and functional heterogeneity in terms of cell types enriched in our MSC culture and calcium production in cardiac MSCs irrespective of their genotype.

Next, we quantified the amount of alizarin red staining via measurement of the optical density (OD405nm) using spectrophotometric absorbance (Figure 6.3C). No significant difference was observed between *pdgfb*$^{+/+}$ and *pdgfb*^{ret} mutants in alizarin red quantification levels after 7- or 14-days incubation with osteogenic media (Figure 6.3C, $p>0.05$). However, I did observe a pattern in increasing optical density values between time points. In average, from day 7 to day 14, the absorbance increased approximately 1.7 times (0.126 to 0.214) in *pdgfb*$^{+/+}$ cardiac MSCs (Table 6.2). There was a 2.9-fold increase in the average optical density (0.085 to 0.250) in *pdgfb*^{ret} mutant cardiac MSCs (Table 6.2).

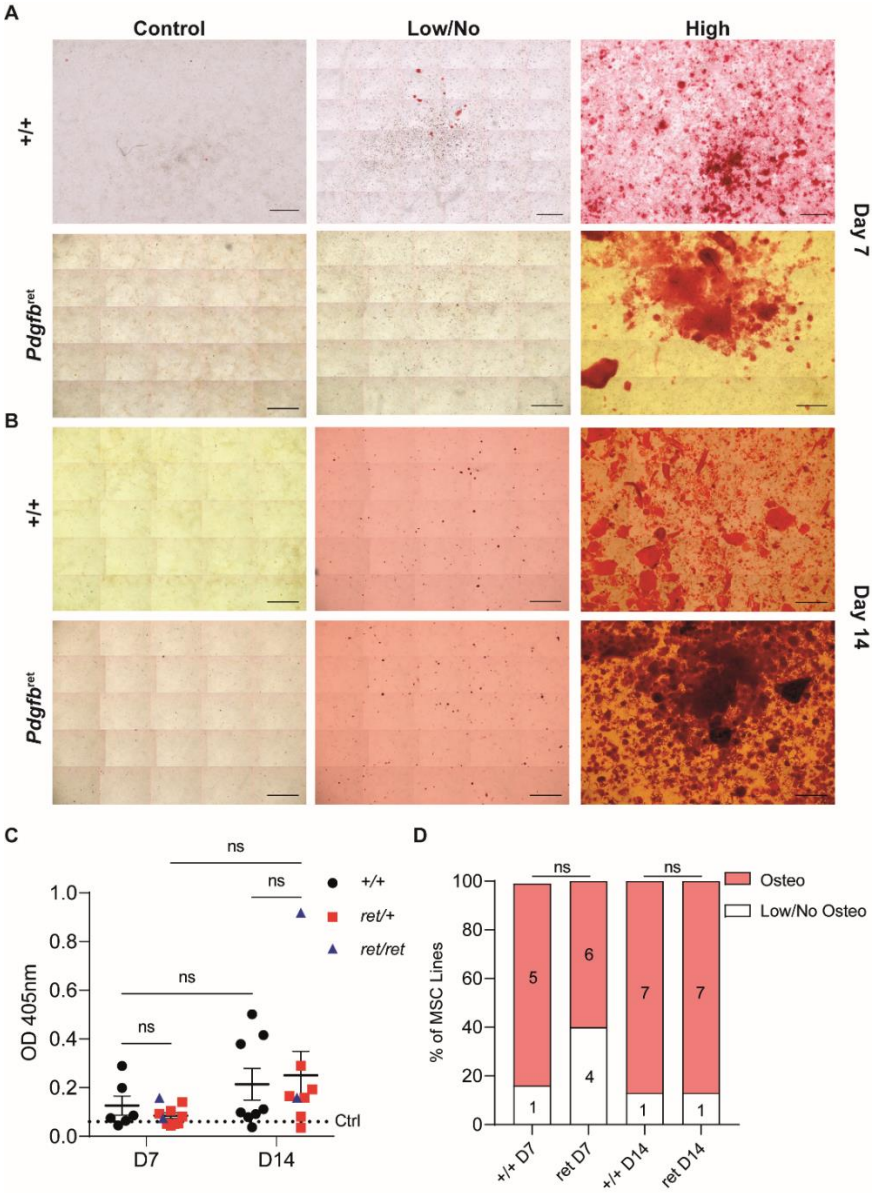

Figure 6.3: Most cardiac MSCs are osteogenic after 14 days, independent of their genotype.

Cardiac MSCs from *pdgfb*$^{+/+}$ (+/+) and *pdgfb*^{ret} mutant (ret) mice were stained with alizarin red after 7 (**A**) and 14 (**B**) days of incubation in osteogenic media. Scale bar =1000µm. (**C**) Optical density (OD405nm) was measured to quantify alizarin red content from +/+ (black dots) and *pdgfb*^{ret} mutant (ret/+ red squares, ret/ret blue triangles) MSCs at day 7(D7) and D14. The control osteogenic threshold value (Ctrl, dotted line) is 0.061. Data= mean±SEM, two-way ANOVA with Tukey's test. (**D**) The proportion of osteogenic (Osteo), with optical density of >0.061, and low/non-osteogenic (Low/No-Osteo, ≤0.061) samples is shown. Numbers within bars are the number of samples tested. Chi-square test with Yates' correction. n=6-10/group. ns=not significant.

Table 6.2: Mean OD405nm values and fold change from day 7 to day 14 for each tissue.

	Mean OD405nm				Fold change	
	Day 7		Day 14		Day 7 to Day 14	
Tissue	+/+	ret	+/+	ret	+/+	ret
Heart	0.126	0.085	0.214	0.250	1.7	2.9
Kidney	0.110	0.077	0.207	0.299	1.9	3.9
Skeletal Muscle	0.104	0.138	0.154	0.365	1.5	2.6
Coronary Vessel	0.063	0.128	0.125	0.367	2.0	2.9

+/+= *pdgfb*$^{+/+}$, ret=*pdgfb*^{ret} mutant

Table 6. 3: Standard Deviation (SD) of mean OD405nm values and fold change in SD from day 7 to day 14 for each tissue.

	Std. Deviation				Fold change	
	Day 7		Day 14		Day 7 to Day 14	
Tissue	+/+	ret	+/+	ret	+/+	ret
Heart	0.097	0.039	0.185	0.280	1.9	7.1
Kidney	0.063	0.035	0.194	0.382	3.1	10.9
Skeletal Muscle	0.102	0.118	0.133	0.384	1.3	3.3
Coronary Vessel	0.030	0.087	0.121	0.363	4.1	4.2

+/+= *pdgfb*$^{+/+}$, ret=*pdgfb*^{ret} mutant

Table 6.4: Minimum, maximum and range of OD405nm values at 7 and 14 days of differentiation.

			Genotype	Tissue			
				Heart	Kidney	Skeletal Muscle	Coronary Vessel
OD405nm Values	Minimum	Day 7	+/+	0.045	0.046	0.042	0.043
			ret	0.044	0.055	0.047	0.047
		Day 14	+/+	0.037	0.038	0.045	0.046
			ret	0.035	0.037	0.05	0.05137
	Maximum	Day 7	+/+	0.289	0.23	0.285	0.1325
			ret	0.158	0.139	0.374	0.32
		Day 14	+/+	0.501	0.507	0.389	0.3805
			ret	0.918	0.925	0.999	0.952
	Range	Day 7	+/+	0.244	0.184	0.243	0.0895
			ret	0.114	0.084	0.327	0.273
		Day 14	+/+	0.464	0.469	0.344	0.3345
			ret	0.883	0.888	0.949	0.9006

+/+= *pdgfb*$^{+/+}$, ret=*pdgfb*^{ret} mutant

Although the differences between these groups were not significant (p>0.05), the trend suggests that there is a greater level of calcium at 14 days compared with 7 days in both *pdgfb*$^{+/+}$ and *pdgfb*^{ret} mutant cardiac MSCs (Figure 6.3). Examination of the optical density data distribution standard deviation (SD) of the mean OD405nm values (Figure 6.3C, Table 6.3) as well as observation of the data distribution, also suggests a greater variance and wider spread of the data at 14 days than 7 days in both *pdgfb*$^{+/+}$ and *pdgfb*^{ret} cardiac MSCs. In support of this, I observed that the minimum OD405nm values for cardiac MSCs were similar at both day 7 and day 14 (Table 6.4). However, the maximum values are much greater at day 14 than 7 days for both *pdgfb*$^{+/+}$ and *pdgfb*^{ret} mutant cardiac MSCs (Table 6.4). The range of OD405nm values was higher for *pdgfb*^{ret} mutant MSCs (0.883) than *pdgfb*$^{+/+}$ MSCs (0.464) at day 14 (Table 6.4). Additionally, between 7 and 14 days there was a 1.9-fold increase in the SD for *pdgfb*$^{+/+}$ MSCs and a 7.1-fold increase in SD for *pdgfb*^{ret} mutant MSCs. This difference in variance and the distribution of optical density values as an indicator of calcium deposition, between *pdgfb*$^{+/+}$ and *pdgfb*^{ret} mutant MSCs, suggests that mutant cardiac MSCs are more heterogenous in terms of their functional osteogenic capacity after 14 days of incubation in osteogenic media.

Optical density values of control (non-osteogenic media) samples were calculated and the average OD405nm value of the control samples was 0.061. This is shown on each figure as a dotted line and labelled as Ctrl. This value was used as the threshold for a sample to be defined as osteogenic (above this threshold) versus non-osteogenic (below). To investigate whether mutant MSC lines show differences in term of osteogenic capacity, I compared the proportion of osteogenic samples in each group after 7 and 14 days of incubation with osteogenic media. At day 7, 83.33% (5/6) of *pdgfb*$^{+/+}$ and 60% (6/10) of *pdgfb*^{ret} mutant MSC lines were osteogenic; however, no significant difference in proportions between these groups was observed (Figure 6.3D, p>0.05). At day 14, I observed that 87% of cardiac MSC cultured from both *pdgfb*$^{+/+}$ (7/8) and *pdgfb*^{ret} (7/8) mutant hearts were osteogenic suggesting that mutant *pdgfb*^{ret} cardiac MSC's ability to undergo osteogenic differentiation *in vitro* is similar to that of WT MSCs.

Taken together, cardiac MSCs from *pdgfb*$^{+/+}$ and *pdgfb*^{ret} mutant tissues do not differ in their osteogenic capacity *in vitro* after 7 days. However, based on the range and data distribution after 14 days mutant MSCs have greater variation in their ability to

deposit calcium. A similar proportion of *pdgfb*$^{+/+}$ and mutant MSC lines exhibited osteogenesis after 7 and 14 days of incubation with osteogenic media, suggesting that mutant cardiac MSCs do not differentiate into osteoblasts with a greater affinity than those isolated from *pdgfb*$^{+/+}$ hearts. To test whether these observations were tissue-specific, I next performed osteogenesis assays of cultured renal, skeletal muscle and large vessel-derived MSCs.

A smaller proportion of *pdgfb*^{ret} mutant renal MSCs were osteogenic after 14 days of incubation in osteogenic media

Renal MSCs from both *pdgfb*$^{+/+}$ and *pdgfb*^{ret} mutant kidneys were incubated in osteogenic media and after 7 or 14 days stained with alizarin red. As previously observed in cardiac MSCs, there were low and high levels of calcium deposition in both *pdgfb*$^{+/+}$ and *pdgfb*^{ret} mutant renal MSCs after day 7 (Figure 6.4A middle and right panel) and day 14 (Figure 6.4B middle and right panel) of incubation with osteogenic media. Staining with alizarin red was also absent in all control samples (Figure 6.4A, B left panels).

Quantification of alizarin red staining by optical density measurement was not significantly different between *pdgfb*$^{+/+}$ and *pdgfb*^{ret} mutant after 7 or 14 days of incubation with osteogenic media (Figure 6.4C, $p>0.05$). There was, however, a 1.9-fold increase in the mean optical density between *pdgfb*$^{+/+}$ renal MSCs from day 7 to day 14 (0.110 to 0.207, Table 6.2). An approximately 3.9-fold increase in the mean optical density (0.77 to 0.299) was observed between day 7 and day 14 in *pdgfb*^{ret} mutant renal MSCs (Table 6.2). This trend is in keeping with that of cardiac MSC lines suggesting that renal MSCs are more osteogenic at 14 days after incubation than after 7 days. I also observed a wider data distribution (Figure 6.4C) and higher SD of mean OD405nm values in *pdgfb*^{ret} mutant MSCs compared with *pdgfb*$^{+/+}$ MSCs after both 7 and 14 days of incubation in osteogenic media (Table 6.3). There was also a 3.1- and 10.9-fold increase in SD in *pdgfb*$^{+/+}$ and *pdgfb*^{ret} mutant MSCs, respectively. I further observed similar minimum OD405nm values for *pdgfb*$^{+/+}$ and *pdgfb*^{ret} mutant renal MSCs at both 7 and 14 days (Table 6.4). The maximum value for *pdgfb*^{ret} mutant MSC lines was greater than *pdgfb*$^{+/+}$ MSC lines (Table 6.4). A greater range in values for both *pdgfb*^{ret} mutant and *pdgfb*$^{+/+}$ after 14 days of differentiation was observed (Table

6.4). This further suggest a greater level of heterogeneity in mutant MSCs compared with *pdgfb*$^{+/+}$ MSCs.

Using the threshold optical density value for osteogenesis (0.061 OD405nm), measured from control samples, I examined the proportion of osteogenic renal MSC samples at day 7 and day 14 of incubation with osteogenic media. At day 7, I found that 86% (6/7) of *pdgfb*$^{+/+}$ samples and 80% (4/5) of *pdgfb*^{ret} MSC samples were osteogenic (Figure 6.5D). At day 14, 80% (4/5) *pdgfb*$^{+/+}$ and 40% (2/5) *pdgfb*^{ret} kidney MSC samples were osteogenic (Figure 6.4D). However, the difference in proportions between samples was not found to significantly differ at either time point (Figure 6.5D, $p>0.05$). Interestingly, a smaller proportion of *pdgfb*^{ret} renal MSCs were osteogenic at 14 days compared with that at day 7 decreasing from 80% to 40% of samples. This data shows that although a smaller proportion of mutant MSCs are osteogenic after 14 days the mean level of alizarin red staining is still higher than that at 7 days. In summary, little difference was observed between *pdgfb*$^{+/+}$ and mutant renal MSCs in terms of osteogenic potential at both 7 and 14 days, with high levels of heterogeneity observed in mutant renal MSCs. This indicates that the tissue of origin may play an important role in defining the functional characteristics of MSCs *in vitro.*

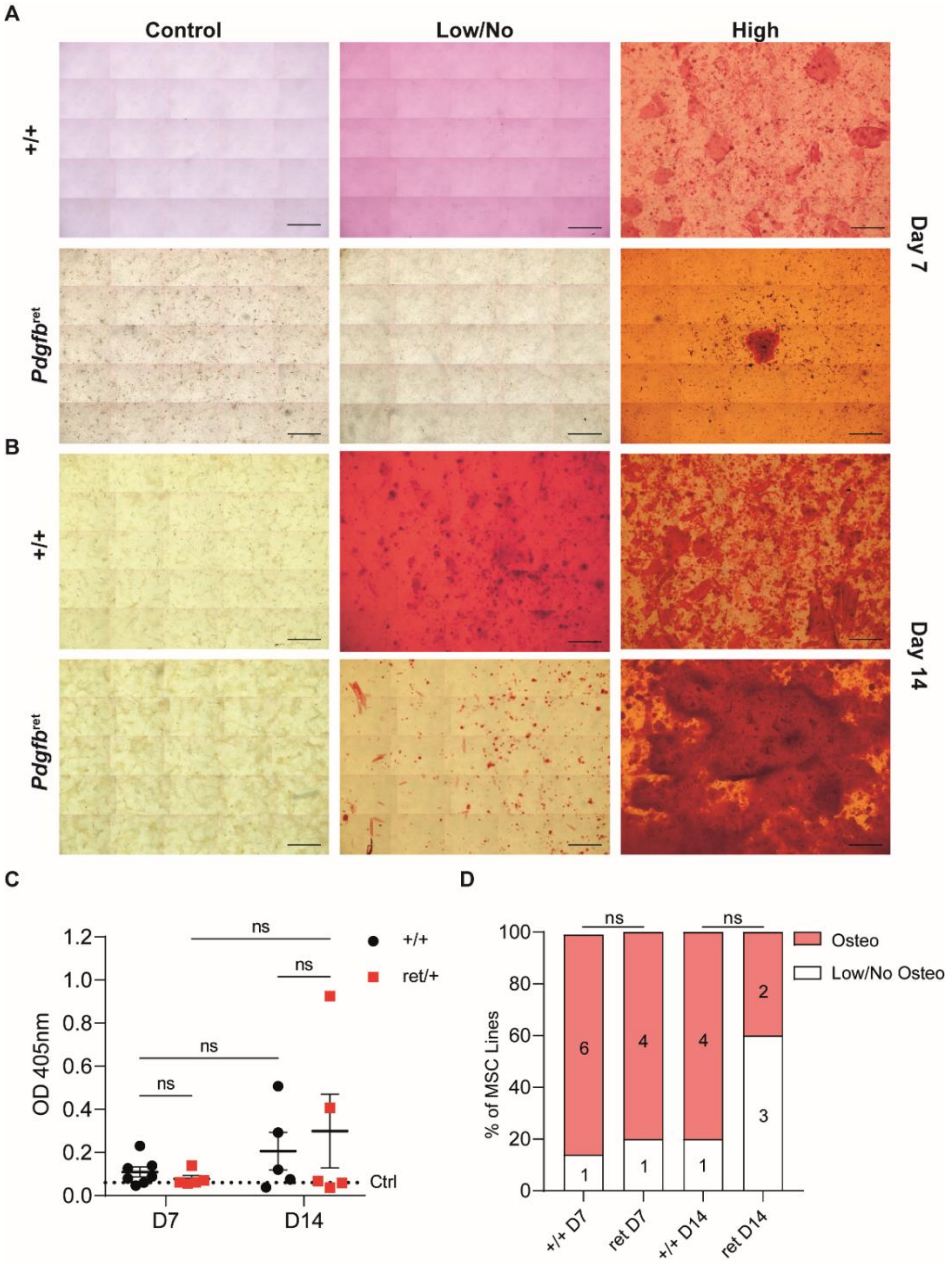

Figure 6.4: *Pdgfb*$^{+/+}$ and *pdgfb*^{ret} mutant renal MSCs exhibit a highly heterogeneous osteogenic differentiation potential *in vitro*.

Renal MSCs from *pdgfb*$^{+/+}$(+/+) and *pdgfb*^{ret} mutant (ret) mice stained with alizarin red after 7 (**A**) and 14 (**B**) days of osteogenic media. Scale bar =1000µm. (**C**) Optical density (OD405nm) of alizarin red staining from +/+ (black dots) and *pdgfb*^{ret} mutant (ret/+ red squares) MSCs at day 7 (D7) and D14.The control osteogenic threshold value (Ctrl, dotted line) is 0.061 OD405nm. Data= mean±SEM, two-way ANOVA with Tukey's test. (**D**) The proportion of osteogenic (Osteo), with optical density of >0.061, and low/non-osteogenic (Low/No-Osteo, ≤0.061) samples is shown. Numbers within bars are the sample number. Chi-square test with Yates' correction. n=5-7/group. ns=not significant.

Most *pdgfb*^{ret} mutant skeletal muscle derived MSCs are already osteogenic at day 7.

Skeletal muscle MSCs from both *pdgfb*$^{+/+}$ and *pdgfb*^{ret} mutant hearts were incubated in osteogenic media for 7 and 14 days. Both control and osteogenic MSCs cultures were stained with alizarin red and calcium deposition was quantified. Control skeletal muscle MSCs did not show any alizarin red staining (Figure 6.5A, B left panels). As with previous MSC tissue sources, we observed heterogeneous outcome in terms of alizarin red staining with both low and high levels of calcium deposition after 7 days (Figure 6.5A middle and right panels) and 14 days (Figure 6.5B middle and right panels) culture in differentiating conditions. This was true for both *pdgfb*$^{+/+}$ and *pdgfb*^{ret} mutant skeletal muscle MSCs.

Quantification of optical density revealed no significant difference between *pdgfb*$^{+/+}$ and *pdgfb*^{ret} mutants in alizarin red levels at either 7 or 14 days of culture (Figure 6.5C). There was a 1.5-fold change in the mean level of alizarin red staining between day 7 and day 14 for *pdgfb*$^{+/+}$ MSC cultures (0.104 to 0.154, Table 6.2, $p>0.05$). However, this increase was higher in *pdgfb*^{ret} mutant samples by about 2.6-fold from 7 to 14 days (0.138 to 0.365; Table 6.2, $p>0.05$). This further shows that MSC lines exhibit greater levels of osteogenesis after 14 days compared to 7 days. The SD was similar for *pdgfb*^{ret} mutant mice and *pdgfb*$^{+/+}$ skeletal muscle MSCs after 7 days of osteogenesis, however, after 14 days the SD was greater for *pdgfb*^{ret} mutant mice (Table 6.3). This difference represented a 3.3-fold change in SD from day 7 to day 14 in *pdgfb*^{ret} mutant MSCs and was in keeping with previous results from cardiac and renal MSC lines, showing a greater variance after 14 days. This may reflect an increase in heterogeneity in *pdgfb*^{ret} mutant MSCs compared with *pdgfb*$^{+/+}$ MSCs. I also observed that after 7 and 14 days the minimum optical density values were similar for both *pdgfb*$^{+/+}$ and *pdgfb*^{ret} mutant MSCs (Table 6.4). The maximum OD405nm values were greater for *pdgfb*^{ret} mutant MSCs compared with *pdgfb*$^{+/+}$ skeletal muscle MSCs (Table 6.4). This pattern was observed in cardiac MSCs but not renal MSCs, suggesting that cardiac and skeletal muscle MSCs are more similar.

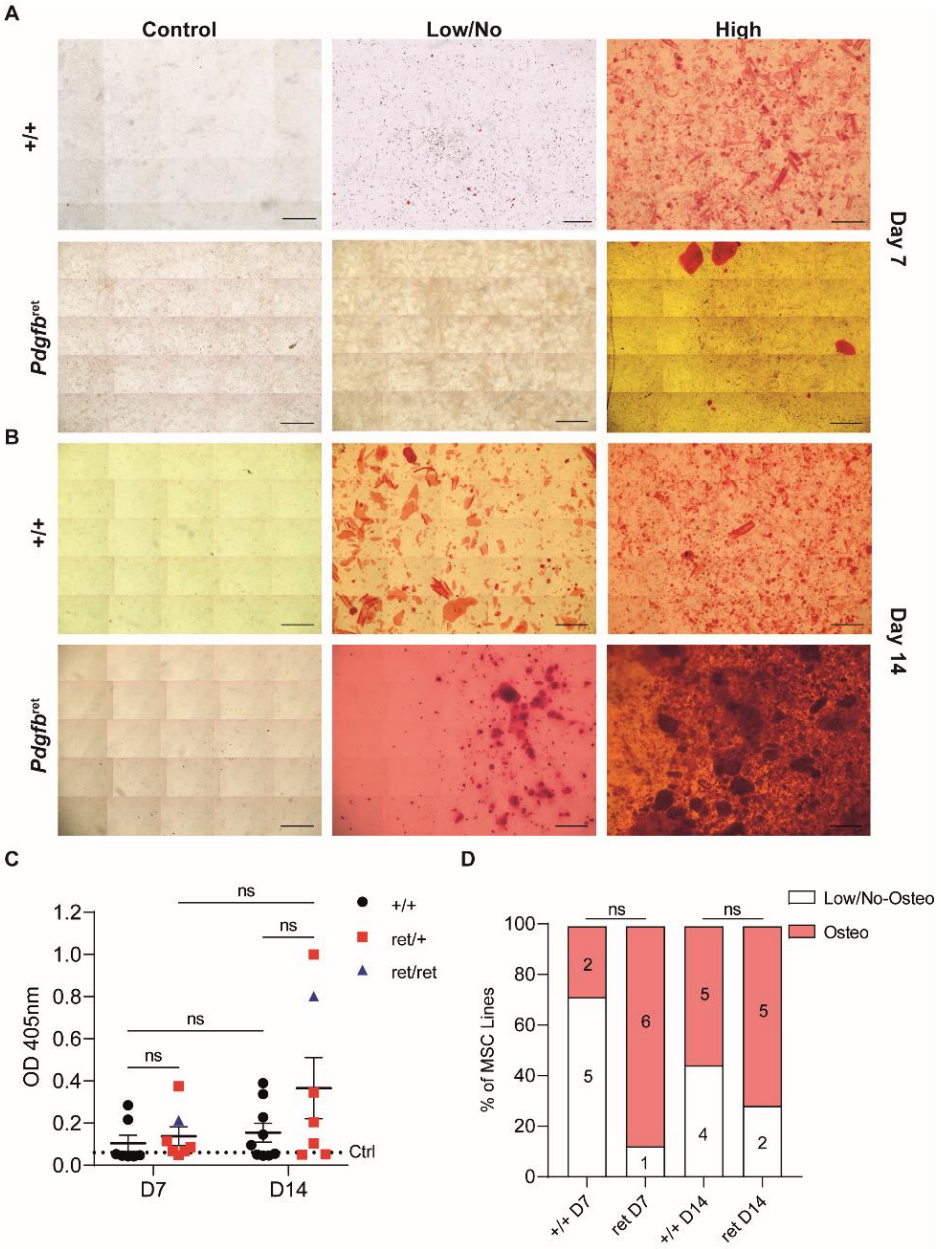

Figure 6.5: The majority of *pdgfb*^{ret} mutant skeletal muscle derived MSCs are already osteogenic at day 7.

Skeletal MSCs from *pdgfb*$^{+/+}$(+/+) and *pdgfb*^{ret} (ret) mutant mice were stained with alizarin red after 7 (**A**) and 14 (**B**) days of incubation in osteogenic media. Scale bar =1000µm Optical density (OD405nm) of alizarin red staining from +/+ (black dots) and *pdgfb*^{ret} mutant (*pdgfb*$^{ret/+}$ =ret/+ red squares, *pdgfb*$^{ret/ret}$ =ret/ret blue triangles) MSCs at 7(D7) and 14 (D14) days of incubation in osteogenic media (**C**). The control osteogenic threshold value (Ctrl, dotted line) is 0.061 OD405nm. Data= mean±SEM, two-way ANOVA with Tukey's test. (**D**) The proportion of osteogenic (Osteo), with optical density of >0.061, and low/non-osteogenic (Low/No-Osteo, ≤0.061) samples is shown. Numbers within bars are the sample number. Chi-square test with Yates' correction. n=7-9/group. ns=not significant.

The range of optical density values was also greater after 14 days of incubation in osteogenic media for mutant skeletal muscle MSCs than *pdgfb*$^{+/+}$ MSCs (Table 6.4).

Next, I compared the proportion of osteogenic and non-osteogenic samples at day 7 and day 14. Interestingly, after 7 days of incubation with osteogenic media, 28.5% (2/7) of *pdgfb*$^{+/+}$ skeletal muscle MSCs were osteogenic compared with 87.5% (6/8) of *pdgfb*^{ret} skeletal muscle MSCs (Figure 6.5D, p>0.05). However, after 14 days of incubation, these proportions were more similar. Indeed, 55% (5/9) of *pdgfb*$^{+/+}$ and 71% (5/7) of *pdgfb*^{ret} mutant skeletal muscle MSCs were osteogenic (Figure 6.5E). This data suggests that *pdgfb*^{ret} mutant skeletal muscle MSCs readily form bone *in vitro*.

Pdgfb^{ret} mutant coronary vessel MSCs display a high rate of osteogenic differentiation.

Finally, MSCs isolated from the large coronary vessels of *pdgfb*$^{+/+}$ and *pdgfb*^{ret} mutant mice were utilised in osteogenic differentiation assays. Alizarin red was not expressed in any control samples as expected (Figure 6.6A, B top left and bottom left panels). Like other organs tested, I also observed a high level of heterogeneity in terms of calcium deposition in *pdgfb*$^{+/+}$ and *pdgfb*^{ret} mutant coronary vessel MSCs at both 7 (Figure 6.6A) and 14 days (Figure 6.6B). Interestingly, some *pdgfb*^{ret} mutant MSCs show a particularly high level of calcium after 14 days of culture (Figure 6.6B, bottom right panel).

Measurement of the optical density of alizarin red staining did not reveal any significant differences between *pdgfb*$^{+/+}$ and *pdgfb*^{ret} mutant MSCs in alizarin red levels after 7 or 14 days of incubation with osteogenic media (Figure 6.6C, p>0.05). For *pdgfb*$^{+/+}$ coronary vessel MSCs there was a 2-fold increase (0.063 to 0.125) in the mean alizarin red levels from 7 to 14 days (Figure 6.6C, Table 6.3). For *pdgfb*^{ret} mutant MSCs, a 2.9-fold increase in the mean alizarin red levels (Figure 6.6C, Table 6.3). This is in keeping with results from other tissues that there is higher amount of calcium deposition in both *pdgfb*$^{+/+}$ and *pdgfb*^{ret} mutant tissues at 14 days than 7 days. It is also in keeping with the trend that there is a greater fold change between 7 and 14 days in *pdgfb*^{ret} mutant tissues than *pdgfb*$^{+/+}$ tissues (Table 6.3). After 7 days, the SD of the mean OD405nm values was greater for mutant coronary vessel MSCs than those from *pdgfb*$^{+/+}$vessels

(Table 6.3). This was also the case after 14 days of culture in differentiating media. Although the fold change in SD was similar for both *pdgfb*$^{+/+}$ and *pdgfb*^{ret} mice (4.1 vs 4.2), the difference in SD may suggest that mutant coronary vessel MSCs are more heterogeneous in terms osteogenic potential than their *pdgfb*$^{+/+}$ counterparts. This idea is further supported by examination of the data distribution in *pdgfb*^{ret} mutant MSCs at 14 days (Figure 6.6C), which shows distinct clusters of MSCs with high, medium, and lower levels of alizarin red expression.

Examination of the minimum, maximum and range of optical density values further corroborates this. Minimum values were similar for both genotypes at both time points (Table 6.3). Maximum values were greater in *pdgfb*^{ret} mutant MSCs than *pdgfb*$^{+/+}$ counterparts after 7 and 14 days (Table 6.3). The range of values was higher for mutant coronary vessel MSCs than *pdgfb*$^{+/+}$ MSCs at both time points (Table 6.3). Taken together this data clearly illustrates a wider data distribution and may further suggest a greater level of heterogeneity in terms of osteogenic potential for mutant MSC lines compared to *pdgfb*$^{+/+}$ MSCs.

I next compared the proportion of samples, which had OD405nm values greater than the osteogenic threshold (0.061). Interestingly, twice more mutant samples were osteogenic after 7 days of incubation in osteogenic media. Indeed, 70% (7/10) of *pdgfb*^{ret} samples were osteogenic in contrast to 33.3% (3/9) of *pdgfb*$^{+/+}$ samples (Figure 6.7D). Although this proportional difference was not significant, this suggest that mutant coronary vessel MSCs start to differentiate into osteoblasts at an earlier time point and thus are primed to become bone. After 14 days, 70% (7/10) of both *pdgfb*$^{+/+}$ and *pdgfb*^{ret} coronary vessel MSC samples were osteogenic.

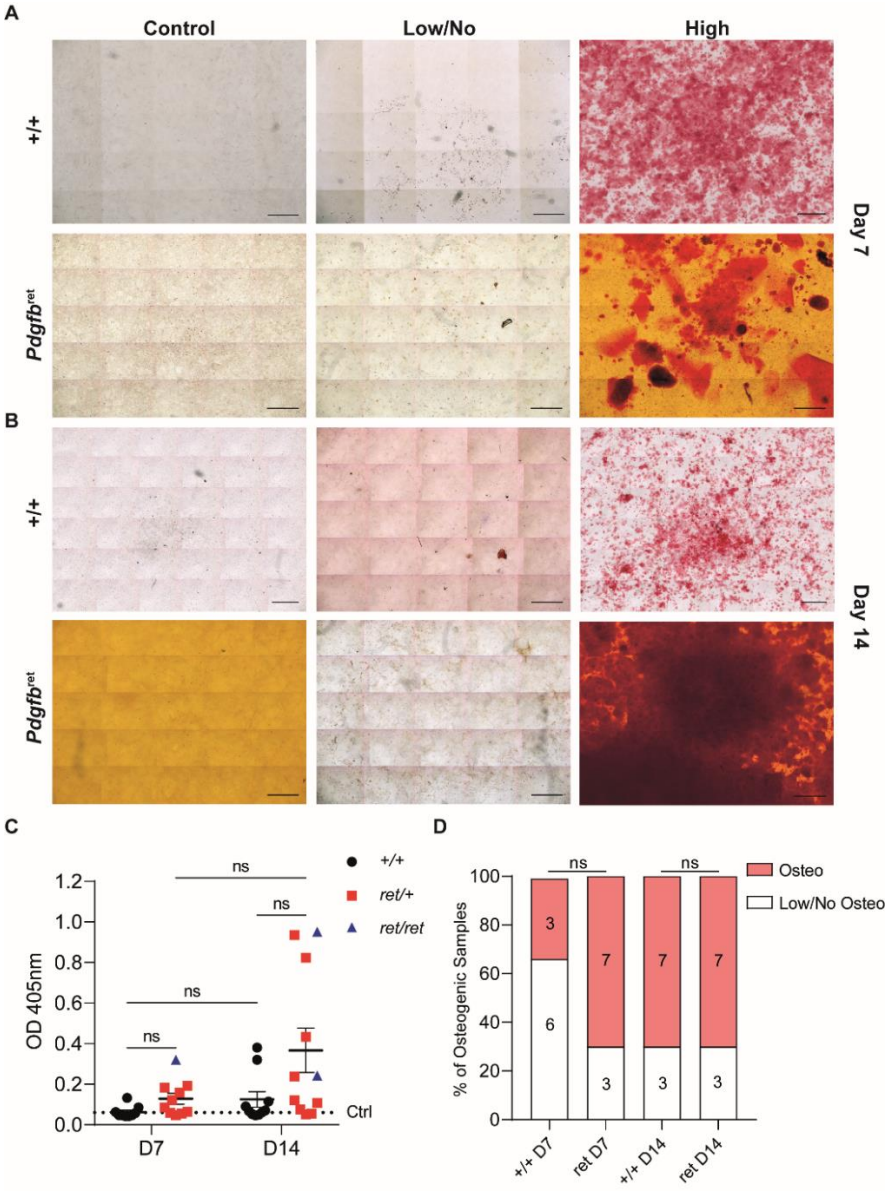

Figure 6. 6: *Pdgfb*^{ret} mutant coronary vessel MSCs differentiate display a high rate of osteogenic differentiation.

Coronary vessel MSCs from *pdgfb*$^{+/+}$(+/+) and *pdgfb*^{ret} (ret) mutant mice were stained with alizarin red after 7 (**A**) and 14 (**B**) days of incubation in osteogenic media. Scale bar =1000µm. Optical density (OD405nm) was measured to quantify alizarin red staining from +/+ (black dots) and *pdgfb*^{ret} mutant (*pdgfb*$^{ret/+}$ =ret/+ red squares, *pdgfb*$^{ret/ret}$ =ret/ret blue triangles) MSCs at 7(D7) and 14 (D14) days of incubation in osteogenic media (**C**). The control osteogenic threshold value (Ctrl, dotted line) is 0.061 OD405nm. Data= mean±SEM, two-way ANOVA with Tukey's test. (**D**) The proportion of osteogenic (Osteo), with optical density of >0.061OD405nm, and non-osteogenic (Low/No Osteo) samples is shown. The numbers within bars are the sample number. Data= percentage of total samples. Chi-square test with Yates' correction. n=9-10/group. ns=not significant.

By 14 days, a greater level of osteogenic heterogeneity exists in *pdgfb*^{ret} mutant coronary vessel MSCs as shown by the large variance in osteogenic quantification. Due to the fact that the pdgfbret mutation is a germline mutation and due to this repeated trend of a greater variance in mutant MSCs than *pdgfb*$^{+/+}$ MSCs by 14 days, I next investigated if there was a global effect on *pdgfb*^{ret} mutant tissues eliminating the tissue source as a variable.

After 14 days, tissues from *pdgfb*^{ret} mutants have greater osteogenic potential and exhibit high heterogeneity in calcium deposition.

I combined all optical density values, previously shown (Figure 6.2-6.6), from *pdgfb*$^{+/+}$ and *pdgfb*^{ret} MSCs tissues to determine whether there was global effect of the *pdgfb*^{ret} germline mutation on the osteogenic differentiation potential of mutant MSCs. At day 7 after incubation with osteogenic media there was no difference in osteogenic potential between *pdgfb*$^{+/+}$ and *pdgfb*^{ret} mutant MSCs (Figure 6.8A, $p>0.05$). Optical density was also not observed to be significantly greater between *pdgfb*$^{+/+}$ mutant MSCs at day 7 and day 14 (Figure 6.7A, $p<0.05$). Similarly, the osteogenic differentiation potential of mutant MSCs at day 7 was not significantly different form *pdgfb*$^{+/+}$ MSCs at day 14 (Figure 6.7A, $p>0.05$). However, *pdgfb*^{ret} mutant MSCs at day 14 had significantly higher alizarin red levels than both *pdgfb*$^{+/+}$ ($p<0.001$) and *pdgfb*^{ret} mutant MSCs ($p=0.001$) at day 7 and *pdgfb*$^{+/+}$ mutant MSCs at day 14 ($p<0.05$). Furthermore, examination of the data distribution (Figure 6.7C) reveals clusters of low, medium and highly osteogenic mutant tissues at day 14 suggesting, at least for a subset of MSC tissues, that the *pdgfb*^{ret} mutation greatly enhances their osteogenic differentiation capacity. Quantification of the average fold change between day 7 and day 14 for all tissues reveals that the increase in osteogenic capacity is greater for *pdgfb*^{ret} mutant MSCs compared with *pdgfb*$^{+/+}$ MSCs (Figure 6.7B).

Evaluation of the average SD values for all tissues combined also revealed high levels of heterogeneity after 14 days of osteogenic capacity in *pdgfb*^{ret} mutant tissues compared with all other groups (Figure 6.7C, $p<0.001$, $p=0.001$). No differences were observed between any of the other groups after 7 or 14 days of incubation (Figure 6.7C, $p>0.05$). The fold change in SD between 7 and 14 days was not significantly greater for *pdgfb*^{ret} mutant MSCs but was shown to be increased. Taken together, this

data shows that MSCs cultured from *pdgfb*^{ret} mutant tissues have high levels of heterogeneity in terms of their osteogenic differentiation capacity. A subset of *pdgfb*^{ret} mutant MSCs are highly osteogenic, exhibiting high levels of calcium deposition not observed in *pdgfb*$^{+/+}$ MSCs after 14 days of incubation in osteogenic media.

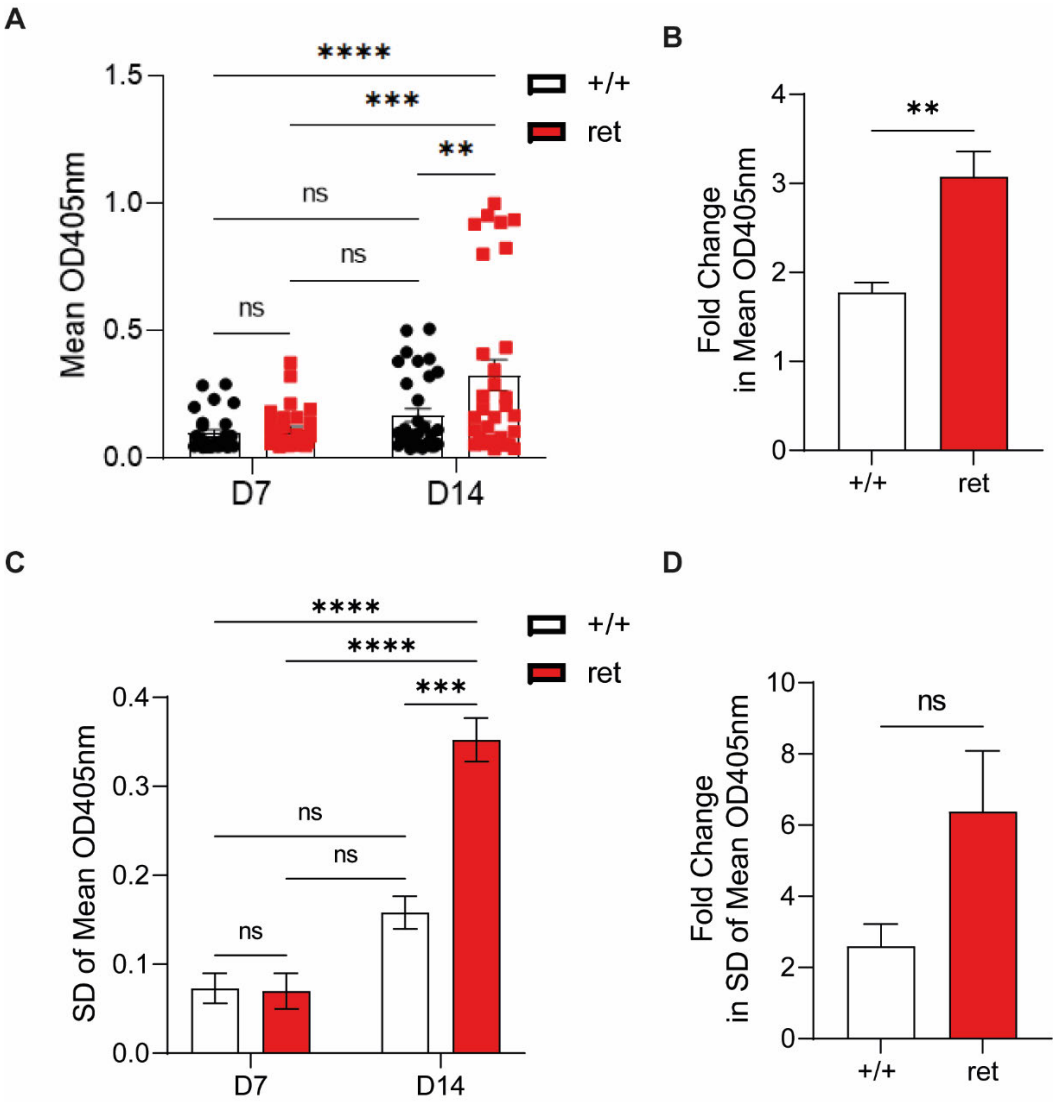

Figure 6.7: Tissues from *pdgfb*^{ret} mutant mice are more osteogenic and exhibit higher levels of heterogeneity in calcium deposition *in vitro.*

Optical density (OD405nm) values for all MSC lines from *pdgfb*$^{+/+}$ (+/+, black circles) and *pdgfb*^{ret} (ret, red squares) mutant tissues; large coronary vessels, hearts, kidneys and skeletal muscle, were collated. The mean OD405nm values after 7 and 14 days of incubation in osteogenic media (**A**), the average fold change in mean OD405nm values from 7 to 14 days for all MSC tissue sources (**B**), the mean standard deviation (SD) of mean OD405nm values (**C**) and the average fold change of SD of mean OD405nm from 7 to 14 days **(D)** was calculated. Data= mean±SEM, two-way ANOVA with Tukey's test or unpaired t-test. n=29-32/group **p<0.001, ***p=0.0001, ****p<0.0001, ns=not significant.

Discussion

In this chapter, I introduced the hypothesis that the *pdgfb*^{ret} mutation affects MSC differentiation potential and suggested that this may be due to pericyte detachment and disruption of pericyte: endothelial cell contact in blood vessels *in vivo*. PDGFB has been shown to play a significant role in modulating PC/MSC behaviour *in vivo* and *in vitro*. We aimed to gain a preliminary understanding of this through establishing MSC cultures and performing *in vitro* MSC osteogenesis assays.

MSC lines from *pdgfb*$^{+/+}$ and *pdgfb*^{ret} mutant tissues exhibited MSC characteristics.

In fulfilment of our primary aim, this study is the first to establish *pdgfb*$^{+/+}$ and *pdgfb*^{ret} mutant MSC lines from multiple tissues that displayed classical MSC characteristics such as a fibroblast-like morphology, plastic adherence, and ability to undergo osteogenic differentiation. The novel observation that MSCs isolated from *pdgfb*^{ret} tissues can undergo osteogenic differentiation suggests that the *pdgfb*^{ret} mutation does not inhibit their differentiation potential *in vitro* but rather enhances this further in a tissue-dependent and time- dependent manner. However, whether MSCs display other classical characteristics was not fully explored.

Both *pdgfb*$^{+/+}$ and *pdgfb*^{ret} mutant MSCs are highly heterogeneous in their osteogenic differentiation capacity.

From the literature, it is established that MSC cultures exhibit high levels of functional heterogeneity, which is one of the main challenges in producing a standardised MSC product for stem cell therapy (Zhou *et al.*, 2021). The tissue source of MSCs has been shown to influence their phenotypic and functional biological characteristics (Craig *et al.*, 2022). Evidence of this exists within my study. I observed an increased fold change of SD from day 7 to 14 in MSC lines from the heart, kidney, and skeletal muscle, however, in the MSCs derived from coronary vessels this was not observed. In the heart, skeletal muscle, and kidneys, MSCs are derived from pericytes of microvessels and capillaries which are directly affected by the *pdgfb*^{ret} mutation. However, in large coronary vessels, the main source of MSCs are adventitial cells as there are smaller

numbers of pericytes found in the large vessel vasa vasorum and sub-endothelial layer. It could be interesting to investigate whether adventitial cells are affected by the *pdgfb*^{ret} mutation *in vivo,* since a previous study showed that large vessel structure is altered being more dilated and with less VSMC layers however they did not investigate changes to the cellular composition of the affected vessels (Nystrom *et al.*, 2006).

Pdgfb^{ret} mutation increases overall MSCs osteogenic differentiation *in vitro.*

A major finding from our study was that *pdgfb*^{ret} mutant MSCs have greater osteogenic potential after 14 days in osteogenic media that *pdgfb*$^{+/+}$ MSCs. Although not significant this trend was observed in each tissue and was significant in combined tissue analysis. However, in PET/CT scans we did not observe any macroscopic calcification out with the brain in the heart, aorta, or kidneys of *pdgfb*$^{ret/ret}$ mice. One factor influencing this could be the fact that *in vivo* the aorta, heart and kidneys lack calcifying stimuli *in vivo* to drive pericyte/MSC osteogenic differentiation. Indeed, the calcifying propensity of sera of *pdgfb*$^{ret/ret}$ mice was identical to *pdgfb*$^{+/+}$ and *pdgfb*$^{ret/+}$ mice who do not develop any ectopic calcification (Zarb *et al.*, 2019). In the brains however the pro-calcifying microenvironment may cause brain calcification in *pdgfb*$^{ret/ret}$ mice (Zarb *et al.*, 2019). *Pdgfb*^{ret} mutant MSCs may have the ability to undergo osteogenesis *in vivo* but lack sufficient osteogenic stimuli. We also observed high heterogeneity in terms of calcium deposition *in vitro* across MSC lines. We observed that increased incubation time leads to increased osteogenic differentiation potential of all MSCs *in vitro*. When we account for the fact that mean and maximum optical density values are consistently higher after 14 days of incubation in osteogenic media in *pdgfb*^{ret} mutant MSCs compared with *pdgfb*$^{+/+}$, it may also suggest that a particular subset of MSCs is more osteogenic than another in the same sample. This is further illustrated when we examine the combined tissue optical density values where clearly a cluster MSC lines obtained from mutant tissues is highly osteogenic. However, what makes this MSC cluster unique in their high osteogenic capacity is unclear.

One hypothesis is that this subset of MSCs are directly derived from partially attached or detached pericytes which exist as a direct consequence of the *pdgfb*^{ret} mutation. The *pdgfb*^{ret} mutation results in altered blood vessel growth, maturation and formation.

This leads to altered capillary and microvessel structure as well as some structural changes in large vessels. Pericytes which are not fully or partially attached may have a different phenotype which may mean they are activated or can more readily differentiate. Previous studies have estimated that *pdgfb*$^{ret/ret}$ mutant mice have a 75% reduction in pericyte coverage in the adult animal and in multiple tissues (Lindblom *et al.*, 2003; Armulik *et al.*, 2010). MSCs expand via clonal expansion *in vitro*, and after a few passages most MSCs in culture may arise from a very few numbers of ancestors which have altered functional properties (Selich *et al.*, 2016). This may, in part, account for the high level of heterogeneity observed in my study.

Evidence from *in vivo* studies to that may support the hypothesis that pericytes from *pdgfb*$^{ret/ret}$ mice have an altered functional properties, is that calcification prone regions of the brain in *pdgfb*$^{ret/ret}$ mice were found to have a higher percentage of pericyte coverage than non-calcified prone areas (Vanlandewijck *et al.*, 2015). This observation, along with further supporting evidence of osteoblast-like, osteoclast-like cells and progenitors found within the calcified regions of *pdgfb*$^{ret/ret}$ brains (Zarb *et al.*, 2019) may indicate that pericytes/MSCs are migrating to the site of calcification and differentiating and undertaking an osteogenic phenotype in response to the pro-calcifying environment. Furthermore, progressive renal dysfunction in pdgfb^{ret} mice was also observed, with structural glomerular abnormalities and deficiency in mesangial cells (pericytes) being observed in late gestation and postnatally (Lindblom *et al.*, 2003). This deficiency was resolved by 1 month of age, which may be due the fact that mesangial pericytes migrate to stabilise glomerular structure. However, pathological glomerulosclerosis and fibrosis was then observed by six months of age which could suggest that pericytes/MSCs have migrated and are activated exacerbating fibrotic disease. Indeed, it has recently been reported that mesenchymal PDGFR signalling dysregulation in mice leads to fibrotic kidney disease (Buhl *et al.*, 2020). My data in conjunction with published data supports the notion that the *pdgfb*^{ret} mutation affecting a subset of pericytes/MSCs enhancing their osteogenic capacity *in vitro*.

A subset of *pdgfb*^{ret} mutant MSCs exhibit high osteogenic potential.

At the level of individual tissues, I did not observe significant differences in the osteogenic capacity of *pdgfb*^{ret} mutant MSCs compared with *pdgfb*$^{+/+}$ counterparts. However, a pattern in increasing osteogenesis and calcium deposition was observed. When all MSC tissues were combined and *pdgfb*$^{+/+}$ and *pdgfb*^{ret} tissues compared, I observed that after 14 days of incubation in osteogenic media, there was significantly higher osteogenic differentiation in tissues from *pdgfb*^{ret} mice. I also recorded a significantly greater fold change from 7 to 14 days in mean optical density values. Furthermore, examination of the data distribution saw low, medium and high level of osteogenesis from MSCs from all *pdgfb*^{ret} tissues after 14 days. Together this data suggests that a population of highly osteogenic MSCs exists in multiple *pdgfb*^{ret} tissues. The significantly increase SD also suggests that after 14 days MSCs from *pdgfb*^{ret} tissues are more heterogeneous in terms of their osteogenic capacity.

I have already discussed the idea that pericytes/MSCs affected with an altered phenotype may be more prone to undergo differentiation depending upon its surrounding cellular and molecular environment but perhaps the *pdgfb*^{ret} mutation may also influence surrounding circulating molecules and the extracellular environment?

The developmental potential of MSCs *in vitro* can be influenced by their environment *in situ* (Gomez-Salazar *et al.*, 2020). In the case of brain calcifications present in *pdgfb*$^{ret/ret}$ mice, the cellular environment is more osteogenic, marked by the presence of osteoblast-like cells expressing Runx2 and endothelial expression ALPL (Zarb *et al.*, 2019). This pro-calcifying environment may in turn effect the behaviour of MSCs *in vitro*. *In vitro*, the fact that none of our MSC cultures spontaneously differentiate supports the need for stimulation by pro-calcifying factors is necessary to initiate MSC differentiation. PDGFB in the brain is released not only by endothelial cells but also neural cells, however, it has been shown that the extent of brain calcification correlates with the release of endothelial PDGFB rather than neuronal PDGFB (Keller *et al.*, 2013). However, whether PDGFB or other members of the same family contribute to brain calcifications directly in *pdgfb*$^{ret/ret}$ mice through their presence and interactions in the surrounding environment is currently unknown. Deletion of the PDGFB retention motif, altering the structure of PDGFB and its tissue distribution may cause other members of the PDGF family to act in a compensatory fashion. Indeed, alongside

PDGFB, PDGFA and PDGFAB are also chemotactic factors for MSCs *in vitro* (Fiedler, Etzel and Brenner, 2004). PDGFAA can also stimulate MSC differentiation into osteoblasts *via* BMP signalling (Li *et al.*, 2014). It would be therefore important to look at the expression levels of other members of PDGF family in multiple tissues to determine whether these molecules play a role in defining the osteogenic phenotype of *pdgfb*^{ret} mutant MSCs *in vitro*.

Future Work

Firstly, I would like to address the question as to whether *pdgfb*^{ret} mutant MSCs from multiple tissues express classical MSC markers. Using immunohistochemistry, I would perform immunocytochemistry and flow cytometry staining for the classical MSC markers, CD73, CD90 and CD105, and investigate whether markers such as CD45, CD19, CD11b, CD34, CD79α and HLA-DR are present. I would assess whether *pdgfb*$^{+/+}$ and mutant MSCs can undergo additional lineage differentiation besides osteogenesis and quantify the results to determine whether mutant MSCs have an enhanced adipogenic and chondrogenic capacity.

In future experiments, I would also separate *pdgfb*$^{ret/+}$ and *pdgb*$^{ret/ret}$ mice into 2 distinct groups to determine whether having two copies of the *pdgfb*^{ret} allele, and by extension, a reduction in pericyte number, may influence MSC behaviour. While initially done, this was not possible due to small number of *pdgb*$^{ret/ret}$ mice obtained from breeding (See Chapter 7: General Discussion). Another experimental modification I would like to evaluate is if further passaging of MSCs would influence their osteogenic potential. The artificial environment in which MSCs are cultured may influence their behaviour. Factors such as culture media, inflammatory stimuli, oxygen tension and the use of 3D scaffolds in culturing all influence MSC *in vitro* behaviour (Hung *et al.*, 2012; Lu *et al.*, 2013; Duval *et al.*, 2017). Expansion in culture may also reduce MSC heterogeneity and provide a more homogenous MSC population (Russell *et al.*, 2010). However, because of this, MSCs may lose some intrinsic biological properties from the niche environment from which they were obtained.

I would also like to perform further characterisation to confirm the identity of osteogenic MSCs *in situ*. As previously stated, MSCs are derived from both pericytes and adventitial cells however one limitation of the current study is that I did not distinguish

between MSCs derived from either cell type. Further experiments are required to investigate the role of *pdgfb*^{ret} mutation on prospectively isolated adventitial cell-derived and pericyte-derived MSCs from various mutant *pdgfb*^{ret} tissues, independently. To expand upon our study and investigate the identity of osteogenic *pdgfb*^{ret} MSCs *in situ* fully, I would perform cell sorting to separate and isolate pericytes and adventitial cells from *pdgfb*$^{+/+}$ and mutant tissues. In humans, it was shown that pericytes can be sorted by the expression of CD146, and their lack of expression of CD34, CD56 and CD45 and adventitial cells may be sorted by CD34 expression and lack of CD31, CD146 and CD45 (Crisan *et al.*, 2012). This would indicate if the *pdgfb*^{ret} mutation affects pericyte or adventitial cell behaviour or perhaps both. Transgenic mouse models, crossed with *pdgfb*$^{ret/ret}$ mice, such as PDGFRβ-GFP, NG2-GFP and Tbx-18 mice would also be useful in assessing pericyte phenotype using flow cytometry.

Since we observed an increased in calcium deposition in *pdgfb*^{ret} MSCs, I would also like to investigate potential transcriptional changes in these cells from all tissues. It would be important to perform RT-qPCR at both 7 and 14 days for osteoprogenitor markers such as RUNX2 and OSX and osteoblast markers, ALPL, COL1A1, COL2A1 and OPN and OCN (Choi *et al.*, 2017) to determine if these are up-regulated. This would indicate whether pdgfb$^{ret/+}$ and *pdgfb*$^{ret/ret}$ MSCs are indeed “primed” towards osteogenesis. Furthermore, I would increase the length of incubation in osteogenic media to determine if this would further enhance the osteogenic capacity of mutant MSCs compared with their *pdgfb*$^{+/+}$ counterparts. It would also be informative to perform RNA sequencing of both *pdgfb*$^{+/+}$ and *pdgfb*^{ret} MSCs derived from multiple organs to identify potential novel markers of osteogenesis that may be involved in vascular calcification. Assessment of the transcriptional phenotype after multiple passages could be performed as perhaps some functional characteristics could be lost with repeated passaging or due to clonal selection and expansion *in vitro*.

Although I hypothesised that phenotypic and functional differences may arise in pericytes, I cannot rule out the possibility that adventitial cells or other cells within the vascular niche may have an altered phenotype. Interestingly, a recent study has described phenotypic changes to endothelial cells lacking pericyte coverage in the blood-brain-barrier (BBB) of *pdgfb*$^{ret/ret}$ mice (Mäe *et al.*, 2021). Using RNA sequencing, Mae and collaborators observed that endothelial cells lacking pericyte

contact retain a BBB specific gene profile, however, their molecular pattern is altered to arterio-venous like state exhibiting changes to growth factors and regulatory proteins (Mäe *et al.*, 2021). Whether this happens to other blood vessel cells in *pdgfb*$^{ret/ret}$ mice in unknown. We observed that large coronary vessels derived MSCs displayed high levels of osteogenesis, this could be in part due to the activity of adventitial derived MSCs rather than those from pericytes. It would therefore be interesting to explore changes to pericyte and other vascular cells' phenotype in *pdgfb*$^{ret/ret}$ mice at the transcriptional and protein level. In addition to sorting experiments, it would be important to characterise both pericytes and adventitial cells in their native niche *in vivo* via immunostaining of the coronary vessels, heart, skeletal muscle, and kidneys. A combination of the cellular markers above could be utilised as they have also been shown to be expressed in mouse pericytes. Other markers to use in immuno-characterisation on frozen or paraffin embedded tissues sections would NG2, αSMA, PDGFRβ, CD34, PDGFRα and Gli-1 all of which have been utilised to identify subsets of perivascular cell populations. Characterization of perivascular cells on sections would also confirm the presence of pericytes which are partially or not fully attached to endothelial cells and may reveal unique markers to separate them from other pericyte populations. It would also be important to use other perivascular cell markers such as NG2 and PDGFRβ in sorting and perform further functional characterisation to determine if different pericyte subsets located within the same tissue, give rise to MSCs displaying altered functional behaviour *in vitro.*

Histological analysis should be performed to full assess blood vessel structure in *pdgfb*^{ret} mutant mice. The use of adventitial markers and histological examination of the adventitia would also indicate whether alterations to the adventitia are present due to the *pdgfb*^{ret} mutation.

Another important set of experiments to conduct would be to determine whether we can attenuate osteogenesis using pharmacological agents *in vitro.* This could be combined with transcription and protein analysis to identify potential molecular targets. Molecules and pharmacological agents have been used to inhibit MSC osteogenesis such as TGFβ3 and naproxen (Moioli, Hong and Mao, 2007; Salem *et al.*, 2014). The use of selective inhibitors would also allow us to determine which pathways contribute to a greater extent driving osteogenesis of MSCs *in vitro*. This may lead to the

identification of novel regulators MSC osteogenic capacity which may enhance vascular calcification and could be targeted *in vivo*.

Conclusion

MSCs are highly heterogenous in terms of their *in vitro* osteogenic potential. *Pdgfb*^{ret} MSCs from all tissues examined display greater osteogenic potential than *pdgfb*$^{+/+}$ counterparts with a subset of highly osteogenic MSCs being identified and this trend is observed when examining each tissues individually. However, more work is required to address further questions arising from our preliminary study and fully characterise the effect of the *pdgfb*^{ret} mutation on MSC biology and function *in vitro*.

Chapter 7: General Discussion and Future Directions

PDGFB/PDGFRβ signalling is important in the development, maintenance, and repair of the cardiovascular system. In this thesis, I aimed to characterise and understand the effects of the *pdgfb*^{ret} mutation on cardiovascular homeostasis using *in vivo* PET/CT and ultrasound imaging, combined with *in vitro* MSC assays. I wished to determine the effect of the *pdgfb*^{ret} mutation on; ectopic extracerebral vascular calcification; cardiac structure and function and the osteogenic potential of mutant MSCs. I also wished to understand whether the sex and age of *pdgfb*$^{ret/ret}$ mice would influence cardiovascular physiology.

Vascular calcification in 12-month-old *pdgfb*$^{ret/ret}$ mutant mice is restricted to the brain.

PDGFs have been implicated, through various mechanisms, to drive vascular calcification. *Pdgfb*$^{ret/ret}$ mice have been validated as a model of idiopathic basal ganglia calcification (IBGC), a condition associated with PDGFB and PDGFRβ mutations in humans (Keller *et al.*, 2013). Importantly, IBGC male patients have a greater extent of calcification than females. In chapter 3, I aimed to determine whether microvascular-associated calcified lesions are restricted to the brain in *pdgfb*$^{ret/ret}$ mice using whole body PET/CT imaging using the radioisotope ^{18}F-NaF activity which binds specifically to calcium deposits and can distinguish between macro and microcalcification. I hypothesised that due to the global nature of the *pdgfb*^{ret} mutation this may lead to extracerebral vessel and tissue calcification.

In confirmation of previous studies, 5/6 *pdgfb*$^{ret/ret}$ mice, 4 male and 2 female, in our cohort developed macroscopic calcium deposition detected on CT scans in regions associated with the thalamus and the pons. However, the extent and regions of calcium deposition showed high levels of interindividual variation. Although we wished to determine the effect of sex on the extent on calcification this was not possible due to the small number of female mice utilised. However, from the scans we were able to conduct, male *pdgfb*$^{ret/ret}$ mice did appear to have a greater extent of vascular calcification than females. However, in disagreement with my preliminary

observations, another study did not report any differences in the amount of brain calcification between male and female *pdgfb*$^{ret/ret}$ mice although this was based on a relatively small (n=3/sex) sample size and they were not explicitly looking for this effect (Zarb *et al.*, 2019). The effect of sex on rodent models of vascular calcification can be model dependent. DBA are the oldest inbred mouse strain which have been previously reported to develop soft tissue calcification (Yamate *et al.*, 1987). They also develop vascular calcification naturally with females being more prone to this phenomenon than males (Herrmann *et al.*, 2020). CY rats, with autosomal dominant polycystic kidney disease caused by a spontaneous mutation in the *Pkdr1* gene, develop calcified lesions with males rats being more greatly affected that females (Moe *et al.*, 2009; Nagao *et al.*, 2010). Fetuin-A is a glycoprotein which carries free fatty acids in the circulation and elevated in patients suffering from obesity, diabetes and metabolic syndrome (Trepanowski, Mey and Varady, 2014). Fetuin-A$^{-/-}$ mice have a healthy lifespan but female ex-breeders (that had been pregnant previously) develop ectopic calcification in the lung, heart and kidneys which may be exacerbated by mineral or vitamin D rich feeding (Jahnen-Dechent *et al.*, 1997). These examples illustrate that sex differences in preclinical models of vascular calcification can depend upon the model being utilised and that understanding these differences may lead us to a greater understanding of disease processes in *pdgfb*$^{ret/ret}$ mice.

Our study is the first to show differences in the extent of heterogeneity in terms of the location within the brains of *pdgfb*$^{ret/ret}$ mice. However, the underlying cause was not clear. One suggestion may be due to variability in tissue distribution of the PDGFBret protein during development meaning some mice have a less exaggerated phenotype than others. However, this hypothesis may be difficult to test. One method may be to test the level of PDGFB present in calcified brain areas as a greater level of PDGFB may correlate with increased calcification. This may be done at the transcriptional and protein using qPCR and western blot. Although this is speculation, this theory may be true as indeed a greater number of pericyte-like cells where identified in calcified lesions in *pdgfb*$^{ret/ret}$ mice (Vanlandewijck *et al.*, 2015) and may have been recruited there by accumulation of the PDGFBret protein in areas with calcified lesions. To further investigate the variability in the extent of *pdgfb*$^{ret/ret}$ mice a greater number of mice should be scanned with PET/CT alongside complementary histological analysis.

In previous studies investigating various aspects of *pdgfb*$^{ret/ret}$ physiology, both *pdgfb*$^{+/+}$ and *pdgfb*$^{ret/+}$ mice were pooled together as controls. Indeed, some studies remarks that *pdgfb*$^{ret/+}$ mice are "indistinguishable" from *pdgfb*$^{+/+}$ littermates (Raines *et al.*, 2011). However, differences in lung structure and brain pericyte coverage were observed in *pdgfb*$^{ret/+}$ heterozygous mice compare to *pdgfb*$^{+/+}$ mice (Pan *et al.*, 2020; Mäe *et al.*, 2021). This may also be the case in other aspects of *pdgfb*$^{ret/+}$ physiology and development. For this reason, I decided to analyse these mice separately. No macroscopic calcium deposition was observed in the brains of either male or female *pdgfb*$^{+/+}$ and *pdgfb*$^{ret/+}$ mice in my cohort.

Whole-body CT scans of aorta, heart and kidneys revealed that these tissues did not develop macroscopic calcified lesions in *pdgfb*$^{+/+}$, *pdgfb*$^{ret/+}$ and *pdgfb*$^{ret/ret}$ mice. Contrary to our initial hypothesis this would suggest that *pdgfb*$^{ret/ret}$ mice do not develop extracerebral vascular calcification after 12 months. Other genetically modified mouse models of vascular calcification typically have a very severe phenotype and die at a relatively young age. Fibroblast growth factor-23 (FGF-23) is produced in the bone and suppress phosphate and vitamin D reuptake in the kidney (Erben, 2018). Deletion of FGF-23 in mice results elevated serum calcium and vitamin D causing kidney calcification and a severely reduced lifespan of a maximum of 13 weeks (Shimada *et al.*, 2004; Razzaque *et al.*, 2006). Deletion of the membrane bound receptor of FGFs in mice known as Klotho, results in a considerably reduced lifespan of around 9 weeks and development of medial aortic calcification (Kuro-o *et al.*, 1997; Hum *et al.*, 2017). Therefore, *pdgfb*$^{ret/ret}$ mice are advantageous over these models as it has a normal life span and can be used to understand the effects of aging and vascular calcification which more closely mimics the human condition. Although *pdgfb*$^{ret/ret}$ mice did not develop vascular calcification in extracerebral locations such as the aorta, heart or kidneys additional microenvironmental cues may be necessary to induce calcification which could be tested in future experiments. For example, in previous studies in other models', vascular calcification was induced by modifications to or a combination of dietary factors This includes increasing vitamin D, phosphate, and cholesterol intake (Lopez *et al.*, 2008; Graciolli *et al.*, 2009; Assmann *et al.*, 2014). There already exists a *pdgfb*$^{ret/ret}$ *ldlr*$^{-/-}$ model which has been used to investigate atherosclerotic development after 10 weeks on a high fat diet (Tillie *et al.*, 2021). However, mice were only 25 weeks old and only male mice were utilised. In future studies, both male and

female *pdgfb*$^{ret/ret}$ *ldlr*$^{-/-}$ mice at 12 months and beyond, combined with PET/CT imaging, would elucidate the sex and aging effects on atherosclerosis and vascular calcification. Another possible way in which vascular calcification could be induced is using a Proprotein convertase subtilisin/kexin type 9(PCSK-9) – adeno-associated virus vector (AAV) (Roche-Molina *et al.*, 2015). PCSK-9 plays a key role in cholesterol homeostasis by reducing low density lipoprotein receptors levels. Use of PCSK-9 AAV delivery combined with a high fat diet resulted in progressive aortic calcification development between 15-20 weeks in wild-type C57BL6/J mice without genetic modification (Goettsch *et al.*, 2016). The use of this method in *pdgfb*$^{ret/ret}$ mice would allow the effect of sex and aging to be studied without further crossing with other mouse lines.

Early cardiac dilatation in male and female *pdgfb*$^{ret/ret}$ mice was resolved by 12 months of age.

Previously, male *pdgfb*$^{ret/ret}$ mice were shown to develop changes to left ventricular structure by 20 weeks of age (Nystrom *et al.*, 2006). Sex plays an important role in the progression of cardiovascular development and disease in both humans and rodents. In chapter 4, using high resolution echocardiography, I investigated the effects of the *pdgfb*^{ret} mutation in aging male and female mice. I were driven by the hypothesis that early changes to cardiac structure may cause a deterioration in the heart function. We observed for the first time that not only male but also female *pdgfb*$^{ret/ret}$ mice exhibit signs of cardiac dilation during early cardiac development. In males, these changes were ameliorated by 6 months of age and in females, changes persisted up to 9 months which indicates different physiological processes in cardiac development in male and female mice. By 12 months no differences were observed between male and female mutant mice and their *pdgfb*$^{+/+}$ and *pdgfb*$^{ret/+}$ littermates. Furthermore, contraction of the heart was not adversely affected at any time point. Combined with the absence of cardiac hypertrophy this would suggest that changes observed in both male and female *pdgfb*$^{ret/ret}$ mice are physiological in nature. However why cardiac dilation resolves over time is unknown. A similar phenotype has been reported following endothelial specific deletion of PDGFB using *Tie1Cre*$^{+}$*, Pdgfb lox/–* mice. This model exhibits similar embryonic heart defects to *pdgfb* null mice at E18.5 but

like *pdgfb*$^{ret/ret}$ mice, they survive into adulthood. Interestingly, heart morphology in *Tie1Cre*$^{+}$*, Pdgfb lox/–* mice began to normalise by 1, 6 and 12 months although no analysis of function was performed (Bjarnegård *et al.*, 2004). This suggests that exposure to endothelial released PDGFBret in *pdgfb*$^{ret/ret}$ mice during development influences later heart structure and function which is resolved in adulthood. It would be interesting to see if similar developmental defects exist in *pdgfb*$^{ret/ret}$ mice in late embryonic and early postnatal development which may normalise with age as observed with morphological changes in the kidneys of *pdgfb*$^{ret/ret}$ mice (Lindblom *et al.*, 2003).

Ventricular dilatation can be caused by volume overload stimulating the production of new sarcomere in series with existing sarcomeres. In *pdgfb*$^{ret/ret}$ mice, volume overload could be induced due to the increased in the blood vessel diameter in the systemic vasculature and capillary beds. Indeed, the aortas of *pdgfb*$^{ret/ret}$ mice have an increased diameter and morphological changes to capillary structure have been demonstrated (Nystrom *et al.*, 2006). As previously suggested blood volume of *pdgfb*$^{ret/ret}$ mice could be measured alongside intramyocardial blood flow using SPECT imaging. In humans blood volume may decline with age and this may also be the case in mice using SPECT imaging would indicate whether changes blood volume in aging may be driving changes in heart structure in *pdgfb*$^{ret/ret}$ mice.

Cardiac dilation may also be a result of oedema in the cardiac tissue caused by increased vascular permeability. This has been demonstrated to some extent in previous studies using a dextran permeability assay; however, it was not specified whether male or females hearts were used nor was the age of the mice (Raines *et al.*, 2011). Aging is known to increase vascular permeability into tissues, particularly in microvessels (Oakley and Tharakan, 2014). Therefore, future investigations could assess vascular permeability using dextran permeability assays on histological cardiac sections from different adult stages from *pdgfb*$^{ret/ret}$ mice as changes to vascular permeability could contribute to the changes in left ventricular structure.

Results from STE also indicated some alterations to segmental strain in *pdgfb*$^{ret/ret}$ mice indicative of diastolic dysfunction. However, this was in a combined cohort of males and females and as such the effect of sex cannot be considered. Changes in segmental strain can preclude reductions in cardiac function. It would therefore be

important to repeat this analysis in separated groups of males and females as this would indicate whether both sexes have altered segmental diastolic function. Strain analysis saw several changes at 9 months of age to segmental radial and longitudinal strain and reverse radial and longitudinal strain suggesting dynamic changes to the myocardium in *pdgfb*$^{ret/ret}$ mice at this time point. Changes occurred commonly on the posterior and anterior wall however of all segments the apex was most effected. It would therefore be important to perform histological analysis on the hearts to understand the cellular changes taking place in those regions. The structure of cardiomyocytes may change in these areas as opposed to others so assessment of their cross-sectional area on histological sections with wheat germ agglutin staining, which marks cellular borders, could be performed.

Pdgfb^{ret} mutant MSCs possess high osteogenic potential.

MSCs are derived from pericytes *in vivo* with PDGFB/PDGFRβ signalling playing a key role in modulating both MSC and pericyte biology. In chapter 6, I wished to establish whether the effects of the *pdgfb*^{ret} mutation would affect MSC osteogenic differentiation potential *in vitro*. Pericytes/MSCs from multiple organs are highly heterogenous in terms of their phenotype and function. We were first able to establish MSC colonies from large coronary vessels, the heart, kidney and skeletal muscle of 3-month-old *pdgfb*$^{+/+}$ and *pdgfb*^{ret} mutant mice which displayed a classical MSC spindle-like morphology and could adhere to plastic. In future studies, further phenotypic characterisation of these cells should be performed by fluorescent staining for MSC markers to fully confirm their identity.

We next performed osteogenic differentiation assays and analysed the cells at 7 and 14 days. Little difference was observed between *pdgfb*$^{+/+}$ and *pdgfb*^{ret} mutant osteogenic potential at 7 days but by 14 days in all tissues, there was an increase in osteogenesis as measured by quantification of Alizarin Red staining. High variation was observed in calcium deposition *in vitro* in both *pdgfb*$^{+/+}$ and *pdgfb*^{ret} mutant MSCs from all tissues, and thus, no significant differences were observed between the groups. This is not a surprise. It is well accepted that MSCs are heterogeneous and contain cells from different origins including pericytes and adventitial cells (Crisan *et*

al., 2008; Corselli, *et al.*, 2012). Cell sorting based on adventitial or pericyte markers prior to seeding them into culture could help to distinguish the effects of *pdgfb*^{ret} mutation on the MSC derived from pericytes from those derived from adventitial cells in culture MSCs have been shown to expand via clonal expansion. Here certain clones are selected for and prosper whereas others do not survive in culture (Pittenger *et al.*, 2019). The mechanisms behind this are poorly understood but this may account for some heterogeneity experienced in our cultures. When we combined MSC samples from all *pdgfb*$^{+/+}$ tissues and compared with combined tissues from *pdgfb*$^{+/+}$ mice and *pdgfb*^{ret} mutants, a significant increase in osteogenic potential was observed in mutants. This indicates that independent of variation from each tissue MSCs from *pdgfb*^{ret} mutant mice have higher osteogenic potential.

Interestingly, the results from our osteogenic assays *in vitro* did not recapitulate what we observed on the PET/CT scans. Indeed, *in vivo,* we observed no extracerebral macrocalcification in *pdgfb*^{ret} mutants. In our experiments, MSCs were isolated from young mice (3 months old) and PET/CT scans were performed in 12-month-old mice. In human MSC transplants the donor age can affect the performance and the outcome. Human bone marrow MSCs from older donors have lower osteogenic and proliferative capacities *in vitro* than those from juvenile donors (Zhou *et al.*, 2008). Aged adipose derived MSCs from humans also exhibit more senescent features with reduced cell viability and increased cell apoptosis (Choudhery *et al.*, 2014). Furthermore, aged adipose MSCs also had reduced adipogenic and osteogenic capacities (Choudhery *et al.*, 2014). Several other studies have shown that aged MSCs *in vivo* have reduced trilineage differentiation capacity (Yang, 2018). Age may therefore affect the differentiation potential of *pdgfb*^{ret} mutant MSCs *in vivo* and may partly explain the differences we observed. To test in the future, osteogenic assays should be performed in MSCs isolated from multiple tissues of young and aged *pdgfb*^{ret} mutant mice. We did attempt to establish MSC lines from 12-month-old mice however perhaps due to the effects of radiation post-PET scanning and staying overnight in the fridge the cells did not survive. In the future given a greater number of aged mice MSC cultures in mice which had not undergone PET scans.

Limitations

This study provides novel insights into the role of *pdgfb*^{ret} mutation on the cardiovascular homeostasis in male and female mice. The strength of this study is that it uses state-of-the-art *in vivo* imaging combined with *in vitro* assays to accomplish this. However, some limitations to the study exist.

Breeding *Pdgfb*$^{ret/ret}$ mice

The main limitation of the study was the small number of *pdgfb*$^{ret/ret}$ mice we obtained through breeding. It was previously reported that female *pdgfb*$^{ret/ret}$ mice have reduced fertility (Lindblom *et al.*, 2003). For that reason, we bred male and female *pdgfb*$^{ret/+}$ mice to get homozygous and heterozygous offspring. Although previous studies report that the pdgfb-ret allele showed mendelian inheritance (Lindblom *et al.*, 2003), in our experience this was not the case. Often litters would be born without any *pdgfb*$^{ret/ret}$ mice consisting solely of *pdgfb*$^{+/+}$ and *pdgfb*$^{ret/+}$ mice. The exact reason for this is unclear. Another issue in our experience with breeding *pdgfb*^{ret} mice was that often female mice would eat their young after birth. Often pups would be born but by the time we were allowed to take tissue for genotyping (post-natal day 14) a very small number of pups remained. We were able however to genotype some dead pups found in the cage as we wished to understand whether mothers were selectively killing the *pdgfb*$^{ret/ret}$ mutant neonates over *pdgfb*$^{+/+}$ and *pdgfb*$^{ret/+}$ neonates. However, the results of this genotyping indicated that mother mice also killed *pdgfb*$^{+/+}$ and *pdgfb*$^{ret/+}$ pups. The reason for this is unknown but could be due to the stress of giving birth, back crossing of the mice, an unreported behaviour issue or stress due construction works being carried our very close to the animal facility producing noise and vibrations. To circumvent this problem in the future foster mothers could be utilised after birth of litters to separate pups from mothers. This would hopefully lead to a greater yield of surviving *pdgfb*$^{ret/ret}$ mice being available for use in future studies.

In the lab the *pdgfb*^{ret} mouse line was also utilised to study its effect on haematopoiesis at embryonic stages. As discussed, global deletion of PDGFB and PDGFRβ mice die perinatally due to haemorrhaging and leakage of blood vessels (Van Den Akker *et al.*, 2008). To determine whether some *pdgfb*$^{ret/ret}$ mice die *in utero,* I examined embryonic genotyping data from the lab (provided by Diana Sa da Bandeira) as well as birth records from Tick@Lab database. Here, I wished to determine whether there were a

greater number of *pdgfb*$^{ret/ret}$ mice present in litters from embryonic development than after birth as this may indicate a developmental defect causing embryonic lethality.

A

		Total Number of Embros or Mice			Percentage of Total (%)		
Stage of Development	Number of Litters	+/+	ret/+	ret/ret	+/+	ret/+	ret/ret
E9.5	1	0	3	4	77.78	22.22	0.00
E10	1	3	3	2	55.56	22.22	22.22
E10.5	4	7	16	13	31.63	28.57	39.80
E11	21	39	101	62	31.63	33.67	34.69
E11.5	2	4	5	5	46.46	20.20	33.33
E14	2	0	12	2	0.00	80.00	20.00
E Total	31	53	140	88	18.37	50.00	31.63
≥P14	N/A	247	426	27	35.71	61.22	3.06

B

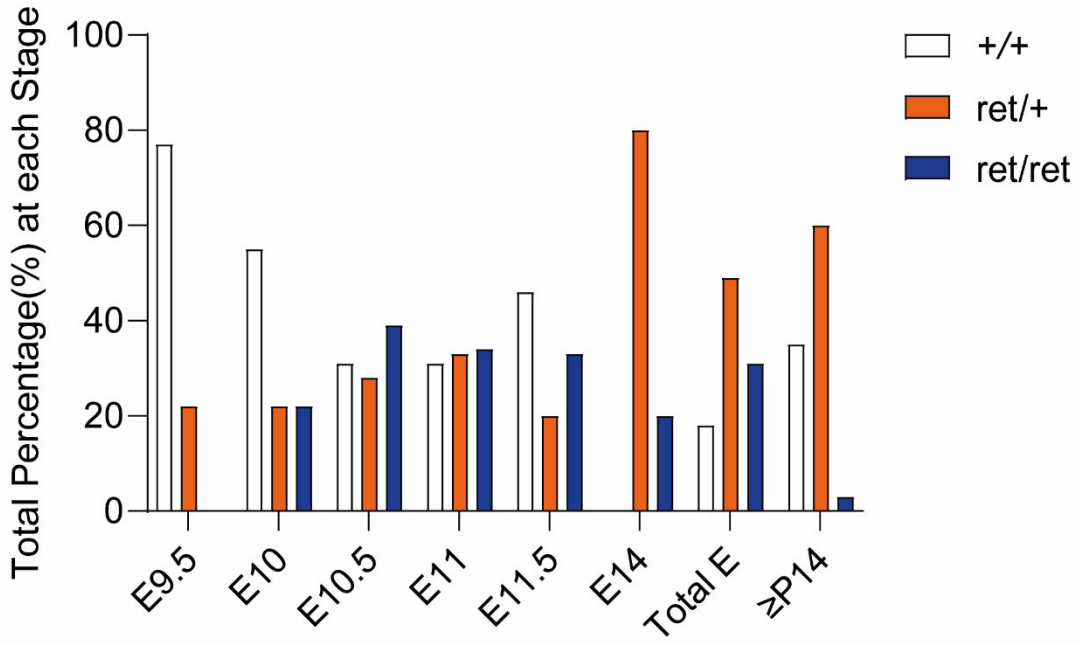

Figure 7.1: A small number of *pdgfb*$^{ret/ret}$ mice survive to postnatal day 14.

The table shows the total number of embryos obtained or at each developmental stage or mice born from genotyping records and the tick@ lab database (**A**). It also shows the percentage of *pdgfb*$^{+/+}$ (+/+), *pdgfb*$^{ret/+}$ (ret/+) and *pdgfb*$^{ret/ret}$ (ret/ret) embryos at each developmental stage with 100% being the sum of +/+, ret/+ and ret/ret, E=Embryonic Day P= postnatal day; E Total= The sum of all mice of each genotype born at embryonic stages; P=Postnatal day. The percentage of mice at each embryonic stage is also shown in graphical form (**B**).

In terms of absolute numbers, a higher number of *pdgfb*$^{+/+}$ (247) and *pdgfb*$^{ret/+}$ (426) mice than *pdgfb*$^{ret/ret}$ (27) mice survived to P14. (Figure7.1A). In terms of the percentage of total mice at P14 *pdgfb*$^{ret/ret}$ account for only 3% of total mice whereas *pdgfb*$^{+/+}$ and *pdgfb*$^{ret/+}$ account for 35% and 62% respectively (Figure7.1A). This differs greatly from what is observed during embryonic development. At each stage of embryonic development at least 2 *pdgfb*$^{ret/ret}$ embryos were found (Figure7.1A) with the total number of embryonic *pdgfb*$^{ret/ret}$ embryos being 88 vs 53 for *pdgfb*$^{+/+}$ and 140 *pdgfb*$^{ret/+}$ embryos. The percentage of the total number of embryos for each genotype was 18% *pdgfb*$^{+/+}$, 50% *pdgfb*$^{ret/+}$ mice and 32% *pdgfb*$^{ret/ret}$. There is approximate 10x fold reduction in the number of *pdgfb*$^{ret/ret}$ mice at P14 vs during embryonic development at all stages (Figure 7.1B). However, we do not have data available for beyond E14 so cannot determine This may indeed suggest that a subset or sizeable percentage of these mice may die in utero or perinatally. This could be due developmental defects or due to the issues listed above but may also be due to killing by mother mice. To fully address this issue, further studies into the embryonic development of *pdgfb*$^{ret/ret}$ mice should be performed to identify any possible haematological defects pre-birth.

Effect of the Coronavirus Pandemic

In March 2020 the first UK coronavirus lockdown was put into place meaning that many in the research community experienced significant disruption to their research. This was particularly impactful on the final experiments in my final year of PhD. We had planned to perform PET/CT scan on one final 12-month-old female *pdgfb*$^{ret/ret}$ mouse which would allow some statistical analysis to be performed and give us a greater indication of the effects of sex on *pdgfb*$^{ret/ret}$ mice on ectopic calcification. This was due to the fact that all animal experiments had to stop and also ^{18}F-NaF production from the clinic was halted and afterwards markedly reduced. Autoradiography on tissue sections from one year old mice could not be performed. Furthermore, we also had to cease breeding and greatly reduce the number of mice in all our colonies. At this time, all non-essential breeding had to stop, and breeding could only be done for colony maintenance. Due to financial and time constraints we

could not breed further mice for use in the time that I had left for completion of my PhD.

Conclusion

Overall, this investigation has provided novel insights into how disruption of normal PDGFB/PDGFRβ signalling affects cardiovascular homeostasis *in vivo* and *MSC* osteogenic differentiation *in vitro.* We have shown that male and female *pdgfb*$^{ret/ret}$ mice exhibit differences in early cardiac development which are ameliorated by 12 months of age and that *pdgfb*$^{ret/ret}$ mice do not develop extracerebral vascular calcification. This information is essential and make this model an ideal *in vivo* model for neuroscientists to study brain calcification (if efficient breeding would allow). We have also shown for the first time that MSC osteogenic differentiation potential is increased by the *pdgfb*^{ret} mutation; however, the mechanism driving these changes requires further investigation.

References

Aird, W. C. (2011) 'Discovery of the cardiovascular system: from Galen to William Harvey', *Journal of Thrombosis and Haemostasis*. John Wiley & Sons, Ltd, 9(1 S), pp. 118–129. doi: 10.1111/J.1538-7836.2011.04312.X.

Van Den Akker, N. M. S. S. *et al.* (2008) 'PDGF-B signaling is important for murine cardiac development: Its role in developing atrioventricular valves, coronaries, and cardiac innervation', *Developmental Dynamics*. Wiley-Liss, Inc., 237(2), pp. 494–503. doi: 10.1002/dvdy.21436.

Alex, L. and Frangogiannis, N. G. (2019) 'Pericytes in the infarcted heart', *Vascular Biology*. Bioscientifica Ltd, 1(1), pp. H23–H31. doi: 10.1530/VB-19-0007.

Alliot, F. *et al.* (1999) 'Pericytes and Periendothelial Cells of Brain Parenchyma Vessels Co-Express Aminopeptidase N, Aminopeptidase A, and Nestin', *J. Neurosci. Res*, 58, pp. 367–378. doi: 10.1002/(SICI)1097-4547(19991101)58:3.

Andrae, J., Gallini, R. and Betsholtz, C. (2008) 'Role of platelet-derived growth factors in physiology and medicine.', *Genes & development*. Cold Spring Harbor Laboratory Press, 22(10), pp. 1276–312. doi: 10.1101/gad.1653708.

Armulik, A. *et al.* (2010) 'Pericytes regulate the blood–brain barrier', *Nature 2010 468:7323*. Nature Publishing Group, 468(7323), p. 557. doi: 10.1038/nature09522.

Arnegard, M. E. *et al.* (2020) 'Sex as a Biological Variable: A 5-Year Progress Report and Call to Action', *https://home.liebertpub.com/jwh*. Mary Ann Liebert, Inc., publishers 140 Huguenot Street, 3rd Floor New Rochelle, NY 10801 USA , 29(6), pp. 858–864. doi: 10.1089/JWH.2019.8247.

Assmann, A. *et al.* (2014) 'The degeneration of biological cardiovascular prostheses under pro-calcific metabolic conditions in a small animal model', *Biomaterials*. Biomaterials, 35(26), pp. 7416–7428. doi: 10.1016/J.BIOMATERIALS.2014.05.034.

Avolio, E. *et al.* (2015) 'Combined Intramyocardial Delivery of Human Pericytes and Cardiac Stem Cells Additively Improves the Healing of Mouse Infarcted Hearts Through Stimulation of Vascular and Muscular RepairNovelty and Significance', *Circulation Research*, 116(10).

Basciani, S. *et al.* (2004) 'Expression of Platelet-Derived Growth Factor (PDGF) in the Epididymis and Analysis of the Epididymal Development in PDGF-A, PDGF-B, and PDGF Receptor β Deficient Mice', *Biology of Reproduction*. Oxford Academic, 70(1), pp. 168–177. doi:

10.1095/BIOLREPROD.103.019232.

Bauer, M. *et al.* (2013) 'Regional Cardiac Dysfunction and Dyssynchrony in a Murine Model of Afterload Stress', *PLoS ONE*. Public Library of Science, 8(4), p. 59915. doi: 10.1371/JOURNAL.PONE.0059915.

Bennett, M. R., Sinha, S. and Owens, G. K. (2016) 'Vascular smooth muscle cells in atherosclerosis', *Circulation research*. NIH Public Access, 118(4), p. 692. doi: 10.1161/CIRCRESAHA.115.306361.

Betsholtz, C. and Keller, A. (2014) 'PDGF, pericytes and the pathogenesis of idiopathic basal ganglia calcification (IBGC)', *Brain pathology (Zurich, Switzerland)*. Brain Pathol, 24(4), pp. 387–395. doi: 10.1111/BPA.12158.

Bhatnagar, P. *et al.* (2015) 'The epidemiology of cardiovascular disease in the UK 2014', *Heart*. BMJ Publishing Group, pp. 1182–1189. doi: 10.1136/heartjnl-2015-307516.

Birbrair, A. *et al.* (2014) 'Type-1 pericytes accumulate after tissue injury and produce collagen in an organ-dependent manner', *Stem Cell Research and Therapy*. BioMed Central Ltd., 5(6), pp. 1–18. doi: 10.1186/SCRT512/FIGURES/9.

Bischoff, J. (2019) 'Endothelial-to-Mesenchymal Transition', *Circulation research*. Circ Res, 124(8), pp. 1163–1165. doi: 10.1161/CIRCRESAHA.119.314813.

Bjarnegård, M. *et al.* (2004) 'Endothelium-specific ablation of PDGFB leads to pericyte loss and glomerular, cardiac and placental abnormalities', *Development*. The Company of Biologists, 131(8), pp. 1847–1857. doi: 10.1242/DEV.01080.

Blau, M., Ganatra, R. and Bender, M. A. (1972) '18F-fluoride for bone imaging', *Seminars in Nuclear Medicine*. W.B. Saunders, 2(1), pp. 31–37. doi: 10.1016/S0001-2998(72)80005-9.

Blenck, C. L. *et al.* (2016) 'The Importance of Biological Sex and Estrogen in Rodent Models of Cardiovascular Health and Disease', 118(8), pp. 1294–1312. doi: 10.1161/CIRCRESAHA.116.307509.

Boheler, K. R. *et al.* (1991) 'Skeletal actin mRNA increases in the human heart during ontogenic development and is the major isoform of control and failing adult hearts.', *Journal of Clinical Investigation*. American Society for Clinical Investigation, 88(1), p. 323. doi: 10.1172/JCI115295.

Bortolotti, F. *et al.* (2015) 'In Vivo Therapeutic Potential of Mesenchymal Stromal Cells Depends on the Source and the Isolation Procedure', *Stem Cell Reports*. Elsevier, 4(3), p. 332. doi: 10.1016/J.STEMCR.2015.01.001.

Brenner, D. J., Hall, E. J. and Phil, D. (2007) 'Computed Tomography — An Increasing Source of

Radiation Exposure', *https://doi.org/10.1056/NEJMra072149*. Massachusetts Medical Society , 357(22), pp. 2277–2284. doi: 10.1056/NEJMRA072149.

Brinton, R. D. (2012) 'Minireview: Translational Animal Models of Human Menopause: Challenges and Emerging Opportunities', *Endocrinology*. The Endocrine Society, 153(8), p. 3571. doi: 10.1210/EN.2012-1340.

Buhl, E. M. *et al.* (2020) 'Dysregulated mesenchymal PDGFR-β drives kidney fibrosis', *EMBO Molecular Medicine*. Wiley-Blackwell, 12(3). doi: 10.15252/EMMM.201911021.

Cain, P. A. *et al.* (2009) 'Age and gender specific normal values of left ventricular mass, volume and function for gradient echo magnetic resonance imaging: A cross sectional study', *BMC Medical Imaging*. BioMed Central, 9(1), pp. 1–10. doi: 10.1186/1471-2342-9-2/TABLES/3.

Caplan, A. I. (1991) 'Mesenchymal stem cells', *Journal of Orthopaedic Research*. John Wiley & Sons, Ltd, 9(5), pp. 641–650. Available at: https://onlinelibrary.wiley.com/doi/full/10.1002/jor.1100090504 (Accessed: 5 August 2020).

Cassiede, P. *et al.* (1996) 'Osteochondrogenic potential of marrow mesenchymal progenitor cells exposed to TGF-beta 1 or PDGF-BB as assayed in vivo and in vitro', *Journal of bone and mineral research : the official journal of the American Society for Bone and Mineral Research*. J Bone Miner Res, 11(9), pp. 1264–1273. doi: 10.1002/JBMR.5650110911.

Cathery, W. *et al.* (2018) 'Concise Review: The Regenerative Journey of Pericytes Toward Clinical Translation', *STEM CELLS*. John Wiley & Sons, Ltd, 36(9), pp. 1295–1310. doi: 10.1002/STEM.2846.

Chan, V. *et al.* (2011) 'Cardiovascular changes during maturation and ageing in male and female spontaneously hypertensive rats', *Journal of Cardiovascular Pharmacology*, 57(4), pp. 469–478. doi: 10.1097/FJC.0B013E3182102C3B.

Chatziioannou, A. F. (2005) 'Instrumentation for Molecular Imaging in Preclinical Research: Micro-PET and Micro-SPECT', *Proceedings of the American Thoracic Society*. American Thoracic Society, 2(6), p. 533. doi: 10.1513/PATS.200508-079DS.

Chen, C.-W. *et al.* (2013) 'Human pericytes for ischemic heart repair.', *Stem cells (Dayton, Ohio)*. NIH Public Access, 31(2), pp. 305–16. doi: 10.1002/stem.1285.

Chen, Q. *et al.* (2010) 'An association between gene expression and better survival in female mice following myocardial infarction', *Journal of Molecular and Cellular Cardiology*. Academic Press, 49(5), pp. 801–811. doi: 10.1016/J.YJMCC.2010.08.002.

Chen, W. C. W. *et al.* (2015) 'Human Myocardial Pericytes: Multipotent Mesodermal Precursors Exhibiting Cardiac Specificity', *Stem cells (Dayton, Ohio)*. NIH Public Access, 33(2), p. 557. doi: 10.1002/STEM.1868.

Cheng, J. *et al.* (2018) 'Targeting pericytes for therapeutic approaches to neurological disorders', *Acta neuropathologica*. Acta Neuropathol, 136(4), pp. 507–523. doi: 10.1007/S00401-018-1893-0.

Chintalgattu, V. *et al.* (2010) 'Cardiomyocyte PDGFR-beta signaling is an essential component of the mouse cardiac response to load-induced stress.', *The Journal of clinical investigation*. American Society for Clinical Investigation, 120(2), pp. 472–84. doi: 10.1172/JCI39434.

Choi, J.-W. *et al.* (2017) 'Rapid Induction of Osteogenic Markers in Mesenchymal Stem Cells by Adipose-Derived Stromal Vascular Fraction Cells', *Cellular Physiology and Biochemistry*. Karger Publishers, 44(1), pp. 53–65. doi: 10.1159/000484582.

Choudhery, M. S. *et al.* (2014) 'Donor age negatively impacts adipose tissue-derived mesenchymal stem cell expansion and differentiation', *Journal of translational medicine*. J Transl Med, 12(1). doi: 10.1186/1479-5876-12-8.

Choudhury, A. *et al.* (2017) 'Studying Diastology with Speckle Tracking Echocardiography: The Essentials', *Annals of Cardiac Anaesthesia*. Wolters Kluwer -- Medknow Publications, 20(Suppl 1), p. S57. doi: 10.4103/0971-9784.197800.

Claesson-Welsh, L. (2015) 'Vascular permeability—the essentials', *Upsala Journal of Medical Sciences*. Upsala Medical Society, 120(3), p. 135. doi: 10.3109/03009734.2015.1064501.

Collier, P., Phelan, D. and Klein, A. (2017) *A Test in Context: Myocardial Strain Measured by Speckle-Tracking Echocardiography*, *Journal of the American College of Cardiology*.

Connelly, P. J. *et al.* (2022) 'Sex steroids receptors, hypertension, and vascular ageing', *Journal of Human Hypertension*, pp. 120–125. doi: 10.1038/s41371-021-00576-7.

Corselli, M. *et al.* (2012) 'The tunica adventitia of human arteries and veins as a source of mesenchymal stem cells', *Stem Cells and Development*. Stem Cells Dev, 21(8), pp. 1299–1308. doi: 10.1089/scd.2011.0200.

Craig, D. J. *et al.* (2022) *Blood Vessel Resident Human Stem Cells in Health and Disease*, *Stem cells translational medicine*. Oxford University Press. doi: 10.1093/stcltm/szab001.

Crisan, M. *et al.* (2008) 'A Perivascular Origin for Mesenchymal Stem Cells in Multiple Human Organs', *Cell Stem Cell*, 3(3), pp. 301–313. doi: 10.1016/j.stem.2008.07.003.

Crisan, M. *et al.* (2012) 'Perivascular cells for regenerative medicine', *Journal of Cellular and Molecular Medicine*. Wiley-Blackwell, 16(12). Available at: /pmc/articles/PMC4393715/?report=abstract (Accessed: 5 August 2020).

Crouch, E. E. and Doetsch, F. (2018) 'FACS isolation of endothelial cells and pericytes from mouse brain microregions', *Nature Protocols 2018 13:4*. Nature Publishing Group, 13(4), pp. 738–751. doi: 10.1038/nprot.2017.158.

Cuijpers, I. *et al.* (2020) 'Microvascular and lymphatic dysfunction in HFpEF and its associated comorbidities', *Basic Research in Cardiology*. Springer, 115(4), p. 39. doi: 10.1007/S00395-020-0798-Y.

Cullinan-Bove, K. and Koos, R. D. (1993) 'Vascular endothelial growth factor/vascular permeability factor expression in the rat uterus: rapid stimulation by estrogen correlates with estrogen-induced increases in uterine capillary permeability and growth', *Endocrinology*. Oxford Academic, 133(2), pp. 829–837. doi: 10.1210/ENDO.133.2.8344219.

Czochra, P. *et al.* (2006) 'Liver fibrosis induced by hepatic overexpression of PDGF-B in transgenic mice', 45(3), pp. 419–428. doi: 10.1016/J.JHEP.2006.04.010.

Dai, D.-F. and Rabinovitch, P. S. (2009) 'Cardiac Aging in Mice and Humans: the Role of Mitochondrial Oxidative Stress', *Trends in cardiovascular medicine*. NIH Public Access, 19(7), p. 213. doi: 10.1016/J.TCM.2009.12.004.

Dandel, M. *et al.* (2009) 'Strain and Strain Rate Imaging by Echocardiography – Basic Concepts and Clinical Applicability', *Current Cardiology Reviews*. Bentham Science Publishers, 5(2), p. 133. doi: 10.2174/157340309788166642.

Ding, L. *et al.* (2020) 'CD10 expression identifies a subset of human perivascular progenitor cells with high proliferation and calcification potentials', 38(2), pp. 261–275. Available at: http://doi.wiley.com/10.1002/stem.3112 (Accessed: 4 August 2020).

Douglas, P. S. *et al.* (1998) 'Hypertrophic remodeling: gender differences in the early response to left ventricular pressure overload', *Journal of the American College of Cardiology*. Elsevier, 32(4), pp. 1118–1125. doi: 10.1016/S0735-1097(98)00347-7.

Duval, K. *et al.* (2017) 'Modeling Physiological Events in 2D vs. 3D Cell Culture', *Physiology*. American Physiological Society, 32(4), p. 266. doi: 10.1152/PHYSIOL.00036.2016.

Dweck, M. R. *et al.* (2014) '18F-sodium fluoride uptake is a marker of active calcification and disease progression in patients with aortic stenosis', *Circulation. Cardiovascular imaging*. Circ Cardiovasc

Imaging, 7(2), pp. 371–378. doi: 10.1161/CIRCIMAGING.113.001508.

Erben, R. G. (2018) 'Physiological actions of fibroblast growth factor-23', *Frontiers in Endocrinology*. Frontiers Media S.A., 9(MAY), p. 267. doi: 10.3389/FENDO.2018.00267/BIBTEX.

Ersbøll, M. *et al.* (2014) 'Early diastolic strain rate in relation to systolic and diastolic function and prognosis in acute myocardial infarction: a two-dimensional speckle-tracking study', *European Heart Journal*. Oxford Academic, 35(10), pp. 648–656. doi: 10.1093/EURHEARTJ/EHT179.

Evanson, R. *et al.* (2014) 'Gender and Age Differences in Growth Factor Concentrations From Platelet-Rich Plasma in Adults', *Military Medicine*. Oxford Academic, 179(7), pp. 799–805. doi: 10.7205/MILMED-D-13-00336.

Favaloro, E. J. *et al.* (1988) 'Further characterization of human myeloid antigens (gp160,95; gp150; gp67): investigation of epitopic heterogeneity and non-haemopoietic distribution using panels of monoclonal antibodies belonging to CD-11b, CD-13 and CD-33', *British Journal of Haematology*. John Wiley & Sons, Ltd, 69(2), pp. 163–171. doi: 10.1111/J.1365-2141.1988.TB07618.X.

Fiedler, J. *et al.* (2002) 'BMP-2, BMP-4, and PDGF-bb stimulate chemotactic migration of primary human mesenchymal progenitor cells', *Journal of cellular biochemistry*. J Cell Biochem, 87(3), pp. 305–312. doi: 10.1002/JCB.10309.

Fiedler, J., Etzel, N. and Brenner, R. E. (2004) 'To go or not to go: Migration of human mesenchymal progenitor cells stimulated by isoforms of PDGF', *Journal of Cellular Biochemistry*. John Wiley & Sons, Ltd, 93(5), pp. 990–998. doi: 10.1002/JCB.20219.

Fletcher, A. *et al.* (2021) '157 18F-sodium fluoride positron emission tomography, aortic disease activity and ischaemic stroke risk', *Heart*. BMJ Publishing Group Ltd and British Cardiovascular Society, 107(Suppl 1), pp. A122–A122. doi: 10.1136/HEARTJNL-2021-BCS.154.

Fletcher, A. J. *et al.* (2022) 'Microcalcification and Thoracic Aortopathy: A Window into Disease Severity', *Arteriosclerosis, Thrombosis, and Vascular Biology*. Lippincott Williams and Wilkins, 42(8), pp. 1048–1059. doi: 10.1161/ATVBAHA.122.317111.

Franco, F. *et al.* (1999) 'Magnetic Resonance Imaging and Invasive Evaluation of Development of Heart Failure in Transgenic Mice With Myocardial Expression of Tumor Necrosis Factor-α', *Circulation*. Lippincott Williams & Wilkins, 99(3), pp. 448–454. doi: 10.1161/01.CIR.99.3.448.

Gallini, R. *et al.* (2016) 'PDGF-A and PDGF-B induces cardiac fibrosis in transgenic mice', *Experimental Cell Research*. Exp Cell Res, 349(2), pp. 282–290. doi: 10.1016/j.yexcr.2016.10.022.

Genové, G., Mollick, T. and Johansson, K. (2014) 'Photoreceptor degeneration, structural remodeling and glial activation: A morphological study on a genetic mouse model for pericyte deficiency', *Neuroscience*. Pergamon, 279, pp. 269–284. doi: 10.1016/J.NEUROSCIENCE.2014.09.013.

Geyer, H. *et al.* (2010) 'Assessment of Myocardial Mechanics Using Speckle Tracking Echocardiography: Fundamentals and Clinical Applications', *Journal of the American Society of Echocardiography*. Mosby, 23(4), pp. 351–369. doi: 10.1016/J.ECHO.2010.02.015.

Gheorghe, A. *et al.* (2018) 'The economic burden of cardiovascular disease and hypertension in low- and middle-income countries: A systematic review', *BMC Public Health*. BioMed Central Ltd., p. 975. doi: 10.1186/s12889-018-5806-x.

Giallauria, F. *et al.* (2013) 'Cardiovascular Calcifications in Old Age: Mechanisms and Clinical Implications', *Current Translational Geriatrics and Experimental Gerontology Reports 2013 2:4*. Springer, 2(4), pp. 255–267. doi: 10.1007/S13670-013-0063-4.

Glinskii, O. V. *et al.* (2013) 'Pulsed Estrogen Therapy Prevents Post-OVX Porcine Dura Mater Microvascular Network Weakening via a PDGF-BB-Dependent Mechanism', *PLOS ONE*. Public Library of Science, 8(12), p. e82900. doi: 10.1371/JOURNAL.PONE.0082900.

Goettsch, C. *et al.* (2016) 'A single injection of gain-of-function mutant PCSK9 adeno-associated virus vector induces cardiovascular calcification in mice with no genetic modification', *Atherosclerosis*. Elsevier, 251, pp. 109–118. doi: 10.1016/J.ATHEROSCLEROSIS.2016.06.011.

Gomez-Salazar, M. *et al.* (2020) 'Five Decades Later, Are Mesenchymal Stem Cells Still Relevant?', *Frontiers in Bioengineering and Biotechnology*. Frontiers Media S.A. doi: 10.3389/fbioe.2020.00148.

Gorcsan, J. *et al.* (2010) 'Relationship of Echocardiographic Dyssynchrony to Long-Term Survival After Cardiac Resynchronization Therapy', *Circulation*. Lippincott Williams & WilkinsHagerstown, MD, 122(19), pp. 1909–1918. doi: 10.1161/CIRCULATIONAHA.110.954768.

Graciolli, F. G. *et al.* (2009) 'Phosphorus overload and PTH induce aortic expression of Runx2 in experimental uraemia', *Nephrology Dialysis Transplantation*. Oxford Academic, 24(5), pp. 1416–1421. doi: 10.1093/NDT/GFN686.

Grandi, A. M. *et al.* (1992) 'Influence of Age and Sex on Left Ventricular Anatomy and Function in Normals', *Cardiology*. Karger Publishers, 81(1), pp. 8–13. doi: 10.1159/000175770.

Griem-Krey, N. *et al.* (2019) 'Autoradiography as a Simple and Powerful Method for Visualization and Characterization of Pharmacological Targets', *JoVE (Journal of Visualized Experiments)*. NLM (Medline), (145), p. e58879. doi: 10.3791/58879.

Grilo, G. A. *et al.* (2020) 'Age- and sex-dependent differences in extracellular matrix metabolism associate with cardiac functional and structural changes', *Journal of Molecular and Cellular Cardiology*, 139, pp. 62–74. doi: 10.1016/J.YJMCC.2020.01.005.

Guimarães-Camboa, N. *et al.* (2017) 'Pericytes of Multiple Organs Do Not Behave as Mesenchymal Stem Cells In Vivo', *Cell Stem Cell*, 20(3), pp. 345-359.e5. doi: 10.1016/j.stem.2016.12.006.

Hajar, R. (2017) 'Coronary Heart Disease: From Mummies to 21st Century', *Heart Views : The Official Journal of the Gulf Heart Association*. Wolters Kluwer -- Medknow Publications, 18(2), p. 68. doi: 10.4103/HEARTVIEWS.HEARTVIEWS_57_17.

Hammes, H. P. *et al.* (2002) 'Pericytes and the Pathogenesis of Diabetic Retinopathy', *Diabetes*. American Diabetes Association, 51(10), pp. 3107–3112. doi: 10.2337/DIABETES.51.10.3107.

Hardy, W. R. *et al.* (2017) 'Transcriptional Networks in Single Perivascular Cells Sorted from Human Adipose Tissue Reveal a Hierarchy of Mesenchymal Stem Cells', *Stem Cells*. Wiley-Blackwell, 35(5), pp. 1273–1289. doi: 10.1002/stem.2599.

Harrington, J. *et al.* (2017) 'A systems biology approach to investigating sex differences in cardiac hypertrophy', *Journal of the American Heart Association*. John Wiley and Sons Inc., 6(8). doi: 10.1161/JAHA.117.005838.

Health Intelligence Team, B. (2022) 'BHF Scotland CVD Factsheet'.

Heldin, C.-H. and Westermark, B. (1999) 'Mechanism of Action and In Vivo Role of Platelet-Derived Growth Factor', *https://doi.org/10.1152/physrev.1999.79.4.1283*. American Physiological SocietyBethesda, MD , 79(4), pp. 1283–1316. doi: 10.1152/PHYSREV.1999.79.4.1283.

Hellström, M. *et al.* (1999) 'Role of PDGF-B and PDGFR-beta in recruitment of vascular smooth muscle cells and pericytes during embryonic blood vessel formation in the mouse.', *Development (Cambridge, England)*. The Company of Biologists, 126(14), pp. 3047–3055. doi: 10.1242/DEV.126.14.3047.

Hellström, M. *et al.* (2001) 'Lack of Pericytes Leads to Endothelial Hyperplasia and Abnormal Vascular Morphogenesis', *The Journal of Cell Biology*, 153(3), pp. 543–554. doi: 10.1083/jcb.153.3.543.

Herrmann, J. *et al.* (2020) 'Research Models for Studying Vascular Calcification', *International Journal of Molecular Sciences*. Multidisciplinary Digital Publishing Institute (MDPI), 21(6). doi: 10.3390/IJMS21062204.

Hiramoto, J. S. *et al.* (2014) 'Gender-Specific Risk Factors for Peripheral Artery Disease in a Voluntary Screening Population', *Journal of the American Heart Association: Cardiovascular and Cerebrovascular Disease*. Wiley-Blackwell, 3(2). doi: 10.1161/JAHA.113.000651.

Hirschi, K. K. *et al.* (1999) 'Endothelial Cells Modulate the Proliferation of Mural Cell Precursors via Platelet-Derived Growth Factor-BB and Heterotypic Cell Contact', *Circulation Research*. Lippincott Williams & Wilkins, 84(3), pp. 298–305. doi: 10.1161/01.RES.84.3.298.

Howe, K. L. and Fish, J. E. (2019) 'Transforming endothelial cells in atherosclerosis', *Nature Metabolism 2019 1:9*. Nature Publishing Group, 1(9), pp. 856–857. doi: 10.1038/s42255-019-0100-5.

Hoyle, G. W. *et al.* (1999) 'Emphysematous lesions, inflammation, and fibrosis in the lungs of transgenic mice overexpressing platelet-derived growth factor', *The American journal of pathology*. Am J Pathol, 154(6), pp. 1763–1775. doi: 10.1016/S0002-9440(10)65432-6.

Hu, Y. *et al.* (2004) 'Abundant progenitor cells in the adventitia contribute to atherosclerosis of vein grafts in ApoE-deficient mice', *Journal of Clinical Investigation*. The American Society for Clinical Investigation, 113(9), pp. 1258–1265. doi: 10.1172/JCI19628.

Hum, J. M. *et al.* (2017) 'Chronic hyperphosphatemia and vascular calcification are reduced by stable delivery of soluble klotho', *Journal of the American Society of Nephrology*. American Society of Nephrology, 28(4), pp. 1162–1174. doi: 10.1681/ASN.2015111266/-/DCSUPPLEMENTAL.

Hung, B. P. *et al.* (2015) 'Platelet-derived growth factor BB enhances osteogenesis of adipose-derived but not bone marrow-derived mesenchymal stromal/stem cells', *Stem cells (Dayton, Ohio)*. NIH Public Access, 33(9), p. 2773. doi: 10.1002/STEM.2060.

Hung, S.-P. *et al.* (2012) 'Hypoxia promotes proliferation and osteogenic differentiation potentials of human mesenchymal stem cells', *Journal of Orthopaedic Research*. John Wiley & Sons, Ltd, 30(2), pp. 260–266. doi: 10.1002/JOR.21517.

Jadeja, S. *et al.* (2013) 'A CNS-Specific Hypomorphic Pdgfr-Beta Mutant Model of Diabetic Retinopathy', *Investigative Ophthalmology & Visual Science*. The Association for Research in Vision and Ophthalmology, 54(5), pp. 3569–3578. doi: 10.1167/IOVS.12-11125.

Jahnen-Dechent, W. *et al.* (1997) 'Cloning and targeted deletion of the mouse fetuin gene', *The Journal of biological chemistry*. J Biol Chem, 272(50), pp. 31496–31503. doi: 10.1074/JBC.272.50.31496.

Jan, M. L. *et al.* (2006) 'A combined micro-PET/CT scanner for small animal imaging', *Nuclear Instruments and Methods in Physics Research Section A: Accelerators, Spectrometers, Detectors and*

Associated Equipment. North-Holland, 569(2), pp. 314–318. doi: 10.1016/J.NIMA.2006.08.106.

Jensen, A. R. *et al.* (2018) 'Neer Award 2018: Platelet-derived growth factor receptor α co-expression typifies a subset of platelet-derived growth factor receptor β–positive progenitor cells that contribute to fatty degeneration and fibrosis of the murine rotator cuff', *Journal of Shoulder and Elbow Surgery*, 27(7), pp. 1149–1161. Available at: https://pubmed.ncbi.nlm.nih.gov/29653843/ (Accessed: 5 August 2020).

Johnson, C. *et al.* (2019) 'Practical tips and tricks in measuring strain, strain rate and twist for the left and right ventricles', *Echo Research and Practice*. BioMed Central, 6(3), p. R87. doi: 10.1530/ERP-19-0020.

Joshi, N. V. *et al.* (2014) 'Will 18F-sodium fluoride PET-CT imaging be the magic bullet for identifying vulnerable coronary atherosclerotic plaques?', *Current cardiology reports*. Curr Cardiol Rep, 16(9). doi: 10.1007/S11886-014-0521-4.

Jung, H. (2021) 'Basic Physical Principles and Clinical Applications of Computed Tomography', *Korean Society of Medical Physics*. Korean Society of Medical Physics, 32(1), pp. 1–17. doi: 10.14316/PMP.2021.32.1.1.

Kalam, K., Otahal, P. and Marwick, T. H. (2014) 'Prognostic implications of global LV dysfunction: A systematic review and meta-analysis of global longitudinal strain and ejection fraction', *Heart*. BMJ Publishing Group Ltd and British Cardiovascular Society, 100(21), pp. 1673–1680. doi: 10.1136/heartjnl-2014-305538.

Kang, Y. J. *et al.* (2005) 'Role of c-Jun N-terminal kinase in the PDGF-induced proliferation and migration of human adipose tissue-derived mesenchymal stem cells', 95(6), pp. 1135–1145. doi: 10.1002/JCB.20499.

Kappert, K. *et al.* (2006) '7-Estradiol attenuates PDGF signaling in vascular smooth muscle cells at the postreceptor level', *Am J Physiol Heart Circ Physiol*, 290, pp. 538–546. doi: 10.1152/ajpheart.00240.2005.-Estrogens.

Karram, K., Chatterjee, N. and Trotter, J. (2005) 'NG2-expressing cells in the nervous system: role of the proteoglycan in migration and glial–neuron interaction', *Journal of Anatomy*. Wiley-Blackwell, 207(6), p. 735. doi: 10.1111/J.1469-7580.2005.00461.X.

Kauer, J. *et al.* (2019) 'CD105 (Endoglin) as negative prognostic factor in AML', *Scientific Reports 2019 9:1*. Nature Publishing Group, 9(1), pp. 1–11. doi: 10.1038/s41598-019-54767-x.

Kawabe, J. I. and Hasebe, N. (2014) 'Role of the vasa vasorum and vascular resident stem cells in

atherosclerosis', *BioMed Research International*. Hindawi Publishing Corporation, 2014. doi: 10.1155/2014/701571.

Keller, A. *et al.* (2013) 'Mutations in the gene encoding PDGF-B cause brain calcifications in humans and mice', *Nature Genetics*. Nature Publishing Group, 45(9), pp. 1077–1082. doi: 10.1038/ng.2723.

Kim, B. S. *et al.* (2021) 'Sex Differences in Coronary Arterial Calcification in Symptomatic Patients', *The American journal of cardiology*. Am J Cardiol, 149, pp. 16–20. doi: 10.1016/J.AMJCARD.2021.03.025.

Kramann, R. *et al.* (2016) 'Adventitial MSC-like Cells Are Progenitors of Vascular Smooth Muscle Cells and Drive Vascular Calcification in Chronic Kidney Disease', *Cell stem cell*. Cell Stem Cell, 19(5), pp. 628–642. doi: 10.1016/J.STEM.2016.08.001.

Krenz, M. and Robbins, J. (2004) 'Impact of beta-myosin heavy chain expression on cardiac function during stress', *Journal of the American College of Cardiology*. Elsevier, 44(12), pp. 2390–2397. doi: 10.1016/J.JACC.2004.09.044.

Krishnan, A. *et al.* (2014) 'A detailed comparison of mouse and human cardiac development', *Pediatric Research 2014 76:6*. Nature Publishing Group, 76(6), pp. 500–507. doi: 10.1038/pr.2014.128.

Krüger-Genge, A. *et al.* (2019) 'Vascular endothelial cell biology: An update', *International Journal of Molecular Sciences*. MDPI AG. doi: 10.3390/ijms20184411.

Kryukov, E. V. *et al.* (2021) 'Possibilities of preclinical diagnosis of anthracycline cardiotoxicity using the technique of "speckle-tracking echocardiography"', *Bulletin of the Russian Military Medical Academy*. ECO-Vector LLC, 23(1), pp. 81–88. doi: 10.17816/brmma63578.

Kubíková, T. *et al.* (2018) 'Numerical and length densities of microvessels in the human brain: Correlation with preferential orientation of microvessels in the cerebral cortex, subcortical grey matter and white matter, pons and cerebellum', *Journal of Chemical Neuroanatomy*. Elsevier, 88, pp. 22–32. doi: 10.1016/J.JCHEMNEU.2017.11.005.

Kumar, N. *et al.* (2011) 'Acquired progressive ataxia and palatal tremor: Importance of MRI evidence of hemosiderin deposition and vascular malformations', *Parkinsonism & Related Disorders*. Elsevier, 17(7), pp. 565–568. doi: 10.1016/J.PARKRELDIS.2011.04.018.

Kuro-o, M. *et al.* (1997) 'Mutation of the mouse klotho gene leads to a syndrome resembling ageing', *Nature 1997 390:6655*. Nature Publishing Group, 390(6655), pp. 45–51. doi: 10.1038/36285.

Kyaw, T. *et al.* (2011) 'Current understanding of the role of B cell subsets and intimal and adventitial B cells in atherosclerosis', *Current opinion in lipidology*. Curr Opin Lipidol, 22(5), pp. 373–379. doi: 10.1097/MOL.0B013E32834ADAF3.

Lang, R. M. *et al.* (2015) 'Recommendations for Cardiac Chamber Quantification by Echocardiography in Adults: An Update from the American Society of Echocardiography and the European Association of Cardiovascular Imaging', *European Heart Journal - Cardiovascular Imaging*. Oxford Academic, 16(3), pp. 233–271. doi: 10.1093/EHJCI/JEV014.

Langenbach, F. and Handschel, J. (2013) 'Effects of dexamethasone, ascorbic acid and β-glycerophosphate on the osteogenic differentiation of stem cells in vitro', *Stem Cell Research and Therapy*. BioMed Central, 4(5), pp. 1–7. doi: 10.1186/SCRT328/FIGURES/1.

Leszczynska, A. *et al.* (2016) 'Differentiation of Vascular Stem Cells Contributes to Ectopic Calcification of Atherosclerotic Plaque', *STEM CELLS*. Wiley-Blackwell, 34(4), pp. 913–923. doi: 10.1002/stem.2315.

Levéen, P. *et al.* (1994) 'Mice deficient for PDGF B show renal, cardiovascular, and hematological abnormalities.', *Genes & development*. Cold Spring Harbor Laboratory Press, 8(16), pp. 1875–87. doi: 10.1101/GAD.8.16.1875.

Levy, D. *et al.* (2010) 'Prognostic Implications of Echocardiographically Determined Left Ventricular Mass in the Framingham Heart Study', *http://dx.doi.org/10.1056/NEJM199005313222203*. Massachusetts Medical Society , 322(22), pp. 1561–1566. doi: 10.1056/NEJM199005313222203.

Li, A. *et al.* (2014) 'PDGF-AA Promotes Osteogenic Differentiation and Migration of Mesenchymal Stem Cell by Down-Regulating PDGFRα and Derepressing BMP-Smad1/5/8 Signaling', *PLOS ONE*. Public Library of Science, 9(12), p. e113785. doi: 10.1371/JOURNAL.PONE.0113785.

Li, F., Jia, H. and Yu, C. (2007) 'ACL reconstruction in a rabbit model using irradiated Achilles allograft seeded with mesenchymal stem cells or PDGF-B gene-transfected mesenchymal stem cells', *Knee surgery, sports traumatology, arthroscopy : official journal of the ESSKA*. Knee Surg Sports Traumatol Arthrosc, 15(10), pp. 1219–1227. doi: 10.1007/S00167-007-0385-X.

Li, J. *et al.* (2004) 'Regulator of G protein signaling 5 marks peripheral arterial smooth muscle cells and is downregulated in atherosclerotic plaque', *Journal of Vascular Surgery*. Mosby, 40(3), pp. 519–528. doi: 10.1016/J.JVS.2004.06.021.

Li, N. *et al.* (2015) 'Vascular Adventitia Calcification and Its Underlying Mechanism', *PLoS ONE*. Public Library of Science, 10(7). doi: 10.1371/JOURNAL.PONE.0132506.

Li, Z. *et al.* (2019) 'Single-cell transcriptome analyses reveal novel targets modulating cardiac neovascularization by resident endothelial cells following myocardial infarction', *European Heart Journal*. Oxford Academic, 40(30), pp. 2507–2520. doi: 10.1093/EURHEARTJ/EHZ305.

Libby, P. *et al.* (2019) 'Atherosclerosis', *Nature Reviews Disease Primers 2019 5:1*. Nature Publishing Group, 5(1), pp. 1–18. doi: 10.1038/s41572-019-0106-z.

Libby, P. (2021) 'The changing landscape of atherosclerosis', *Nature 2021 592:7855*. Nature Publishing Group, 592(7855), pp. 524–533. doi: 10.1038/s41586-021-03392-8.

Lindahl, P. *et al.* (1997) 'Pericyte loss and microaneurysm formation in PDGF-B-deficient mice.', *Science (New York, N.Y.)*. American Association for the Advancement of Science, 277(5323), pp. 242–5. doi: 10.1126/SCIENCE.277.5323.242.

Lindahl, P. *et al.* (1998) 'Paracrine PDGF-B/PDGF-Rbeta signaling controls mesangial cell development in kidney glomeruli', *Development*. The Company of Biologists, 125(17), pp. 3313–3322. doi: 10.1242/DEV.125.17.3313.

Lindblom, P. *et al.* (2003) 'Endothelial PDGF-B retention is required for proper investment of pericytes in the microvessel wall.', *Genes & development*. Cold Spring Harbor Laboratory Press, 17(15), pp. 1835–40. doi: 10.1101/gad.266803.

Lopez, I. *et al.* (2008) 'The effect of calcitriol, paricalcitol, and a calcimimetic on extraosseous calcifications in uremic rats', *Kidney international*. Kidney Int, 73(3), pp. 300–307. doi: 10.1038/SJ.KI.5002675.

Lu, Z. *et al.* (2013) 'Activation and promotion of adipose stem cells by tumour necrosis factor-alpha preconditioning for bone regeneration', *Journal of Cellular Physiology*. John Wiley & Sons, Ltd, 228(8), pp. 1737–1744. doi: 10.1002/JCP.24330.

De Lucia, C. *et al.* (2019) 'Echocardiographic Strain Analysis for the Early Detection of Left Ventricular Systolic/Diastolic Dysfunction and Dyssynchrony in a Mouse Model of Physiological Aging', *The Journals of Gerontology Series A: Biological Sciences and Medical Sciences*. Oxford University Press, 74(4), p. 455. doi: 10.1093/GERONA/GLY139.

M, D. *et al.* (2006) 'Minimal criteria for defining multipotent mesenchymal stromal cells. The International Society for Cellular Therapy position statement', *Cytotherapy*. Cytotherapy, 8(4), pp. 315–317. doi: 10.1080/14653240600855905.

Maas, A. H. E. M. and Appelman, Y. E. A. (2010) 'Gender differences in coronary heart disease', *Netherlands Heart Journal*. Springer, 18(12), p. 598. doi: 10.1007/S12471-010-0841-Y.

MacAskill, M. G. *et al.* (2020) 'Characterisation of an atherosclerotic micro-calcification model using ApoE−/− mice and PET/CT', *International Journal of Cardiology. Heart & Vasculature*. Elsevier, 31, p. 100672. doi: 10.1016/J.IJCHA.2020.100672.

Mäe, M. A. *et al.* (2021) 'Single-Cell Analysis of Blood-Brain Barrier Response to Pericyte Loss', *Circulation Research*. Lippincott Williams & WilkinsHagerstown, MD, pp. E46–E62. doi: 10.1161/CIRCRESAHA.120.317473.

Manwani, B. and McCullough, L. D. (2012) 'Estrogen in ischemic stroke: the Debate Continues', *European journal of neurology : the official journal of the European Federation of Neurological Societies*. NIH Public Access, 19(10), p. 1276. doi: 10.1111/J.1468-1331.2012.03746.X.

Marcus, J. T. *et al.* (1999) 'MRI-derived left ventricular function parameters and mass in healthy young adults: Relation with gender and body size', *The International Journal of Cardiac Imaging 1999 15:5*. Springer, 15(5), pp. 411–419. doi: 10.1023/A:1006268405585.

Matsunari, I. (2020) 'Microvascular function measurement in mice: From large to small', *Journal of Nuclear Cardiology 2020 28:6*. Springer, 28(6), pp. 2657–2659. doi: 10.1007/S12350-020-02097-1.

McMullen, J. R. and Jennings, G. L. (2007) 'DIFFERENCES BETWEEN PATHOLOGICAL AND PHYSIOLOGICAL CARDIAC HYPERTROPHY: NOVEL THERAPEUTIC STRATEGIES TO TREAT HEART FAILURE', *Clinical and Experimental Pharmacology and Physiology*. Blackwell Publishing Asia, 34(4), pp. 255–262. doi: 10.1111/j.1440-1681.2007.04585.x.

Mensah, G. A. *et al.* (2017) 'Decline in Cardiovascular Mortality: Possible Causes and Implications', *Circulation research*. NIH Public Access, 120(2), p. 366. doi: 10.1161/CIRCRESAHA.116.309115.

Merz, A. A. and Cheng, S. (2016) 'Sex differences in cardiovascular ageing', 102(11). doi: 10.1136/HEARTJNL-2015-308769.

Methner, C. *et al.* (2019) 'Pericyte constriction underlies capillary derecruitment during hyperemia in the setting of arterial stenosis', *American Journal of Physiology - Heart and Circulatory Physiology*. American Physiological Society, 317(2), pp. H255–H263. doi: 10.1152/AJPHEART.00097.2019/ASSET/IMAGES/LARGE/ZH40071928630004.JPEG.

Mezzasoma, L. *et al.* (2020) 'ANP and BNP Exert Anti-Inflammatory Action via NPR-1/cGMP Axis by Interfering with Canonical, Non-Canonical, and Alternative Routes of Inflammasome Activation in Human THP1 Cells', *International journal of molecular sciences*. Int J Mol Sci, 22(1), pp. 1–17. doi: 10.3390/IJMS22010024.

Mihajlica, N., Betsholtz, C. and Hammarlund-Udenaes, M. (2018a) 'Pharmacokinetics of pericyte

involvement in small-molecular drug transport across the blood-brain barrier', *European Journal of Pharmaceutical Sciences*. Elsevier B.V., 122, pp. 77–84. doi: 10.1016/j.ejps.2018.06.018.

Mihajlica, N., Betsholtz, C. and Hammarlund-Udenaes, M. (2018b) 'Rate of small-molecular drug transport across the blood-brain barrier in a pericyte-deficient state', *European Journal of Pharmaceutical Sciences*. Elsevier B.V., 124, pp. 182–187. doi: 10.1016/j.ejps.2018.08.009.

Mitchell, T. S. *et al.* (2008) 'RGS5 expression is a quantitative measure of pericyte coverage of blood vessels', *Angiogenesis*. Springer, 11(2), pp. 141–151. doi: 10.1007/S10456-007-9085-X/FIGURES/4.

Moe, S. M. *et al.* (2009) 'A rat model of chronic kidney disease-mineral bone disorder', *Kidney International*. Elsevier, 75(2), pp. 176–184. doi: 10.1038/KI.2008.456.

Moioli, E. K., Hong, L. and Mao, J. J. (2007) 'Inhibition of osteogenic differentiation of human mesenchymal stem cells', *Wound repair and regeneration : official publication of the Wound Healing Society [and] the European Tissue Repair Society*. NIH Public Access, 15(3), p. 413. doi: 10.1111/J.1524-475X.2007.00244.X.

Montagne, A. *et al.* (2018) 'Pericyte degeneration causes white matter dysfunction in the mouse central nervous system', *Nature Medicine 2018 24:3*. Nature Publishing Group, 24(3), pp. 326–337. doi: 10.1038/nm.4482.

Mor-Avi, V. *et al.* (2011) 'Current and evolving echocardiographic techniques for the quantitative evaluation of cardiac mechanics: ASE/EAE consensus statement on methodology and indications endorsed by the Japanese Society of Echocardiography', *Journal of the American Society of Echocardiography : official publication of the American Society of Echocardiography*. J Am Soc Echocardiogr, 24(3), pp. 277–313. doi: 10.1016/J.ECHO.2011.01.015.

Moran, C. M. *et al.* (2013) 'High-resolution echocardiography in the assessment of cardiac physiology and disease in preclinical models', *Experimental Physiology*. John Wiley & Sons, Ltd, 98(3), pp. 629–644. doi: 10.1113/EXPPHYSIOL.2012.068577.

Moran, C. M. and Thomson, A. J. W. (2020) 'Preclinical Ultrasound Imaging—A Review of Techniques and Imaging Applications', *Frontiers in Physics*. Frontiers Media S.A., 8, p. 124. doi: 10.3389/FPHY.2020.00124/BIBTEX.

Morikawa, S. *et al.* (2002) 'Abnormalities in Pericytes on Blood Vessels and Endothelial Sprouts in Tumors', *The American Journal of Pathology*. Elsevier, 160(3), pp. 985–1000. doi: 10.1016/S0002-9440(10)64920-6.

Moss, A. J. *et al.* (2020) 'Ex vivo 18F-fluoride uptake and hydroxyapatite deposition in human

coronary atherosclerosis', *Scientific Reports 2020 10:1*. Nature Publishing Group, 10(1), pp. 1–9. doi: 10.1038/s41598-020-77391-6.

Murray, I. R. *et al.* (2017) 'Skeletal and cardiac muscle pericytes: Functions and therapeutic potential', *Pharmacology & therapeutics*. NIH Public Access, 171, p. 65. doi: 10.1016/J.PHARMTHERA.2016.09.005.

Nagao, S. *et al.* (2010) 'Polycystic kidney disease in Han:SPRD Cy rats is associated with elevated expression and mislocalization of SamCystin', *American Journal of Physiology - Renal Physiology*. American Physiological Society, 299(5), p. F1078. doi: 10.1152/AJPRENAL.00504.2009.

Naito, H., Iba, T. and Takakura, N. (2020) 'Mechanisms of new blood-vessel formation and proliferative heterogeneity of endothelial cells', *International Immunology*. Oxford Academic, 32(5), pp. 295–305. doi: 10.1093/INTIMM/DXAA008.

Nakagawa, Y., Nishikimi, T. and Kuwahara, K. (2019) 'Atrial and brain natriuretic peptides: Hormones secreted from the heart', *Peptides*. Elsevier, 111, pp. 18–25. doi: 10.1016/J.PEPTIDES.2018.05.012.

Nehls, V., Denzer, K. and Drenckhahn, D. (1992) 'Pericyte involvement in capillary sprouting during angiogenesis in situ', *Cell and Tissue Research 1992 270:3*. Springer, 270(3), pp. 469–474. doi: 10.1007/BF00645048.

Nehls, V. and Drenckhahn, D. (1991) 'Heterogeneity of microvascular pericytes for smooth muscle type alpha-actin', *The Journal of cell biology*. J Cell Biol, 113(1), pp. 147–154. doi: 10.1083/JCB.113.1.147.

Nicolas, G. *et al.* (2015) 'Brain calcification process and phenotypes according to age and sex: Lessons from SLC20A2, PDGFB, and PDGFRB mutation carriers; Brain calcification process and phenotypes according to age and sex: Lessons from SLC20A2, PDGFB, and PDGFRB mutation carriers'. doi: 10.1002/ajmg.b.32336.

Nikolakopoulou, A. M. *et al.* (2017) 'Regional early and progressive loss of brain pericytes but not vascular smooth muscle cells in adult mice with disrupted platelet-derived growth factor receptor-β signaling', *PLOS ONE*. Public Library of Science, 12(4), p. e0176225. doi: 10.1371/JOURNAL.PONE.0176225.

Nutt, R. (2002) 'The History of Positron Emission Tomography', *Molecular Imaging & Biology*. No longer published by Elsevier, 4(1), pp. 11–26. doi: 10.1016/S1095-0397(00)00051-0.

Nystrom, H. *et al.* (2006) 'Platelet-derived growth factor B retention is essential for development of

normal structure and function of conduit vessels and capillaries☆', *Cardiovascular Research*. Lippincott, Williams & Wilkins, Philadelphia, 71(3), pp. 557–565. doi: 10.1016/j.cardiores.2006.05.019.

O'Farrel, F. M. *et al.* (2017) 'Capillary pericytes mediate coronary no-reflow after myocardial ischaemia', *eLife*, 6. doi: 10.7554/eLife.29280.

Oakley, R. and Tharakan, B. (2014) 'Vascular Hyperpermeability and Aging', *Aging and Disease*. JKL International LLC, 5(2), p. 114. doi: 10.14336/AD.2014.0500114.

Ohlsson, R. *et al.* (1999) 'PDGFB Regulates the Development of the Labyrinthine Layer of the Mouse Fetal Placenta', *Developmental Biology*. Academic Press, 212(1), pp. 124–136. doi: 10.1006/DBIO.1999.9306.

Olivetti, G. *et al.* (1995) 'Gender differences and aging: effects on the human heart', *Journal of the American College of Cardiology*. J Am Coll Cardiol, 26(4), pp. 1068–1079. doi: 10.1016/0735-1097(95)00282-8.

Ouyang, L. *et al.* (2018) 'Roles of platelet-derived growth factor in vascular calcification', *Journal of Cellular Physiology*. Wiley-Blackwell, 233(4), pp. 2804–2814. doi: 10.1002/jcp.25985.

Pagourelias, E. D. *et al.* (2017) 'Echo Parameters for Differential Diagnosis in Cardiac Amyloidosis: A Head-to-Head Comparison of Deformation and Nondeformation Parameters', *Circulation: Cardiovascular Imaging*. Circ Cardiovasc Imaging, 10(3). doi: 10.1161/CIRCIMAGING.116.005588.

Pan, P. *et al.* (2020) 'Aggravated pulmonary injury after subarachnoid hemorrhage in PDGF-Bret/retmice', *Chinese Neurosurgical Journal*. BioMed Central, 6(1), pp. 1–9. doi: 10.1186/S41016-020-00193-2/FIGURES/5.

Park, M. *et al.* (2013) 'APPL1 transgenic mice are protected from high-fat diet-induced cardiac dysfunction', *American Journal of Physiology - Endocrinology and Metabolism*. Am J Physiol Endocrinol Metab, 305(7). doi: 10.1152/ajpendo.00257.2013.

Pasch, A. *et al.* (2012) 'Nanoparticle-based test measures overall propensity for calcification in serum', *Journal of the American Society of Nephrology*. American Society of Nephrology, 23(10), pp. 1744–1752. doi: 10.1681/ASN.2012030240/-/DCSUPPLEMENTAL.

Paulin, D. and Li, Z. (2004) 'Desmin: a major intermediate filament protein essential for the structural integrity and function of muscle', *Experimental cell research*. Exp Cell Res, 301(1), pp. 1–7. doi: 10.1016/J.YEXCR.2004.08.004.

Pescatore, L. A., Gamarra, L. F. and Liberman, M. (2019) 'Multifaceted Mechanisms of Vascular Calcification in Aging', *Arteriosclerosis, Thrombosis, and Vascular Biology*. Lippincott Williams & WilkinsHagerstown, MD, 39(7), pp. 1307–1316. doi: 10.1161/ATVBAHA.118.311576.

Pittenger, M. F. *et al.* (2019) *Mesenchymal stem cell perspective: cell biology to clinical progress*, *npj Regenerative Medicine*. Nature Research. doi: 10.1038/s41536-019-0083-6.

Proudfoot, D. (2019) 'Calcium Signaling and Tissue Calcification', *Cold Spring Harbor Perspectives in Biology*. Cold Spring Harbor Laboratory Press, 11(10), p. a035303. doi: 10.1101/CSHPERSPECT.A035303.

Raines, E. W. (2004) 'PDGF and cardiovascular disease', *Cytokine & Growth Factor Reviews*. Pergamon, 15(4), pp. 237–254. doi: 10.1016/J.CYTOGFR.2004.03.004.

Raines, S. M. *et al.* (2011a) 'Loss of PDGF-B activity increases hepatic vascular permeability and enhances insulin sensitivity', *American Journal of Physiology-Endocrinology and Metabolism*. American Physiological Society Bethesda, MD, 301(3), pp. E517–E526. doi: 10.1152/ajpendo.00241.2011.

Raines, S. M. *et al.* (2011b) 'Loss of PDGF-B activity increases hepatic vascular permeability and enhances insulin sensitivity', *American Journal of Physiology-Endocrinology and Metabolism*. American Physiological Society Bethesda, MD, 301(3), pp. E517–E526. doi: 10.1152/ajpendo.00241.2011.

Razzaque, M. S. *et al.* (2006) 'Premature aging-like phenotype in fibroblast growth factor 23 null mice is a vitamin D-mediated process', *The FASEB Journal*. John Wiley & Sons, Ltd, 20(6), pp. 720–722. doi: 10.1096/FJ.05-5432FJE.

Renard, D. *et al.* (2014) 'Thalamic Lesions: A Radiological Review', *Behavioural Neurology*. Hindawi Limited, 2014. doi: 10.1155/2014/154631.

Roche-Molina, M. *et al.* (2015) 'Induction of sustained hypercholesterolemia by single adeno-associated virus-mediated gene transfer of mutant hPCSK9', *Arteriosclerosis, thrombosis, and vascular biology*. Arterioscler Thromb Vasc Biol, 35(1), pp. 50–59. doi: 10.1161/ATVBAHA.114.303617.

Rodgers, J. L. *et al.* (2019) 'Cardiovascular Risks Associated with Gender and Aging', *Journal of Cardiovascular Development and Disease*. Multidisciplinary Digital Publishing Institute (MDPI), 6(2). doi: 10.3390/JCDD6020019.

Roth, G. A. *et al.* (2020) 'Global Burden of Cardiovascular Diseases and Risk Factors, 1990–2019:

Update From the GBD 2019 Study', *Journal of the American College of Cardiology*. Elsevier, 76(25), pp. 2982–3021. doi: 10.1016/J.JACC.2020.11.010.

Russell, K. C. *et al.* (2010) 'In Vitro High-Capacity Assay to Quantify the Clonal Heterogeneity in Trilineage Potential of Mesenchymal Stem Cells Reveals a Complex Hierarchy of Lineage Commitment', *STEM CELLS*. John Wiley & Sons, Ltd, 28(4), pp. 788–798. doi: 10.1002/STEM.312.

Saeed, A. A. *et al.* (2014) 'Effects of a Disrupted Blood-Brain Barrier on Cholesterol Homeostasis in the Brain', *The Journal of Biological Chemistry*. American Society for Biochemistry and Molecular Biology, 289(34), p. 23712. doi: 10.1074/JBC.M114.556159.

Saito, Y. *et al.* (2005) 'Cerebellopontine calcification: A new entity of idiopathic intracranial calcification?', *Acta Neuropathologica*. Springer, 110(1), pp. 77–83. doi: 10.1007/S00401-005-1011-Y/TABLES/2.

Salem, O. *et al.* (2014) 'Naproxen affects osteogenesis of human mesenchymal stem cells via regulation of Indian hedgehog signaling molecules', *Arthritis Research and Therapy*. BioMed Central Ltd., 16(4), pp. 1–9. doi: 10.1186/AR4614/FIGURES/5.

Salton, C. J. *et al.* (2002) 'Gender differences and normal left ventricular anatomy in an adult population free of hypertension: A cardiovascular magnetic resonance study of the Framingham Heart Study Offspring cohort', *Journal of the American College of Cardiology*. American College of Cardiology FoundationWashington, D.C., 39(6), pp. 1055–1060. doi: 10.1016/S0735-1097(02)01712-6.

Sameer Bardeesi, A. A. *et al.* (2017) 'A novel role of cellular interactions in vascular calcification', *J Transl Med*, 15, p. 95. doi: 10.1186/s12967-017-1190-z.

Santhanam, L. *et al.* (2021) 'Skeleton-secreted PDGF-BB mediates arterial stiffening', *The Journal of Clinical Investigation*. American Society for Clinical Investigation, 131(20). doi: 10.1172/JCI147116.

Sauzay, C. *et al.* (2019) 'CD90/Thy-1, a cancer-associated cell surface signaling molecule', *Frontiers in Cell and Developmental Biology*. Frontiers Media S.A., 7(APR), p. 66. doi: 10.3389/FCELL.2019.00066/BIBTEX.

Schaible, T. F. *et al.* (1984) 'The effects of gonadectomy on left ventricular function and cardiac contractile proteins in male and female rats.', *Circulation Research*, 54(1), pp. 38–49. doi: 10.1161/01.RES.54.1.38.

Schnelle, M. *et al.* (2018) 'Echocardiographic evaluation of diastolic function in mouse models of heart disease', *Journal of Molecular and Cellular Cardiology*. Academic Press, 114, pp. 20–28. doi:

10.1016/J.YJMCC.2017.10.006.

Selich, A. *et al.* (2016) 'Massive Clonal Selection and Transiently Contributing Clones During Expansion of Mesenchymal Stem Cell Cultures Revealed by Lentiviral RGB-Barcode Technology', 5(5), pp. 591–601. Available at: /pmc/articles/PMC4835246/ (Accessed: 22 March 2022).

Senbanjo, L. T. and Chellaiah, M. A. (2017) 'CD44: A Multifunctional Cell Surface Adhesion Receptor Is a Regulator of Progression and Metastasis of Cancer Cells', *Frontiers in Cell and Developmental Biology*. Frontiers Media SA, 5(MAR), p. 18. doi: 10.3389/FCELL.2017.00018.

Seo, M. S. *et al.* (2000) 'Photoreceptor-Specific Expression of Platelet-Derived Growth Factor-B Results in Traction Retinal Detachment', *The American Journal of Pathology*. American Society for Investigative Pathology, 157(3), p. 995. doi: 10.1016/S0002-9440(10)64612-3.

Shankman, L. S. *et al.* (2015) 'KLF4-dependent phenotypic modulation of smooth muscle cells has a key role in atherosclerotic plaque pathogenesis', *Nature Medicine 2015 21:6*. Nature Publishing Group, 21(6), pp. 628–637. doi: 10.1038/nm.3866.

Shaw, L. J. *et al.* (2018) 'Sex differences in calcified plaque and long-term cardiovascular mortality: observations from the CAC Consortium', *European heart journal*. Eur Heart J, 39(41), pp. 3727–3735. doi: 10.1093/EURHEARTJ/EHY534.

Shepherd, D. L. *et al.* (2016) 'Early Cardiac Dysfunction in the Type 1 Diabetic Heart Using Speckle-Tracking Based Strain Imaging', *Journal of molecular and cellular cardiology*. NIH Public Access, 90, p. 74. doi: 10.1016/J.YJMCC.2015.12.001.

Shimada, T. *et al.* (2004) 'Targeted ablation of Fgf23 demonstrates an essential physiological role of FGF23 in phosphate and vitamin D metabolism', *The Journal of Clinical Investigation*. American Society for Clinical Investigation, 113(4), pp. 561–568. doi: 10.1172/JCI19081.

Shioi, A. and Ikari, Y. (2018) 'Plaque Calcification During Atherosclerosis Progression and Regression', *Journal of Atherosclerosis and Thrombosis*. Japan Atherosclerosis Society, 25(4), p. 294. doi: 10.5551/JAT.RV17020.

Silver, F. H., Horvath, I. and Foran, D. J. (2001) 'Viscoelasticity of the vessel wall: the role of collagen and elastic fibers', *Critical reviews in biomedical engineering*. Crit Rev Biomed Eng, 29(3), pp. 279–301. doi: 10.1615/CRITREVBIOMEDENG.V29.I3.10.

Simard, L. *et al.* (2017) 'Sex-Related Discordance Between Aortic Valve Calcification and Hemodynamic Severity of Aortic Stenosis: Is Valvular Fibrosis the Explanation?', *Circulation research*. Circ Res, 120(4), pp. 681–691. doi: 10.1161/CIRCRESAHA.116.309306.

de Simone, G. *et al.* (1991) 'Gender differences in left ventricular anatomy, blood viscosity and volume regulatory hormones in normal adults', *The American Journal of Cardiology*. Excerpta Medica, 68(17), pp. 1704–1708. doi: 10.1016/0002-9149(91)90333-G.

Simone, G. de (2004) 'Concentric or Eccentric Hypertrophy: How Clinically Relevant Is the Difference?', *Hypertension*. Lippincott Williams & Wilkins, 43(4), pp. 714–715. doi: 10.1161/01.HYP.0000121363.08252.A7.

de Simone, G. *et al.* (2005) 'Body composition and fat distribution influence systemic hemodynamics in the absence of obesity: the HyperGEN Study', *The American Journal of Clinical Nutrition*. Oxford Academic, 81(4), pp. 757–761. doi: 10.1093/AJCN/81.4.757.

De Simone, G. *et al.* (1995) 'Gender Differences in Left Ventricular Growth', *Hypertension*. Lippincott Williams & Wilkins, 26(6 I), pp. 979–983. doi: 10.1161/01.HYP.26.6.979.

Singh, A., Tandon, S. and Tandon, C. (2021) 'An update on vascular calcification and potential therapeutics', *Molecular Biology Reports*. Springer Science and Business Media B.V., 48(1), pp. 887–896. doi: 10.1007/S11033-020-06086-Y/FIGURES/1.

Smiseth, O. A. *et al.* (2016) 'Myocardial strain imaging: how useful is it in clinical decision making?', *European Heart Journal*. Oxford University Press, 37(15), p. 1196. doi: 10.1093/EURHEARTJ/EHV529.

Sondergaard, C. *et al.* (2009) 'Assessment of the Impact of Enforced Expression of Platelet Derived Growth Factor Beta in Human Mesenchymal Stem Cells and Contribution to Blood Flow Restoration.', *Blood*. Content Repository Only!, 114(22), p. 3568. doi: 10.1182/BLOOD.V114.22.3568.3568.

Soriano, P. (1994) 'Abnormal kidney development and hem1. Soriano P. Abnormal kidney development and hematological disorders in PDGF beta-receptor mutant mice. Genes Dev [Internet]. 1994 Aug 15 [cited 2017 Aug 8];8(16):1888–96. Available from: http://www.ncbi.nlm.nih.gov/pub', *Genes & development*, 8(16), pp. 1888–96. Available at: http://www.ncbi.nlm.nih.gov/pubmed/7958864 (Accessed: 8 August 2017).

Stamelou, M. *et al.* (2013) 'Progressive ataxia and palatal tremor associated with dense pontine calcification: A unique case', *Movement disorders : official journal of the Movement Disorder Society*. Europe PMC Funders, 28(8), p. 1155. doi: 10.1002/MDS.25310.

Stuart Foster, F., Hossack, J. and Lee Adamson, S. (2011) 'Micro-ultrasound for preclinical imaging', *Interface Focus*. The Royal Society, pp. 576–601. doi: 10.1098/rsfs.2011.0037.

Su, H. *et al.* (2021) 'Emerging Role of Pericytes and Their Secretome in the Heart', *Cells 2021, Vol. 10,*

Page 548. Multidisciplinary Digital Publishing Institute, 10(3), p. 548. doi: 10.3390/CELLS10030548.

Summerhill, V. and Orekhov, A. (2019) *Pericytes in Atherosclerosis*, *Advances in Experimental Medicine and Biology*. Springer New York LLC. Available at: https://link.springer.com/chapter/10.1007/978-3-030-16908-4_13 (Accessed: 4 August 2020).

Tallquist, M. D., French, W. J. and Soriano, P. (2003) 'Additive Effects of PDGF Receptor β Signaling Pathways in Vascular Smooth Muscle Cell Development', *PLOS Biology*. Public Library of Science, 1(2), p. e52. doi: 10.1371/JOURNAL.PBIO.0000052.

Tallquist, M. and Kazlauskas, A. (2004) 'PDGF signaling in cells and mice', *Cytokine & Growth Factor Reviews*. Pergamon, 15(4), pp. 205–213. doi: 10.1016/J.CYTOGFR.2004.03.003.

Tannenberg, P. *et al.* (2018) 'Extracellular retention of PDGF-B directs vascular remodeling in mouse hypoxia-induced pulmonary hypertension', *American Journal of Physiology-Lung Cellular and Molecular Physiology*. American Physiological Society Bethesda, MD , 314(4), pp. L593–L605. doi: 10.1152/ajplung.00054.2017.

Tarascio, M. *et al.* (2017) 'Speckle-Tracking Layer-Specific Analysis of Myocardial Deformation and Evaluation of Scar Transmurality in Chronic Ischemic Heart Disease', *Journal of the American Society of Echocardiography*. Mosby, 30(7), pp. 667–675. doi: 10.1016/J.ECHO.2017.03.015.

Thompson, R. C. *et al.* (2013) 'Atherosclerosis across 4000 years of human history: the Horus study of four ancient populations', *The Lancet*. Elsevier, 381(9873), pp. 1211–1222. doi: 10.1016/S0140-6736(13)60598-X.

Tillie, R. J. H. A. *et al.* (2021) 'A switch from cell-associated to soluble PDGF-B protects against atherosclerosis, despite driving extramedullary hematopoiesis', *Cells*. Cells, 10(7). doi: 10.3390/cells10071746.

Tobb, K., Kocher, M. and Bullock-Palmer, R. P. (2022) 'Underrepresentation of women in cardiovascular trials- it is time to shatter this glass ceiling', *American Heart Journal Plus: Cardiology Research and Practice*. Elsevier, 13, p. 100109. doi: 10.1016/J.AHJO.2022.100109.

Tomoaia, R. *et al.* (2019) 'Understanding the role of echocardiography in remodeling after acute myocardial infarction and development of heart failure with preserved ejection fraction', *Medical Ultrasonography*, 21(1), pp. 69–76. Available at: https://medultrason.ro/medultrason/index.php/medultrason/article/view/1768 (Accessed: 8 October 2021).

Tournoux, F. *et al.* (2011) 'Validation of non invasive measurements of cardiac output in mice using

echocardiography', *Journal of the American Society of Echocardiography : official publication of the American Society of Echocardiography*. NIH Public Access, 24(4), p. 465. doi: 10.1016/J.ECHO.2010.12.019.

Trepanowski, J. F., Mey, J. and Varady, K. A. (2014) 'Fetuin-A: a novel link between obesity and related complications', *International Journal of Obesity 2015 39:5*. Nature Publishing Group, 39(5), pp. 734–741. doi: 10.1038/ijo.2014.203.

Turiello, R., Pinto, A. and Morello, S. (2020) 'CD73: A Promising Biomarker in Cancer Patients', *Frontiers in Pharmacology*. Frontiers Media S.A., 11, p. 1808. doi: 10.3389/FPHAR.2020.609931/BIBTEX.

Vanlandewijck, M. *et al.* (2015) 'Functional Characterization of Germline Mutations in PDGFB and PDGFRB in Primary Familial Brain Calcification', *PLOS ONE*. Edited by M. G. Castro. Public Library of Science, 10(11), p. e0143407. doi: 10.1371/journal.pone.0143407.

Vazquez-Liebanas, E. *et al.* (2022) 'Adult-induced genetic ablation distinguishes PDGFB roles inblood-brain barrier maintenance and development', *Journal of Cerebral Blood Flow & Metabolism*. SAGE Publications, 42(2), p. 264. doi: 10.1177/0271678X211056395.

Vegeto, E., Benedusi, V. and Maggi, A. (2008) 'Estrogen anti-inflammatory activity in brain: a therapeutic opportunity for menopause and neurodegenerative diseases', *Frontiers in neuroendocrinology*. NIH Public Access, 29(4), p. 507. doi: 10.1016/J.YFRNE.2008.04.001.

Vengrenyuk, Y. *et al.* (2015) 'Cholesterol loading reprograms the microRNA-143/145-myocardin axis to convert aortic smooth muscle cells to a dysfunctional macrophage-like phenotype', *Arteriosclerosis, thrombosis, and vascular biology*. Arterioscler Thromb Vasc Biol, 35(3), pp. 535–546. doi: 10.1161/ATVBAHA.114.304029.

Wang, Y. *et al.* (2017) 'Smooth muscle cell recruitment to lymphatic vessels requires PDGFB and impacts vessel size but not identity', *Development (Cambridge, England)*. Company of Biologists, 144(19), p. 3590. doi: 10.1242/DEV.147967.

Wang, Y. *et al.* (2018) 'Imaging Cardiovascular Calcification', *Journal of the American Heart Association: Cardiovascular and Cerebrovascular Disease*. Wiley-Blackwell, 7(13). doi: 10.1161/JAHA.118.008564.

Weintraub, R. G., Semsarian, C. and Macdonald, P. (2017) 'Dilated cardiomyopathy', *Lancet (London, England)*. Lancet, 390(10092), pp. 400–414. doi: 10.1016/S0140-6736(16)31713-5.

Winkler, E. A., Bell, R. D. and Zlokovic, B. V. (2010) 'Pericyte-specific expression of PDGF beta

receptor in mouse models with normal and deficient PDGF beta receptor signaling', *Molecular Neurodegeneration*. BioMed Central, 5(1), pp. 1–11. doi: 10.1186/1750-1326-5-32/FIGURES/3.

Woodward, H. J. *et al.* (2021) 'Regulatory Role of Sex Hormones in Cardiovascular Calcification', *International Journal of Molecular Sciences*. Multidisciplinary Digital Publishing Institute (MDPI), 22(9), p. 4620. doi: 10.3390/IJMS22094620.

Xiong, G. *et al.* (2017) 'Men and Women Differ in the Biochemical Composition of Platelet-Rich Plasma':, *https://doi.org/10.1177/0363546517740845*. SAGE PublicationsSage CA: Los Angeles, CA, 46(2), pp. 409–419. doi: 10.1177/0363546517740845.

Xu, Y. and Sun, Z. (2015) 'Molecular Basis of Klotho: From Gene to Function in Aging', *Endocrine Reviews*. Oxford Academic, 36(2), pp. 174–193. doi: 10.1210/ER.2013-1079.

Yamate, J. *et al.* (1987) 'Observations on soft tissue calcification in DBA/2NCrj mice in comparison with CRJ:CD-l mice', *Laboratory Animals*, 21, pp. 289–298.

Yang, Y. H. K. (2018) 'Aging of mesenchymal stem cells: Implication in regenerative medicine', *Regenerative Therapy*. Japanese Society for Regenerative Medicine, 9, p. 120. doi: 10.1016/J.RETH.2018.09.002.

Yao, J. *et al.* (2015) 'Serine Protease Activation Essential for Endothelial-Mesenchymal Transition in Vascular Calcification', *Circulation research*. Circ Res, 117(9), pp. 758–769. doi: 10.1161/CIRCRESAHA.115.306751.

Yao, Y., Shahbazian, A. and Boström, K. I. (2008) 'Proline and γ-carboxylated glutamate residues in matrix Gla protein are critical for binding of bone morphogenetic protein-4', *Circulation Research*. Lippincott Williams & Wilkins, 102(9), pp. 1065–1074. doi: 10.1161/CIRCRESAHA.107.166124.

Yingchoncharoen, T. *et al.* (2013) 'Normal Ranges of Left Ventricular Strain: A Meta-Analysis', *Journal of the American Society of Echocardiography*. Mosby, 26(2), pp. 185–191. doi: 10.1016/J.ECHO.2012.10.008.

Yu, C. M. *et al.* (2007) 'Usefulness of Tissue Doppler Velocity and Strain Dyssynchrony for Predicting Left Ventricular Reverse Remodeling Response After Cardiac Resynchronization Therapy', *The American Journal of Cardiology*. Excerpta Medica, 100(8), pp. 1263–1270. doi: 10.1016/J.AMJCARD.2007.05.060.

Zakiniaeiz, Y. *et al.* (2016) 'Focus: Sex and Gender Health: Balance of the Sexes: Addressing Sex Differences in Preclinical Research', *The Yale Journal of Biology and Medicine*. Yale Journal of Biology and Medicine, 89(2), p. 255. Available at: /pmc/articles/PMC4918870/ (Accessed: 17 July 2022).

Zarb, Y. *et al.* (2019) 'Ossified blood vessels in primary familial brain calcification elicit a neurotoxic astrocyte response', *Brain*. Oxford University Press, 142(4), p. 885. doi: 10.1093/BRAIN/AWZ032.

Zeng, Y. H. *et al.* (2021) 'Mutation Analysis of MYORG in a Chinese Cohort With Primary Familial Brain Calcification', *Frontiers in Genetics*. Frontiers Media S.A., 12, p. 1857. doi: 10.3389/FGENE.2021.732389/BIBTEX.

Zhang, L. *et al.* (2021) 'Contributions of the Endothelium to Vascular Calcification', *Frontiers in Cell and Developmental Biology*. Frontiers Media SA, 9. doi: 10.3389/FCELL.2021.620882.

Zhang, T. Y. *et al.* (2021) 'Effect of aging and sex on cardiovascular structure and function in wildtype mice assessed with echocardiography', *Scientific Reports*. Nature Publishing Group, 11(1), p. 22800. doi: 10.1038/s41598-021-02196-0.

Zhou, S. *et al.* (2008) 'Age-related intrinsic changes in human bone-marrow-derived mesenchymal stem cells and their differentiation to osteoblasts', *Aging Cell*. John Wiley & Sons, Ltd, 7(3), pp. 335–343. doi: 10.1111/J.1474-9726.2008.00377.X.

Zhou, T. *et al.* (2021) 'Challenges and advances in clinical applications of mesenchymal stromal cells', *Journal of Hematology & Oncology 2021 14:1*. BioMed Central, 14(1), pp. 1–24. doi: 10.1186/S13045-021-01037-X.

Zhu, D. *et al.* (2012) 'Mechanisms and Clinical Consequences of Vascular Calcification', *Frontiers in Endocrinology*. Frontiers Media SA, 3(AUG). doi: 10.3389/FENDO.2012.00095.

Zuo, H. *et al.* (2020) 'Myocardial Deformation Pattern Differs between Ischemic and Non-ischemic Dilated Cardiomyopathy: The Diagnostic Value of Longitudinal Strains', *Ultrasound in Medicine & Biology*. Elsevier, 46(2), pp. 233–243. doi: 10.1016/J.ULTRASMEDBIO.2019.10.006.

Zymek, P. *et al.* (2006) 'The Role of Platelet-Derived Growth Factor Signaling in Healing Myocardial Infarcts', *Journal of the American College of Cardiology*, 48(11), pp. 2315–2323. doi: 10.1016/j.jacc.2006.07.060.